

Progressive Damage and Failure Analysis of 3D Textile Composites Subjected to Flexural Loading

by

Dianyun Zhang

A dissertation submitted in partial fulfillment
of the requirements for the degree of
Doctor of Philosophy
(Aerospace Engineering)
in The University of Michigan
2014

Doctoral Committee:

Professor Anthony M. Waas, Chair
Assistant Professor Samantha H. Daly
Assistant Professor Mark R. Pankow, North Carolina State University
Associate Professor Veera Sundararaghavan
Chian-Fong Yen, Army Research Laboratory

© Dianyun Zhang 2014
All Rights Reserved

In loving memory of my grandmother, Meifang Zhu, who has been a constant source of love and caring, and will be forever in my heart.

ACKNOWLEDGEMENTS

First and foremost, I would like to thank my advisor, Professor Anthony Waas, for his support, encouragement, and guidance throughout my studies at the University of Michigan. Thank you for giving me my first opportunity to conduct research as an undergraduate student and introducing me the beauty of solid mechanics. Thank you for always having faith in me and instilling in me what it means to be an excellent researcher, engineer, and instructor. I have been truly inspired by your numerous innovative ideas, your enthusiasm for solving engineering problems, and your passion for teaching and research throughout these years.

A special thanks goes out to Professor Mark Pankow, not only for serving on my doctoral committee, but also for giving me tremendous help and guidance as a mentor throughout my Ph.D. studies. Your support and encouragement is invaluable. I would also like to thank my other dissertation committee members: Professor Samantha Daly, Professor Veera Sundararaghavan, and Dr. Chian-Fong Yen. Your valuable comments and suggestions on my thesis work have been greatly appreciated.

I am grateful to my colleagues from the Composite Structures Laboratory at the University of Michigan: Dr. Mark Pankow, Amit Salvi, Dr. Wooseok Ji, Dr. Evan Pineda, Dr. Christian Heinrich, Dr. Pavana Prabhakar, Dr. Scott Stapleton, Dr. Paul Davidson, Dr. Royan D’Mello, Dr. Eugene Kheng, Dr. Trisha Sain, Dr. Wu Xu, Dr. Jie (Vincent) Wang, Brian Justusson, Pascal Meyer, Zach Kier, Lucas Hansen, Nhung Nguyen, Jiawen Xie, Ashith Joseph, Cyrus Kosztowny, Solver Thorsson, Stewart Boyd, Marianna Maiaru, Armanj Hasanyan, Deepak Patel, and David Singer. It has been an absolute pleasure and a learning experience working with such a bright and friendly group. Additionally, I would like to express my gratitude towards all the technical and administrative staff in the Department of Aerospace Engineering at the University of Michigan for their help and support.

Thanks to my great friends: Jin Yan, Xiaoning Jin, Changyuan Yu, Wu Xiao, Shuyu Wang, Shiming Duan, Jie Zhu, Congzhen Qiao, Qian Zhang, Xueqing Li, Peter Zhoujie Lyu, Yuntao Chen, Zhaojian Li, Shinuo Weng, Yanli Wang, Hai Wang, Keqin Cao, Lingxi Yuan, and Min Zhu. Pursuing a doctoral degree is a long journey, mixed

with hope and frustration, joy and tears. I cannot survive without your support.

Last but not least, I would like to thank my beloved parents, Jingsong Zhu and Guoxian Zhang. Thank you for always having faith in me and providing me with an exceptional education opportunity. This thesis would not have been possible without your love, encouragement, and support.

The author would like to acknowledge the support of Textile Engineering and Manufacturing (T.E.A.M.) Inc., RI, and Albany Engineered Composites, Inc., NY, for providing the testing specimens. The author is also grateful for financial sponsorship from the Army Research Office (Dr. Larry Russel, Program Manager) and the encouragement and support of Dr. Chian-Fong Yen at the Army Research Laboratory, Aberdeen Proving Ground, MD.

TABLE OF CONTENTS

DEDICATION	ii
ACKNOWLEDGEMENTS	iii
LIST OF FIGURES	ix
LIST OF TABLES	xiv
LIST OF APPENDICES	xvi
ABSTRACT	xvii
CHAPTER	
I. Introduction	1
1.1 Motivation	1
1.2 Hierarchy of Textile Composites	3
1.3 Failure Mechanisms in Textile Composites	5
1.4 Modeling Strategy for Textile Composites	8
1.4.1 Multiscale Modeling	9
1.4.2 Mesoscale Model	9
1.4.3 Micromechanical Analysis	11
1.4.4 Computational Damage and Failure Models	12
1.5 Research Objectives and Thesis Outline	13
II. Material Microstructure and Characterization	16
2.1 Introduction	16
2.2 Textile Architecture	17
2.3 Material Systems Investigated in This Dissertation	18
2.4 Fabrications and Manufacturing Induced Imperfections	23
2.4.1 Geometry Imperfections in the Layer-to-Layer 3D Textile Composites	23
2.4.2 Thermal Effects on the Hybrid 3DTCs	24

2.5	Microscopy Studies	25
2.6	Fiber Properties	26
2.7	Matrix Properties	28
2.8	Conclusions	30
III. Characterization of the Flexural Response of 3DTCs		31
3.1	Introduction	31
3.2	Testing Configurations	31
3.3	Quasi-Static Three-Point and Four-Point Bend Tests	36
3.3.1	Albany 2 Panels Subjected to Flexural Loading	36
3.3.2	Hybrid Panels Subjected to Flexural Loading	40
3.3.3	Effects of Hybridization Obtained Through Quasi-Static Three-Point Bend Tests	46
3.4	Dynamic Three-Point Bend Tests	52
3.4.1	MTS: 2 in/sec	52
3.4.2	Drop Tower Test	56
3.5	Conclusions	62
IV. Modeling Progressive Microdamage and Failure in a Polymer Matrix		64
4.1	Introduction	64
4.2	Modeling the Microdamage in Matrix Based upon Modified J_2 Deformation Theory of Plasticity	66
4.3	Modeling the Failure of the Matrix Material Using the SCA	70
4.3.1	SCA Formulation	70
4.3.2	Characteristic Length Scale Associated with the Traction-Separation Law	76
4.3.3	Tensile Failure	79
4.3.4	Compressive Failure	80
4.4	Example – Mesh Objectivity	81
4.5	Conclusions	85
V. A Micromechanics-Based Multiscale Model for a Single Fiber Tow		87
5.1	Introduction	87
5.2	Tow Microstructure	91
5.3	Micromechanics Model	92
5.3.1	Computation of E_1^c , ν_{12}^c , and F_{i1} components by applying ϵ_{11}^c	93
5.3.2	Computation of G_{12}^c and F_{i4} components by applying γ_{12}^c	95
5.3.3	Computation of the transverse properties	98

5.3.4	Matrix strain contours under a single applied composite strain	107
5.4	Multiscale Modeling Methodology for Nonlinear Composites	113
5.5	Model Validation	115
5.5.1	Finite Element Model	115
5.5.2	Elastic Properties	117
5.5.3	Nonlinear Response	120
5.6	Conclusions	126
VI. Fiber Tow Failure Mechanisms		128
6.1	Introduction	128
6.2	Failure Mechanisms of a Single Fiber Tow	129
6.3	Compressive Failure: A Micromechanical Study on Kink Banding 131	
6.3.1	Micromechanics-Based Two-Scale Model for a Single Fiber Tow	132
6.3.2	In-Situ Matrix Properties	133
6.3.3	FE Model	136
6.3.4	Results: Compressive Strength	138
6.4	Implementation of the SCA to Model the Failure Response of a Single Fiber Tow	142
6.5	Conclusion	145
VII. Mechanics Based Multiscale Modeling of Progressive Damage and Failure of 3D Woven Composites		146
7.1	Introduction	146
7.2	Multiscale Modeling Framework	149
7.2.1	Global-Local Hybrid Finite Element Model	149
7.2.2	Determination of the Homogenized Composite Properties	151
7.2.3	Construction of the Mesoscale Model	152
7.2.4	Matrix Constitutive Relations Used in the Mesoscale Model	156
7.2.5	Fiber Tow Constitutive Relations Used in the Mesoscale Model	156
7.2.6	Boundary Conditions and Analysis Procedures	161
7.3	Results: Albany 2 Subjected to Quasi-Static Three-Point Bending	162
7.3.1	Elastic Response (Strain Contours)	162
7.3.2	Progressive Damage and Failure Response	163
7.4	Results: Hybrid 3DTC	168
7.4.1	Quasi-Static analysis	168
7.4.2	Dynamic Analysis (Drop Tower Test)	174
7.5	Conclusions	180

VIII. Concluding Remarks	181
APPENDICES	184
A. Determination of the Crack Orientation Transformation Matrix	185
B. Transformations between the Cartesian and Cylindrical Coordinates .	189
C. Formulation for the Extended Generalized Self-Consistent Method . .	190
D. Computation of the Matrix Strain Fields Using Finite Element Analysis	194
E. Formulations for the Concentric Cylinder Model and Mori-Tanaka Method	196
E.1 Concentric Cylinder Model	196
E.2 Mori-Tanaka Method	197
F. Computation of the Macroscopic Effective Properties of 3D Textile Composites	200
F.1 Fiber Tow Stiffness in the 1 – 2 – 3 Coordinate System (Local Coordinates)	200
F.2 Stiffness in the $x' - y' - z'$ Coordinate System (Ply Coordinates)	201
F.3 Stiffness in the $x - y - z$ Coordinate System (Global Coordinates)	202
F.4 RUC Stiffness	203
BIBLIOGRAPHY	206

LIST OF FIGURES

Figure

1.1	Hierarchy of textile composites. Each hierarchical level is associated with a characteristic length scale.	4
1.2	Matrix cracking on a tension specimen shows an architecture dependent effect. The crack paths are represented by the black lines. . . .	6
1.3	Internal cracking in the failed tension specimen.	7
1.4	Fiber tow kinking observed in a 2D triaxially braided textile composite subjected to compression.	7
1.5	Rate dependent compressive response of 3D textile composites. The failed specimen shows a failure mode transition from kind banding at low rates to delamination at higher rates of loading.	8
2.1	Z-fiber weaving architecture.	18
2.2	Layer-to-layer interlock architecture.	18
2.3	Ideal textile architecture of the layer-to-layer interlock glass fiber 3DTC (Albany 2).	19
2.4	The glass fiber preform of Albany 2 after the matrix burnout test.	20
2.5	3D hybrid Z-fiber orthogonal interlock textile architectures.	21
2.6	Cross sections of the cured 3D hybrid textile composites.	22
2.7	Manufacturing effect on the textile architecture (Albany 2).	24
2.8	Initial curvatures observed in the hybrid unsymmetric panels.	24
2.9	Optical micrographs of Albany2 specimen. The fiber tow is idealized to undulate as a sinusoidal wave with an elliptical cross section.	26
2.10	Optical micrographs for the thin unsymmetric specimens. The warp and weft tows are assumed to be straight with rectangular cross sections, and the binder tows are of elliptical cross sections.	27
2.11	Representative uniaxial stress-strain responses for SC-15 epoxy in tension and compression.	29
3.1	Schematics of three-point and four-point bend testing configurations. The side surface of the specimen is speckled as indicated.	33
3.2	Testing matrix.	34
3.3	Various flexural configurations are studied to investigate the textile architecture-dependent effect.	35

3.4	Representative load-displacement responses for Albany 2 specimens subjected to 3-pt bend tests. Surface strain patterns using DIC capture the damage occurrences.	37
3.5	Kink band formation on the compression side of the Albany 2 specimen.	38
3.6	Experimental 3-pt and 4-pt load-displacement responses for Albany 2 panels (warp).	38
3.7	Progressive damage events for Albany 2 panel subjected to quasi-static 4-point bending. Matrix cracks are illustrated by the black lines. The specimen is loaded along the warp direction.	39
3.8	Experimental three-point load-displacement responses for various hybrid architectures.	41
3.9	Progressive damage events for the thin unsymmetric panel subjected to quasi-static 3-point bending. The specimen is loaded along the warp direction.	42
3.10	Progressive damage events for the thick unsymmetric panel subjected to quasi-static 3-point bending. The specimen is loaded along the warp direction.	43
3.11	Progressive damage events for the thick symmetric panel subjected to quasi-static 3-point bending. The specimen is loaded along the warp direction.	44
3.12	Axial surface strain contours showing the tensile matrix cracking. The material architectures are shown to the right.	45
3.13	Kink bands were observed on the compression side of the flexed specimen. The post-damage surface was polished and examined under both optical microscope and SEM.	46
3.14	Schematic of experimental load-displacement response for 3D woven composite subjected to flexural loading. The observed damage events are annotated along with the deformation history.	47
3.15	Flexural stress versus strain relations for various hybrid architectures.	48
3.16	Defined failure characteristics to compare the performance of the different hybrid architectures.	48
3.17	Experimental load-displacement responses for each of the testing configurations of the thin unsymmetric panels at two loading rates. The dynamic three-point bend tests were performed using MTS testing machine at a loading rate of 2 in/sec.	53
3.18	Experimental load-displacement responses for each of the testing configurations of the thick unsymmetric panels at two loading rates. The dynamic three-point bend tests were performed using MTS testing machine at a loading rate of 2 in/sec.	54
3.19	Experimental load-displacement responses for the thick symmetric panels testing along both warp and weft directions at two loading rates. The dynamic three-point bend tests were performed using MTS testing machine at a loading rate of 2 in/sec.	55
3.20	Drop tower test setup.	57

3.21	Experimental load-displacement responses for each of the testing configurations of the thin unsymmetric panels from drop tower tests. . .	58
3.22	Experimental load-displacement responses for each of the testing configurations of the thick unsymmetric panels from drop tower tests. . .	59
3.23	Experimental load-displacement responses for each of the testing configurations of the thick symmetric panels from drop tower tests. . .	59
3.24	Experimental load-displacement responses for each of the testing configurations of the thin unsymmetric panels at the four different loading rates.	60
3.25	Experimental load-displacement responses for each of the testing configurations of the thick unsymmetric panels at the four different loading rates.	61
3.26	Experimental load-displacement responses for each of the testing configurations of the thick symmetric panels at the four different loading rates.	61
4.1	Schematic of matrix constitutive behavior including damage and failure.	65
4.2	Representative uniaxial stress-strain response for polymer matrix. The evolution of pre-peak nonlinearity is modeled through a secant moduli approach.	67
4.3	Traction-separation laws.	71
4.4	Crack morphology. There exist one normal and two shear crack components at the crack interface in 3D stress state.	72
4.5	Discrete cracks are smeared out within a finite element.	77
4.6	Stress-strain softening response is related to the traction-separation law through a characteristic length, h	77
4.7	Characteristic length, h . The length of the element projected on the crack normal is used as the characteristic element length.	78
4.8	Crack evolution is dictated using degrading secant crack stiffness. . .	78
4.9	Boundary conditions for a RUC subjected to uniaxial tension. A uniform displacement field is prescribed.	83
4.10	Four different mesh sizes used in mesh objectivity study. The cracked elements are shown in red.	84
4.11	Load-displacement responses for RUC subjected to tension with four different mesh sizes. The peak load and the fracture energy are unaffected by the element size.	85
5.1	The cross section of a single fiber tow under SEM.	88
5.2	Fiber tow is represented as a unidirectional fiber-reinforced composite.	92
5.3	Two-phase concentric cylinder model.	96
5.4	Projection of the concentric cylinders onto the $x_1 - x_2$ plane. The concentric pair is subjected to an axial shear strain, γ_{12}^c	99
5.5	Illustration of the generalized self-consistent method.	100
5.6	Matrix strain contours under $\epsilon_{11}^c = 0.1\%$. The constituent fiber is IM-7 carbon fiber.	109
5.7	Matrix strain contours under $\epsilon_{22}^c = 0.1\%$. The constituent fiber is IM-7 carbon fiber.	110

5.8	Matrix strain contours under $\gamma_{12}^c = 0.1\%$. The constituent fiber is IM-7 carbon fiber.	111
5.9	Matrix strain contours under $\gamma_{23}^c = 0.1\%$. The constituent fiber is IM-7 carbon fiber.	112
5.10	3D finite element model.	117
5.11	The composite effective elastic moduli computed from various micromechanics models.	118
5.12	The composite effective axial normal stress versus strain response.	122
5.13	The composite effective transverse normal stress versus strain response.	123
5.14	The composite effective axial shear stress versus strain response.	124
5.15	The composite effective transverse shear stress versus strain response.	125
6.1	Fiber failure modes.	130
6.2	Matrix failure mode.	130
6.3	Uniaxial responses of SC-15 epoxy resin obtained from the four different tests.	135
6.4	The stress versus strain responses of SC-15 epoxy resin used in the two-scale micromechanics model to compute the fiber tow compressive strength.	135
6.5	Boundary conditions for the fiber tow subjected to uniaxial compression with initial fiber misalignment angle ϕ_0 . $\zeta_1 - \zeta_2$ coordinate system designates the instantaneous material frame where “1” defines the fiber direction.	137
6.6	Normalized axial stress versus strain response for glass fiber tow using the three different mesh sizes. The initial fiber misalignment angle is 1° , and the fiber volume fraction is 60%.	139
6.7	Deformed shapes at various loading levels. The contours show the axial shear strain in the instantaneous material frame $\zeta_1 - \zeta_2$ illustrated in Figure 6.5(b).	140
6.8	Kink band formation computed using the three different mesh sizes.	141
6.9	Traction-separation law for fiber tows that accounts for the difference between tension and compression.	144
7.1	Illustration of the three different scales used in the proposed global-local modeling framework.	150
7.2	Mesoscale model for Albany 2. In each model, only a unit width of fiber tows are modeled along its axial direction. The tows running along the width are assumed to be straight.	153
7.3	RUC for thin unsymmetric hybrid 3DTC. The RUC is broken down into various constituents.	154
7.4	Mesoscale models for thin unsymmetric hybrid 3DTC. The two models are different in width and length.	155
7.5	Boundary conditions for the 3DTC subjected to three-point bending. The flexural response is modeled using a global-local FE model.	161
7.6	Comparison of the axial strain fields at a load point displacement of 2 mm (Albany 2).	163

7.7	Comparison of the load-displacement responses obtained from the experiment and the computational model. The Albany 2 specimen is loaded along the warp direction. The evolution of matrix cracking and the deformed shapes of the fiber tows at the labeled points are shown in Figure 7.8 and Figure 7.9, respectively.	165
7.8	Evolution of matrix cracking during the deformation (Albany 2, Case B). The cracked elements are shown in red.	166
7.9	Evolution of fiber tow crack strains during the deformation (Albany 2, Case B). The crack strains are shown in absolute values.	167
7.10	Comparison of the load-displacement responses obtained from the experiment and the computational model using Model A. The thin unsymmetric hybrid panel is loaded along the weft direction under quasi-static three point bending with the glass layers in compression. The deformed shapes at the labeled points are shown in Figure 7.12.	169
7.11	Deformed shapes at the last step of the implicit simulation.	169
7.12	Evolution of fiber tow crack strains during the deformation computed using the explicit solver (hybrid). The crack strains are shown in absolute values.	170
7.13	Load-displacement responses obtained from the two different mesoscale models.	171
7.14	Deformation response obtained from the modified model compared against the previous result. The modified model is able to capture the tow tensile breakage.	173
7.15	Comparison of the deformation responses obtained from the experiment and the computational model with the failure characteristics of Case 2. The thin unsymmetric hybrid composite panel is loaded along the weft direction with the glass layers in compression. The initial impact velocity is 3866 mm/sec (152 in/sec).	176
7.16	Load-displacement responses for various cases used in the parametric study. The failure characteristics for each case are summarized in Table 7.9. The thin unsymmetric hybrid composite panel is loaded along the weft direction with the glass layers in compression. The initial impact velocity is 3866 mm/sec (152 in/sec).	177
7.17	Comparison of the deformation responses obtained from the experiment and the computational model. The thin unsymmetric hybrid composite panel is loaded along the weft direction with the carbon layers in compression. The initial impact velocity is 3866 mm/sec (152 in/sec).	179
A.1	Crack orientation. The local crack orients in the $1' - 2' - 3'$ coordinate with the crack normal aligned with the $1'$ -direction	188
D.1	Three-phase finite element model for the transverse problem.	195
F.1	$x' - z'$ plane profile of an undulating fiber tow.	201

LIST OF TABLES

Table

2.1	Panel thickness and constituent fractions for the 3D hybrid woven composites.	20
2.2	Fiber tow geometry for Albany 2.	25
2.3	Fiber tow geometry for the thin unsymmetric panel.	26
2.4	Fiber volume fractions for different constituent fiber tows.	27
2.5	Elastic modulus and ultimate strength for IM-7 carbon fiber, S-2 glass fiber, and Kevlar.	28
2.6	Static properties for SC-15 epoxy in tension and compression. . . .	29
3.1	Flexural test configurations.	33
3.2	Elastic properties and failure characteristics.	51
3.3	Experimental setup for drop tower test. The thick panel includes the thick symmetric and unsymmetric one.	56
4.1	Material properties used in the mesh objectivity study.	83
5.1	Elastic properties for IM-7 carbon fiber, S-2 glass fiber, and SC-15 matrix.	108
5.2	The nonlinear properties of SC-15 matrix.	115
6.1	Nonlinear matrix properties used in the two-scale micromechanics model to compute the fiber tow compressive strength.	136
6.2	Three different mesh sizes used in the mesh sensitivity study to compute the fiber tow compressive strength.	136
6.3	Computed compressive strength for carbon and glass fiber tows using various initial fiber misalignment angles.	142
7.1	Homogeneous properties of the macroscale model. x , y , and z designate the axes shown in Figure 7.2 for Albany 2 and Figure 7.3 for the thin unsymmetric hybrid panel.	152
7.2	Matrix nonlinear properties and failure characteristics used in the mesoscale FE model.	157
7.3	Elastic properties of the fibers and matrix used in the FE model. . .	158
7.4	Elastic properties of fiber tows computed using the proposed micromechanics model.	159
7.5	Matrix nonlinear properties used in the two-scale micromechanics model for modeling the pre-peak nonlinear response of the fiber tows.	159
7.6	Failure characteristics of the constituent tows.	160

7.7	Failure characteristics used in the three different cases for Albany 2.	163
7.8	Failure characteristics used in the quasi-static analysis for the thin unsymmetric hybrid composite with the “glass layer in compression” configuration.	168
7.9	Failure characteristics used in the drop tower simulation for the thin unsymmetric hybrid composite with the “glass layer in compression” configuration.	174
7.10	Failure characteristics used in the drop tower simulation for the thin unsymmetric hybrid composite with the “carbon layer in compression” configuration.	174
D.1	Boundary conditions for the transverse normal and transverse shear problem. The boundary conditions are prescribed on each outer surface of the rectangle. L_1 , L_2 , and L_3 are the length of the rectangle along x_1 , x_2 , and x_3 directions, respectively.	195

LIST OF APPENDICES

Appendix

A.	Determination of the Crack Orientation Transformation Matrix	185
B.	Transformations between the Cartesian and Cylindrical Coordinates .	189
C.	Formulation for the Extended Generalized Self-Consistent Method . .	190
D.	Computation of the Matrix Strain Fields Using Finite Element Analysis	194
E.	Formulations for the Concentric Cylinder Model and Mori-Tanaka Method	196
F.	Computation of the Macroscopic Effective Properties of 3D Textile Composites	200

ABSTRACT

Progressive Damage and Failure Analysis of 3D Textile Composites Subjected to Flexural Loading

by

Dianyun Zhang

Chair: Anthony M. Waas

3D textile composites (3DTCs) are becoming increasingly attractive as light-weight materials for a variety of structural load bearing applications, including those in the aerospace, marine, automotive, and energy generation sectors. Compared with layered prepreg tape-type laminated composites, 3DTCs offer a distinct cost advantage, tailored properties, and enhanced damage tolerance. The term *textile* here is referred to as an interlaced structure, known as a dry preform, which consists of fiber tows (or bundles) that contain many thousands of individual fibers either woven or braided together. In order to maximize the benefit of designing with 3DTCs, it is important to develop a robust, physics-based computational tool to understand how their deformation response is affected by the textile architecture and constituent properties.

The focus of this research is to investigate the deformation response of 3DTCs through flexural tests. The experimental results are subsequently used as a basis for the development of a multiscale mechanics based model for the deformation, damage and failure response of 3DTCs, predominantly under flexural loading. Two distinct types of 3DTCs, a layer-to-layer interlock glass fiber 3DTC and a Z-fiber orthogonal interlock hybrid 3DTC, have been studied in order to understand the architecture-dependent effect.

Quasi-static flexural tests were performed either on a screw-driven loading device or on a hydraulically activated loading machine. To achieve higher loading rates, tests were carried out using a drop tower facility, which can provide different impact velocities by varying the height of the weight that is dropped onto the specimen. The digital image correlation (DIC) technique was utilized to map the deformation

history and identify the failure modes. Although the experimental results show both architecture-dependent and rate-dependent effects, fiber tow kinking, which developed on the compressive side of the specimen was found to be a strength limiting mechanism for this class of materials. Distributed matrix cracking was observed in regions of predominant tension.

A mechanics based multiscale computational model was developed for 3DTCs based upon a global-local modeling strategy, in which the influence of textile architecture is incorporated in a mesoscale finite element model, while the composite is homogenized at the macroscale. The mesoscale model is a collection of representative unit cells that are composed of different types of fiber tows embedded in a surrounding matrix medium. Matrix microdamage, manifested as a pre-peak nonlinear stress versus strain response, is modeled using a modified J_2 deformation theory of plasticity through a secant moduli approach. The fiber tow pre-peak nonlinear response is computed using a novel, two-scale model, in which the subscale micromechanical analysis is carried out in closed form based upon on a unit cell of a fiber-matrix concentric cylinder. Therefore, the influence of matrix microdamage at the microscale manifests as the progressive degradation of the fiber tow stiffness at the mesoscale. The post-peak strain softening responses of the fiber tows and the surrounding polymer matrix are modeled through the smeared crack approach, which is designed to be mesh objective.

The load-deflection response, along with the progressive damage and failure events, including matrix cracking, tow kinking, and tow tensile breakage, are successfully predicted through the proposed multiscale model for the two material systems studied. Since all the inputs are from the constituent level, the model is useful in understanding how the 3DTC macroscopic response is influenced by the geometry of textile architecture and the constitutive response of the constituents.

CHAPTER I

Introduction

1.1 Motivation

Over the past few decades, fiber-reinforced laminated composites have emerged as light-weight materials with widespread use in military aircraft, general aviation, and space launch vehicles. Starting with small quantities implemented in military aircraft, composite materials have been increasingly deployed in commercial aircraft, from secondary wing and tail components to primary load-carrying structures. Encouragingly, over 50 percent of the primary structures in the latest generation of aircraft, such as the Airbus 350 XWB and the Boeing 787 Dreamliner, have been made of composite materials, including the fuselage and wings. A significant weight reduction is achieved owing to the use of composite materials, resulting in lower fuel consumption and enhanced aerodynamic performance. However, high manufacturing costs and low damage tolerance are the two major technical barriers that limit the use of prepreg tape-type laminated composites in other civil application areas such as marine, construction, automotive, and energy generation sectors [1].

In order to overcome these barriers, textile composite technology has been developed with an intent to reduce manufacturing costs and improve damage tolerance. Textile composites are composed of textile reinforcements combined with a polymer matrix material. The term *textile* here is referred to as an interlaced structure, known as a dry preform, which consists of fiber tows (or bundles) that contain many thousands of individual fibers either woven or braided together. 3D reinforcements, which can be achieved using stitching, Z-pins, or 3D weaving, have gained benefit from mechanical bindings through the thickness, for example, in a structural panel [2]. Previous studies have shown that 3D textile composites (3DTCs) can offer increased resistance to delamination and have the ability to contain (localize) the area of damage due to delamination [3, 4, 5, 6].

Since textiles can be mass-produced at a low cost using modern, automated manufacturing techniques, textile composites achieve a significant cost advantage over prepreg tape-type laminated composites, making them viable to be used in automotive, energy saving industrial sectors, and sports gear. Textile reinforcements with complicated internal geometry can be manufactured using a computer-aided weaving loom, thus, the properties of textile composites can be easily tailored for specific applications by varying the types of fibers and weaving architectures. This allows for a single component exhibiting different material properties, for example, high stiffness in one area while increased shear strength in another. CFM International has successfully demonstrated the implementation of 3D woven composites for their Leading Edge Aviaton Propulsion (LEAP) engine fan blades [7]. The textile preform is designed with varied thicknesses such that the blade is thinner at the top and thicker at the bottom to improve the durability of the structure. Owing to the tailored properties and geometries, the 3D woven engine has shown a significant weight reduction and cost advantage over a similar composite engine such as the General Electric GE90 [7]. Moreover, textile composites are suitable for large structural components with complicated shapes, for example, the six-meter diameter dome-shaped rear pressure bulkhead of the Airbus A380, which is manufactured by resin film infusion with non-crimp stitched biaxial carbon fibers. In addition, there are also a number of applications of textile composites in the field of medicine. Splinting materials are becoming the largest medical market for textile composites [1]. Such materials are required to fit to the complicated contours of limbs, while patient comfort urges the materials to maintain high stiffness and light weight. Other biomedical applications include walking support frames, bone plates, and surgical implants [1].

Increased attention is being paid to the advantage of designing with textiles for tailored properties and enhanced performance. In order to maximize the benefit of using textile composites, it is important to develop a robust, physics based computational tool to understand how their deformation response is affected by the textile architecture and constituent properties. Virtual testing, which is based upon modeling and simulation using a computer, has been increasingly employed for the design of structural components. Even though real physical testing remains valuable and necessary in a verification process due to its reliability, virtual testing provides an efficient way to explore new material systems with optimized properties through a large number of “what-if” type computations. Virtual testing is capable of considering more design possibilities while dramatically reducing the cost of physical prototypes and testing, and shortening the product development cycle. In addition, numerical simulation

is an important methodology to understand the material behavior, for example, the constituent in-situ properties within the textile composite, which is difficult to characterize individually through physical tests. Thus, it is critical to develop a reliable and validated numerical tool to predict the mechanical response of textile composites under various in-service loads.

Earlier studies on textile composites mainly focus on the prediction of effective homogeneous responses. A number of analytical models have been developed to compute the elastic properties, including elastic moduli [8, 9, 10, 11] and bending stiffness [12]. However, it should be noted that the textile geometry of an as-fabricated composite experiences various degrees of distortions due to manufacturing processes such as curing and consolidation. It has been pointed out by many researchers, including Cox et al. [13], Huang and Waas [14], and Rao et al. [15], that although the geometric distortion of textile architecture has little effect on the composite elastic moduli, manufacturing induced imperfections can significantly affect the resulting damage and failure behavior, such as strength, strain to failure, and fatigue life. Therefore, it is important to understand the manufacturing induced effects on the composite macroscopic responses, including both elastic properties and failure characteristics. Since this family of materials has been extensively used for crashworthy components, experiencing severe in-service loading scenarios such as impact, shock, and blast, it is critical to incorporate damage and failure mechanisms into a computational framework. The predictive capability of the numerical model need to be demonstrated through a set of coupon-level tests by comparing the numerical simulation results with the corresponding experiments.

1.2 Hierarchy of Textile Composites

Textile composites contain hierarchical structures that can be broken down into various constituent levels, as shown in Figure 1.1. Based upon the length scale, the composite can be differentiated into three primary scales as (1) fibers at the *microscale*; (2) representative unit cells (RUCs) containing internal structures of textile reinforcements at the *mesoscale*; and (3) textile composite structures at the *macroscale*. The microscale is associated with fiber diameters of 5 – 10 μm . The mesoscale is characterized by fiber tows with lengths typically ranging from 1 mm to 10 mm. Textile composite structures that contain multiple RUCs with length scales of 1 – 10 m and above are considered as the macroscale.

The hierarchical nature of textile composites makes the characterization and mod-

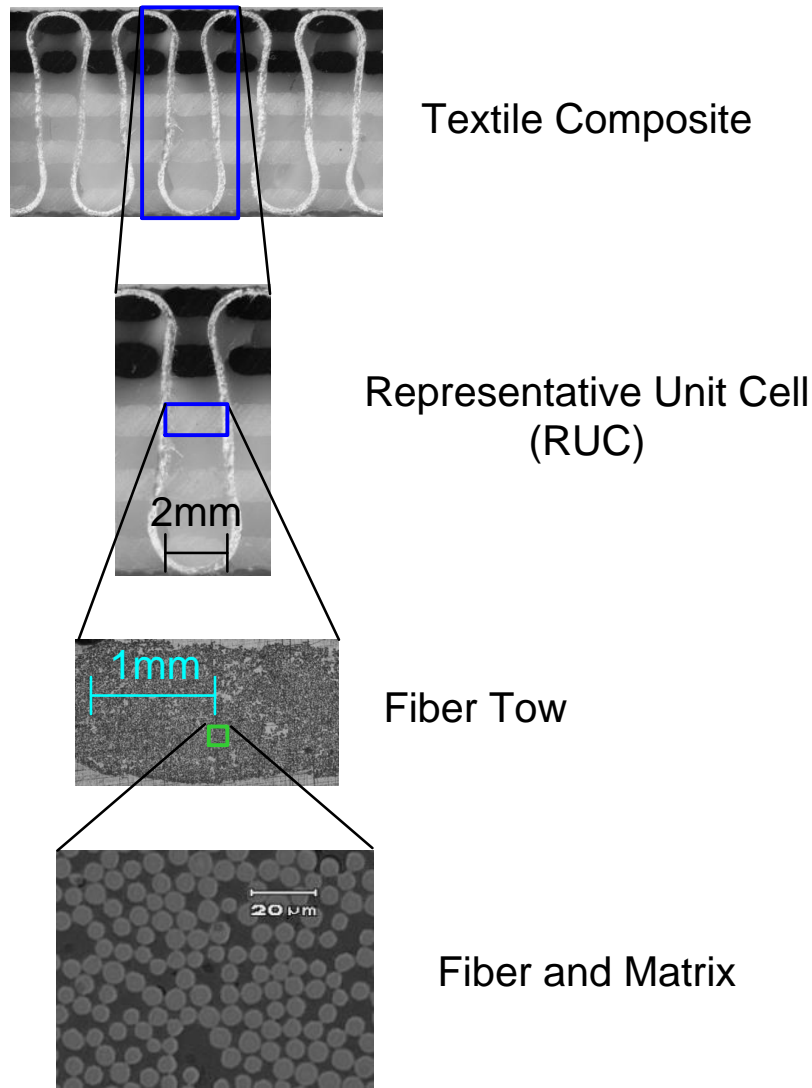


Figure 1.1: Hierarchy of textile composites. Each hierarchical level is associated with a characteristic length scale.

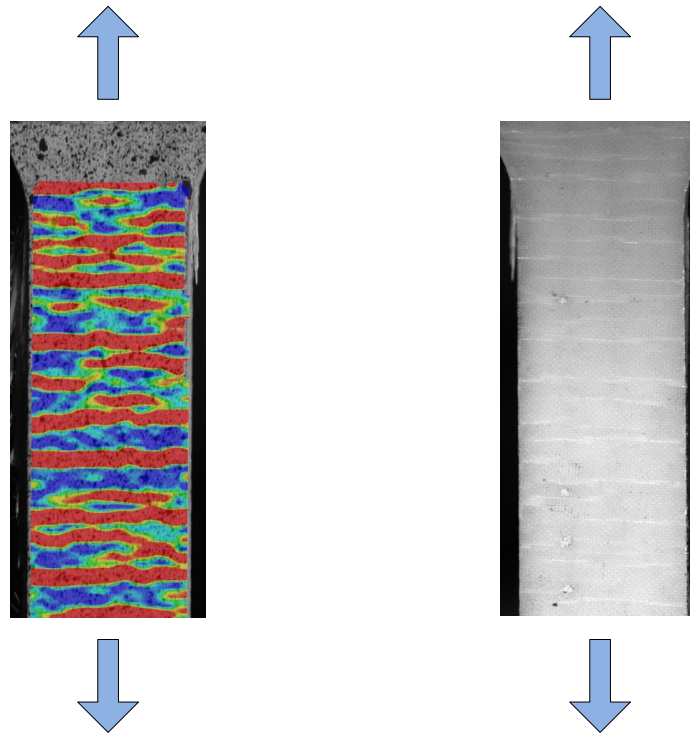
eling of such materials a great challenge. Coupon-level testing is only able to provide the overall, macroscopic response of textile composites, while the properties of the fiber tows and surrounding matrix within the composites are difficult to characterize directly. Experiments need to be specifically designed to better understand the constituent behavior. Alternatively, a robust numerical model at the microscale, or at the atomic-scale, can be used to determine the constituent properties at the mesoscale including both linear and nonlinear responses. Due to the heterogeneity of textile composites, each constituent experiences complicated loading histories, resulting in

various damage and failure mechanisms evolving across different length scales. Thus, the computational model must use micromechanical considerations to couple the influence of microstructure on the macroscale response while remaining computationally efficient for large scale structural analysis including damage tolerance and durability.

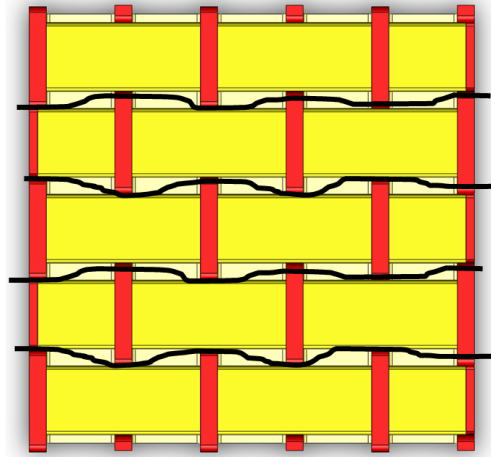
1.3 Failure Mechanisms in Textile Composites

Understanding damage and failure of textile composites is critical for widespread use of the materials with maximal benefit from their architecture. It has been reported by a number of researchers that although 3D reinforcements can improve the resistance to delamination, the insertion of through-the-thickness Z-fibers tends to decrease the ultimate strength in tension [13, 16, 17, 18, 19]. The failure is typically initiated due to matrix cracking between the fiber tows, and the location is also related to the strain concentrations caused by the presence of Z-fibers. The surface strain histories, which can be obtained through a digital image correlation (DIC) technique, show a strong architecture dependent result [20, 21]. Figure 1.2(a) shows the surface strain contours for a Z-fiber architecture 3DTC subjected to uniaxial tension. The site of the strain concentration indicates the onset of matrix cracking, which is evident from the image simultaneously taken on the opposite unpainted surface, as shown in Figure 1.2(b). These matrix cracks tend to occur at the locations where the Z-fibers go through into the preform, causing a matrix pocket, as illustrated in Figure 1.2(c), [19]. To further investigate the internal matrix cracking patterns, the failed specimen was cut down the middle in the direction of the tension load, and the exposed internal surface was soaked in a dye penetrant. As shown in Figure 1.3, cracks tend to occur in the matrix around the fiber tows, orientated perpendicular to the tension direction, while additional cracks are observed at the interface of the warp and weft tows, running along the loading direction [22]. Further investigation of the crack initiation and progression is important to understand the load transfer between the constituent materials and the influence of architecture on the progressive failure response of 3DTCs.

The compressive failure of textile composites has been extensively studied by Cox et al. [8, 23], Quek et al. [24], Huang and Waas [14], and De Carvalho et al.[25]. In their studies, although matrix cracking is observed, fiber tow kinking is determined as a strength limiting failure mechanism for this class of materials subjected to compression. Figure 1.4(a) shows the fiber tow kinking observed in a 2D triaxially braided textile composite right after the peak load has been reached.



(a) Surface strain contour plots overlaid on the tension specimen [19]. (b) Matrix cracking develops on the tension specimen [19].



(c) Illustration of crack paths [19].

Figure 1.2: Matrix cracking developed on the tension specimen shows an architecture dependent effect. The crack paths are represented by the black lines [19].

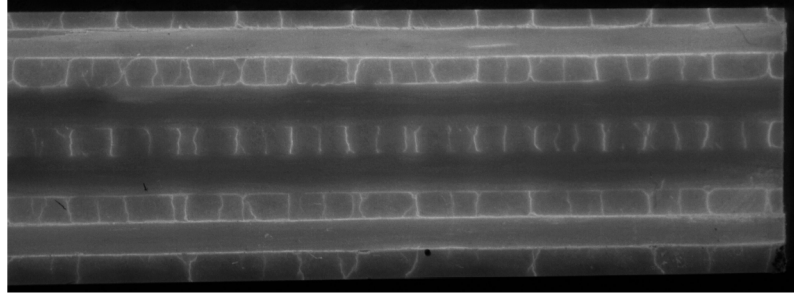
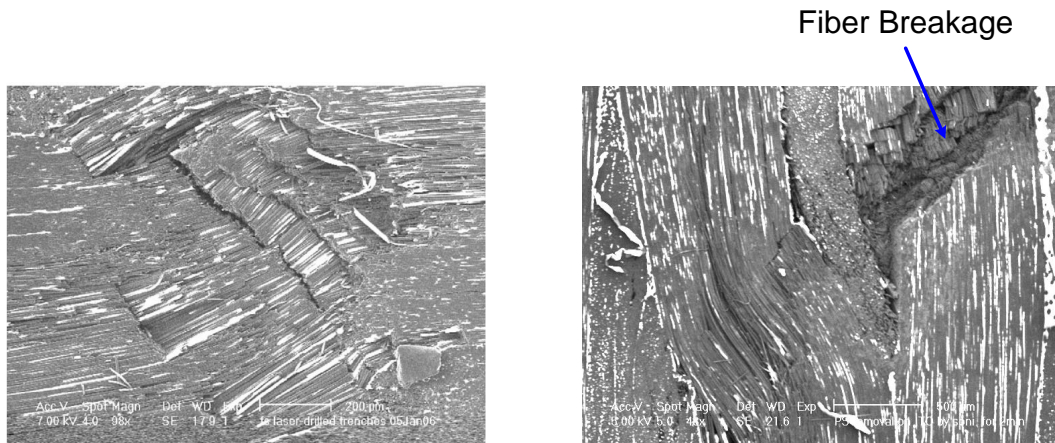


Figure 1.3: Internal cracking in the failed tension specimen [22].

The load drops dramatically after kink band formation, followed by a load plateau, while the fibers are completely broken within the band, as shown in Figure 1.4(b) [26]. The main physical event associated with the kink band formation is the rotation of the fibers in a band within a degrading matrix. The rotation of fibers gives rise to high localized shear strains that drive the shear degradation of the matrix material between the fibers. The shear degradation in turn increases the rotation of the fibers creating a positive feedback loop that culminates in a limit-load type instability. The effect of matrix cracking on the compressive strength of textile composites has been discussed in Ref. [27].



(a) Kink bands at the peak load.

(b) Kink bands at the load plateau.

Figure 1.4: Fiber tow kinking observed in a 2D triaxially braided textile composite subjected to compression [26].

Compared with laminated composites, textile composites are able to demonstrate higher damage tolerance since the interlaced fiber tows have the ability to prevent

the delamination from occurring and localize the area of damage. Thus, this type of material has become a promising candidate for crashworthy components, which are expected to experience high-rate loads in service, such as impact, shock, and blast. The rate dependent compressive response of 3DTCs has been investigated by Pankow et al. [6] through a set of split Hopkinson bar tests. The authors have reported an increase in strength, along with a transition in failure modes at elevated loading rates. The failure mode is dominated by kink band formation at low rates, as shown in Figure 1.5(a), while delamination has been observed at much higher rates, as shown in Figure 1.5(b). It is worth mentioning that the polymer matrix shows a rate dependent behavior where the yield strength increases with an increased strain rate. Thus, when the 3DTC is subjected to an elevated loading rate, the increased matrix yield strength suppresses fiber tow kinking, while the mode of splitting is controlled by the matrix fracture toughness [6].

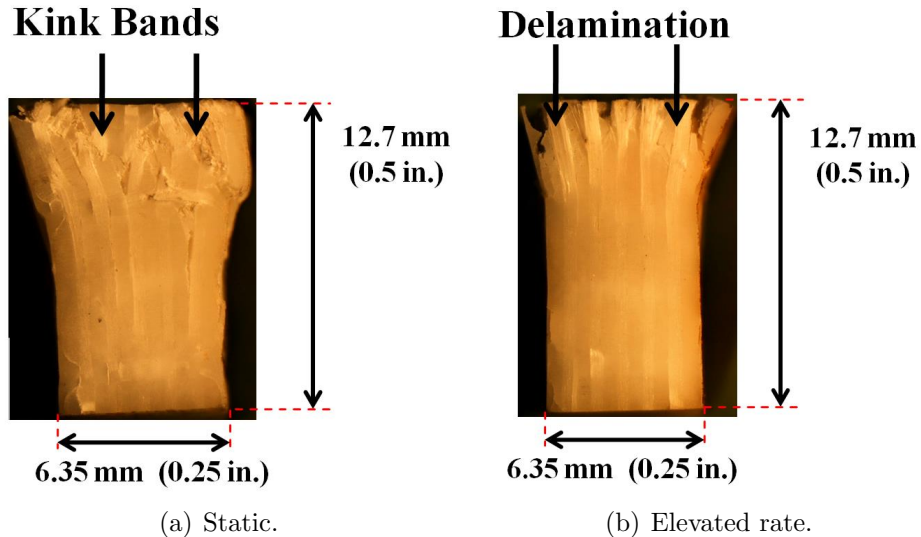


Figure 1.5: Rate dependent compressive response of 3D textile composites. The failed specimen shows a failure mode transition from kind banding at low rates to delamination at higher rates of loading [6].

1.4 Modeling Strategy for Textile Composites

The development of a robust, predictive computational model for textile composites is important for implementation of this family of materials. The challenge in developing a reliable model lies in the complexity of textile geometry, the pres-

ence of a hierarchical structure with various length scales, and little knowledge on the constituent behavior. Errors are accumulated and progressed from one hierarchical level to another, resulting in predictions that may encompass a high level of uncertainty [28]. For large scale structural analysis, homogenization at the macroscale is essential to achieve computational efficiency, however, the model also needs to consider the influence of textile microstructure since damage and failure progresses at the constituent material scale.

1.4.1 Multiscale Modeling

Multiscale modeling, in which information is shared across two or more different length scales, is an efficient modeling methodology for heterogeneous materials such as composites. Based upon the hierarchical level exhibited in textiles, the model can be generally differentiated into three different scales: a micromechanics model at the fiber and matrix level to determine the effective fiber tow properties, a mesoscale textile architecture based model at the fiber tow level through a collection of RUCs that incorporates the damage and failure analysis for the constituents (fiber tows and surrounding matrix material), and a macroscale model at the structural level in which the textile composite is treated as a homogeneous solid. Data across the different scales can be either passed from one hierarchical level to another (passed up through homogenization or down through localization), or shared simultaneously in a multiscale computational framework [29]. An extensive review of various multiscale models for textile composites is given by Bogdanovich [30].

1.4.2 Mesoscale Model

The key element in multiscale modeling for textile composites is the development of a robust, generic, and physics-based mesoscale model that can account for localization due to textile architecture while the model is homogenized at a certain hierarchical level, for example, the tow level. The constituent relations, which are obtained from either experiment or a lower level analysis, are directly implemented in the mesoscale model such that the composite macroscopic response can be captured. The damage and failure that evolves at the the mesoscale finally manifests as the progressive deterioration of the composite effective stiffness at the macroscale.

In the literature, a number of mesoscale finite element (FE) models have been developed, including both linear elastic and failure analysis [26, 31, 32]. The textile geometry of the as-fabricated composite can be characterized by inspecting the

cross-sectional images using an optical microscope or a scanning electron microscope (SEM). In some instances, X-ray micro-computed tomography (micro CT-scan) can be utilized to determine the internal structural variations, and the measured geometric information is directly inputted into a textile software such as WiseTex [33] to create a mesoscale textile model. It has been reported by a couple of researchers that the damage and failure developed in the constituent materials can be captured via a stiffness degradation scheme base upon continuum damage mechanics (CDM) [34, 35, 36, 37]. However, the mesoscale FE model usually contains a large amount of elements due to the irregular geometry of the surrounding matrix material, resulting in computational inefficiency since these matrix elements do not carry the primary loads. The FE model also experiences difficulty when the fiber tows are interacting with each other while rotating along the the three coordinate directions. Thus, idealization of the textile architecture is necessary to build a mesoscale FE model. Moreover, CDM has been proven to be pathologically mesh dependent since no characteristic length scale is associated with damage evolution. When it is implemented for textile composites, it is difficult to measure the scalar variables that govern the damage progression.

An alternative approach to model the composite response at the mesosocale is the 3D Mosaic material model proposed by Bogdanovich [38]. The key in the “Mosaic” concept is to represent a composite structure at any hierarchical level as a Mosaic assemblage of an arbitrary number of distinct homogeneous anisotropic material blocks [30]. For the application to textile composites, the textile RUC is treated as an assembly of 3D unidirectional composites (a representation of fiber tows) embedded with 3D matrix blocks. Material characteristics, including linear elastic properties and ultimate failure strains, are assigned to the unidirectional composite block, while a set of property “reduction factors” are introduced to both unidirectional composite and matrix bricks within the unit cell. The model has demonstrated a fairly good representation on the progressive failure response of a 3D Z-fiber orthogonal woven composite, as shown in Ref. [39].

Finally, it should be mentioned that the mesocale model, which serves as a link between the macroscopic homogeneous response and the micromechanical analysis on the individual fibers and matrix, is built based upon periodicity existing in the textile preform. An efficient mesoscale model requires a “minimum” region to be modeled, while the RUC should not only represent the geometric characteristics but also capture the macroscopic response including damage and failure. Issues associated with the mesoscale modeling, such as the representation of textile architecture, periodic

boundary conditions, and characterization of constituent properties are addressed in Chapter VII.

1.4.3 Micromechanical Analysis

In textile composites, the microstructure of a single fiber tow, which is composed of thousands or tens of thousands of individual fibers that are embedded in a surrounding matrix material, can be represented as a unidirectional fiber-reinforced composite. The computation of the effective homogenized properties of such a material is the most fundamental problem among numerous composite theories, resulting in a multitude of micromechanics models available in the literature, including analytical, semi-analytical, and full numerical methods.

One of the most fundamental homogenization theories to compute the effective moduli of a unidirectional fiber-reinforced composite is the concentric cylinder model (CCM) developed by Hashin and Rosen [40], in which they assumed the composite medium can be represented by a series of concentrically assembled cylinders composed of an inner fiber core and outer matrix annulus. This model, as it was originally proposed, is based upon a variational bounding method proposed by Hashin and Shtrikman [41, 42, 43]. The exact closed-form solutions for four of the five elastic constants of a unidirectional fiber-reinforced composite was first presented by Hill [44]. However, the fifth constant, which is the transverse shear modulus, cannot be rigorously determined from the CCM. The lower bound of this modulus obtained by Hashin [45] has been widely accepted [46, 47].

In order to better predict the transverse shear modulus analytically, Christensen and Lo [47] proposed a generalized self-consistent method (GSCM) in which both the fiber and matrix material are concentrically embedded in an infinite homogeneous medium of the equivalent composite properties. This method is also known as the Generalized Self-Consistent Method (GSCM), following the original Self-Consistent Method (SCM) in which the fiber is directly embedded in the equivalent infinite medium. However, it should be pointed out that their original formulation implements the wrong composite constitutive relations in the transverse plane (the plane perpendicular to the fiber direction). Nevertheless, their pioneering work in seeking the closed-form solutions for the transverse properties is significant, and the model can be further extended to compute the local constituent fields in the transverse plane, as demonstrated in Chapter V.

A distinct theoretical method to compute the composite effective moduli is based upon Eshelby's equivalent (inclusion) principle [48], in which the elastic field of an

ellipsoidal inclusion inside an infinite matrix medium was studied. However, their solutions were only valid for composites with dilute fiber concentrations due to the neglect of interactions between inclusions. At finite concentrations, the average stress in the matrix is perturbed by the presence of inclusions, and this phenomenon was first investigated by Mori and Tanaka [49]. The combination of Eshelby’s idea on equivalent inclusion and Mori-Tanaka’s concept of “average stress” results in a series of important studies on micromechanics problems, especially the computation of the effective properties of composites [50, 51, 52, 53, 54, 55]. A comprehensive review on various topics in micromechanics is given in Mura [56]. The effective properties of a unidirectional fiber-reinforced composite, based on Eshelby’s principle, was first proposed by Tandon and Weng [57], and later, a more compact form of the solutions was presented by Benveniste [58].

It is worth mentioning that these analytical models are developed with a focus to compute the composite *linear* elastic properties in terms of the constituent properties and volume fractions without recourse to the spatial variation within the composite volume at the microscale (the scale of a few fibers). These homogenization techniques have been extensively used in the linear analysis of composite structures. In addition, these analytical micromechanics methods also find utility in case of damage and failure analysis by extending the formulation to the nonlinear regime through a secant moduli approach [59, 60, 61, 62]. Reviews on other important micromechanics models, including the transformation field analysis, generalized method of cells, and full finite element analysis (FEA), are provided in Chapter V.

1.4.4 Computational Damage and Failure Models

Over the past few decades, a multitude of damage and failure models have been developed in order to dictate the material nonlinear response. In this research, damage and failure are distinguished in such a manner that **damage** governs any nonlinear response that preserves the positive definiteness of the material stiffness matrix; while **failure** is defined as internal structural changes that results in a post-peak strain softening response in the stress-strain relation. When damage and failure mechanics are intended to be implemented in a FE framework, it is efficient to treat the highly distributed cracks as a continuum solid with degrading stiffness, for example, the CDM approach discussed in Section 1.4.2. However, when the positive definiteness of the material tangent stiffness matrix is lost, failure will be localized within a single element in a FE computational model. Thus, if no length scale is introduced, the energy dissipated during failure progression becomes a function of mesh size, resulting

a mesh dependent result. To restore mesh objectivity, both the crack band [63] and smeared crack approach (SCA) [64] have been developed with an intent to relate the post-peak strain softening behavior with a traction-separation law that contains a characteristic length scale. Thus, the total energy dissipated during failure evolution can be equated to the fracture toughness of the material through this length scale, indicating the transition from a strain-based description for material with a positive-definite stiffness tensor to a displacement-based theory for failure progression. The formulation for the SCA is provided in Chapter IV.

However, even though the mesh objectivity can be justified in the crack band or SCA at a certain length scale, problems arise when these fracture models are implemented in a multiscale modeling framework due to the inconsistent length scales across the different scales. The validation of the multiscale approach to model the material strain softening behavior has been argued by Bažant [65]. In order to overcome this ambiguity, the material softening model implemented in this research is restricted to the mesoscale model, which is used to simulate the entire region where failure occurs. Details of modeling the progressive failure response of textile composites are given in Chapter VII. The idea of connecting length scales across scales has been recently addressed by Pineda et al. [66].

1.5 Research Objectives and Thesis Outline

In this research, the deformation response of 3DTCs has been investigated through flexural tests. The experimental results are subsequently used as a basis for developing a multiscale mechanics model for 3DTC deformation, damage and failure response, predominantly under flexural loading. Two distinct types of 3DTCs, a layer-to-layer interlock glass fiber 3DTC and a Z-fiber orthogonal interlock hybrid 3DTC, have been studied in order to understand how the composite response is influenced by the textile architecture and constituent properties. The predictive capability of the proposed numerical model is illustrated by comparing the computational results from the two material systems with experiment, including the load-deflection response and failure characteristics.

Chapter II provides a detailed description of the two types of 3DTCs investigated in this dissertation. The layer-to-layer interlock 3DTC is made of pure glass fibers, while the Z-fiber orthogonal interlock hybrid 3DTC is manufactured by integrally weaving three different fibers (carbon, glass, and Kevlar) together. Both dry preforms are subsequently impregnated and cured through a Vacuum Assist Resin Transfer

Molding (VARTM) process to form a solid panel. Microscopic studies are carried out using an optical microscope in conjunction with a SEM to determine the geometric characteristics of each architecture. Manufacturing induced imperfections, including unintended geometric distortion of textile architecture and thermal effects on hybrid 3DTCs are discussed in this chapter. The measured tow dimensions along with the constituent properties are subsequently used as inputs to a textile architecture based mesoscale FE model.

Chapter III presents the results of an experimental investigation on the flexural response of 3DTCs, obtained through both quasi-static and dynamic tests. Various testing configurations have been considered in order to fully understand the architecture-dependent effect and determine the strength limiting mechanisms for 3DTCs subjected to flexural loading. Quasi-static tests were performed on either a screw-driven loading device or a hydraulically activated loading machine, depending on the stiffness of the composite panels. To achieve higher loading rates, tests were carried out using a drop tower facility, which can provide different impact velocities by varying the height of the weight that is dropped onto the specimen. The DIC technique was utilized to map the deformation history and identify the failure modes. The experimental investigation suggests that the observed failure modes, for example, matrix cracking, is greatly affected by the textile architecture. Thus, an architecture based numerical model that incorporates damage and failure constitutive relations is expected to predict the progressive failure response of 3DTCs.

The modeling strategy for an isotropic polymer matrix material, including damage and failure analysis is presented in Chapter IV. The pre-peak nonlinear stress versus strain response, which is attributed to the evolution of matrix microdamage, is modeled using a modified J_2 deformation theory of plasticity through a secant moduli approach. The accumulation of matrix microdamage can result in matrix macroscopic cracking, followed by a post-peak strain softening behavior that is modeled through the SCA. Mesh objectivity of the SCA is demonstrated through a uniaxial tension test on a RUC with various mesh sizes.

A novel, micromechanics based, two-scale model for computing the pre-peak nonlinear response of a single fiber tow is established in Chapter V. The microstructure of a fiber tow can be represented as a unidirectionally aligned fiber-reinforced composite, resulting in a transversely isotropic solid at the mesoscale. The effective fiber tow response is computed through micromechanical analysis using the fiber-matrix concentric cylinder model as the basic repeat unit. In addition, micromechanics is used to relate the fiber tow strains to the fiber and matrix strains through a 6 by 6

transformation matrix. The resolved spatial variation of the matrix fields are compared with the corresponding FE model to demonstrate the accuracy of the proposed micromechanics model. The evolution of the fiber tow nonlinear response is assumed to be governed by two scalar, strain based variables that are related to the extreme value of an appropriately defined matrix equivalent strain, and the matrix secant moduli are used to compute the tow secant moduli for nonlinear analysis. The accuracy of the proposed two-scale model on the prediction of the composite pre-peak nonlinear response is evaluated by comparison to a full FE model. Since fully analytical solutions are utilized for the micromechanical analysis, the proposed method offers a distinct computational advantage and is implemented to compute the fiber tow constitutive relations in a mesoscale FE model of 3DTCs.

Various failure mechanisms of a fiber tow are examined in Chapter VI, including fiber tow breakage, tow kinking, and transverse cracking. When catastrophic failure occurs, the load carrying capability of a fiber tow at the mesoscale is lost, resulting in a post-peak strain softening response. A micromechanical analysis based upon the two-scale model proposed in Chapter V is carried out to numerically determine the compressive strength of a fiber tow, which is subsequently used as the failure initiation criterion. The effects of matrix in-situ properties, fiber misalignment angles, and mesh objectivity on the prediction of tow kinking strength are discussed. The failure evolution, including both tension and compression failure, is modeled using the SCA with a specific traction-separation law that is designed for a fiber tow.

A mechanics based multiscale computational model is established in Chapter VII to predict the flexural response of 3DTCs, predominately under three-point bending. The model is developed based upon a global-local modeling strategy, in which the influence of textile architecture is incorporated in a mesoscale FE model that contains detailed geometric information for the fiber tows and matrix, while the composite is homogenized at the macroscale. The tow pre-peak nonlinear response is modeled using the two-scale model developed in Chapter V, in which the subscale micromechanical analysis is carried out in closed form. The post-peak strain softening responses of both the fiber tows and the surrounding polymer matrix are modeled through the SCA. The predictive capability of the proposed model is illustrated through the two distinct 3DTCs by comparing the computational results with the experiments, including the load-deflection response and the failure characteristics, such as matrix cracking, tow kinking, and tow tensile fracture.

CHAPTER II

Material Microstructure and Characterization

2.1 Introduction

A number of structural components have been recently manufactured using 3DTCs, such as the dome-shaped pressure bulkhead and wing trailing edge panels in the Airbus A380, rocket nozzles, turbine engine rotors, and wind turbine blades, as described in Ref. [1]. An extensive review of numerous potential applications for 3D textile composites (3DTCs) is provided in [67]. One of the driving forces for the increased use of textile composites is the low manufacturing cost. The development of weaving techniques dates back to the Jacquard loom in the 19th century. Mass production of textiles can be achieved at a reasonable cost using modern, computer-aided manufacturing technique. Moreover, the computer-controlled Jacquard loom is capable of producing textile reinforcements for components of complicated geometry according to design specifications.

Previous studies have shown that 3DTCs offer enhanced mechanical performance and better damage tolerance than 2D laminated composites [4, 68]. The through-the-thickness reinforcements in 3DTCs have the ability to contain the damage area and prevent the spread of delamination that often occurs in layered prepreg tape type laminated composites [3, 4, 5, 6]. Various 3D woven architectures are available in the textile literature, including layer-to-layer interlock, through-the-thickness angle interlock, and Z-fiber orthogonal interlock. Recently, 3D hybrid textile composites were manufactured by weaving three different fibers (carbon, glass, and Kevlar) into a single textile preform which is subsequently impregnated and cured through a Vacuum Assist Resin Transfer Molding (VARTM) process to form a solid panel. Different hybridized architectures can be achieved by varying the percentage and lay-up of each type of constituent fiber tows. It has been pointed out by Hufenbach et al. [69] that hybrid composites can be tailored for specific structural applications by varying

the combination of constituent fibers and weaving architecture to achieve enhanced mechanical properties including stiffness, strength, and energy absorption.

This chapter provides a detailed description of 3DTCs that are investigated in this dissertation. The textile architectures, including the terminology used in the textile literature, are provided in Section 2.2 and 2.3. The fabrication process and the geometric distortion of the textile architecture resulting from the manufacturing process are discussed in Section 2.4. The microscopy studies on various types of 3DTCs including the geometric characteristics of each architecture are provided in Section 2.5. The mechanical properties for the constituent fibers and polymer matrix are reported in Section 2.6 and 2.7 respectively.

2.2 Textile Architecture

3DTCs are different from the layered laminated composites or 2D textile composites in that there exist inter-plane movements of fiber tows that bind multiple layers together to enhance the through-the-thickness performance. Two main types of 3D weaving, Z-fiber orthogonal interlock and layer-to-layer interlock architectures, are extensively discussed in [2]. As shown in Figure 2.1, the Z-fiber architecture has a series of solid warp and weft tows, forming a $0/90^\circ$ array to maintain the in-plane layers. This is much like a coarse cross-ply laminate, however, each layer contains distinct fiber tows. The Z-fibers, running in the same direction as the warp tows, are drawn from top to bottom to bind multiple weft layers together. These Z-fibers are inserted in-between the warp tows, and can alternate their path along the weft direction to form various repeating textile architectures. The Z-fiber architecture exhibits almost straight warp and weft tows due to the tension applied to the fiber tows during the weaving process.

In the layer-to-layer interlock architecture, Z-fibers are removed, and the warp tows are woven through multiple weft fiber layers, as schematically shown in Figure 2.2. Since the warp tows are no longer straight, this architecture exhibits more compliance than the Z-fiber architecture, and is affected by the manufacturing process that makes the textile architecture to be different from the expected ideal one. The geometry distortion can have a great impact on the damage behavior and the resulting mechanical properties such as strength, strain to failure, and fatigue life. The aspect of manufacturing induced effect is addressed in Section 2.4.

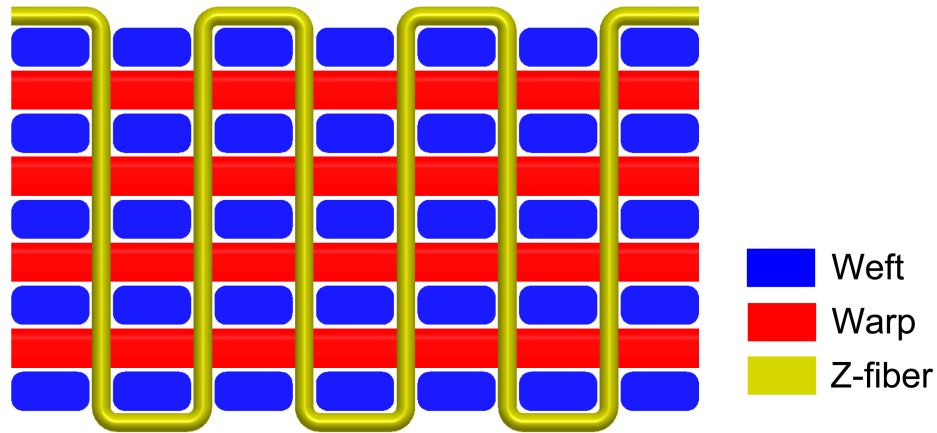


Figure 2.1: Z-fiber weaving architecture.

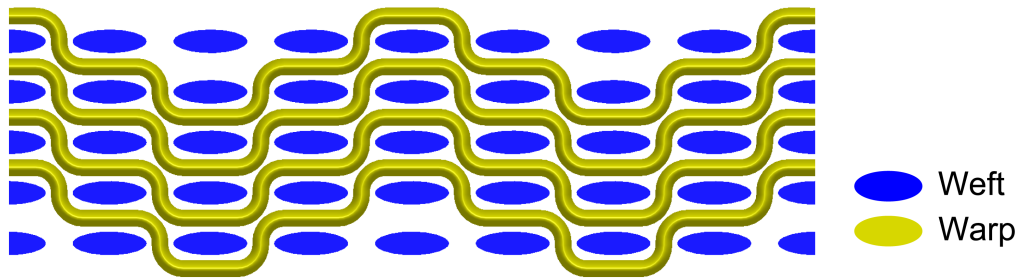


Figure 2.2: Layer-to-layer interlock architecture.

2.3 Material Systems Investigated in This Dissertation

There are two distinct types of 3DTCs investigated in this dissertation. The first type is a layer-to-layer interlock glass fiber composite. The dry textile preform is made of S2 glass fibers provided by Albany Engineered Composites, Inc., NY. The ideal textile architecture is schematically shown in Figure 2.3, in which the planes that contain warp tows alternate with a period of four along the weft direction to achieve a repeated textile pattern. This material is also named as Albany 2 throughout this dissertation, which is consistent with the notation used in Ref. [2]. Figure 2.4 shows the fiber reinforcements of the specimen after matrix burnout. The matrix burnout tests were performed by Dr. Mark Pankow and Mr. Amit Salvi at the University of Michigan. The test is initially used to determine the percentage of void content for various 3D glass woven composites [2].

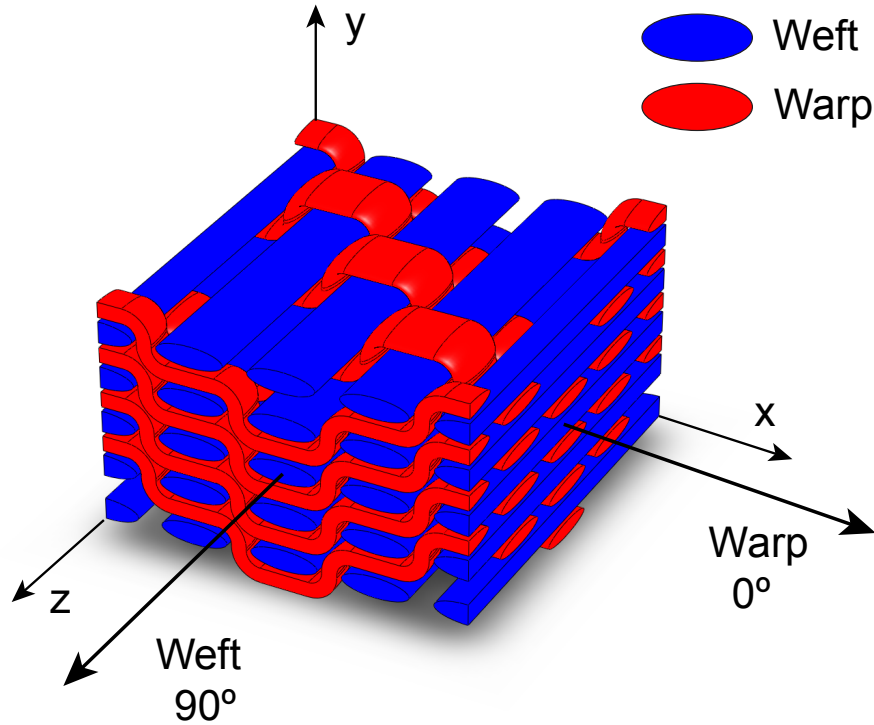


Figure 2.3: Ideal textile architecture of the layer-to-layer interlock glass fiber 3DTC (Albany 2).

The second type of 3DTCs has a hybrid Z-fiber orthogonal interlock textile architecture, in which three different types of fibers, IM-7 carbon, S2 glass, and Kevlar are integrally woven into a single textile preform. All the hybrid architectures are provided by Textile Engineering and Manufacturing (T.E.A.M.), Inc., RI. The carbon fiber is used owing to the relatively high stiffness and strength, the glass for its relatively low cost (high strength per unit cost), and Kevlar for its high resistance (characterized by its toughness) to failure [19]. In this dissertation, three different hybrid architectures, as schematically shown in Figure 2.5, are investigated to understand the effect of hybridization on the resulting flexural response, as discussed in Chapter III. The first two architectures contain four layers of carbon (two layers in the warp and weft directions, respectively) at one side, and the remainder are the glass layers. The difference in the overall thickness allows for studying the size-scaling effects by normalizing the result with respect to the panel thickness. The details are presented in Section 3.3.3. These two architectures are considered to be unsymmetric in the sense that the types of the layered constituent fibers are unsymmetric with respect to the mid-plane of the composite panel. The third architecture, in which the

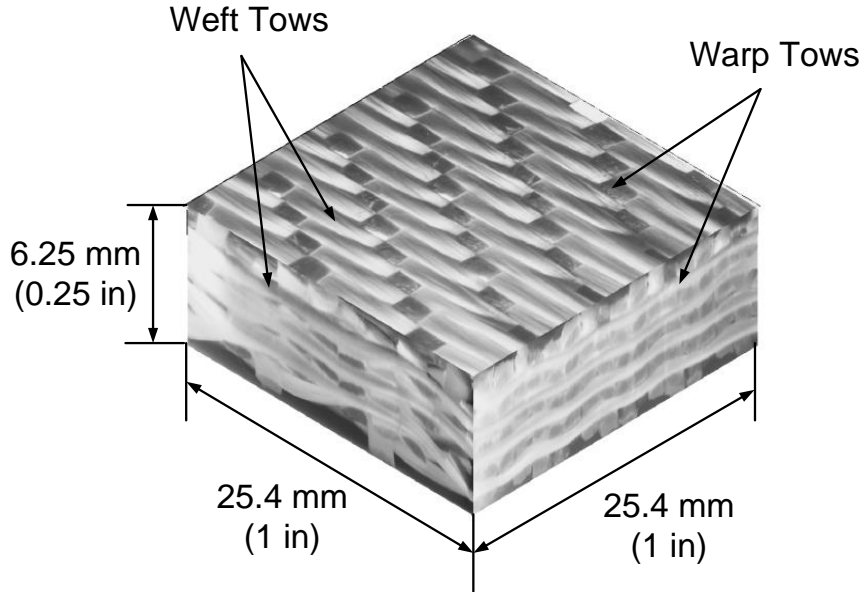


Figure 2.4: The glass fiber preform of Albany 2 after the matrix burnout test.

carbon layers are used for both outer surfaces (four layers of carbon on each side), is denoted as a symmetric panel. Among all the architectures, the planes that contain Z-fibers alternate along the weft direction with a period of two to achieve a repeating textile pattern. The geometric characteristics for these architectures are summarized in Table 2.1. The percentage of the carbon content in each architecture is simply calculated by dividing the number of carbon layers by the total layers of the composite. The images of the polished surfaces are shown in Figure 2.6, which are further examined under microscopy to characterize the textile architecture. The microscopy studies on these types of materials are discussed in Section 2.5.

Table 2.1: Panel thickness and constituent fractions for the 3D hybrid woven composites.

	Thickness (mm)	# of Layers	# of Carbon Layers	% Carbon
Thin Unsymmetric	8.79 ± 0.15	9	4	44.4
Thick Unsymmetric	15.96 ± 0.23	17	4	23.5
Thick Symmetric	16.80 ± 0.32	17	8	47.1

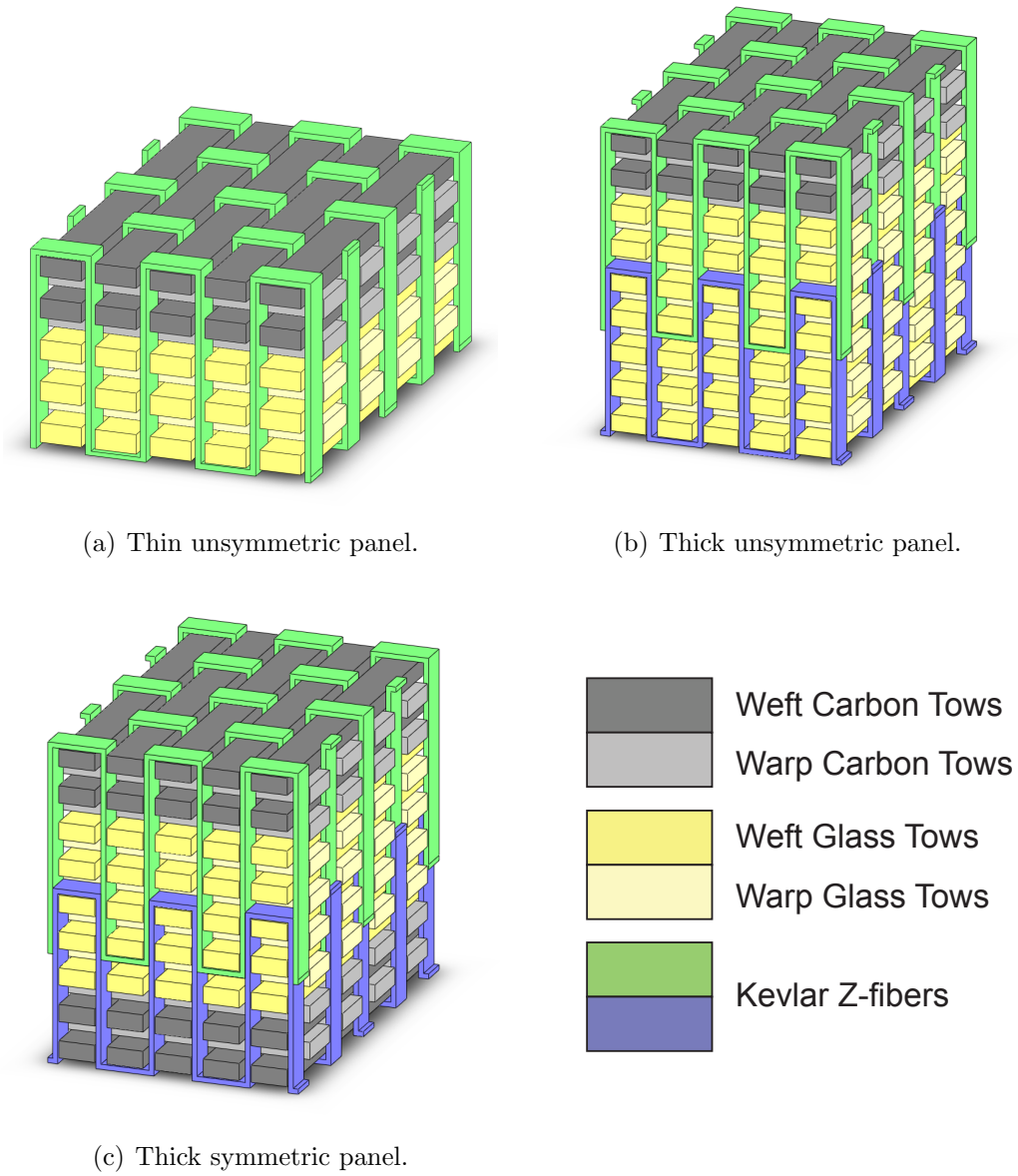
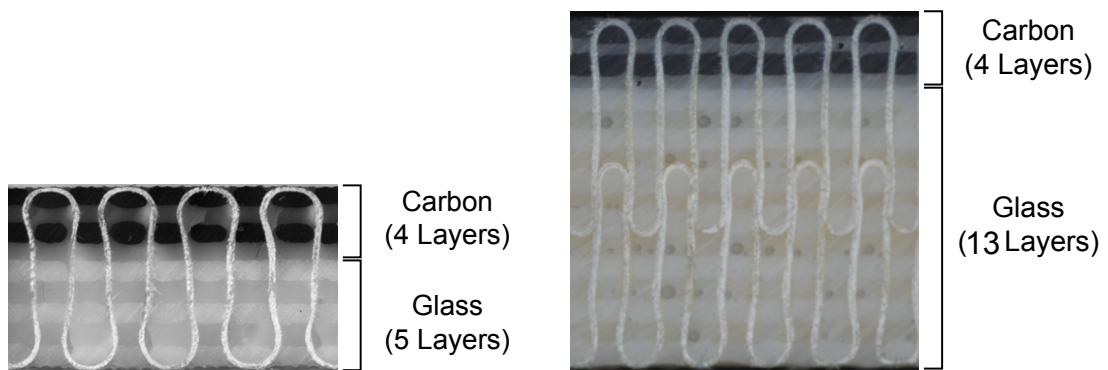
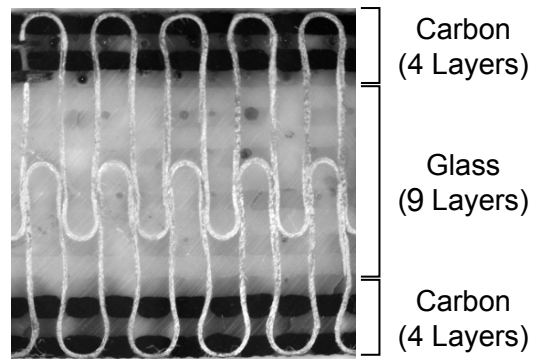


Figure 2.5: 3D hybrid Z-fiber orthogonal interlock textile architectures.



(a) Thin unsymmetric panel.

(b) Thick unsymmetric panel.



(c) Thick symmetric panel.

Figure 2.6: Cross sections of the cured 3D hybrid textile composites.

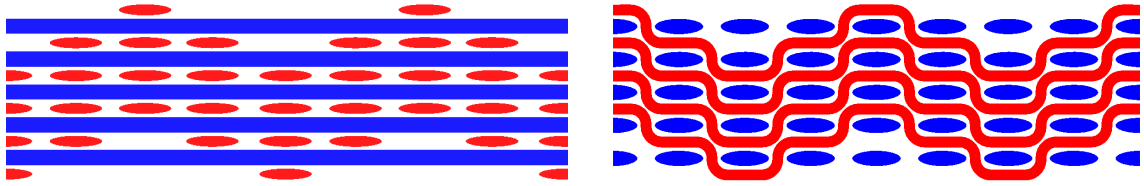
2.4 Fabrications and Manufacturing Induced Imperfections

Both the glass fiber layer-to-layer interlock and hybrid orthogonal Z-fiber textile preforms are infused with SC-15 epoxy resin using a VARTM process to form a solid panel. Impregnation and cure of the textile preform were carried out at the Army Research Laboratory in Aberdeen, MD. VARTM is adapted from traditional Resin Transfer Molding (RTM) by replacing the upper half mold with a vacuum bag to enhance the impregnation of the fiber reinforcements. Details of the VARTM technique and fabrication process are provided in [1, 2, 70, 71]. VARTM offers distinct advantages over RTM including lower tooling cost, shorter mold time, and ability to manufacture large structural components.

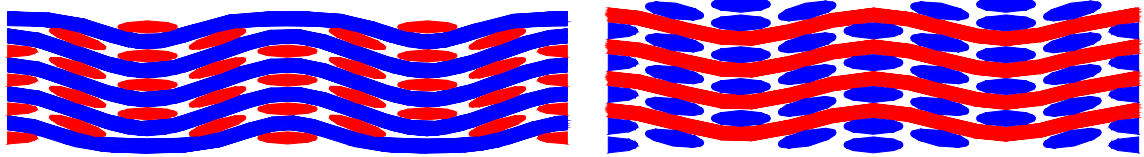
2.4.1 Geometry Imperfections in the Layer-to-Layer 3D Textile Composites

In the layer-to-layer architecture, the warp tows are used as weavers that are woven through multiple layers, showing large undulations along the weaving path. Compared with the Z-fiber architecture, in which the warp tows are running straight, the layer-to-layer architecture shows much more compliance, and therefore it is more easily affected by the fabrication process, for example, the tension exerted on the fiber tows during the weaving process and the mold pressure applied during the curing process, as schematically shown in Figure 2.7. In the VARTM process with a single-sided mold, atmospheric pressure is exerted on the textile preform through the vacuum bag covering, forcing the fiber tows to be settled in a new position that is different from the predesigned one. This manufacturing induced geometrical imperfection of the textile architecture in the as-fabricated composite panel is evident from the optical microscopic images of Albany 2 sample shown in Figure 2.9.

It has been pointed out by Song et al. [72] that each manufacturing process is associated with a unique set of characteristics that result in a produced part deviating from the expected ideal geometry. The set of such deviations, which is unique to each manufacturing process, is termed the “manufacturing imperfection signature”. Obtaining the manufacturing imperfection signature of the textile composite is important to determine the damage characteristics, such as strength, strain to failure, and fatigue life, which has been reported by many researchers [13, 14, 15]. The importance of incorporating the unintended geometric deviations of the woven fabric into a textile architecture based finite element model has been recently addressed by Zhang et al. [31].



(a) Ideal textile architecture.



(b) Schematics of the actual textile architecture.

Figure 2.7: Manufacturing effect on the textile architecture (Albany 2).

2.4.2 Thermal Effects on the Hybrid 3DTCs

Although the Z-fiber interlock hybrid 3DTCs do not experience much geometry distortion during the fabrication process due to their rigid warp and weft tows, they do show some degree of initial curvature in the unsymmetric panels because of the mismatch of the thermal expansion coefficients for different constituent fibers. When cured, the unsymmetric panels experience different thermal strains in the carbon and glass layers, resulting in minor bending in the specimens, as schematically shown in Figure 2.8. The initial curvature can be estimated using classical lamination theory as provided in Ref.[19]. For the thin unsymmetric panels, the initial radii of curvature in the two principal directions were found to be approximately 500-600 inches for a 6 in by 6 in square panel [19].

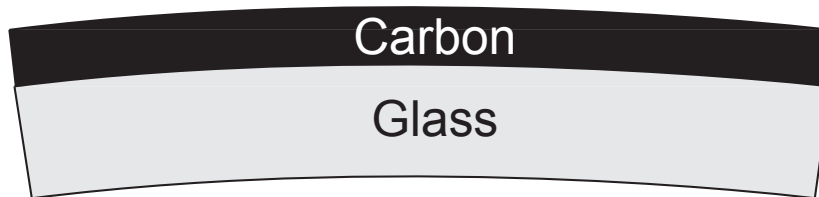


Figure 2.8: Initial curvatures observed in the hybrid unsymmetric panels.

Table 2.2: Fiber tow geometry for Albany 2.

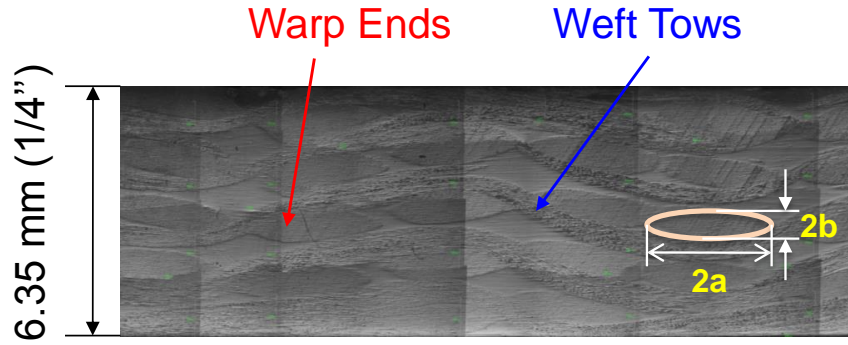
	Weft tow	Warp tow
Major axis (2a) (mm)	2.15 ± 0.11	2.51 ± 0.13
Minor axis (2b) (mm)	0.62 ± 0.05	0.53 ± 0.05
Wave length (2L) (mm)	11.80 ± 0.15	9.29 ± 0.16
Amplitude (A) (mm)	0.74 ± 0.07	0.45 ± 0.03

2.5 Microscopy Studies

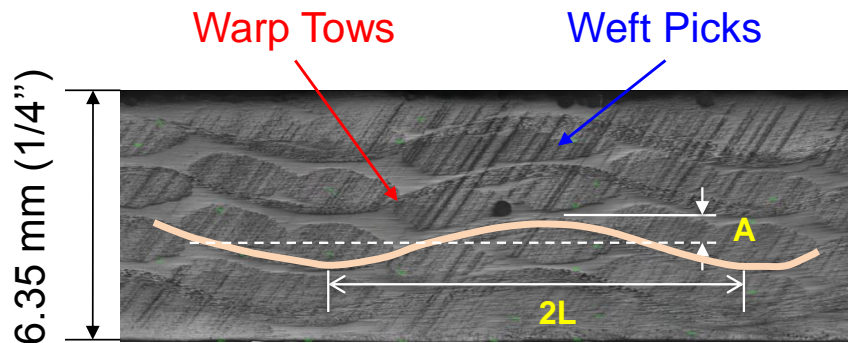
In order to obtain a thorough understanding of the microstructure of the cured composite, cross sectional microscopic images were inspected to characterize the textile geometry. Specimens were cut along the warp and weft directions into 1 in by 1 in blocks, and polished using a multi-speed rotating grinder/polisher. Microscopic photographs were taken on the polished cross sectional surfaces to allow for the direct measurement of fiber tow dimensions. The characterization is focused on Albany 2 and the thin unsymmetric hybrid specimens, and the measured dimensions are used as inputs to a textile architecture based finite element model presented in Chapter VII.

For Albany 2 specimen, as shown in Figure 2.9, both the warp and weft fiber tows are idealized to undulate as sinusoidal waves with elliptical cross sections. The measured tow dimensions are summarized in Table 2.2. The fiber volume fraction in a fiber tow is determined to be $58\% \pm 8\%$ by analyzing a scanning electron microscopic (SEM) image. The volume fraction of warp, weft, and matrix provided by the manufacturer are 24.78%, 32.76%, and 42.45%, respectively.

The micrographs for the thin unsymmetric specimen are shown in Figure 2.10, in which both the warp and weft tows are assumed to be straight with rectangular cross sections, and the binder tows are of elliptical cross sections. SEM images were taken on the cross section of each type of constituent fiber tow to investigate how the fibers are distributed inside the tow and to determine the average fiber volume fraction. The measured fiber tow dimensions for the thin unsymmetric hybrid architecture and the fiber volume fraction of each constituent tow are summarized in Table 2.3 and Table 2.4, respectively.



(a) Weft cross section.



(b) Warp cross section.

Figure 2.9: Optical micrographs of Alany2 specimen. The fiber tow is idealized to undulate as a sinusoidal wave with an elliptical cross section.

Table 2.3: Fiber tow geometry for the thin unsymmetric panel.

	a (mm)	b(mm)
Warp Carbon Tow	2.85 ± 0.12	1.00 ± 0.06
Warp Glass Tow	2.90 ± 0.33	1.11 ± 0.11
Weft Carbon Tow	1.77 ± 0.42	0.83 ± 0.10
Weft Glass Tow	1.83 ± 0.29	0.92 ± 0.06
Z-fiber Kevlar	1.44 ± 0.15	0.28 ± 0.06

2.6 Fiber Properties

S-2 glass fiber is a competitive candidate for textile reinforcement in composite structural applications. It delivers 25% more linear-elastic stiffness than conventional glass fibers, and offers enhanced strength, impact and fatigue resistance, and stability

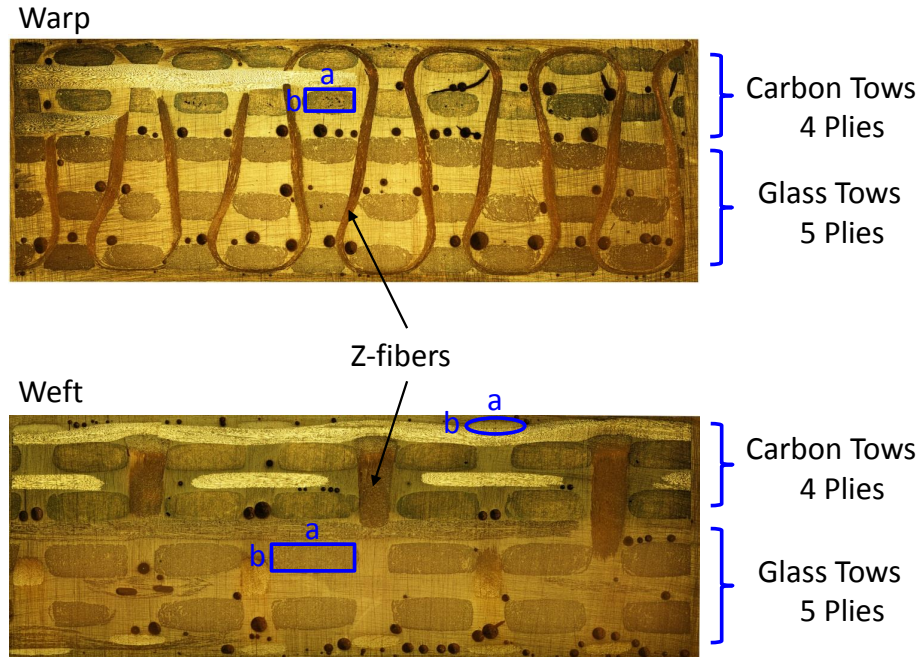


Figure 2.10: Optical micrographs for the thin unsymmetric specimens. The warp and weft tows are assumed to be straight with rectangular cross sections, and the binder tows are of elliptical cross sections.

Table 2.4: Fiber volume fractions for different constituent fiber tows.

	Glass tow	Carbon tow	Kevlar tow
Albany 2	$58\% \pm 8\%$		
Hybrid	$60\% \pm 4\%$	$56\% \pm 5\%$	$69\% \pm 7\%$

under extreme temperature and corrosive environments [73]. This family of glass fibers also shows a distinct cost advantage over carbon fibers and the ability to absorb high energy. In this research, S-2 glass fibers are used in both Albany 2 and the hybrid textile preforms.

IM-7 carbon fiber is used in the hybrid preform due to its extraordinary high stiffness. Unlike glass fiber, which shows isotropy during linear-elastic loading, carbon fiber is usually considered as an orthotropic material with weak transverse and shear properties. Surface treatment has been introduced to IM-7 carbon fiber, effectively improving its strength and shear properties.

Kevlar is the registered trademark for a para-aramid synthetic fiber developed at DuPont [74]. It provides superior light-weight tensile strength and toughness, as

well as outstanding shock and impact resistance. However, the compressive strength of Kevlar is noticeably lower than the tensile strength, suggesting that it be best used in combination with other types of fibers, such as carbon or glass, to optimize the overall structural performance. In the current hybrid woven composites, Kevlar filaments are used as Z-fibers that weave multiple layers together to prevent the spread of delamination between layers. This makes the best use of its high toughness and resistance to failure. In addition, as an organic fiber, Kevlar tends to be more flexible than glass and carbon, hence, it has the potential to eliminate geometric imperfections caused by the through-the-thickness weavers.

The elastic properties along with the strength of S-2 glass, IM-7 carbon and Kevlar fibers are summarized in Table 2.5. These values are taken from various sources [75, 76, 77, 74, 19].

Table 2.5: Elastic modulus and ultimate strength for IM-7 carbon fiber, S-2 glass fiber, and Kevlar.

	E_1 (GPa)	E_2 (GPa)	ν_{12} -	G_{12} (GPa)	G_{23} (GPa)	Strength (MPa)	Failure strain (%)
IM7 Carbon	276.0	15.0	0.279	12.0	5.02	5670	2.0
S-2 Glass	93.8		0.23	38.1		4890	5.7
Kevlar	112		0.36	41.2		3620	2.4

2.7 Matrix Properties

Both the pure glass layer-to-layer interlock preform (Albany 2) and the hybrid preforms are infused with SC-15 epoxy resin, which is a two-phased toughened thermoset polymer containing part A (resin mixture of diglycidylether epoxy toughener) and part B (hardener mixture of cycloaliphatic amine polyoxy-lalkylamine) [78]. Owing to its low viscosity, SC-15 is a good candidate for the VARTM process since it is able to shorten the time for wetting fiber tows and improving the impregnation of reinforcements.

A set of static tension and compression tests were performed on the post-cured SC-15 specimens at ARL by Mr. Brian Justusson according to ASTM standard D638 and D695 respectively. The specimens were cured using the same curing cycle as that used for the woven composites studied in this research. Representative tension and compression stress-strain responses are shown in Figure 2.11, and the characteristic

properties are summarized in Table 2.6 based on the average results from a minimum of 5 tests. It can be immediately concluded that SC-15 behaves differently in tension and compression, and the compression results yield a higher elastic modulus and failure strength. This finding is remarkable, suggesting that the damage and failure mechanisms for tension and compression are different. To understand this unique behavior, a further investigation on the polymer matrix at the individual chain level, possibly using molecular dynamics (MD), is recommended for future work. Moreover, it should be mentioned that the in-situ response of the polymer matrix material inside a fiber tow is different from the virgin resin properties due to the presence of the fibers in the curing process. An extensive discussion on the determination of the matrix in-situ properties is provided in Chapter VI.

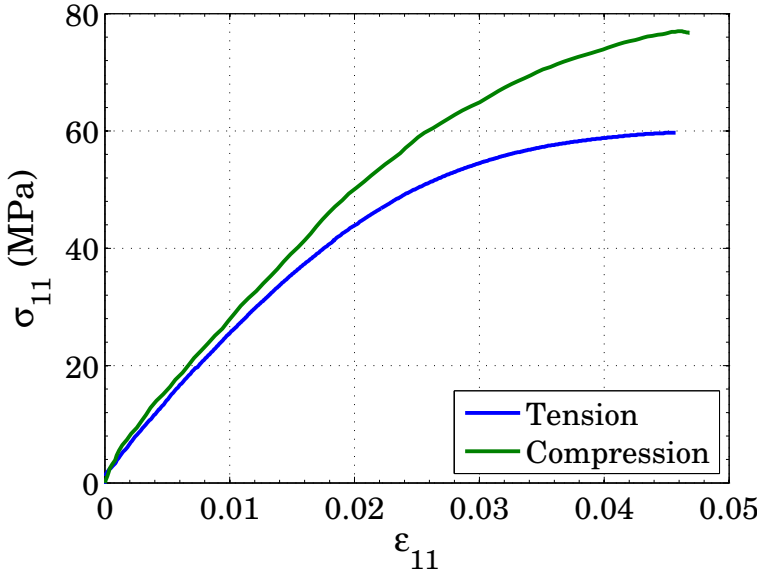


Figure 2.11: Representative uniaxial stress-strain responses for SC-15 epoxy in tension and compression.

Table 2.6: Static properties for SC-15 epoxy in tension and compression.

	E (GPa)	ν -	Failure strength (MPa)	Failure strain (%)
Tension	2.20 ± 0.18	0.36 ± 0.08	58.31 ± 2.24	4.23 ± 0.48
Compression	2.51 ± 0.03	0.40 ± 0.07	76.95 ± 1.01	4.84 ± 0.69

Rate dependent behavior of SC-15 is reported in [12, 2], finding that the yield stress and the subsequent nonlinear hardening response increase with increased loading

rates. A material model that accounts for the rate dependent effect is presented in [32, 79]. Studying the high strain rate behavior of this type of material is particularly important when the textile composites are subjected to high rates of loading such as shock and impact.

2.8 Conclusions

Various textile architectures, including the layer-to-layer interlock pure glass fibers and Z-fiber orthogonal interlock of three different types of fibers (carbon, glass, and Kevlar), are examined using an optical microscope and SEM to determine the fiber tow dimensions and the fiber volume fraction of each constituent tow. The microscopy studies on the cured composite samples show that the fabrication process has a great impact on the final textile architecture, making it deviate from the ideal designed one. The measured geometric characteristics are used as inputs to a textile architecture based FE model, in which the manufacturing induced imperfections should be incorporated to determine the damage behavior of this class of materials. In hybrid composites, different types of fibers are used because of their unique properties. SC-15 resin epoxy is used as a binding matrix due to its low viscosity, which is suitable for the VARTM process. The mechanical properties of the fibers and matrix provide important information for the development of the material constitutive models discussed in Chapter IV, V, and VI.

CHAPTER III

Characterization of the Flexural Response of 3DTCs

3.1 Introduction

This chapter presents the results of an experimental investigation on the flexural response of 3DTCs, obtained from both three-point and four-point bend tests at various loading rates. In order to investigate the architecture-dependent effect, specimens were loaded along the two major fiber directions, warp and weft, respectively. Quasi-static tests were run either on a screw-driven device (Instron) or on a hydraulically activated loading machine (MTS) depending on the stiffness of the different composite panels. The MTS can achieve a loading rate up to 2 in/sec, and for higher loading rates, a drop tower was utilized by varying the height of the dropped weights. A summary of various testing configurations are provided in Section 3.2. The results of the quasi-static tests for Albany 2 and hybrid 3DTCs are reported in Section 3.3.1 and Section 3.3.2, respectively. The dynamic flexural response of hybrid 3DTCs is discussed in Section 3.4.

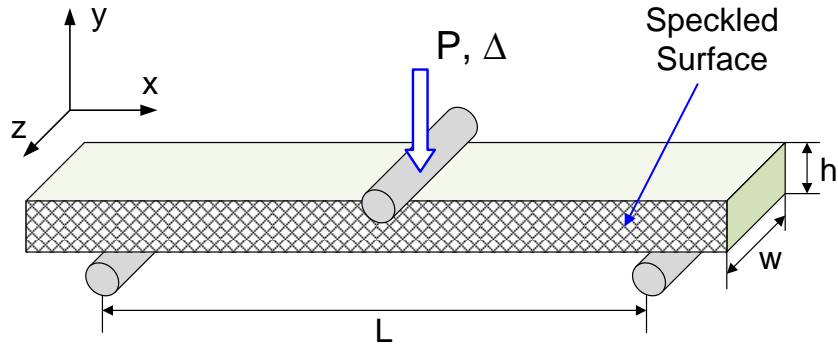
3.2 Testing Configurations

The flexural response of 3DTCs were studied through a set of three-point and four-point bend tests, as schematically shown in Figure 3.1. For Albany 2 specimens, only quasi-static tests were carried out using the Instron machine with a loading rate of 1mm/min. Specimens were cut along the warp and weft direction respectively, with a length of 120 mm and a width of 19 mm using a diamond saw. The bottom span for both three-point and four-point bend tests are 90 mm, and the upper span for four-point bend test is 45 mm. The hybrid panels were cut with a length of 160

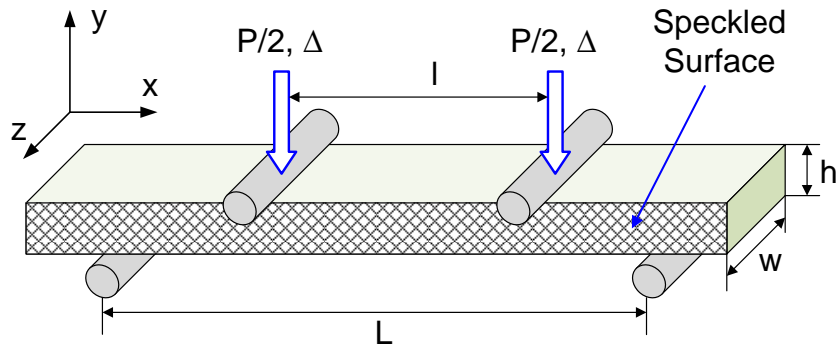
mm and a width of 25.4 mm using a water jet. The upper and bottom span are 60 mm and 120 mm respectively. Both the upper and lower rollers are 0.5 in diameter. For hybrid 3DTCs, both of the quasi-static tests were performed using the MTS machine at a loading rate of 0.0004 in/sec. The quasi-static four-point bend tests were carried out only on the thin unsymmetric panels, since the thick panels require a much longer support span to achieve a four-point loading condition. The dynamic flexural response of the hybrid panels was first investigated using a loading rate of 2 in/sec. The set-up is similar to the quasi-static testing, but tabs were attached to the two bottom supports such that the specimen was secured during the impact event. To achieve higher loading rates, the three-point bend tests were performed using a drop tower. This facility can provide different impact velocities by varying the height of the weight that is dropped onto the specimen. Two different heights were selected in the present study. The specimen dimensions and loading configurations are summarized in Table 3.1, and the testing matrix is shown in Figure 3.2.

In order to investigate the failure modes associated with the deformation history, the outer surfaces of the composite panels were speckled, which were subsequently used to obtain the surface strain fields via a DIC technique, while the outer surfaces of the other specimens were polished such that the axial tows can be captured using a high resolution camera. Images of the outer surface were taken during deformation using a 12 Megapixel camera at 5-second time intervals. The full field surface strain histories were obtained via the DIC software ARAMIS.

Figure 3.3 shows various flexural testing configurations studied in this research. The 3DTCs were loaded in both the warp and weft directions. In addition, for the unsymmetric hybrid panels, there exist two distinct testing configurations: the carbon layer in compression and the glass layer in compression, both of which were tested to investigate an architecture-dependent effect.



(a) Three-point bend test.



(b) Four-point bend test.

Figure 3.1: Schematics of three-point and four-point bend testing configurations. The side surface of the specimen is speckled as indicated.

Table 3.1: Flexural test configurations.

	Albany 2	Hybrid
Bottom Span (L)	90 mm (3.54 in)	120 mm (4.72 in)
Upper Span (l)	45 mm (1.77 in)	60 mm (2.36 in)
Thickness (h)	6.35 mm (0.25 in)	Thin Unsymmetric: 8.79 mm (0.35 in) Thick Unsymmetric: 16.80 mm (0.66 in) Thick Symmetric: 15.96 mm (0.63 in)
Width (w)	19.05 mm (0.75 in)	25.4 mm (1 in)
Loading Frame	Instron	MTS, Drop Tower
Loading Rate	1 mm/sec	0.0004 in/sec, 2 in/sec, >100 in/sec

Specimen	Static		Dynamic (3-Pt)		
	3-Pt	4-Pt	MTS	Drop Tower	
			2 in/sec	H = 15 in	H = 30 in
Albany 2	Done	Done	N/A	N/A	N/A
Thin Unsymmetric	Done	Done	Done	Done	Done
Thick Unsymmetric	Done	N/A	Done	Done	Done
Thick Symmetric	Done	N/A	Done	Done	Done

Done
 N/A

Figure 3.2: Testing matrix.

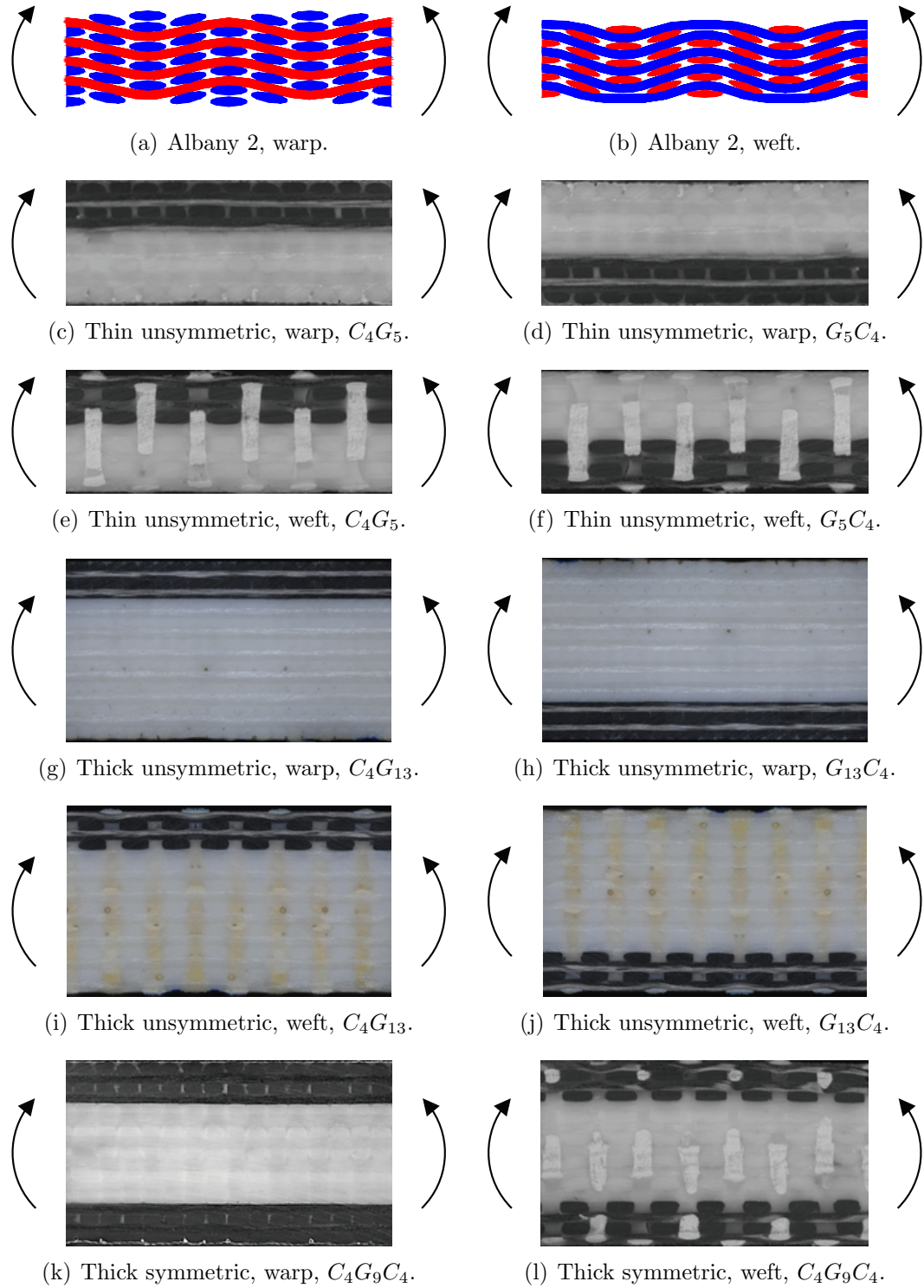


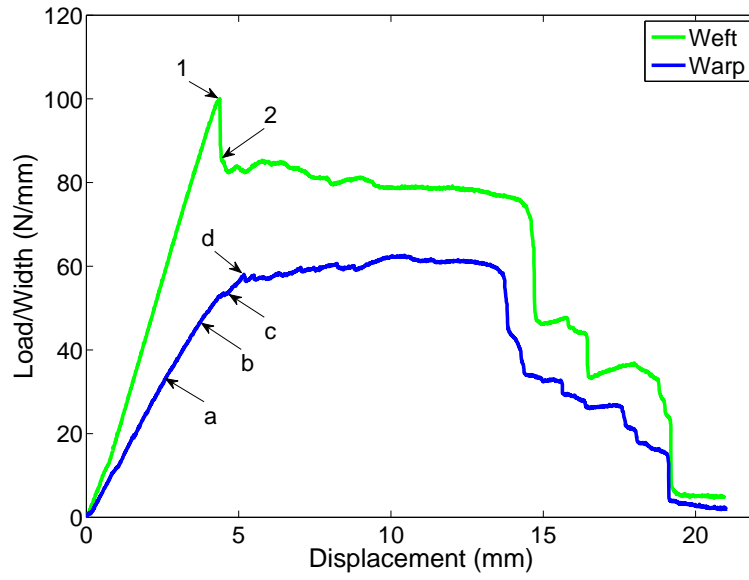
Figure 3.3: Various flexural configurations are studied to investigate the textile architecture-dependent effect.

3.3 Quasi-Static Three-Point and Four-Point Bend Tests

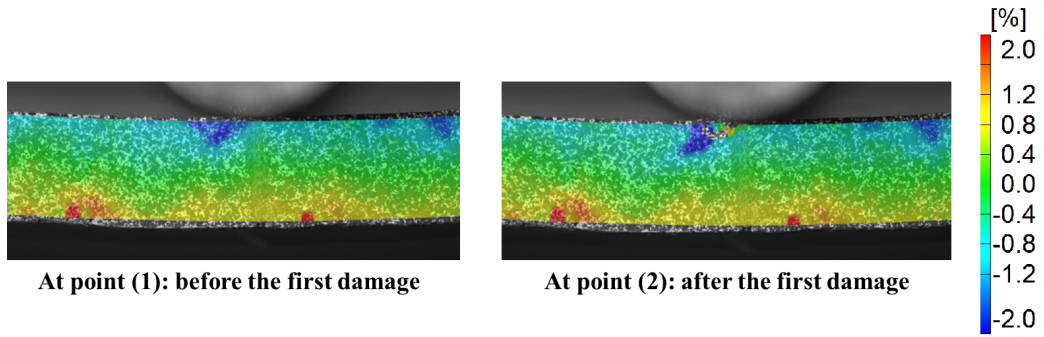
3.3.1 Albany 2 Panels Subjected to Flexural Loading

Representative load-displacement responses for Albany 2 panels subjected to quasi-static three-point bending are shown in Figure 3.4(a). The load presented here is normalized with respect to the width of the specimen such that the variation in the specimen width due to cutting can be accounted for. The weft loading direction shows higher initial stiffness than the warp direction due to the fact that there is one additional axial tow in the weft direction to carry the bending moment. Overall, for both directions the woven composites exhibit similar “plastic-like” behavior, more representative of metals, indicating considerable damage tolerance of this type of material. When the panel was loaded in the weft direction, the first damage occurred at the point that deviates from the proportional loading due to fiber tow kinking on the compression side. The kink band formation can be better observed under a SEM, as shown in Figure 3.5. The DIC patterns before and after the first damage occurrence are shown in Figure 3.4(b). However, when the material was loaded in the warp direction, matrix micro-cracking occurred on the tension side and progressed in the center of the specimen prior to the kinking on the compression side. These cracks were captured by the DIC strain distributions as shown in Figure 3.4(c).

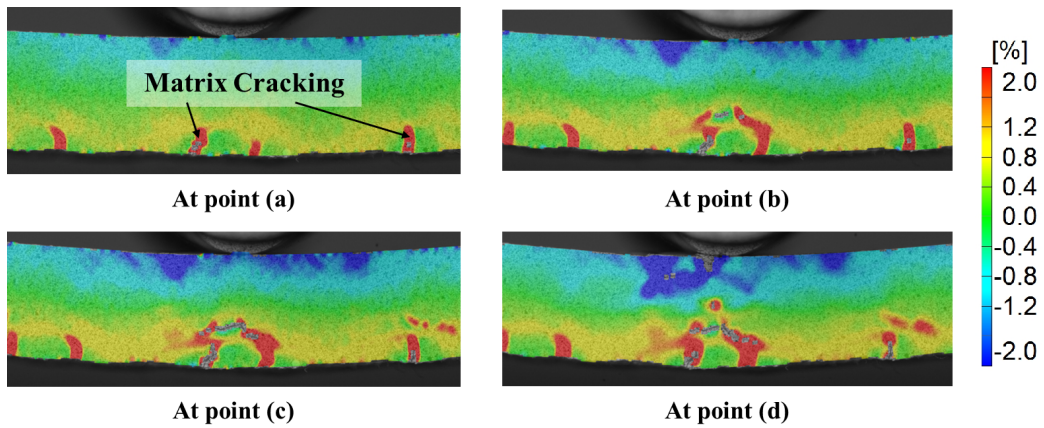
Figure 3.6 shows the load-displacement responses from quasi-static four-point bend tests, and the results are compared against the ones from three-point bend tests. It is worth noting that the load plateau in a four-point bend is almost twice the magnitude of the one in three-point bend, indicating that the compressive bending moment that the material can carry is almost the same in both flexural tests. Figure 3.7 shows the progressive damage events for Albany 2 specimen under four-point bend testing along the warp direction, presenting similar damage modes that were observed from three-point bend tests. Before the first load drop, matrix micro-cracking initiates at the bottom of the specimen due to tension. These cracks progress slowly, however, no significant load drop occurs until a kink band develops on the compression side. With continued deformation, more kink bands develop and progress, resulting in the load plateau in the load-displacement response. Therefore, it can be concluded that the load capacity of this type of material subjected to flexural deformation is controlled by the compressive strength of the fiber tow. This finding agrees with the flexural test results of hybrid panels discussed in Section 3.3.2.



(a) Experimental load-displacement responses.



(b) Axial surface strain patterns (weft), ϵ_{xx} .



(c) Axial surface strain patterns (warp), ϵ_{xx} .

Figure 3.4: Representative load-displacement responses for Albany 2 specimens subjected to 3-pt bend tests. Surface strain patterns using DIC capture the damage occurrences.

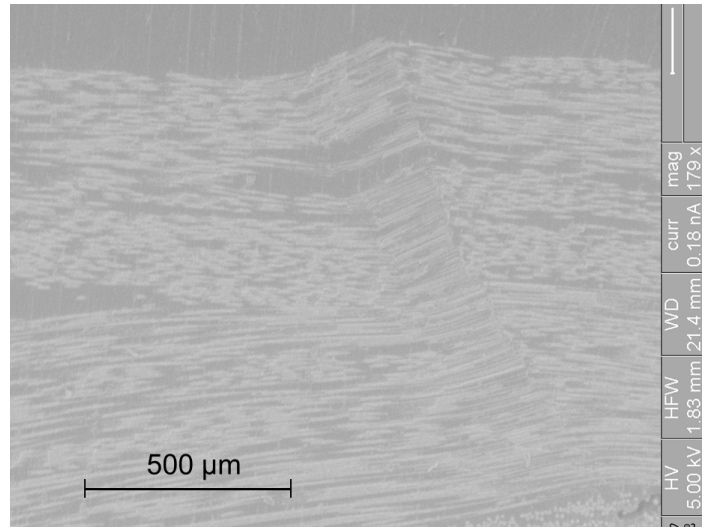


Figure 3.5: Kink band formation on the compression side of the Albany 2 specimen.

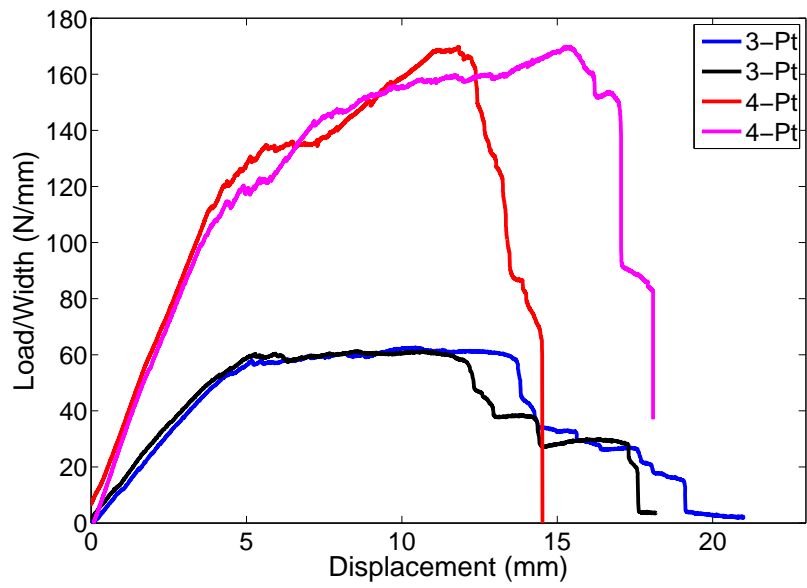
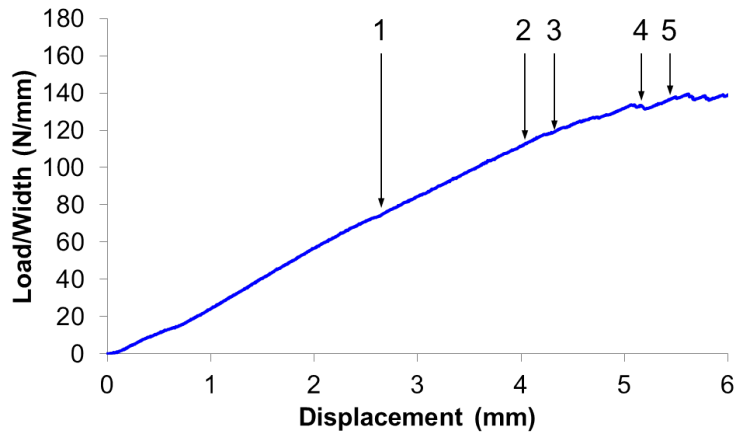
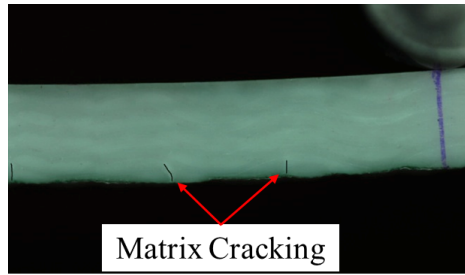


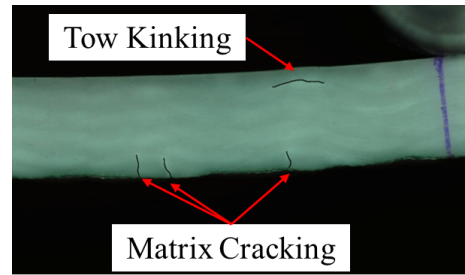
Figure 3.6: Experimental 3-pt and 4-pt load-displacement responses for Albany 2 panels (warp).



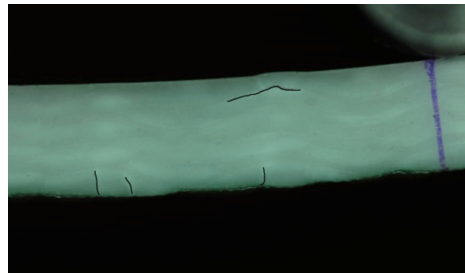
(a) Experimental load-displacement response.



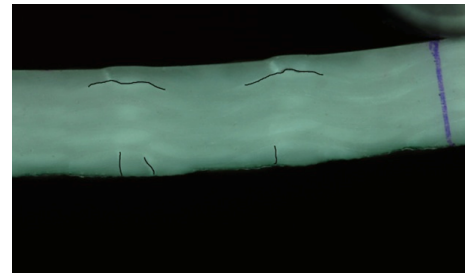
(b) At point (1).



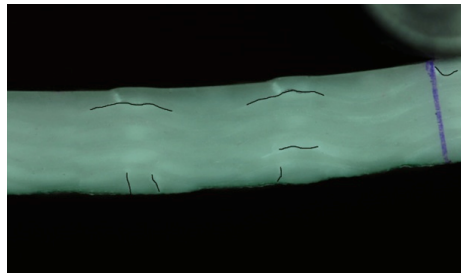
(c) At point (2).



(d) At point (3).



(e) At point (4).



(f) At point (5).

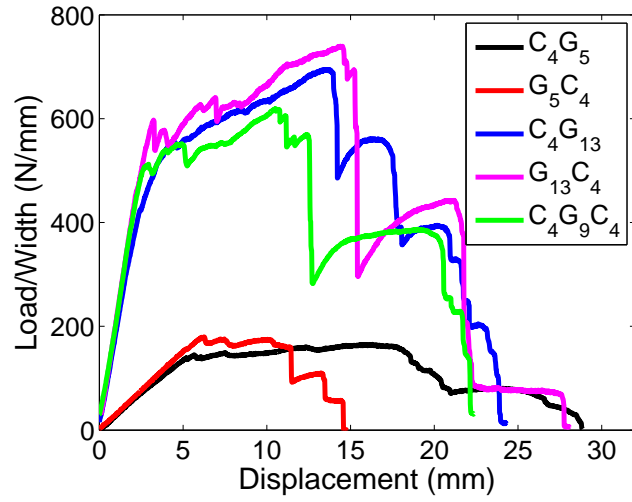
Figure 3.7: Progressive damage events for Albany 2 panel subjected to quasi-static 4-point bending. Matrix cracks are illustrated by the black lines. The specimen is loaded along the warp direction.

3.3.2 Hybrid Panels Subjected to Flexural Loading

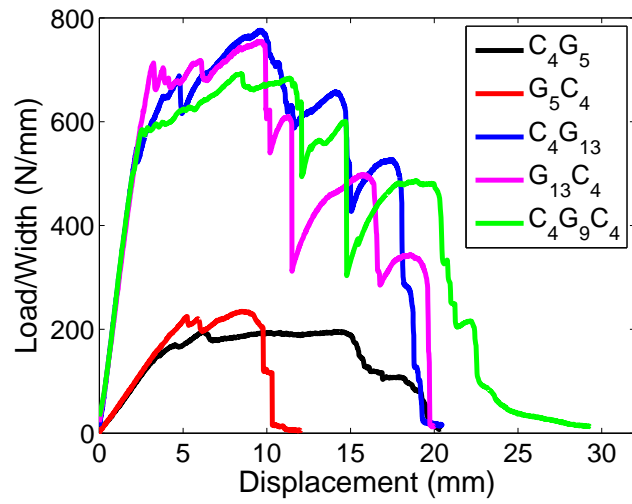
The experimental load-displacement responses for the different architectures loaded in various configurations are shown in Figure 3.8. These responses exhibit similar trends that the initial proportional loading is followed by a load plateau, indicating considerable damage tolerance for this class of materials. Figure 3.9 shows the response for the thin unsymmetric panel loaded along the warp direction, in which a series of images showing the observed damage events are related to the loading history. These images clearly show that the first damage occurred at the point that deviates from the proportional loading, and corresponds to fiber tow kinking on the compressive side of the flexed beam. When the beam deforms further, more kink bands are formed on the compressive side, accompanied by matrix cracking at the bottom, until a significant load drop, which is due to fiber tow rupture on the tensile side. Similar progressive damage mechanisms were observed for the thick unsymmetric and symmetric panels, as shown in Figure 3.10 and 3.11, respectively.

The tensile matrix cracking can be clearly seen from the DIC results, as shown in Figure 3.12. The surface strain contours show the area of strain localization due to the textile architecture, indicating the location that the matrix material starts to crack. In order to further investigate the observed compressive failure occurring in the fiber tow, tests were stopped at (or immediately after) the onset of the first load drop. The middle damaged area was cut from the specimen and cast into an epoxy molding. The damaged surface was subsequently polished and examined under both optical and scanning electron microscopes, as shown in Figure 3.13. The kink band formation, including fiber breakage and matrix cracking, is clearly seen in the SEM images.

The damage modes exhibited in the experiments are consistent for all three different architectures under various loading configurations, and can be summarized in Figure 3.14. The experimental results show that the peak load is determined by the fiber tow kinking strength. This agrees with the findings reported in Refs. [23, 31, 80] that kink band formation is the strength controlling mechanism of failure. It is worth noting that matrix cracking prevails during the deformation. In some instance, matrix cracking can occur before the fiber tow kinking, which has been observed in Albany 2 (discussed in Section 3.3.1). Although it seems from the experiments that these tensile cracks have little impact on the overall flexural response, the effect of the matrix cracking on the stress redistribution within the fiber tow is unclear. A further investigation of matrix cracking is carried out through a computational model, as discussed later in Chapter IV and VII.

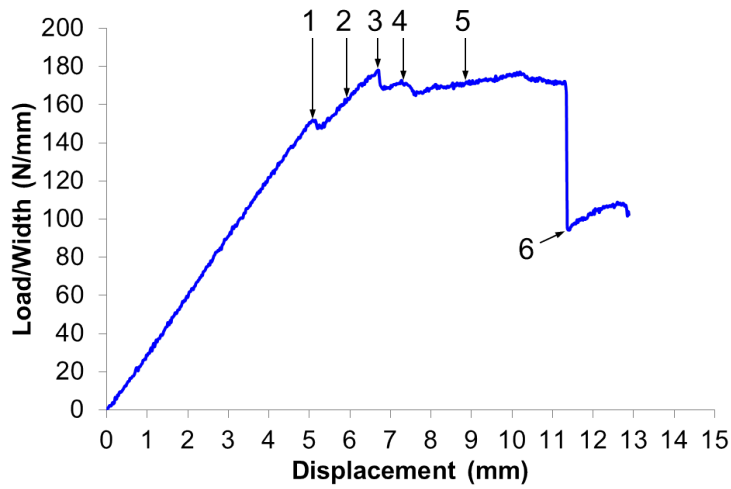


(a) Warp.

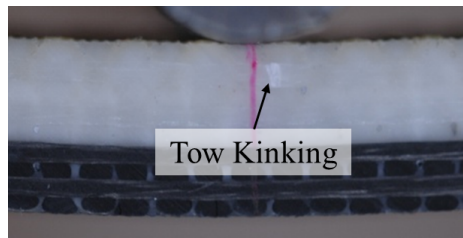


(b) Weft.

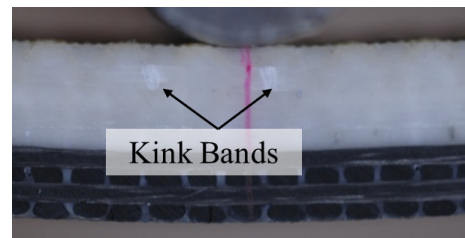
Figure 3.8: Experimental three-point load-displacement responses for various hybrid architectures.



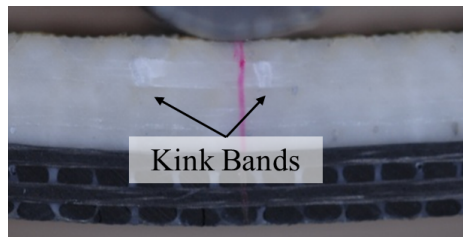
(a) Experimental load-displacement response.



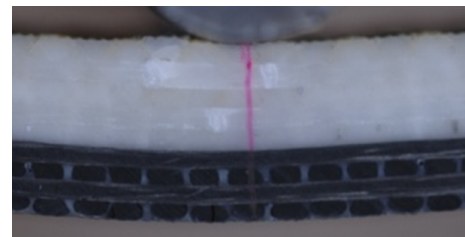
(b) At point (1).



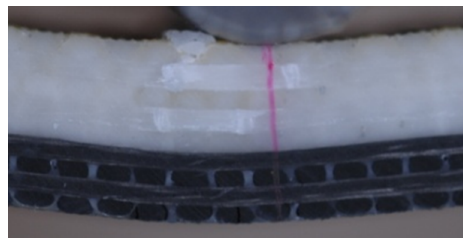
(c) At point (2).



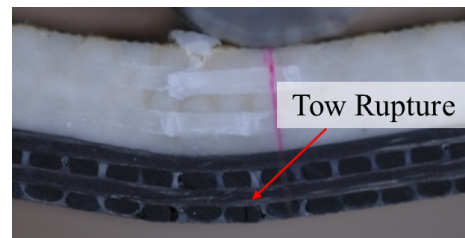
(d) At point (3).



(e) At point (4).

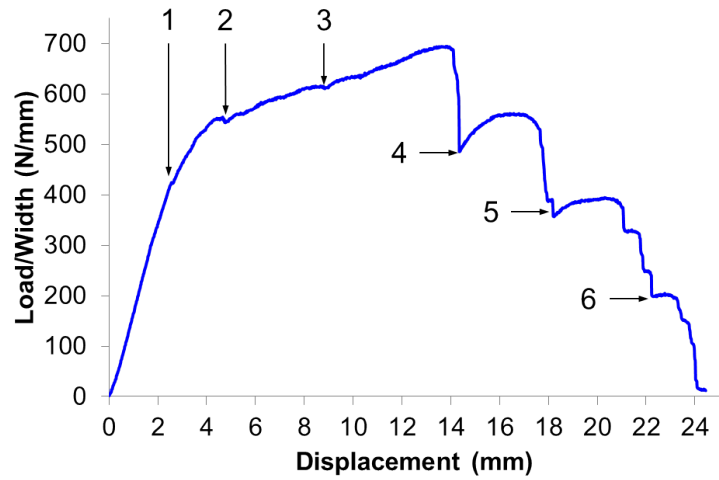


(f) At point (5).

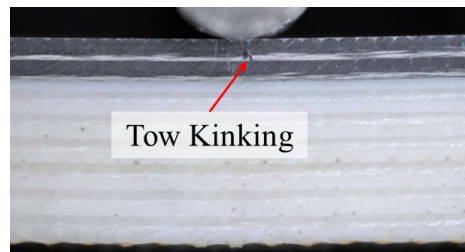


(g) At point (6).

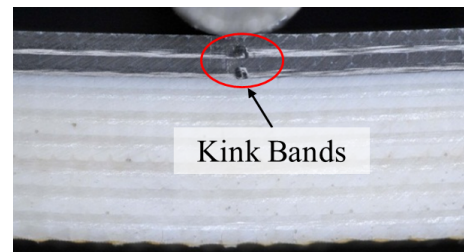
Figure 3.9: Progressive damage events for the thin unsymmetric panel subjected to quasi-static 3-point bending. The specimen is loaded along the warp direction.



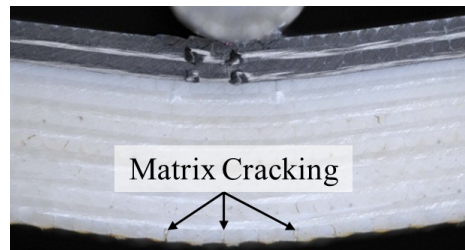
(a) Experimental load-displacement response.



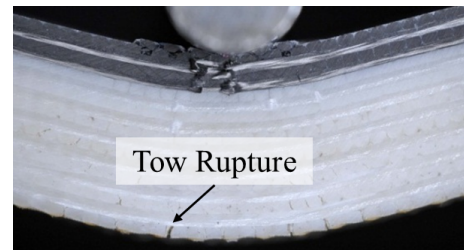
(b) At point (1).



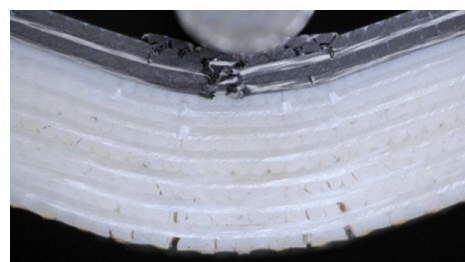
(c) At point (2).



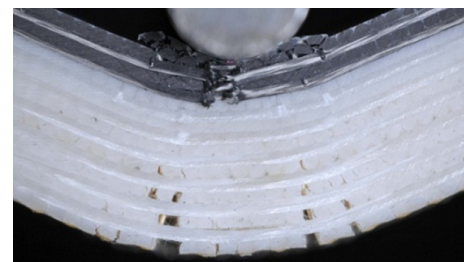
(d) At point (3).



(e) At point (4).

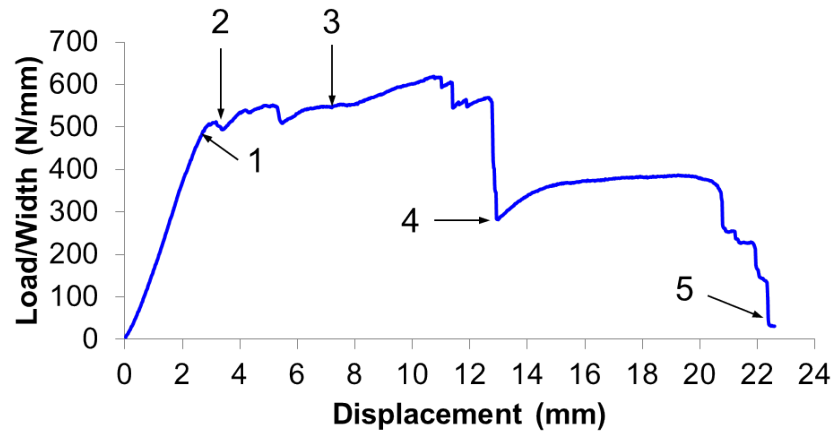


(f) At point (5).

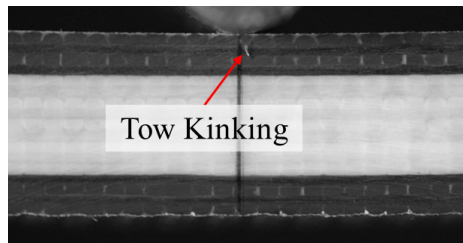


(g) At point (6).

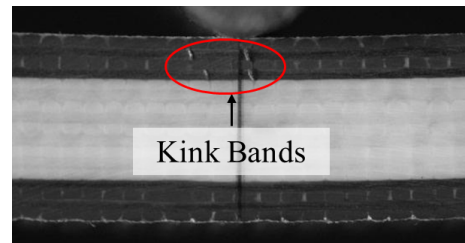
Figure 3.10: Progressive damage events for the thick unsymmetric panel subjected to quasi-static 3-point bending. The specimen is loaded along the warp direction.



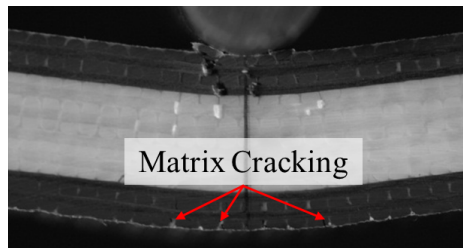
(a) Experimental load-displacement response.



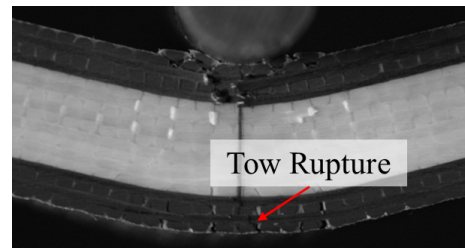
(b) At point (1).



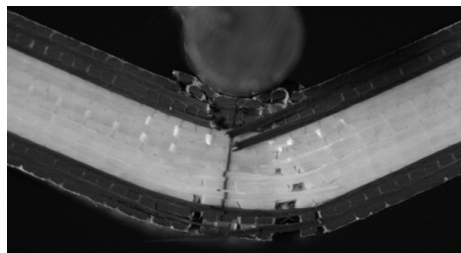
(c) At point (2).



(d) At point (3).

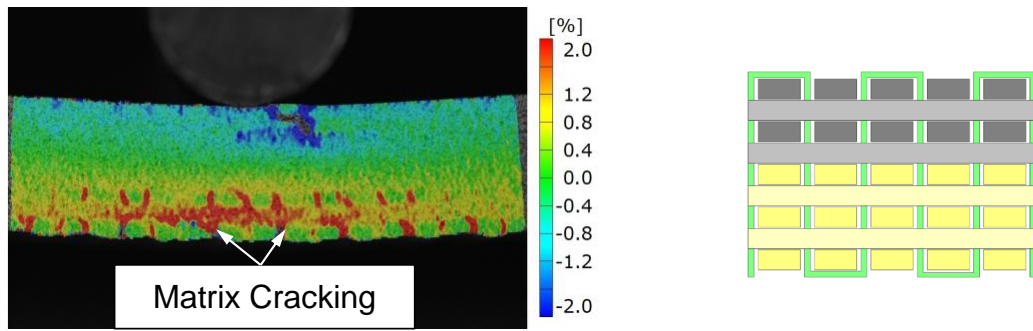


(e) At point (4).

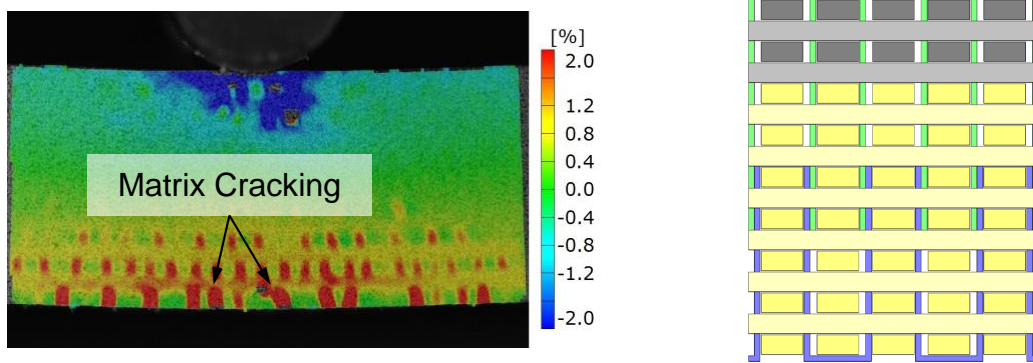


(f) At point (5).

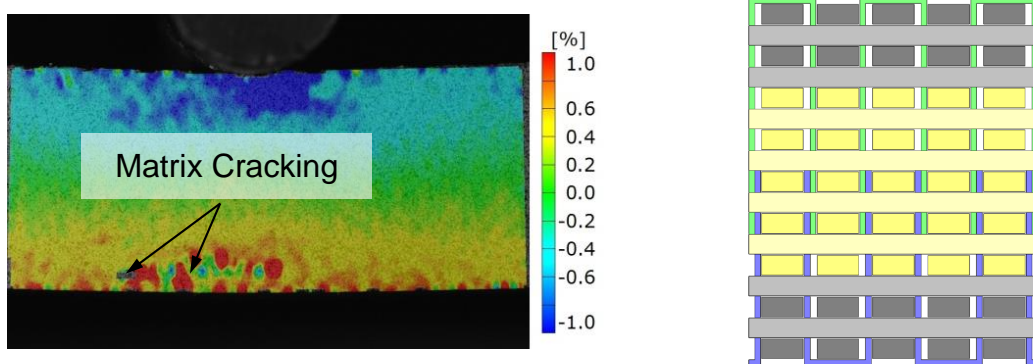
Figure 3.11: Progressive damage events for the thick symmetric panel subjected to quasi-static 3-point bending. The specimen is loaded along the warp direction.



(a) Thin unsymmetric, warp, C_4G_5 .



(b) Thick unsymmetric, warp, C_4G_{13} .



(c) Thick symmetric, warp, $C_4G_9C_4$.

Figure 3.12: Axial surface strain contours showing the tensile matrix cracking. The material architectures are shown to the right.

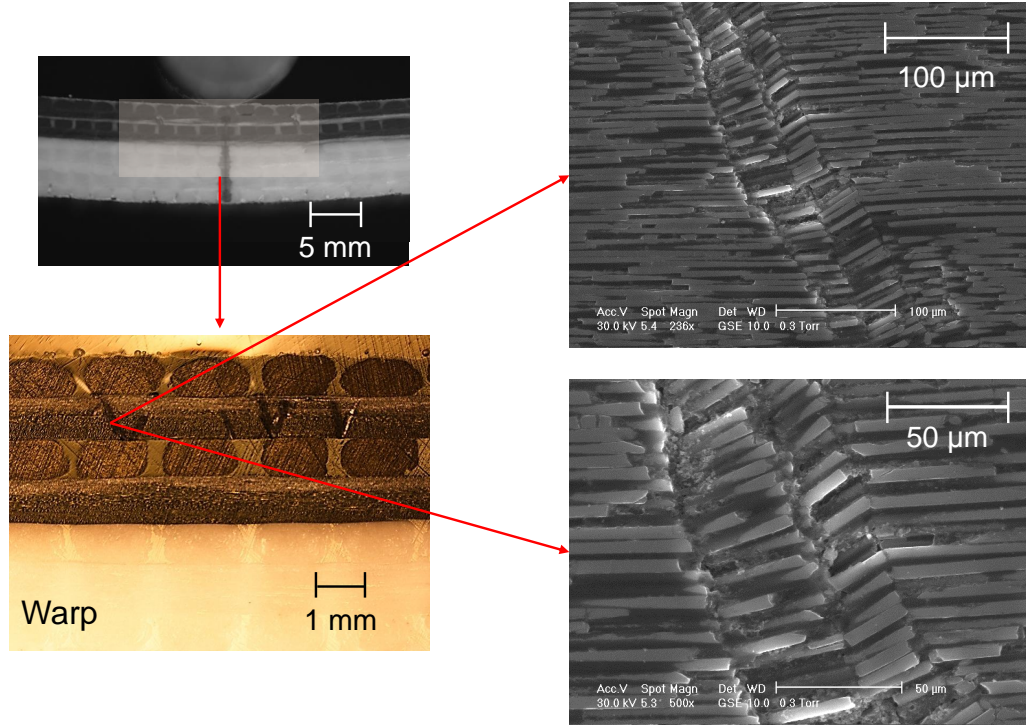


Figure 3.13: Kink bands were observed on the compression side of the flexed specimen. The post-damage surface was polished and examined under both optical microscope and SEM.

3.3.3 Effects of Hybridization Obtained Through Quasi-Static Three-Point Bend Tests

In order to compare the quasi-static three-point bend test results of various hybrid panels, the measured centerline load (P) and displacement (Δ) are utilized to compute the flexural stress, σ_f , and the flexural strain, ϵ_f , which are defined as the stress and strains on the outer surface at the mid-point, respectively, according to [81].

$$\sigma_f = \frac{3PL}{2bh^2} \left[1 + 6 \left(\frac{D}{L} \right)^2 - 4 \left(\frac{h}{L} \right) \left(\frac{D}{L} \right) \right] \quad (3.1)$$

$$\epsilon_f = \frac{6Dh}{L^2} \quad (3.2)$$

where L is the support span, and b and h are the width and depth of the specimen,

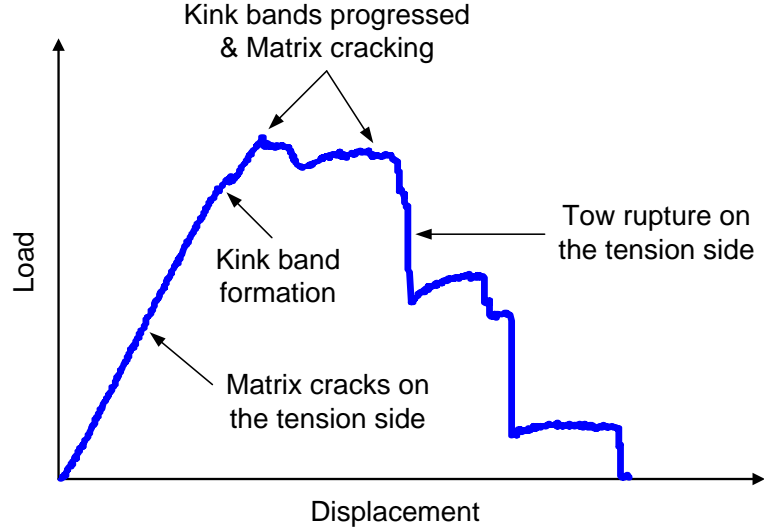


Figure 3.14: Schematic of experimental load-displacement response for 3D woven composite subjected to flexural loading. The observed damage events are annotated along with the deformation history.

respectively. The flexural modulus of elasticity, E_B , can be computed as,

$$E_B = \frac{mL^3}{4bh^3} \quad (3.3)$$

where m is the slope of the initial linear portion of the load-displacement response. It should be noted that for such highly orthotropic materials, the maximum stress may not always occur on the outer surface of the specimen. Hence, an appropriate beam theory, or a mechanics based model including those executed using FEA should be employed to identify the maximum stress and strain to failure, as a function of the textile architecture. That aspect is the subject of a separate study. The equations above allow for the comparison of the flexural responses among specimens with different architectures through the directly measured quantities in the experiment.

Figure 3.15 shows the flexural stress-strain relations for various test architectures. Compared with the load-displacement responses shown in Figure 3.8, these stress versus strain responses are closer to each other in the initial slope and peak load, indicating that these normalized quantities can be used to characterize the flexural properties for different architectures. Moreover, the material shows a progressive failure response, and it is difficult to identify the break point on the flexural stress-strain response. This aspect is not discussed in ASTM standard D790-10 [81]. Here, it is assumed that the material fails when the load drops by more than 20%. Thus, in order to compare the performance for the different hybrid architectures, the failure

characteristics used in the present study are, 1) the flexural yield stress, σ_{fY} , defined as the stress at the point that deviates from the initial proportional limit, 2) the maximum flexural stress, σ_{fM} , which is the maximum flexural stress achieved during the bending, and 3) the strain to failure, ϵ_{fM} , which is defined as the break point that corresponds to a 20% load drop. These defined failure characteristics are shown in Figure 3.16. It is worth noting that these failure properties are defined differently from those in the ASTM standard and utilized here for comparison purposes only.

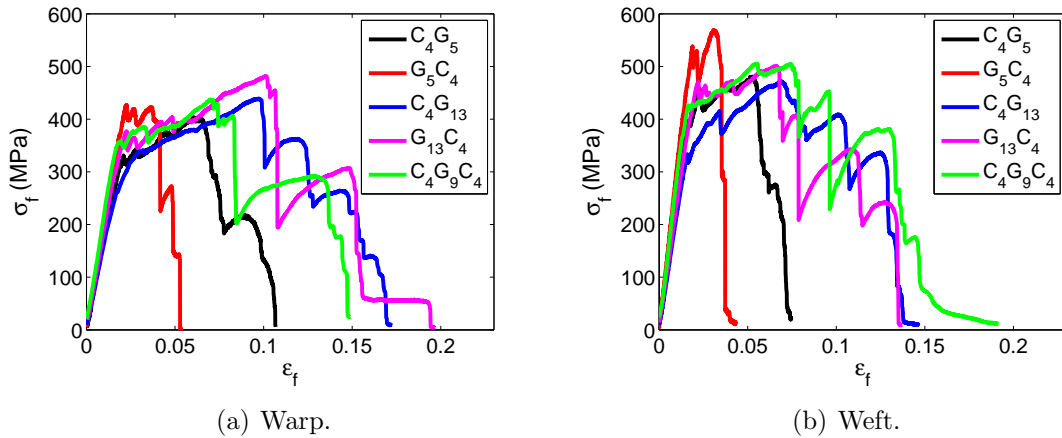


Figure 3.15: Flexural stress versus strain relations for various hybrid architectures.

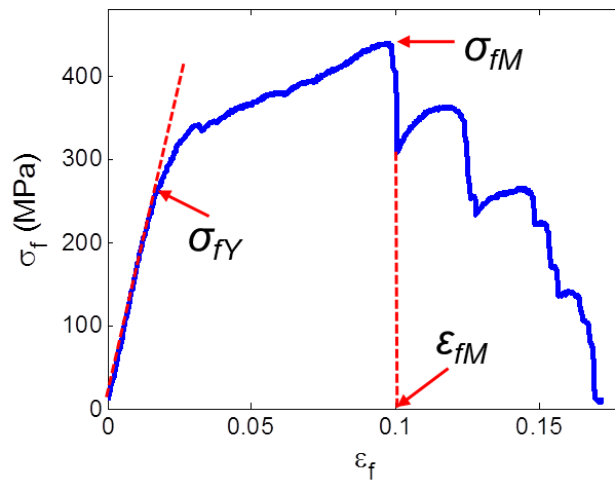


Figure 3.16: Defined failure characteristics to compare the performance of the different hybrid architectures.

The flexural modulus of elasticity and failure characteristics for the three different hybrid architectures are summarized in Table 3.2. It can be immediately concluded that the weft direction is stiffer (higher tangent modulus of elasticity) than the warp direction due to the fact that there is one additional axial fiber tow layer in the weft direction. For these textile architectures, the axial tows are on the outermost layers in the weft direction, carrying most of the bending moment. In addition, the thick unsymmetric panel yields the lowest elastic modulus due to the decreased percentage of carbon fibers. However, though the symmetric panel contains the highest percentage of carbon fibers, it does not show a significant increase in the bending stiffness, which is different from the results in tension [19]. It is also worth noting that for the unsymmetric panels, the “glass layers in compression” configuration shows a higher stiffness than the “carbon layers in compression”. This finding indicates that the material asymmetry can result in a shift of the bending axis from the geometric mid-plane. Hence, it is suggested that the flexural response of the hybrid panels be investigated through a more advanced theory [82, 83] or a FE model that incorporates the geometry of textile architecture, such as the one proposed in Chapter VII.

The “glass layers in compression” presents higher yield and maximum flexural stress and maximum ultimate strength than the “carbon layers in compression” in both the thick and thin unsymmetric panels. It has been shown previously that the yield flexural stress, which corresponds to the point that deviates from the initial proportional loading, is due to the kink band formation in the fiber tow. The kink bands are formed and progress on the compressive side of the specimen with further deformation, limiting the maximum load capacity of this class of materials. Hence, it can be concluded that the “glass layers in compression” exhibits higher compressive strength than the “carbon layers in compression”. The compressive failure of composite materials have been extensively investigated in the past, resulting in a series of important studies on fiber kinking [84, 85, 86, 87, 88, 89, 90, 91, 59, 92]. It is established that kink band formation is due to both geometric nonlinearity (fiber misalignment) and material nonlinearity (matrix degradation) in fiber reinforced composites. The misaligned fibers lead to localized shear strains and accompanied transverse strains, driving the degradation of the matrix material between the fibers. The matrix degradation in turn allows the fibers to rotate more easily, resulting in the formation of a kink band. Aspects in the predicting of kinking strength using a mechanics based FE model are discussed in Chapter VI.

When the unsymmetric panels are subjected to bending, the outermost carbon layers carry a larger percentage of the bending moment than the glass layers. Thus, if

it is assumed that the carbon and glass fibers have the same degree of misalignment, then in the instance that the carbon layers are in compression, the matrix inside the carbon tows will experience higher shear strains, resulting in a lower flexural yield stress. On the other hand, the “carbon layers in compression” gives higher ultimate strain to failure, indicating that the bottom glass layers present considerable energy absorption. The ultimate strains to failure for IM-7 carbon fibers and S-2 glass fibers are approximately 1.8% and 5.7%, respectively. Hence, it is expected that the glass tows can provide higher strain to failure in tension than the carbon tows. This result agrees with the findings reported in Ref. [19] that the pure glass architecture shows the highest ultimate tensile strength among all the hybrid configurations.

As shown in Figure 3.15, although the three different hybrid textile composites studied in this paper vary in the constituent fraction and panel thickness, the flexural stress-strain relation shows similar response and variation in the magnitude of the yield flexural stress, and the maximum flexural stresses are in the range of 11.8% and 11.0%, respectively. If it is assumed that the hybrid textile composites exhibit the same degree of fiber misalignment, the compressive strength of this type of material shall have a strong dependence on the matrix nonlinear properties. As a result, increasing the content of carbon fibers *cannot help increase the flexural strength*. However, it is also worth noting that the mechanism associated with fiber tow kinking in textile composites is complicated due to the complex textile geometry and the influence of the surrounding matrix. In order to further understand the tow kinking behavior and to better predict the kinking stress, the development of an architecture based 3D FE model is motivated. This work is presented in Chapter VII.

Table 3.2: Elastic properties and failure characteristics.

		E_B (GPa)	σ_{fY} (MPa)	σ_{fM} (MPa)	ϵ_{fM} (%)	
Thin	Warp	C_4G_5	$16.90 \pm 1.1\%$	$322.43 \pm 4.6\%$	$399.22 \pm 2.2\%$	$7.45 \pm 11.5\%$
		G_5C_4	$19.46 \pm 3.4\%$	$368.60 \pm 0.7\%$	$427.17 \pm 1.3\%$	$4.15 \pm 2.6\%$
Unsymmetric	Warp	C_4G_5	$29.13 \pm 5.6\%$	$347.33 \pm 5.7\%$	$472.00 \pm 4.9\%$	$5.55 \pm 3.2\%$
	Weft	G_5C_4	$32.12 \pm 4.3\%$	$402.63 \pm 4.7\%$	$579.53 \pm 1.6\%$	$3.98 \pm 10.9\%$
Thick	Warp	C_4G_{13}	$16.43 \pm 6.0\%$	$275.17 \pm 7.7\%$	$448.40 \pm 2.9\%$	$9.81 \pm 2.5\%$
		$G_{13}C_4$	$18.16 \pm 5.4\%$	$319.10 \pm 6.4\%$	$457.35 \pm 7.5\%$	$9.46 \pm 11.5\%$
Unsymmetric	Warp	C_4G_{13}	$22.38 \pm 6.0\%$	$307.00 \pm 4.3\%$	$481.18 \pm 2.9\%$	$10.87 \pm 4.5\%$
	Weft	$G_{13}C_4$	$22.97 \pm 5.6\%$	$403.73 \pm 3.9\%$	$516.22 \pm 4.2\%$	$7.89 \pm 19.5\%$
Symmetric	Warp	$C_4G_9C_4$	$22.26 \pm 4.2\%$	$355.90 \pm 3.8\%$	$441.88 \pm 5.2\%$	$7.14 \pm 4.9\%$
	Weft	$C_4G_9C_4$	$30.09 \pm 1.5\%$	$362.37 \pm 0.8\%$	$514.91 \pm 1.7\%$	$6.81 \pm 13.9\%$

3.4 Dynamic Three-Point Bend Tests

3.4.1 MTS: 2 in/sec

The dynamic flexural response of hybrid 3DTCs was first investigated using the MTS machine at a loading rate of 2 in/sec with a predetermined end deformation of 1 in. The deformation history was captured using a high-speed camera, Photron SA.5, recording images at 10,000 fps. The recorded load-deflection responses for the three different hybrid architectures are shown in Figure 3.17 - 3.19, and the corresponding results from the quasi-static tests are overlaid to show the rate-dependent effect.

The dynamic flexural response shows a similar load-deflection trend and progressive damage compared with the quasi-static response. When the loading rate is increased to 2 in/sec, the specimen tends to carry a higher load compared to that from static testing. The increase in the maximum load is most significant in the instance that the glass layers are in compression. This is because the compressive strength is controlled by the kink band formation, which is the result of fiber misalignment and matrix nonlinearity, as discussed in Section 3.3.2. This indicates that the matrix material inside the fiber tow behaves differently and exhibits different rate-dependent effects in the carbon and glass. This is evident in the testing of a (+45/−45) laminated composite panel composed of either pure carbon or pure glass fibers. The matrix static stress versus strain response obtained from the laminate shear test shows different nonlinear behavior in the carbon and glass, while both panels were manufactured using the same curing cycles as the one used for fabricating the hybrid panels, as shown in Section 6.3.2. In order to further understand the effect of loading rate on the in-situ matrix material, the pure glass and carbon laminates should be first tested under a higher rate. Investigating the in-situ matrix response is important, because it affects the formation of kink bands which limit the load carrying capacity.

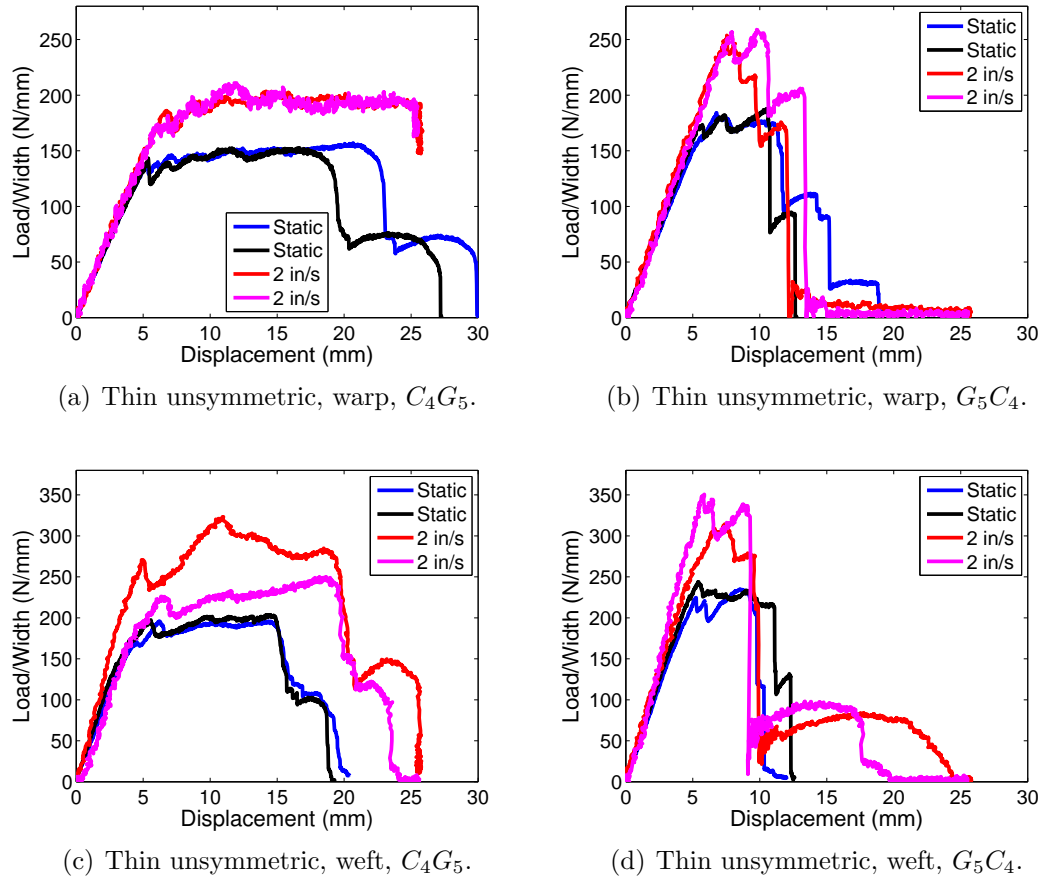


Figure 3.17: Experimental load-displacement responses for each of the testing configurations of the thin unsymmetric panels at two loading rates. The dynamic three-point bend tests were performed using MTS testing machine at a loading rate of 2 in/sec.

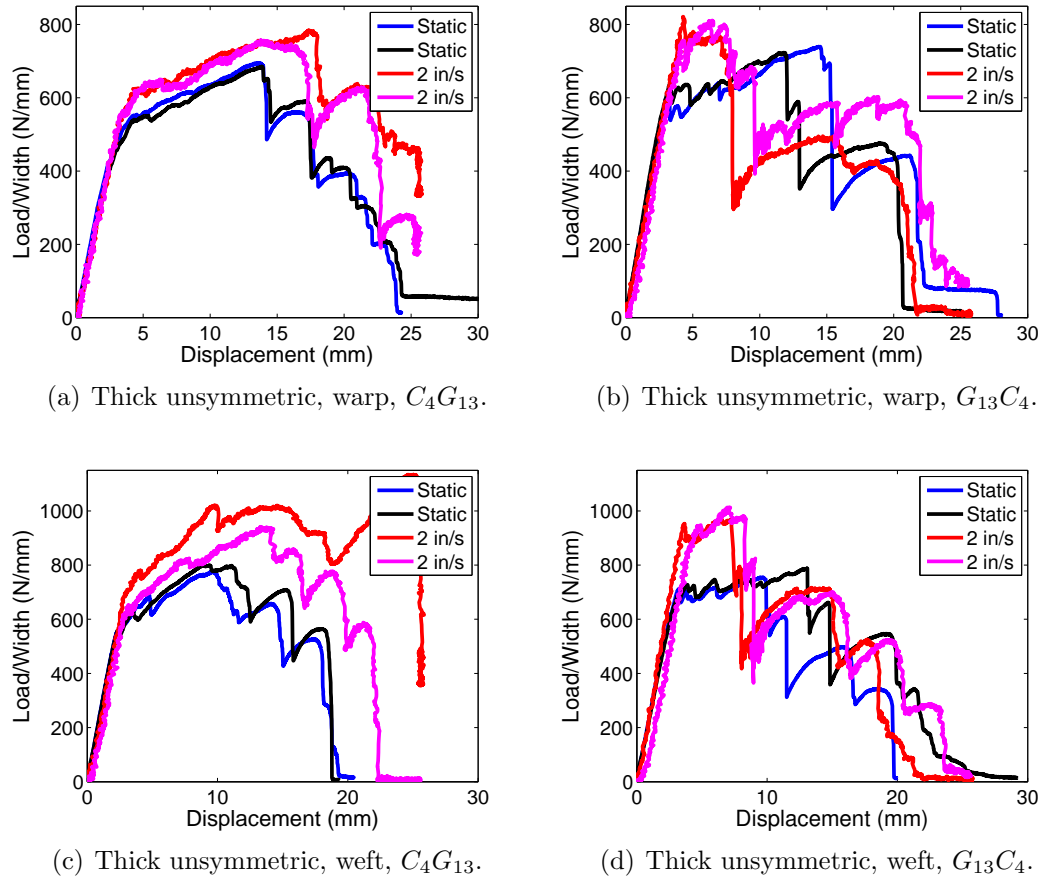


Figure 3.18: Experimental load-displacement responses for each of the testing configurations of the thick unsymmetric panels at two loading rates. The dynamic three-point bend tests were performed using MTS testing machine at a loading rate of 2 in/sec.

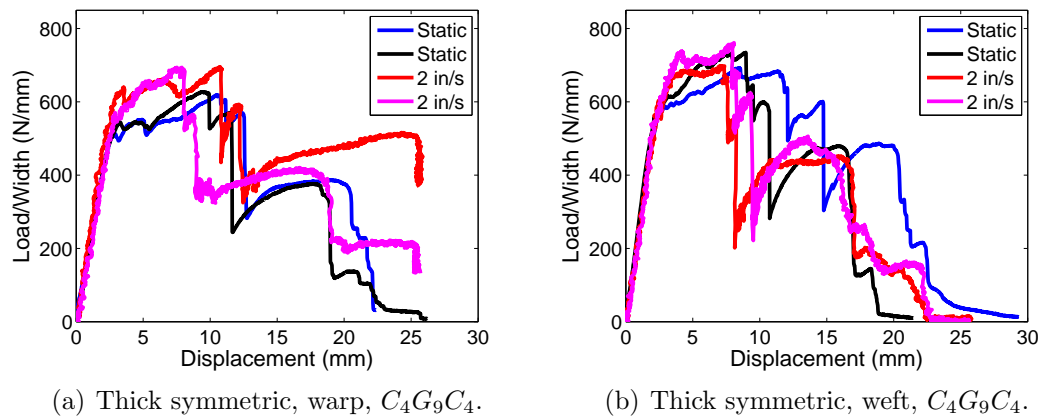


Figure 3.19: Experimental load-displacement responses for the thick symmetric panels testing along both warp and weft directions at two loading rates. The dynamic three-point bend tests were performed using MTS testing machine at a loading rate of 2 in/sec.

Table 3.3: Experimental setup for drop tower test. The thick panel includes the thick symmetric and unsymmetric one.

Specimen	Height		Velocity		Mass (kg)	Energy (J)
	(in)	(m)	(in/sec)	(m/sec)		
Thick Panel	15	0.38	108	2.73	63.1	235.0
	30	0.76	152	3.87	63.1	470.0
Thin Panel	15	0.38	108	2.73	25.1	93.5
	30	0.76	152	3.87	25.1	187.0

3.4.2 Drop Tower Test

In order to obtain a higher loading rate, the dynamic three-point bend tests were performed using a drop tower facility, as shown in Figure 3.20. Different impact velocities can be achieved by varying the height of the weight that is dropped onto the specimen, and the impact energy (E) is calculated as $E = mgh$, where m is the mass of the weight, h is the predetermined height, and $g = 9.8m/sec^2$. In the present study, two different heights, 15 in and 30 in, were chosen to achieve impact velocities of 108 in/sec and 152 in/sec, respectively. The mass of the weight that is dropped on the thick panels, including the thick symmetric and thick unsymmetric ones, is 63.1 kg to fail the specimens, while the weight is reduced to 25.1 kg for tests on the thin unsymmetric panels due to safety reasons. The experimental setup and the calculated impact energy for each testing configuration are summarized in Table 3.3. The impact force is measured using a Kistler 9104A load cell, which is mounted between the dropped mass and the impactor. Two Photron SA.5 high-speed cameras were utilized to capture the deformation history of the specimen, with one focused on the speckled surface of the dropped mass and the other on the specimen. The displacement of the impactor is calculated through the images of the speckled dropped mass via the DIC technique. The initial impact velocity obtained from the DIC result based upon the few frames before contact is correlated well with the velocity calculated using the equations for a free-falling object. The two cameras were synchronized with a recording rate of 15,000 fps.

The experimental load-deflection responses for the three different hybrid architectures are shown in Figure 3.21 – 3.23. Similar to the quasi-static testing results, the first damage event that affects the initial proportional loading is determined to be fiber tow kinking on the compressive side. When the specimen deforms further, more kink bands are formed on the compressive side, followed by a significant load

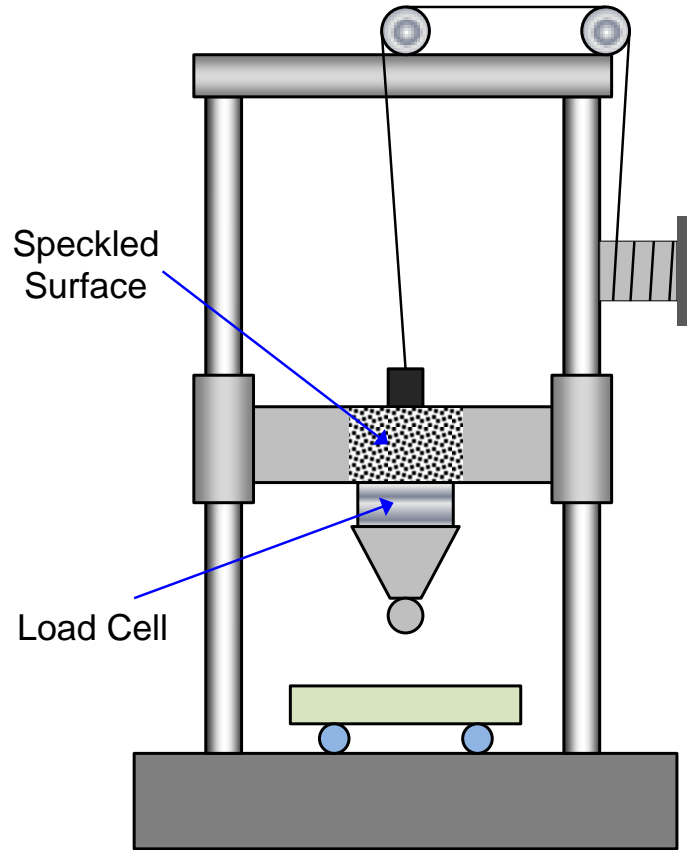


Figure 3.20: Drop tower test setup.

drop due to tow breakage on the tensile side. In the static test, a “load plateau” is observed during the progression of kink banding, however, the load recorded from the drop tower test shows a “chattering” response in this progressive damage regime. The peak loads obtained from the two different impact velocities are almost the same, however, the final catastrophic failure is significantly affected by the loading rates in the “glass layer in tension” testing configuration for both of the unsymmetric panels. For the thick unsymmetric panel under the impact velocity of 108 in/sec, the post-test specimen still remains a certain degree of load-carrying capability since the final load even does not drop much in the “glass layer in tension” configuration, as shown in Figure 3.22(a) and (c). However, the catastrophic strain to failure is not affected by the impact velocity in the “carbon layer in tension” configuration, as shown in Figure 3.21(b) and (c), Figure 3.22(b) and (c), and Figure 3.23.

The load-deflection responses for each hybrid architecture at the four different loading rates (quasi-static, 2 in/sec, 108 in/sec, and 152 in/sec) are shown in Figure

3.24 – 3.26. The rate-dependent effect is more significant in the glass layers than that in the carbon layers, for both tension (tow breakage) and compression (tow kinking) failure responses. It is also worth noting that the highest peak load occurs at the loading rate of 2 in/sec for each testing configuration. Elevated loading rates achieved by the drop tower does not lead to an increase in the peak load, which is controlled by the tow kinking strength. However, it should be pointed out that the drop tower facility is different from the MTS machine in that additional kinetic energy is introduced to the testing framework by the dropped weight. Therefore, it is critical to further investigate the effect of kinetic energy on the progressive damage and failure response of 3DTCs through both experimental and computational analysis. A computational model that captures both rate-dependent and architecture-dependent effects is presented in Chapter VII.

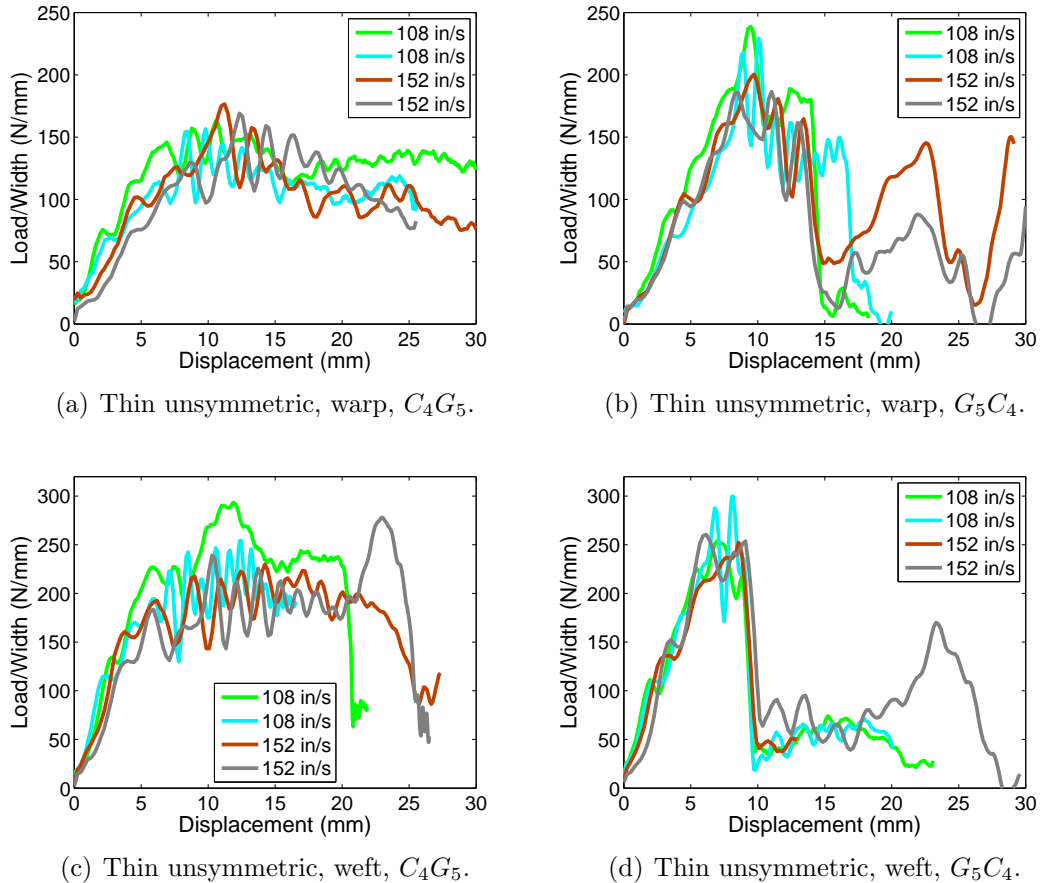


Figure 3.21: Experimental load-displacement responses for each of the testing configurations of the thin unsymmetric panels from drop tower tests.

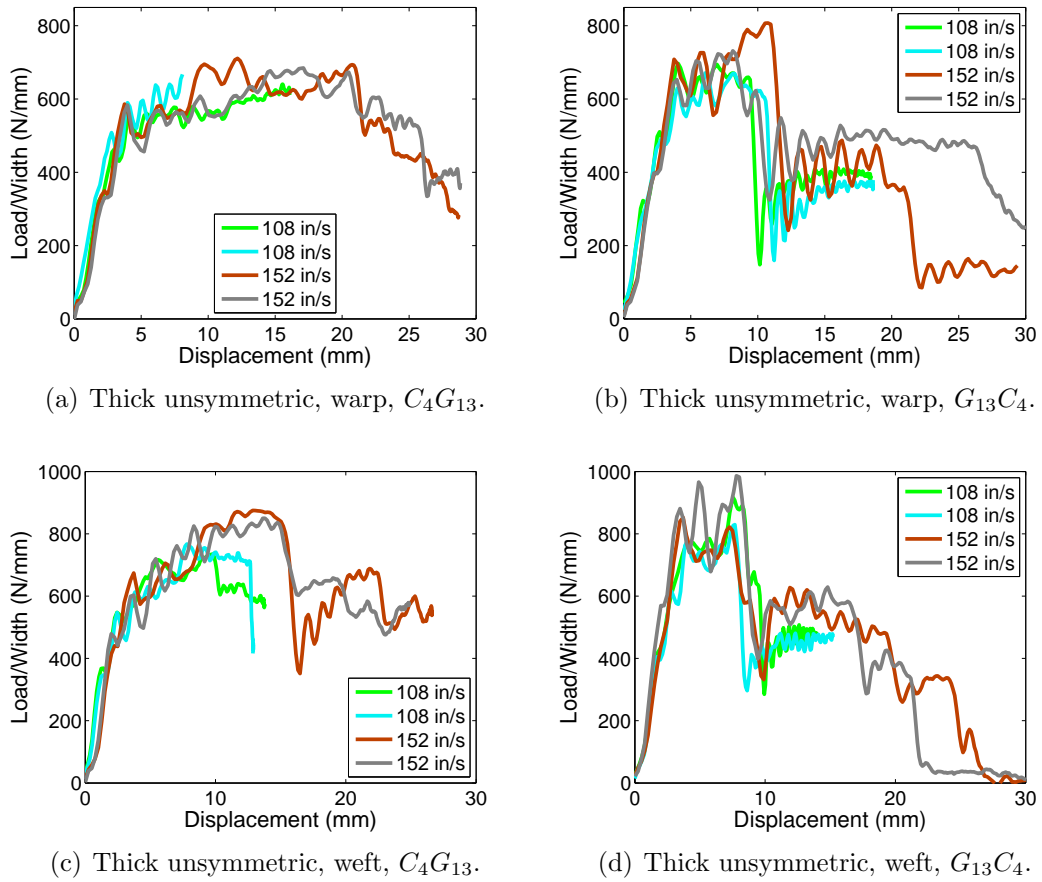


Figure 3.22: Experimental load-displacement responses for each of the testing configurations of the thick unsymmetric panels from drop tower tests.

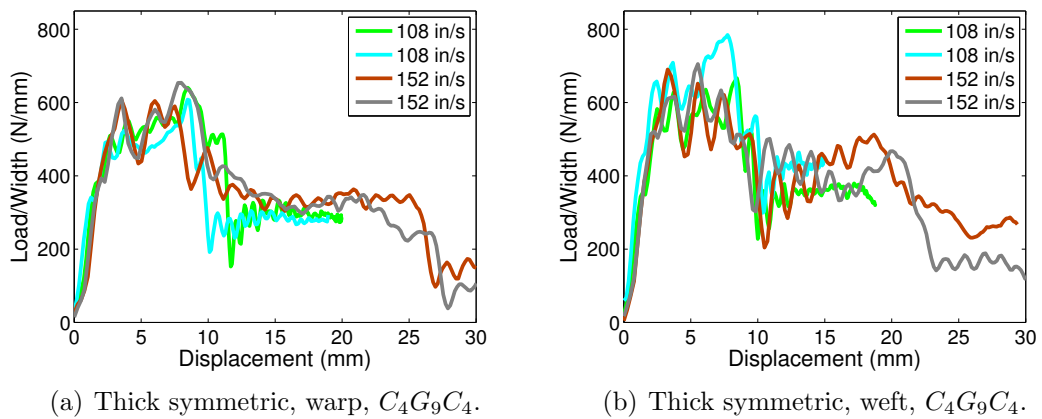
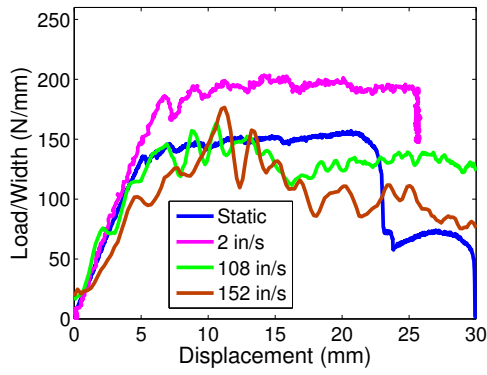
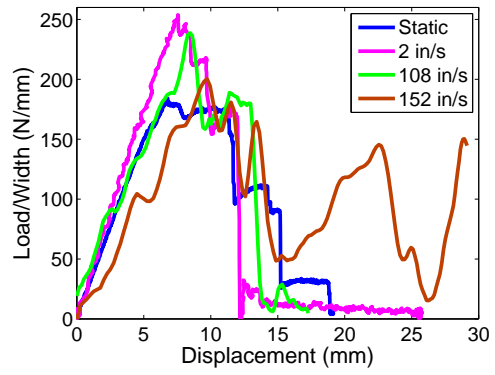


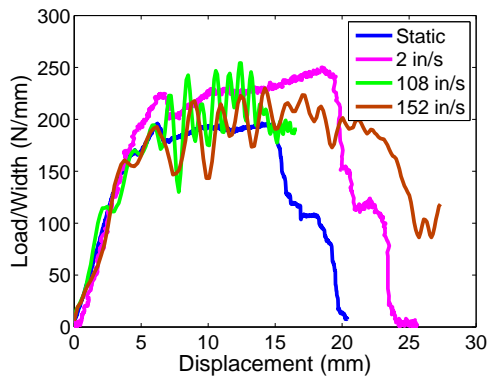
Figure 3.23: Experimental load-displacement responses for each of the testing configurations of the thick symmetric panels from drop tower tests.



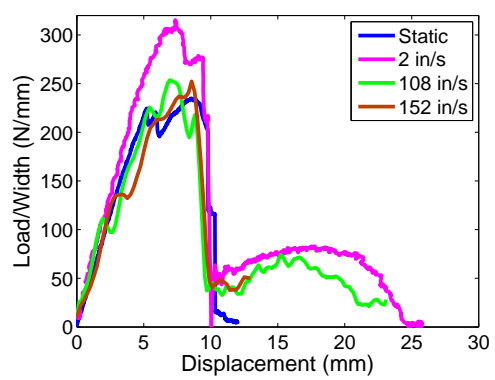
(a) Thin unsymmetric, warp, C_4G_5 .



(b) Thin unsymmetric, warp, G_5C_4 .

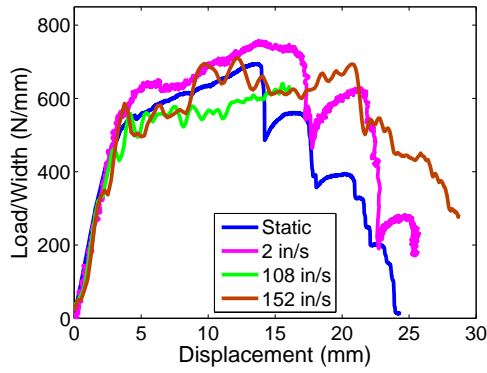


(c) Thin unsymmetric, weft, C_4G_5 .

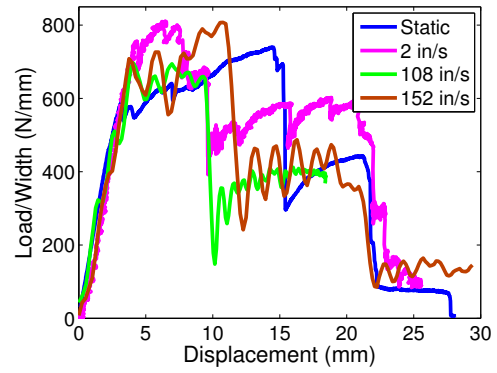


(d) Thin unsymmetric, weft, G_5C_4 .

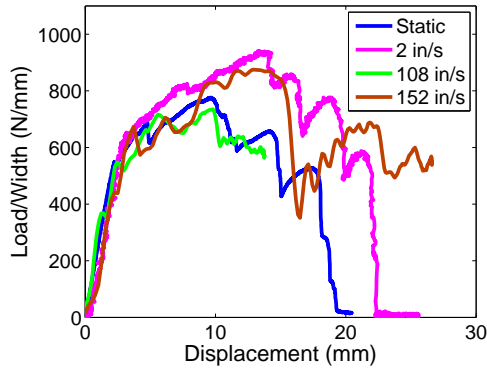
Figure 3.24: Experimental load-displacement responses for each of the testing configurations of the thin unsymmetric panels at the four different loading rates.



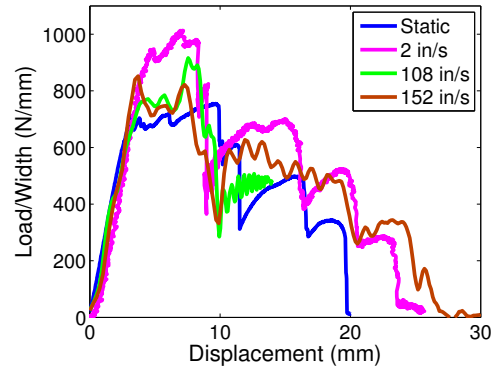
(a) Thick unsymmetric, warp, C_4G_{13} .



(b) Thick unsymmetric, warp, $G_{13}C_4$.

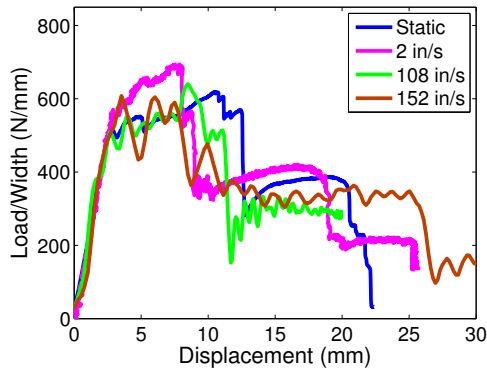


(c) Thick unsymmetric, weft, C_4G_{13} .

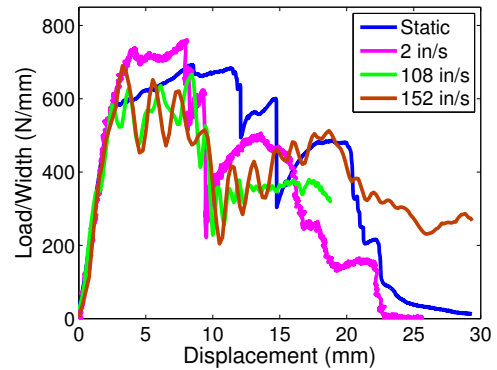


(d) Thick unsymmetric, weft, $G_{13}C_4$.

Figure 3.25: Experimental load-displacement responses for each of the testing configurations of the thick unsymmetric panels at the four different loading rates.



(a) Thick symmetric, warp, $C_4G_9C_4$.



(b) Thick symmetric, weft, $C_4G_9C_4$.

Figure 3.26: Experimental load-displacement responses for each of the testing configurations of the thick symmetric panels at the four different loading rates.

3.5 Conclusions

The flexural response of two distinct material systems, a layer-to-layer interlock pure glass fiber 3DTC (Albany 2) and Z-fiber orthogonal interlock hybrid 3DTCs of three different architectures, have been examined through both quasi-static and dynamic tests. The quasi-static load-displacement responses show similar behavior for various architectures. It is observed that the load deviates from the initial proportional loading due to fiber tow kinking on the compressive side of the specimen. With continued deformation, additional kink bands are formed on the compressive side, while the progression of matrix cracking is captured using a DIC technique. The observed load plateau indicates that this class of materials exhibit considerable damage tolerance. The final significant load drop was observed due to fiber tow rupture on the tensile side. The flexural response of hybrid textile composites show a strong dependence on the fiber lay-ups, and the addition of carbon fiber layers do not always improve the performance, including the bending modulus, flexural strength, and strain to failure.

The dynamic three-point bend tests were performed only on the hybrid panels at three different loading rates. The MTS machine can achieve a loading rate of 2 in/sec, and the drop tower provides higher impact velocities of 108 in/sec and 152 in/sec by setting the height of the dropped weight to be 15 in and 30 in, respectively. The dynamic response shows a similar load-deflection trend and progressive damage behavior compared with the quasi-static response. The highest peak load is obtained at the loading of 2 in/sec, while the elevated loading rates achieved using the drop tower result in a decrease in the peak load that is controlled by the tow kinking strength. However, it should be pointed out that the drop tower facility is different from the MTS machine in that additional kinetic energy is introduced to the testing framework by the dropped weight. Thus, the progressive damage and failure response of 3DTCs is also affected by the energy transfer between the kinetic energy of the dropped impactor to the strain energy stored in the deformed beam.

Although the experimental results show an architecture-dependent effect, fiber tow kinking on the compressive side of the specimen is determined to be a strength limiting mechanism for this class of materials. The tow kinking phenomenon along with matrix cracking due to strain localization indicate the importance of the textile architecture on the failure mechanisms of this class of material. Hence an architecture based numerical model that incorporates constitutive relations that encompass damage is expected to predict the failure modes observed in the experiment. A

computational model that captures both rate-dependent and architecture-dependent effects is presented in Chapter [VII](#).

CHAPTER IV

Modeling Progressive Microdamage and Failure in a Polymer Matrix

4.1 Introduction

Matrix cracking is prevalent in fiber-reinforced composite materials when subjected to mechanical loading. As shown in Chapter III, matrix cracking is observed on the tensile side of a flexed 3DTC panel and progressed throughout the specimen. In addition, the experimental stress-strain responses for the monolithic matrix material under tension and compression (see Figure 2.11) suggest that the material exhibits nonlinearity before reaching the peak stress. In this work, damage and failure are distinguished in such a manner that **damage** governs any nonlinear response that preserves the positive definiteness of the material stiffness tensor; whereas **failure** is defined as the structural changes that result in post-peak strain softening in the stress versus strain response. Figure 4.1 shows a representative full constitutive response of a polymer matrix including damage and failure behavior. The pre-peak nonlinear behavior is attributed to matrix microdamage due to the growth of voids and flaws in the matrix, and is considered as a damage mechanism. The accumulation of matrix microdamage finally results in matrix macroscopic cracking that is categorized as a failure mechanism due to the loss of the positive definiteness of the material tangent stiffness tensor.

A multitude of damage and failure models have been developed over the past few decades, with an intent to be implemented in a FE modeling framework. In this sense, continuum damage mechanics (CDM) has emerged as an efficient way for modeling the nonlinear behavior of the material with growing damage, such as the evolution of matrix cracking in composite materials and crack propagation in concrete. Rather than treating the highly distributed cracks individually, CDM captures the

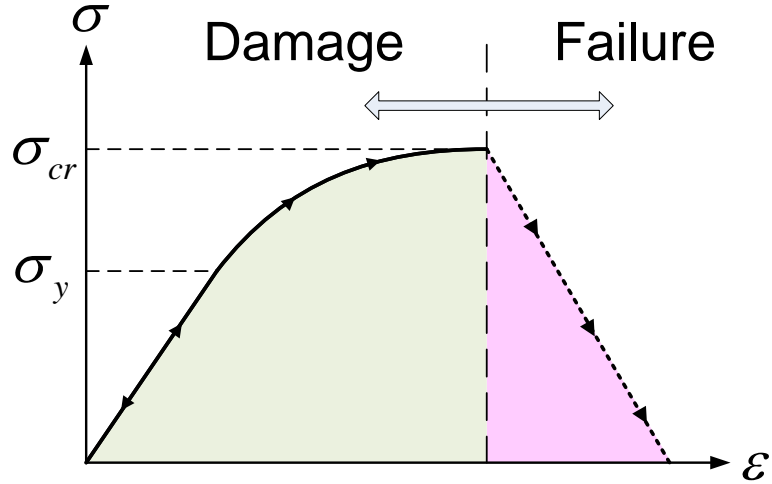


Figure 4.1: Schematic of matrix constitutive behavior including damage and failure.

average effects of these progressively distributed cracks by reducing the components of the material stiffness tensor. It assumes that the cracks, which are considered as discontinuities at a lower scale, can be represented as a continuous medium at a larger scale by scaling the area of damage with respect to a finite volume. In the CDM theory, a representative volume element (RVE) is introduced, in which all the material properties are represented by homogenized variables. Therefore, the damage and failure behavior can be modeled using a set of scalar damage variables that are associated with certain observed damage/failure mechanisms. The idea of using scalar damage variables was first proposed by Kachanov [93], and later, a number of practical applications of CDM were published in [94, 95, 96, 97, 98, 99]. Implementation of CDM in modeling the damage and failure in composite materials has been reported in [100, 101, 102, 103, 104, 105].

Although CDM has the ability to capture the material strain softening behavior, this method is pathologically mesh dependent since no characteristic length scale is associated with the damage evolution. When implementing CDM in a FE framework, failure will be localized within a single element, and the energy dissipated due to failure becomes a function of element size. In essence, the element size becomes the characteristic length. Consequently, in the limit of zero element size, the amount of energy dissipation also approaches zero. In order to restore mesh objectivity, that is, to prevent element size from being the characteristic length, nonlocal theory [106, 107] and gradient-based theory [108, 109] have been developed by enforcing a characteristic length, which is independent of element size, to be associated with damage evolution equations.

An alternative method to preserve mesh objectivity is to associate the post-peak strain softening behavior with a traction-separation law such that the total strain energy dissipated during the failure process can be equated to the fracture toughness of the material, thereby introducing a characteristic element length which is related to energy dissipation. Both the crack band [63] approach and smeared crack approach (SCA) [64] have been developed with this motivation. In these theories, the pre-peak stress-strain response is modeled using a standard continuum theory (such as elasticity, plasticity, CDM, Schapery theory [110, 111]), while the post-peak strain softening failure behavior is represented through a traction-separation law that incorporates a characteristic length. This characteristic length is related to element size through an equation that includes material properties, including fracture toughness, fracture strength, and elastic modulus. Implementation of various failure initiation criteria and subsequent evolution laws for modeling progressive failure in composite materials has been reported in [112, 113, 114, 115]. Recently, Pineda et al. [116] investigated the capability of utilizing the crack band theory to predict the progressive matrix cracking within a fiber-matrix microstructure.

In this chapter, the modeling strategy for an isotropic matrix material is presented, including damage and failure analysis. The matrix microdamage, manifested as the pre-peak nonlinear stress versus strain response, is modeled using a modified J_2 deformation theory of plasticity, as formulated in Section 4.2. The secant moduli are degraded with the progression of microdamage, however, the positive definiteness of the tangent stiffness tensor is still preserved. When a critical stress state is reached, failure is initiated and the post-peak strain softening behavior is modeled through the SCA. The SCA, originally developed to capture tensile cracks (mode-I) in concrete, is extended to model matrix macroscopic cracking in both tension and compression, as given in Section 4.3. An example of demonstrating mesh objectivity of the SCA to model the post-peak strain softening behavior is given in Section 4.4. The implementation of this matrix material model to the mesoscale textile architecture based FE model is presented in Chapter VII, in which the progression of matrix cracking in 3D woven composites is successfully captured.

4.2 Modeling the Microdamage in Matrix Based upon Modified J_2 Deformation Theory of Plasticity

The pre-peak nonlinear behavior of a polymer matrix material is the result of matrix microdamage. The evolution of such a damage mechanism accounts for pro-

gressive deterioration of the material stiffness, however, the tangent stiffness tensor still remains positive-definite. It has been shown by Sicking [117] that a polymer matrix exhibits loading path independence behavior through a combined tension and torsion test. Hence, for such an isotropic material, the state of stress can be uniquely determined from the state of strain through a secant modulus as long as the material does not unload. It further assumes that the evolution of damage is an irreversible process, therefore, once the matrix stiffness tensor is degraded due to microdamage, it cannot be recovered. Such behavior suggests that a modified J_2 deformation theory of plasticity be employed to model the nonlinear stress-strain relation of this type of material. The present constitutive model is different from the original theory in that the degrading secant moduli are utilized to compute the material stiffness tensor during unloading, as schematically shown in Figure 4.2.

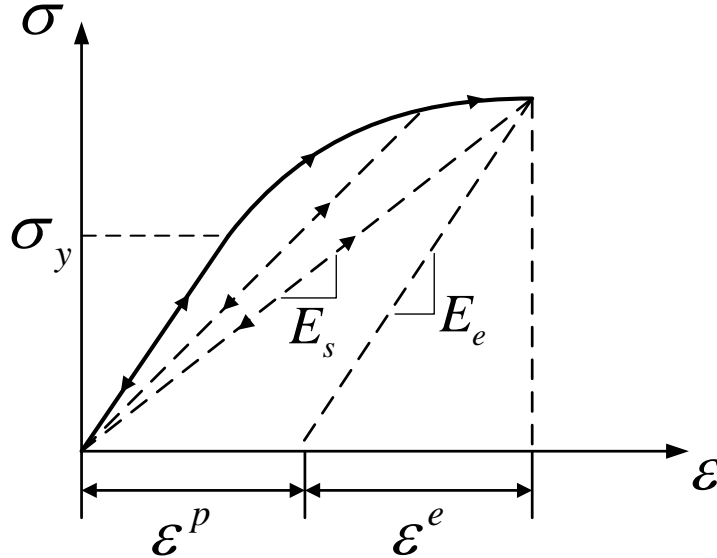


Figure 4.2: Representative uniaxial stress-strain response for polymer matrix. The evolution of pre-peak nonlinearity is modeled through a secant moduli approach.

In the classical theory of plasticity, it is assumed that the total strains, ϵ_{ij} , can be decomposed into elastic strains, ϵ_{ij}^e , and plastic strains, ϵ_{ij}^p , for small strains, as,

$$\epsilon_{ij} = \epsilon_{ij}^e + \epsilon_{ij}^p \quad (4.1)$$

For a J_2 -material, the plastic strain is related to the stress deviator, s_{ij} , as,

$$\epsilon_{ij}^p = \phi(J_2)s_{ij} \quad (4.2)$$

where the scalar, $\phi(J_2)$, is a material property determined by experiment. From the uniaxial stress-strain response shown in Figure 4.2.

$$\epsilon_{11}^p = \phi(J_2)s_{11} = \epsilon_{11} - \epsilon_{11}^e = \frac{\sigma_{11}}{E_s} - \frac{\sigma_{11}}{E_e} = \frac{3}{2} \left(\frac{1}{E_s} - \frac{1}{E_e} \right) s_{11} \quad (4.3)$$

where E_e and E_s are the material elastic and secant Young's moduli, respectively. Hence,

$$\phi(J_2) = \frac{3}{2} \left(\frac{1}{E_s} - \frac{1}{E_e} \right) \quad (4.4)$$

$$\epsilon_{ij}^p = \frac{3}{2} \left(\frac{1}{E_s} - \frac{1}{E_e} \right) s_{ij} \quad (4.5)$$

Substituting Eq. (4.5) into Eq. (4.1), results in,

$$\begin{aligned} \epsilon_{ij} &= \frac{1 + \nu_e}{E_e} \sigma_{ij} - \frac{\nu_e}{E_e} \sigma_{kk} \delta_{ij} + \frac{3}{2} \left(\frac{1}{E_s} - \frac{1}{E_e} \right) s_{ij} \\ &= \left[\frac{1 + \nu_e}{E_e} + \frac{3}{2} \left(\frac{1}{E_s} - \frac{1}{E_e} \right) \right] \sigma_{ij} - \left[\frac{\nu_e}{E_e} + \frac{1}{2} \left(\frac{1}{E_s} - \frac{1}{E_e} \right) \right] \sigma_{kk} \delta_{ij} \end{aligned} \quad (4.6)$$

where ν_e is the elastic Poisson's ratio. In order to simplify Eq. (4.6), a secant Poisson's ratio, ν_s , is defined as,

$$\nu_s = \frac{1}{2} + \frac{E_s}{E_e} \left(\nu_e - \frac{1}{2} \right) \quad (4.7)$$

Hence, Eq. (4.6) is reduced to,

$$\epsilon_{ij} = \frac{1 + \nu_s}{E_s} \sigma_{ij} - \frac{\nu_s}{E_s} \sigma_{kk} \delta_{ij} \quad (4.8)$$

Therefore, the total stress versus strain relation for a nonlinear material can be formulated using secant moduli, E_s and ν_s , Eq. (4.8) appears in form like the relation for a linear elastic material. For an isotropic material, other material constants, such as μ and λ , can be extended to secant quantities in a similar manner as,

$$\mu_s = \frac{E_s}{2(1 + \nu_s)} \quad \lambda_s = \frac{\nu_s E_s}{(1 + \nu_s)(1 - 2\nu_s)} \quad (4.9)$$

Thus, the total stress-strain constitutive relation can be written as,

$$\sigma_{ij} = 2\mu_s \epsilon_{ij} + \lambda_s \epsilon_{kk} \delta_{ij} \quad (4.10)$$

In order to utilize a uniaxial stress-strain response to determine the material response under multi-axial loading, two equivalent variables, the equivalent stress, σ_{eq} , and the equivalent strain, ϵ_{eq} , are introduced and related through E_s as,

$$\sigma_{eq} = E_s \epsilon_{eq} \quad (4.11)$$

According to J_2 deformation theory, σ_{eq} is defined as,

$$\begin{aligned} \sigma_{eq} &= \sqrt{3J_2} \\ &= \sqrt{\frac{1}{2} [(\sigma_{11} - \sigma_{22})^2 + (\sigma_{22} - \sigma_{33})^2 + (\sigma_{33} - \sigma_{11})^2] + 3(\sigma_{12}^2 + \sigma_{13}^2 + \sigma_{23}^2)} \end{aligned} \quad (4.12)$$

Squaring both sides of Eq. (4.11), it gives $\sigma_e^2 = E_s^2 \epsilon_{eq}^2$. Since $\sigma_e^2 = 3J_2 = \frac{3}{2} s_{ij} s_{ij}$, it follows that,

$$\epsilon_{eq}^2 = \frac{3}{2} \frac{1}{E_s^2} s_{ij} s_{ij} \quad (4.13)$$

Noting that,

$$s_{ij} = 2\mu_s e_{ij} = \frac{E_s}{1 + \nu_s} e_{ij} \quad (4.14)$$

where e_{ij} are the strain deviators. Substituting Eq. (4.14) into Eq. (4.13), it results in,

$$\epsilon_{eq}^2 = \frac{3}{2} \frac{1}{(1 + \nu_s)^2} e_{ij} e_{ij} \quad (4.15)$$

Taking the square root of both sides of Eq. (4.15) leads to,

$$\epsilon_{eq} = \frac{1}{1 + \nu_s} \sqrt{\frac{1}{2} [(\epsilon_{11} - \epsilon_{22})^2 + (\epsilon_{22} - \epsilon_{33})^2 + (\epsilon_{33} - \epsilon_{11})^2] + \frac{3}{4} (\gamma_{12}^2 + \gamma_{13}^2 + \gamma_{23}^2)} \quad (4.16)$$

It can be shown that when the matrix is subjected to a uniaxial tension state ($\sigma_{11} > 0$ and other $\sigma_{ij} = 0$), σ_{eq} is reduced to σ_{11} according to Eq. (4.12). On the other hand, the non-zero strains in a uniaxial tensile stress state are $\epsilon_{11} > 0$ and $\epsilon_{22} = \epsilon_{33} = -\nu_s \epsilon_{11}$. Substituting these relations into Eq. (4.16), ϵ_{eq} is readily reduced to ϵ_{11} . Thus, a simple uniaxial stress-strain response from tensile testing can be used to construct the effective stress versus effective strain response, and no other measurements are required.

In this research, the matrix nonlinear stress-strain relation is characterized using an exponential relation as,

$$\sigma_{eq} = \sigma_y - \frac{K_1}{K_2} \left(e^{-K_2 \epsilon_{eq}} - e^{-K_2 \frac{\sigma_y}{E_e}} \right) \quad (4.17)$$

where σ_y is the yield stress in a simple uniaxial tension test, and K_1 and K_2 are the two material constants that govern the evolution of matrix microdamage. These material properties can be determined from the experimental stress-strain response shown in Figure 2.11.

4.3 Modeling the Failure of the Matrix Material Using the SCA

The accumulation of matrix microdamage leads to the initiation of matrix macroscopic cracking, followed by a post-peak strain softening response in the stress versus strain response. In this research, the evolution of matrix failure is modeled using the SCA, which is originally developed by Rots et al. [64] to model crack propagation and fracture in concrete. In the SCA, it is hypothesized that distributed cracks are “smeared” out over a certain width within the finite element such that the effect of progressive cracking is represented by a macroscopic strain softening behavior in a continuum scheme. Here, a characteristic length scale is introduced to associate this strain softening response with the traction-separation law (see Figure 4.3), indicating the transition from a strain-based description for material with a positive-definiteness stiffness tensor to a displacement-based theory for failure progression. Mesh objectivity is restored by equating the total energy release rate during failure to the material fracture toughness. The general formulation of the SCA for an isotropic material is provided in Section 4.3.1, followed by the failure initiation criterion and evolution law for two different failure modes, tension (mode-I) and compression (mode-II) presented in Section 4.3.3 and 4.3.4, respectively.

4.3.1 SCA Formulation

The formulation of the SCA for an isotropic material presented in this section is similar to that reported in Refs. [64, 118, 119]. In the pre-peak regime, the material response is governed by a standard continuum theory such as elasticity, plasticity, or CDM. When failure initiates, it is assumed that the total strain, ϵ , is decomposed into a continuum strain, ϵ^{co} , and cracked strain, ϵ^{cr} , as,

$$\epsilon = \epsilon^{co} + \epsilon^{cr} \quad (4.18)$$

Again, this additive decomposition assumes small strain. In a continuum scheme, ϵ^{co} can be further decomposed into elastic, plastic, and thermal strains, if they are

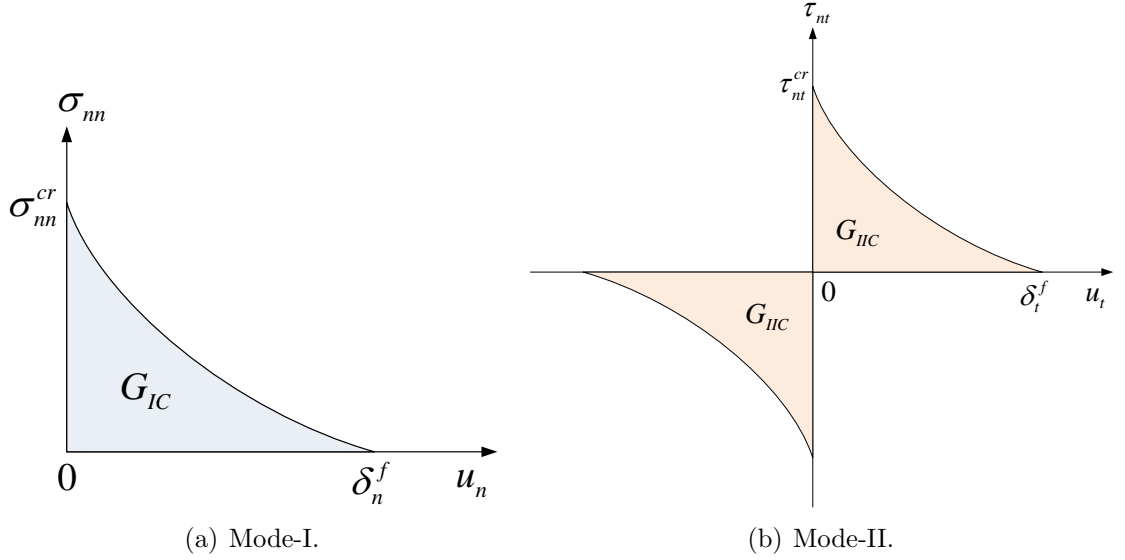


Figure 4.3: Traction-separation laws.

present. In the current study, the matrix nonlinear response is modeled as a degrading secant solid as shown earlier, therefore, the secant strains at the onset of failure initiation is used for ϵ^{co} . Here, ϵ , ϵ^{co} , and ϵ^{cr} are presented in the global coordinates.

Figure 4.4 shows the crack morphology in 3D. At the crack interface, there exist three relative displacements between the crack faces. One is the crack opening displacement, and the other two are the crack sliding displacements. The subscript n and t are used to designate the directions normal to the crack and tangential to the crack, respectively. The key to the SCA is to embed cracks into a continuum, hence, the mode-I crack opening displacement is represented by a local smeared normal crack strain, ϵ_{nn}^{cr} , and the two mode-II crack sliding displacements are replaced by two local smeared shear crack strains, γ_{t1}^{cr} and γ_{t2}^{cr} . These local crack strains are defined in the local coordinates that incorporate crack orientation, and can be related to the global coordinates through a transformation matrix, \mathbf{N} , as,

$$\epsilon^{cr} = \mathbf{N}e^{cr} = \mathbf{N} \begin{Bmatrix} \epsilon_{nn}^{cr} \\ \gamma_{t1}^{cr} \\ \gamma_{t2}^{cr} \end{Bmatrix} \quad (4.19)$$

where e^{cr} is a vector that contains local crack strains, and \mathbf{N} is a 6 by 3 transformation matrix depending on crack orientation. The derivation for \mathbf{N} in terms of the direction cosines of the crack plane is provided in Appendix A.

In the instance that multiple cracks occur at one sampling point, or integration

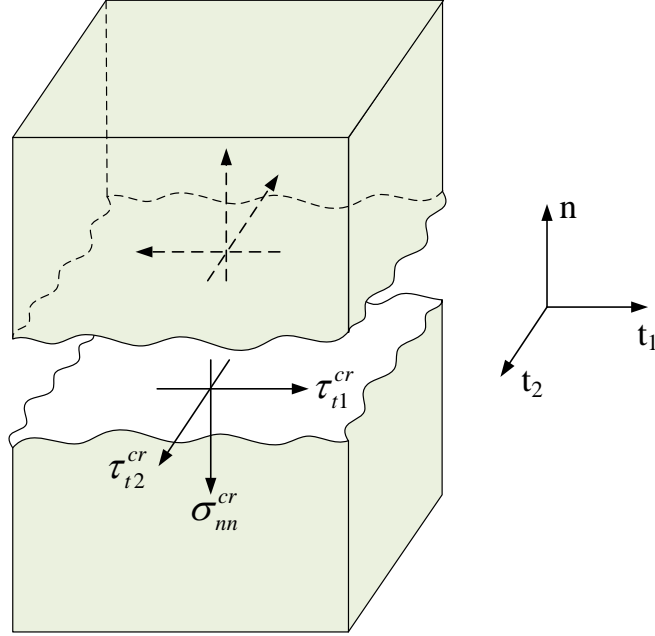


Figure 4.4: Crack morphology. There exist one normal and two shear crack components at the crack interface in 3D stress state.

point in FEA, the vector that assembles the local crack strains has the form [120],

$$\mathbf{e}^{cr} = \left[\epsilon_{nn1}^{cr} \quad \gamma_{t11}^{cr} \quad \gamma_{t12}^{cr} \quad \epsilon_{nn2}^{cr} \quad \gamma_{t21}^{cr} \quad \gamma_{t22}^{cr} \quad \cdots \quad \epsilon_{nnK}^{cr} \quad \gamma_{tK1}^{cr} \quad \gamma_{tK2}^{cr} \right]^T \quad (4.20)$$

where the superscript T denotes a transpose. The size of the local crack strain vector, \mathbf{e}^{cr} , depends on the number of open cracks, K . Consequently, for a 3D solid, \mathbf{N} becomes a 6 by $3 * K$ matrix, dictating the transformation of crack strains from local to global coordinates for each individual open crack. In the current study, only a single crack is allowed for each integration point, and the relation is reduced to Eq. (4.19).

Similarly, the interface stresses at the crack interface, \mathbf{s}^{cr} , can be transferred to the global stress state, $\boldsymbol{\sigma}$, through,

$$\mathbf{s}^{cr} = \left\{ \begin{array}{c} \sigma_{nn}^{cr} \\ \tau_{t1}^{cr} \\ \tau_{t2}^{cr} \end{array} \right\} = \mathbf{N}^T \boldsymbol{\sigma} \quad (4.21)$$

The crack interface stresses are related to the local crack strains through,

$$\mathbf{s}^{cr} = \mathbf{D}^{cr} \mathbf{e}^{cr} \quad (4.22)$$

where \mathbf{D}^{cr} is the crack interface stiffness matrix that dictates the failure evolution in the post-peak strain softening regime. For a single crack in a 3D solid, \mathbf{D}^{cr} can be expanded as,

$$\mathbf{D}^{cr} = \begin{bmatrix} D_c & 0 & 0 \\ 0 & G_{c1} & 0 \\ 0 & 0 & G_{c2} \end{bmatrix} \quad (4.23)$$

where D_c is the secant stiffness across the crack interface due to crack opening, and G_{c1} and G_{c2} are the two secant shear stiffness governed by crack sliding. These quantities identify the modes of failure and are related to the corresponding traction-separation laws with a characteristic length scale. The off-diagonal terms are assumed to be zero, indicating that there is no coupling between the normal and shear crack components. The coupling between the crack shear and opening displacements, known as crack dilatancy, has been extensively studied by Bažant and Gambarova [121], Walraven [122], Walraven and Reinhardt [123], and Gambarova and Karakoç [124]. Further investigation on crack propagation at the atomic level is motivated to characterize the material behavior at the crack tip. Since the simple uncoupled relation in Eq. (4.23) is sufficient to dictate the effect of macroscopic strain softening behavior of a cracked material, while crack dilatancy is not accounted for in this study.

In addition, if multiple cracks occur, \mathbf{D}^{cr} is a diagonal matrix with a variable size depending on the number of cracks, K , as,

$$\mathbf{D}^{cr} = \begin{bmatrix} \mathbf{D}_1^{cr} & & & \\ & \mathbf{D}_2^{cr} & & \\ & & \ddots & \\ & & & \mathbf{D}_K^{cr} \end{bmatrix} \quad (4.24)$$

where each submatrix, \mathbf{D}_i^{cr} ($i = 1, 2, \dots, K$), has the form as in Eq. (4.23). All the off-diagonal submatrices are zero, indicating that there is no coupling effect between different cracks. Various criteria can be utilized to identify failure initiation and provide crack orientation. In this chapter, the matrix material is assumed to fail either in tension or in compression. The determination of the components of the \mathbf{D}^{cr} matrix is given in Section 4.3.3 for tensile failure and Section 4.3.4 for compressive failure.

It should be pointed out that the sudden loss of the positive definiteness of the material tangent stiffness tensor may result in oscillations in the numerical solutions corresponding to the post-peak softening regime. Hence, a damping matrix, \mathbf{D}^{da} , is introduced to modify the stress-strain relation at the crack interface, and Eq. (4.22) becomes [119],

$$\mathbf{s}^{cr} = \mathbf{D}^{cr} \mathbf{e}^{cr} + \mathbf{D}^{da} \dot{\mathbf{e}}^{cr} \quad (4.25)$$

Consequently, the crack progression becomes a time dependent property by the use of a damping matrix. The crack strain rate, $\dot{\mathbf{e}}^{cr}$, is approximated at each time step using a backward finite difference scheme as,

$$\dot{\mathbf{e}}^{cr} \approx \frac{\mathbf{e}^{cr}(t + \Delta t) - \mathbf{e}^{cr}(t)}{\Delta t} = \frac{\mathbf{e}^{cr} - \mathbf{e}_{old}^{cr}}{\Delta t} \quad (4.26)$$

Substituting Eq. (4.26) into Eq. (4.25) provides the expression for the local crack stresses as,

$$\mathbf{s}^{cr} = \mathbf{D}^{cr} \mathbf{e}^{cr} + \frac{1}{\Delta t} \mathbf{D}^{da} \mathbf{e}^{cr} - \frac{1}{\Delta t} \mathbf{D}^{da} \mathbf{e}_{old}^{cr} \quad (4.27)$$

The constitutive relation for a continuum is,

$$\boldsymbol{\sigma} = \mathbf{D}^{co} \boldsymbol{\epsilon}^{co} \quad (4.28)$$

where \mathbf{D}^{co} is the continuum stiffness tensor. In the current study, since the matrix material is modeled as a secant degrading solid in the pre-peak regime, \mathbf{D}^{co} is computed using the secant Young's modulus, E_s and secant Poisson's ratio (see Eq. (4.7)) at the onset of failure initiation. Combining Eq. (4.18), (4.19), and (4.28) results in,

$$\boldsymbol{\sigma} = \mathbf{D}^{co} [\boldsymbol{\epsilon} - \boldsymbol{\epsilon}^{cr}] = \mathbf{D}^{co} [\boldsymbol{\epsilon} - \mathbf{N} \mathbf{e}^{cr}] \quad (4.29)$$

Noting Eq. (4.21) and (4.27),

$$\mathbf{D}^{cr} \mathbf{e}^{cr} + \frac{1}{\Delta t} \mathbf{D}^{da} \mathbf{e}^{cr} - \frac{1}{\Delta t} \mathbf{D}^{da} \mathbf{e}_{old}^{cr} = \mathbf{N}^T \boldsymbol{\sigma} \quad (4.30)$$

Substituting Eq. (4.29) into Eq. (4.30) provides,

$$\mathbf{D}^{cr} \mathbf{e}^{cr} + \frac{1}{\Delta t} \mathbf{D}^{da} \mathbf{e}^{cr} - \frac{1}{\Delta t} \mathbf{D}^{da} \mathbf{e}_{old}^{cr} = \mathbf{N}^T \mathbf{D}^{co} [\boldsymbol{\epsilon} - \mathbf{N} \mathbf{e}^{cr}] \quad (4.31)$$

Consequently, the relation between the local crack strains and the total global strains

can be obtained by rearranging Eq. (4.31) as,

$$\mathbf{e}^{cr} = \left[\mathbf{D}^{cr} + \mathbf{N}^T \mathbf{D}^{co} \mathbf{N} + \frac{1}{\Delta t} \mathbf{D}^{da} \right]^{-1} \left[\mathbf{N}^T \mathbf{D}^{co} \boldsymbol{\epsilon} + \frac{1}{\Delta t} \mathbf{D}^{da} \mathbf{e}_{old}^{cr} \right] \quad (4.32)$$

Finally, the relation between the total stress and total strain in the post-peak regime is computed by substituting Eq. (4.32) into Eq. (4.29), which gives,

$$\begin{aligned} \boldsymbol{\sigma} = & \left[\mathbf{D}^{co} - \mathbf{D}^{co} \mathbf{N} \left(\mathbf{D}^{cr} + \mathbf{N}^T \mathbf{D}^{co} \mathbf{N} + \frac{1}{\Delta t} \mathbf{D}^{da} \right)^{-1} \mathbf{N}^T \mathbf{D}^{co} \right] \boldsymbol{\epsilon} \\ & - \frac{1}{\Delta t} \mathbf{D}^{co} \mathbf{N} \left[\mathbf{D}^{cr} + \mathbf{N}^T \mathbf{D}^{co} \mathbf{N} + \frac{1}{\Delta t} \mathbf{D}^{da} \right]^{-1} \mathbf{D}^{da} \mathbf{e}_{old}^{cr} \end{aligned} \quad (4.33)$$

Noting that the original SCA by Rots et al. [64] is formulated in an incremental fashion such that the loading path dependency is accounted for, however, Eq. (4.33) gives the total stress versus total strain relation, which is similar to that presented in Ref. [119]. The total stress versus strain scheme is suitable for large time increments, and the stress at the end of each time increment can be exactly determined based upon the corresponding traction-separation law.

Since the components in \mathbf{D}^{cr} are related to the traction-separation law and are functions of local crack strains, Eq. (4.32) represents a group of highly nonlinear equations involving local crack strains. Newton's method is employed to solve for \mathbf{e}^{cr} , that satisfies,

$$\mathbf{f}(\mathbf{e}^{cr}) = \left[\mathbf{D}^{cr} + \mathbf{N}^T \mathbf{D}^{co} \mathbf{N} + \frac{1}{\Delta t} \mathbf{D}^{da} \right] \mathbf{e}^{cr} - \mathbf{N}^T \mathbf{D}^{co} \boldsymbol{\epsilon} - \frac{1}{\Delta t} \mathbf{D}^{da} \mathbf{e}_{old}^{cr} = \mathbf{0} \quad (4.34)$$

Therefore, the local crack strains are computed using a successive iterative scheme. At the k^{th} iteration step,

$$[\mathbf{e}^{cr}]^{(k)} = [\mathbf{e}^{cr}]^{(k-1)} - \left[\frac{d\mathbf{f}}{d\mathbf{e}^{cr}} \right]^{-1} \mathbf{f}(\mathbf{e}^{cr}) \quad (4.35)$$

where $\mathbf{J} = \left[\frac{d\mathbf{f}}{d\mathbf{e}^{cr}} \right]$ defines the Jacobian matrix in a nonlinear system. Iteration continues until $\mathbf{f}(\mathbf{e}^{cr})$ approaches zero, or a suitable tolerance is met between two successive values of \mathbf{e}^{cr} . Once the local strains are solved, they are substituted into Eq. (4.33) to compute the total stress at the end of an increment.

4.3.2 Characteristic Length Scale Associated with the Traction-Separation Law

In the SCA, the distributed cracks are “smeared” out within a finite element, and the effect of crack progression is dictated as a post-peak strain softening in the stress versus strain response. To restore mesh objectivity, a characteristic length is introduced such that the total energy release rate during failure in a continuum element is equal to the fracture toughness. The fracture toughness, or the critical energy release rate, G_C , is defined by the area under the traction-separation law that dictates the cohesive behavior of crack propagation (see Figure 4.3).

$$G_C = \int_0^{\delta_f} \sigma(u) du \quad (4.36)$$

where u is the crack displacement within the fracture zone, as schematically shown in Figure 4.5(a). In the SCA, u represents the crack opening acting across a certain width within a finite element, denoted as the crack band width, h , as shown in Figure 4.5(b). Assuming that all the cracks are uniformly distributed over the crack band, and ϵ^{cr} is the accumulation of all the crack strains over the fracture zone,

$$u = h \epsilon^{cr} \quad (4.37)$$

If g_c is defined as the area under the softening branch of the stress-crack strain response, then substitute Eq. (4.37) into Eq. (4.36) results in,

$$G_C = \int_0^{\delta_f} \sigma(h\epsilon^{cr})h d\epsilon^{cr} = h \int_0^{\epsilon_f^{cr}} \sigma(\epsilon^{cr}) d\epsilon^{cr} = h g_c \quad (4.38)$$

Therefore, the strain-based description for a softening material is related to the displacement-based traction-separation laws through the characteristic length, h . In a FE setting, h is chosen based upon the element type, element size, element shape, and the integration scheme [64]. Typically the length of the element projected onto the crack normal is used as a characteristic element length, as shown in Figure 4.7.

In the present study, a 1D uncoupled traction-separation law is employed, consequently, Eq. (4.23) becomes,

$$\mathbf{D}^{cr} = \begin{bmatrix} E^{cr} & 0 & 0 \\ 0 & G_1^{cr} & 0 \\ 0 & 0 & G_2^{cr} \end{bmatrix} \quad (4.39)$$

where E^{cr} is the secant crack modulus resulting from normal crack strain (mode-I type of failure), while G_1^{cr} and G_2^{cr} are associated with shear crack strains (mode-II type of failure). In the current study, secant crack stiffness is used so that the softening response follows the traction-separation law exactly, as shown in Figure 4.8. To prevent healing from happening, it is required that,

$$\dot{E}^{cr} < 0 \quad \text{and} \quad \dot{G}^{cr} < 0 \quad (4.40)$$

Hence, once the crack stiffness is degraded, it cannot be recovered. The loading and unloading behavior during the evolution of the failure process is specified in Figure 4.8.

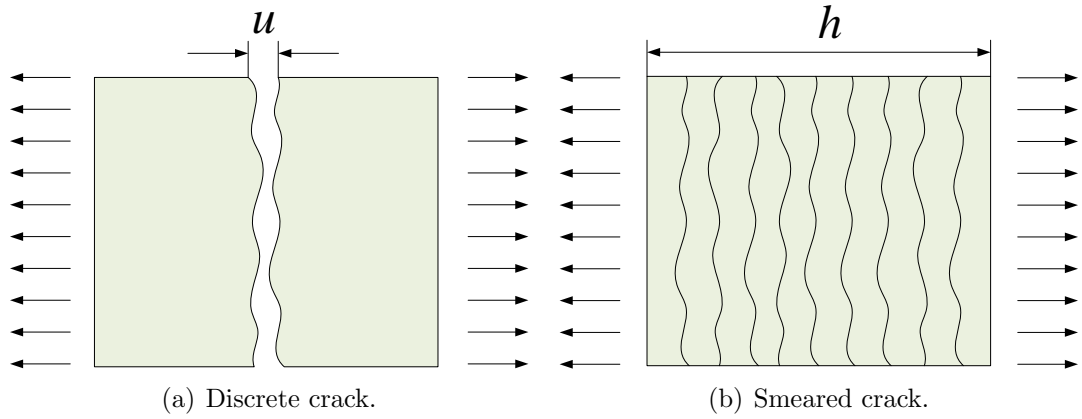


Figure 4.5: Discrete cracks are smeared out within a finite element.

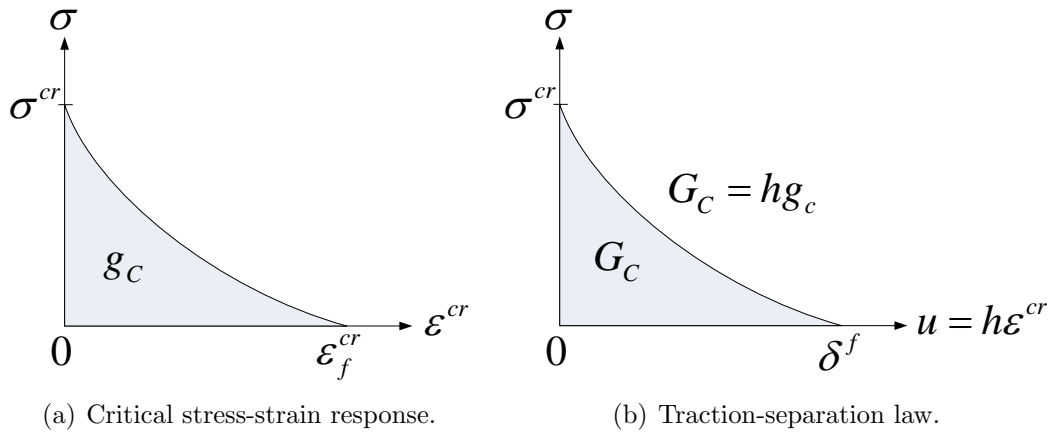


Figure 4.6: Stress-strain softening response is related to the traction-separation law through a characteristic length, h .

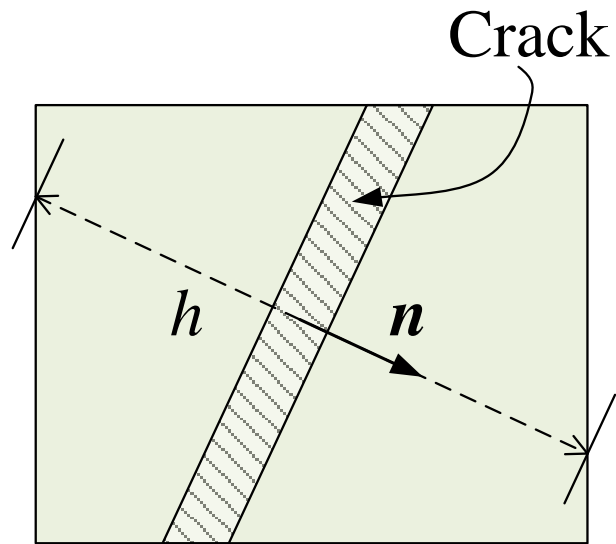


Figure 4.7: Characteristic length, h . The length of the element projected on the crack normal is used as the characteristic element length.

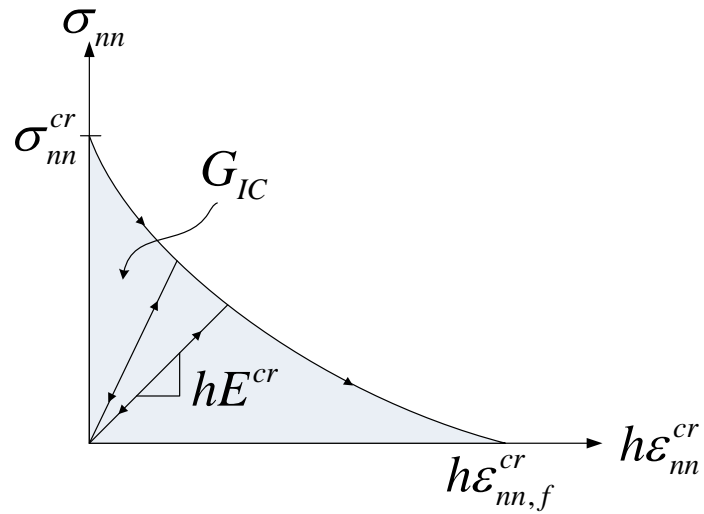


Figure 4.8: Crack evolution is dictated using degrading secant crack stiffness.

4.3.3 Tensile Failure

Matrix tensile cracking is a common failure mechanism in composite materials under loading. In a monolithic material, cracks are likely to grow under pure mode-I condition since this type of failure mode is energetically favorable. In textile composites, cracks in the surrounding matrix may be subjected to mixed-mode loading due to the presence of fiber tows, or at microscale, the crack orientation of the matrix inside the fiber tow can be affected by the individual fibers. However, in this study, it is assumed that tensile cracks grow under pure mode-I conditions, oriented with the maximum principal stress plane. For a given stress state, the principal stresses, σ_1 , σ_2 , and σ_3 , and the corresponding principal axes \mathbf{n}_1 , \mathbf{n}_2 , and \mathbf{n}_3 , are first computed. The primary condition to initiate a tensile crack is that the maximum principal stress with the maximum magnitude is in tension.

$$|\sigma_1| > |\sigma_2| > |\sigma_3| \quad \text{and} \quad \sigma_1 > 0 \quad (4.41)$$

The failure criterion and the subsequent evolution law for the instance that $\sigma_1 < 0$ is given in Section 4.3.4. Maximum tensile stress criterion is used for tensile crack initiation as,

$$\frac{\sigma_1}{\sigma^{cr}} = 1 \quad (4.42)$$

where σ^{cr} is the cohesive strength, or the critical fracture stress, in the mode-I traction separation law as illustrated in Figure 4.3(a). In practical applications, it is further assumed that once the crack is initiated, the crack orientation, determined from the principal stress direction, is fixed during the failure evolution.

Various shapes can be used to describe the post-peak branch of the traction-separation law, such as linear, bi-linear, or exponential softening curves. In the current work, the mode-I traction-separation law is described as,

$$\sigma_{nn} = \sigma^{cr} \exp\left(-\frac{\sigma^{cr} h}{G_{IC}} \epsilon_{nn}^{cr}\right) \quad (4.43)$$

Where G_{Ic} is the mode-I fracture toughness of the material. Here, a characteristic length, h , which is associated with element size, is introduced to restore mesh objectivity and to relate a displacement-based traction-separation law to a stress-strain description for a continuum material, as discussed in Section 4.3.2. The secant crack

stiffness is calculated by dividing σ_{nn} by ϵ_{nn}^{cr} as,

$$E^{cr} = \sigma^{cr} \exp\left(-\frac{\sigma^{cr} h}{G_{IC}} \epsilon_{nn}^{cr}\right) \frac{1}{\epsilon_{nn}^{cr}} \quad (4.44)$$

In concrete fracture mechanics, shear retention factor is usually used to indicate the percentage of shear capacity that is retained after cracking [64, 118, 125]. In this study, it is assumed that the crack interface is free of both normal and shear tractions if all the fracture energy has been dissipated. The two crack shear moduli, G_1^{cr} and G_2^{cr} , are degraded according to E^{cr} as,

$$G_1^{cr} = G_2^{cr} = \frac{E^{cr}}{2(1 + \nu)} \quad (4.45)$$

where ν is the Poisson's ratio of the material. Here, the crack shear stiffness evolves only as a function of ϵ_{nn}^{cr} , indicating that the cracks grow under mode-I dominated conditions. It is possible that the crack shear moduli are degraded with respect to γ_{t1}^{cr} or γ_{t2}^{cr} , and a mixed-mode traction-separation law should be introduced to ensure that the shear failure evolves under mode-II conditions [114, 126]. However, such a complicated failure mechanism requires further study of crack progression behavior at the microscale, and it is not considered in the current study. Once the crack stiffness matrix, \mathbf{D}^{cr} , is computed at the given local crack strains, Eq. (4.32) can be solved using the aforementioned iteration scheme (Eq. (4.34) and (4.35)) to determine the consistent local crack strains at each time increment. Finally, the total stresses are updated at the end of an increment using Eq. (4.33).

4.3.4 Compressive Failure

Experiments show that matrix materials fail in compression as well. In this instance, since the normal traction at the crack tip is subjected to compression, it is impossible for the cracks to grow under mode-I conditions. This scenario occurs when the principal stress with the maximum magnitude is in compression ($\sigma_1 < 0$). It has been pointed out by a number of researchers [127, 128, 129, 130] the compressive failure in brittle and quasi-brittle material is attributed to the internal friction, dictated as mode-II shear fracture. Hence, when $\sigma_1 < 0$, the Mohr-Coulomb failure criterion is employed to identify the crack initiation in the matrix, and the crack orientation is aligned with the plane of maximum principal shear stress. The Mohr-Coulomb

criterion defines a critical combination of normal and shear stresses as [131, 132],

$$|\tau| = c - \sigma \tan \phi \quad (4.46)$$

where τ and σ are the normal and shear stresses on the failure plane, which is the plane of maximum principal shear stress. Here, c is a material constant, and ϕ is the angle of internal friction, both of which are obtained from the measured values of tensile and compressive strength in uniaxial tests as [131],

$$\phi = \sin^{-1} \left(\frac{\sigma_c - \sigma_t}{\sigma_c + \sigma_t} \right) \quad \text{with} \quad 0 \leq \phi < \frac{\pi}{2}, \quad c = \frac{1}{2} \sqrt{\sigma_c \sigma_t} \quad (4.47)$$

where σ_t and σ_c are the strength in tension and compression, respectively. Equation (4.47) also indicates that $\sigma_t < \sigma_c$ for the Mohr-Coulomb criterion. To initiate a crack to grow under compression, it is required that,

$$\frac{|\tau|}{\tau^{cr}} = 1 \quad \text{and} \quad \sigma_1 < 0 \quad (4.48)$$

where τ^{cr} is the cohesive shear strength in mode-II traction-separation law. Absolute value is used in Eq. (4.48), indicating that mode-II is an anti-symmetric fracture mode. Once the crack is initiated, it grows with a fixed orientation determined from the plane of maximum principal shear stress. It has been shown by Pineda et al. [116] that the local crack shear strain can be used to degrade the crack shear modulus. The evolution of failure, characterized by the secant crack shear modulus, is related to mode-II traction-separation law with exponential softening behavior as,

$$G^{cr} = \tau^{cr} \exp \left(-\frac{\tau^{cr} h}{G_{IIC}} \gamma_t^{cr} \right) \frac{1}{\gamma_t^{cr}} \quad (4.49)$$

When the cracks grow under mode-II conditions, the normal traction at the crack interface is in compression, preventing a crack from opening. Therefore, only the shear moduli are degraded, and the normal stiffness remains intact.

4.4 Example – Mesh Objectivity

In order to verify mesh objectivity of the SCA in a FEA framework, a uniaxial tension test was performed on a unit volume cube with four different mesh sizes. As shown in Figure 4.10, the RUC is discretized into $3 \times 3 \times 3$, $5 \times 5 \times 5$, $11 \times 11 \times 11$, and $21 \times 21 \times 21$ elements respectively. The material elastic-damaging properties are

calibrated with the tension response of SC-15 epoxy shown in Figure 2.11. The value of fracture toughness is taken from the literature [133]. In the SCA formulation presented in Section 4.3.1, a damping matrix, \mathbf{D}^{da} , is introduced to smoothen and stabilize the post-peak solutions. Since the damping matrix is formulated at the crack tip, it is reasonable to assume that \mathbf{D}^{da} is in the same form as \mathbf{D}^{cr} . For a single crack in a 3D solid, \mathbf{D}^{da} is expanded as,

$$\mathbf{D}^{da} = \begin{bmatrix} \beta_1 \cdot h & 0 & 0 \\ 0 & \beta_2 \cdot h & 0 \\ 0 & 0 & \beta_3 \cdot h \end{bmatrix} \quad (4.50)$$

where h is the characteristic element length. Since there is no physical law to govern the relations among β_1 , β_2 , and β_3 , it is simply assumed that $\beta_2 = \beta_3 = \frac{\beta_1}{2 \cdot (1 + \nu)} = \frac{\beta}{2 \cdot (1 + \nu)}$. Even though the choice of β_i ($i = 1, 2, 3$) is not unique, one should make sure that the values of β_i 's do not affect the prediction of the critical stress. If the values of β_i 's are too large, the FEA result will overshoot the critical stress. On the other hand, if the values of β_i 's are too small, the FEA solver may encounter convergence issues in the post-peak softening regime due to the sudden loss of the positive definiteness of the tangent stiffness tensor. The proper selection of the damping matrix can help speed-up the computation, meanwhile the fracture response is correctly predicted. For multiple cracks, \mathbf{D}^{da} becomes,

$$\mathbf{D}^{da} = \begin{bmatrix} \mathbf{D}_1^{cr} & & & \\ & \mathbf{D}_2^{cr} & & \\ & & \dots & \\ & & & \mathbf{D}_K^{da} \end{bmatrix} \quad (4.51)$$

where each submatrix, \mathbf{D}_i^{da} ($i = 1, 2, \dots, K$), is expanded as Eq. (4.50). All the material properties that are used in the mesh objectivity study are summarized in Table 4.1.

Figure 4.9 illustrates the boundary conditions for a RUC subjected to uniaxial tension. A uniform displacement field is prescribed on the surface CDGF ($U_1 = \delta$), while the opposite surface (surface BAHE) is constrained along the x_1 -direction ($U_1 = 0$). Additionally, the point A is fixed ($U_1 = U_2 = U_3 = 0$) to prevent rigid body motion, and the point B is restrained from moving along the x_2 -direction ($U_2 = 0$). The elements that lie on the mid-plane perpendicular to the loading direction are assigned a 0.5% lower critical stress than the rest of elements, so that the cracks are

Table 4.1: Material properties used in the mesh objectivity study.

Property	Value
E (GPa)	2.487
ν	0.35
σ_y (MPa)	30
K_1 (MPa)	4500
K_2 (MPa)	58.31
σ^{cr} (MPa)	60
G_{IC} (N/mm)	1.5
β (MPa·sec)	1

localized within the RUC, as shown in Figure 4.10.

The resulting load (P) versus displacement (δ) responses for the four different mesh sizes are plotted in Figure 4.11. It clearly shows that the computed fracture characteristics, including the peak load and the fracture energy dissipation, are independent of the mesh size. Mesh objectivity of the SCA is verified through this example.

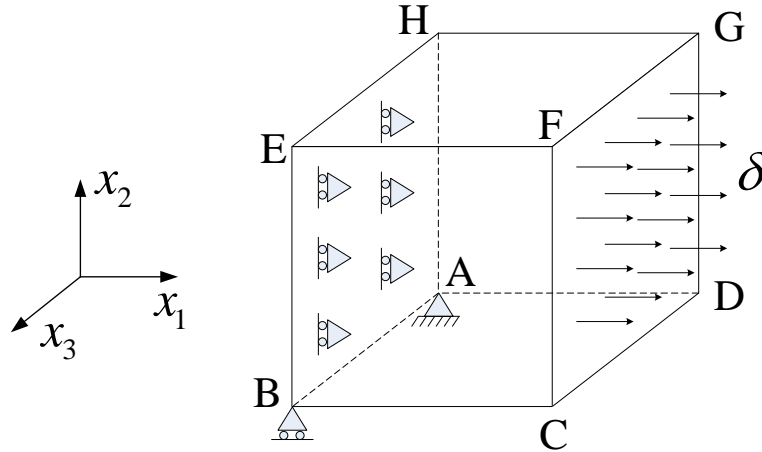
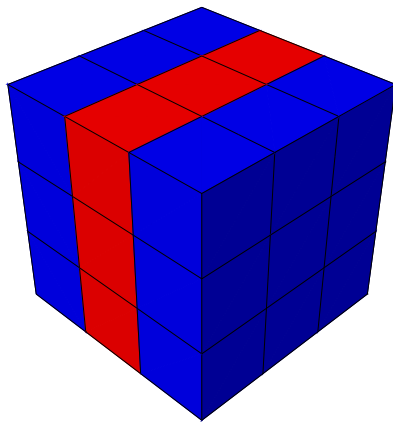
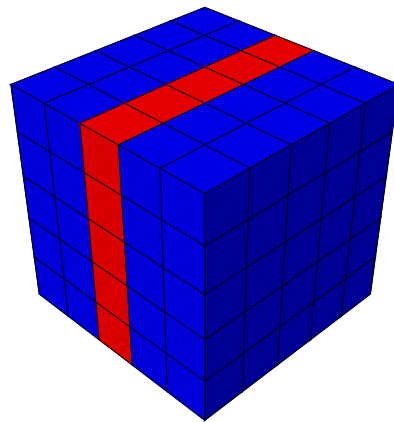


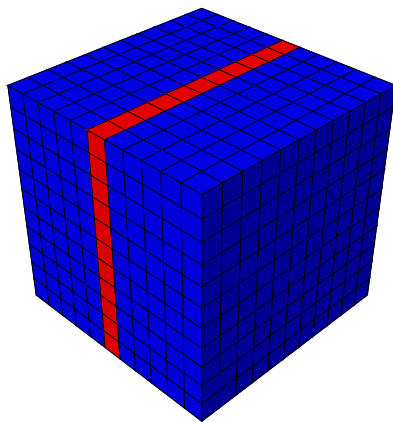
Figure 4.9: Boundary conditions for a RUC subjected to uniaxial tension. A uniform displacement field is prescribed.



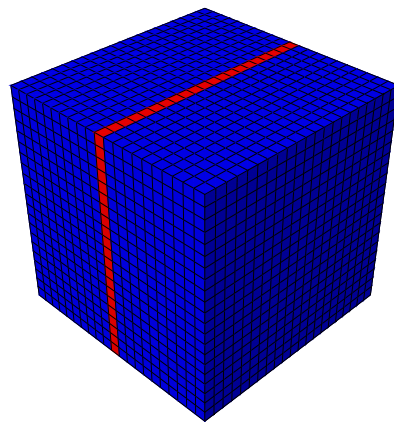
(a) $3 \times 3 \times 3$ elements



(b) $5 \times 5 \times 5$ elements



(c) $11 \times 11 \times 11$ elements



(d) $21 \times 21 \times 21$ elements

Figure 4.10: Four different mesh sizes used in mesh objectivity study. The cracked elements are shown in red.

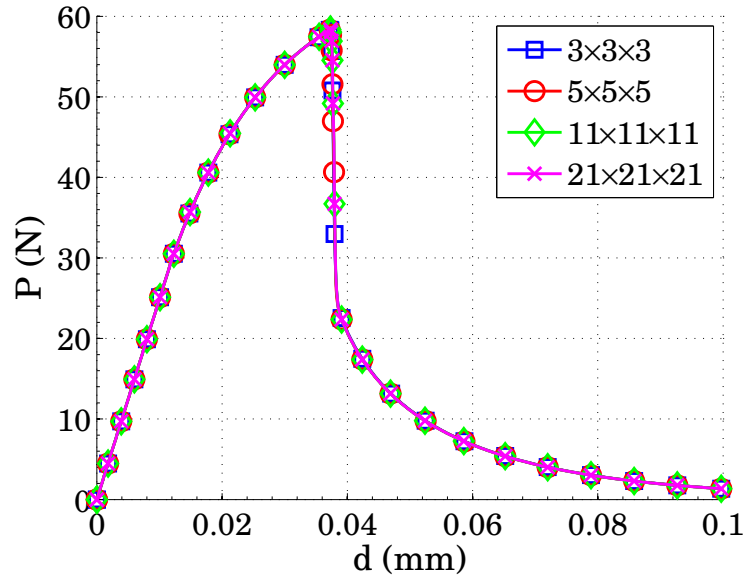


Figure 4.11: Load-displacement responses for RUC subjected to tension with four different mesh sizes. The peak load and the fracture energy are unaffected by the element size.

4.5 Conclusions

This chapter presents the modeling strategy for the polymer matrix material within the 3D textile composites investigated in this research. The pre-peak nonlinear stress versus strain response is attributed to the matrix microdamage and is modeled as a degrading secant solid based upon a modified J_2 deformation theory of plasticity. The coalescence of matrix microdamage finally causes macroscopic cracking, resulting in a post-peak strain softening behavior and the positive definiteness of the material tangent stiffness matrix is lost. It is assumed that the matrix material fails either in tension or compression. If the principal stress with the maximum magnitude is in tension, the cracks grow under pure mode-I conditions with the orientations aligned with the plane of the maximum principal stress; while if the principal stress with the maximum magnitude is in compression, the matrix fractures, resulting from local internal fracture (Mohr-Coulomb criterion), and is dictated as mode-II shear failure, and the crack orientation is aligned with the plane of maximum principal shear stress. Both tension and compression failure behavior are modeled using the SCA, in which the cracks are assumed to be smeared out over a certain width within a finite element. In a FE setting, a characteristic element length is introduced such that the post-peak

strain softening response can be associated with a traction-separation law. Mesh objectivity of the SCA is verified through a uniaxial tension test on a RUC with four different mesh sizes. The implementation of the proposed matrix nonlinear-fracture model in the mesoscale textile architecture based FE model is presented in Chapter [VII](#).

CHAPTER V

A Micromechanics-Based Multiscale Model for a Single Fiber Tow

5.1 Introduction

A single fiber tow within a textile composite is composed of thousands or tens of thousands of individual fibers embedded in a matrix medium. A cross sectional SEM image of a glass fiber tow is shown in Figure 5.1. In view of the modeling strategy for textile composites, modeling each individual fiber inside a tow is impractical under the current computational capability, hence, a homogenized model on the fiber tow-level, or a multiscale computational framework with an efficient subscale micromechanical analysis scheme is desired. In the literature, a number of micromechanics models have been developed, including analytical, semi-analytical, and fully numerical methods. Reviews on various homogenization techniques are given in [75, 134].

The analytical models, including the concentric cylinder model (CCM) [40], the generalized self-consistent method (GSCM) [47], and the Mori-Tanaka (M-T) method [49], have been developed with a focus to obtain closed-form solutions for composite effective elastic properties in terms of the constituent properties and their volume fractions without recourse to spatial variations within composite volumes at the scale of a few fibers. These homogenization techniques have been extensively used in the linear analysis for composite structures. In addition, these analytical micromechanics methods also find utility in case of damage and failure analysis by extending their utility to the nonlinear regime through a secant moduli approach [59, 60, 61, 62]. However, these methods, based upon the homogenization technique and the average of the constituent properties, neglect the local stress and strain concentrations within the constituent materials and usually result in an overestimation of the composite nonlinear behavior. Because damage and failure are governed by extreme properties of

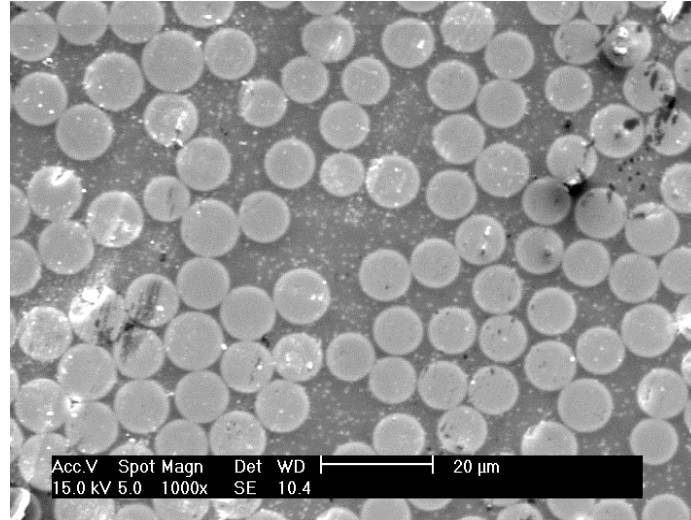


Figure 5.1: The cross section of a single fiber tow under SEM.

the fields and not necessarily by the average properties, these methods find difficulty in extension to progressive damage development and failure analysis of composite structures.

In order to resolve the local fields in the constituent materials at the microscale, and to obtain a better prediction of the composite nonlinear response, a multitude of semi-analytical methods have been developed. The microstructure of a unidirectional fiber-reinforced composite material is represented by a repeating unit cell (RUC), which can be subsequently partitioned into a number of subregions. The global composite effective constitutive law is governed by the constitutive relation in the subregions in which the local fields are expressed in terms of the Fourier series. This method was first proposed by Nemat-Nasser et al. [135] to compute the composite elastic constants, and was later improved by Accorsi and Nemat-Nasser [136] to provide bounds for nonlinear composites. Ideally, the exact description of the effective behavior of a composite material containing nonlinear phase requires infinitely many internal variables. The transformation field analysis (TFA), proposed by Dvorak [137, 138], is an efficient approximation method to reduce the number of unknowns in the system. The effective composite constitutive relation, governed by the local stress and strains fields in each constituent, is derived through eigenstrains (or transformation strains) and concentration factor tensors. The eigenstrains, which accounts for all the nonlinear effects including plasticity, viscoplasticity and damage, are approximated to be piecewise uniform. The global fields are related to the local fields through the concentration factors that are determined from a micromechanics model such as M-T method. The TFA was later extended to nonuniform transfor-

mation field analysis (NTFA) by Michel and Suquet [139] to better approximate the nonuniform local fields in the nonlinear constituent phase.

Alternatively, the composite effective nonlinear constitutive relation can be obtained through a generalized variational principle, which results in a number of studies on deriving bounds for nonlinear composites. Ponte Castañeda [140] extended the Hashin-Shtrikman variational principle for linear material to the nonlinear regime through a second-order homogenization method. The nonlinear potential for each phase is replaced by a second-order Taylor expansion evaluated at the appropriately defined phase average strains. This method is later improved to incorporate field fluctuations in the constituent phases such that the bounds for nonlinear composite material can be better predicted [141, 142]. However, there exists a duality gap between the stress-based and strain-based estimates, and this requires further investigation.

The method of cells (MOC), developed by Aboudi [143], is another powerful semi-analytical method to approximate the composite effective behavior. In the MOC, the RUC is divided into four subcells, one of which represents the fiber, and the remaining three subcells are occupied by the matrix. The subcell displacement vector is assumed to be linearly expanded in terms of the local subcell coordinates. The continuity conditions of the displacement and traction at the interfaces between subcells and between adjacent RUCs are imposed on an average basis, resulting in a set of equations that relate the local microscopic strains to the global macroscopic strains through a concentration tensor, thus the local strain fields can be solved by knowing the applied fields. The local stress fields are readily resolved from the local constitutive relations, and the composite effective properties are determined from the local fields via a volume average. The MOC was later extended to the generalized method of cells (GMC) by Paley and Aboudi [144] in which the RUC is discretized into an arbitrary number of subcells such that the fiber geometry and packing arrangement can be accounted for. In order to improve the prediction of the local fields, the high-fidelity generalized method of cells (HFGMC) was developed by Aboudi et al. [145], in which the subcell displacement fields are expanded using second-order approximations. It has been shown that the HFGMC provides accurate prediction on the composite nonlinear response as well as the gradients in the local fields [146, 147], compared to FE based fully 3D analysis. The HFGMC also shows capability in damage and failure analysis at the constituent scales such as fiber-matrix debonding and matrix cracking [116, 148, 149, 150]. The semi-analytical methods offer a distinct advantage over the analytical methods in that the spatial variations in the local fields are better resolved,

and the methods achieve computational advantage over fully numerical methods. However, the computational time increases rapidly if more details of the nonlinear effects in the local fields are required to be captured.

The exact variations of the local fields within the constituent materials can be obtained through fully numerical methods such as FEA, in which the micromechanics is modeled through a RUC with detailed fiber geometry and packing arrangements. Some of the important issues in the FE model include the correct boundary conditions imposed on the RUC [151, 152, 153] and the minimum size of the RUC to represent the macroscopic properties of the composite [154, 155, 156, 157]. Recently, Totry et al. [158, 159] investigated the failure behavior of a fiber-reinforced composite under multiaxial loading using a 3D RUC, in which detailed information for the fiber and matrix properties as well as the damage and failure mechanics are implemented using FEA.

The purpose of this chapter is to establish a two-scale computational framework for computing the nonlinear response of a single fiber tow, with a focus on the sub-scale micromechanical analysis. The microstructure of a fiber tow can be represented as a unidirectionally aligned fiber-reinforced composite, resulting in a transversely isotropic solid at the mesoscale, as discussed in Section 5.2. The effective fiber tow response is computed through micromechanical analysis using the fiber-matrix concentric cylinder model as the basic repeat unit. In addition, micromechanics is used to relate the fiber tow strains to the fiber and matrix strains through a 6 by 6 transformation matrix, as provided in Section 5.3. The resolved spatial variation of the matrix fields are compared with the corresponding FE model to demonstrate the accuracy of the proposed micromechanics model. It has been shown in Chapter IV that the polymer matrix material exhibits pre-peak nonlinear stress versus strain response, which is attributed to the matrix microdamage due to the growth of voids and flaws in the polymer. The evolution of matrix microdamage at the microscale manifests as the progressive degradation of the fiber tow stiffness at the mesoscale. Thus, it is further assumed that the evolution of the fiber tow effective nonlinear stress versus strain response can be captured through two scalar variables that are related the extreme values of appropriately defined matrix equivalent strains, as discussed in Section 5.4. The accuracy of the proposed two-scale micromechanics based model on the prediction of fiber tow pre-peak nonlinear responses is evaluated by comparison to a discrete FE model shown in Section 5.5.

It should be pointed out that the focus of this chapter is on the fiber tow pre-peak nonlinear response that preserves the positive definiteness of the material stiffness

tensor. However, in experiments, catastrophic failure mechanisms have been observed, including fiber tow breakage, tow kinking, and transverse cracking, resulting in a loss of load carrying capability at the macroscale, followed by a post-peak strain softening response. Since the positive definiteness of the tangent stiffness matrix is lost, the aforementioned two-scale model will provide mesh dependent results in a FE framework if no characteristic length is introduced. The modeling of the fiber tow failure behavior using a mesh objective method is presented in Chapter VI.

5.2 Tow Microstructure

The microstructure of a single fiber tow can be represented as a unidirectional aligned fiber-reinforced composite. In the instance that the fiber tow undulates along its longitudinal direction, each infinitesimal section of a fiber tow can be considered as a unidirectional composite, with its local coordinate aligned with the tow orientation [11], as schematically shown in Figure 5.2. Hence, computing the fiber tow stress versus strain relation is equivalent to establishing a constitutive model for a unidirectional composite. Thus, in this chapter, the term “composite” is referred to the “fiber tow”.

The effective response of a unidirectional composite is transversely isotropic, requiring five independent constants to form the composite stiffness tensor. Although the choices of these elastic constants are not unique, the axial modulus, E_1^c , the axial Poisson’s ratio, ν_{12}^c , the axial shear modulus, G_{12}^c , the plane-strain bulk modulus, K_{23}^c , and the transverse shear modulus, G_{23}^c , are used throughout this research. Therefore, the stiffness tensor for a transversely isotropic material can be written in terms of these elastic constants as,

$$\mathbf{C}^c = \begin{bmatrix} E_1^c + 4\nu_{12}^c K_{23}^c & 2\nu_{12}^c K_{23}^c & 2\nu_{12}^c K_{23}^c & 0 & 0 & 0 \\ 2\nu_{12}^c K_{23}^c & K_{23}^c + G_{23}^c & K_{23}^c - G_{23}^c & 0 & 0 & 0 \\ 2\nu_{12}^c K_{23}^c & K_{23}^c - G_{23}^c & K_{23}^c + G_{23}^c & 0 & 0 & 0 \\ 0 & 0 & 0 & G_{23}^c & 0 & 0 \\ 0 & 0 & 0 & 0 & G_{12}^c & 0 \\ 0 & 0 & 0 & 0 & 0 & G_{12}^c \end{bmatrix} \quad (5.1)$$

Other important constants, including the transverse modulus, E_2^c , and transverse

Poisson's ratio, ν_{23}^c , can be computed as,

$$E_2^c = \frac{4G_{23}^c K_{23}^c}{K_{23}^c + \psi G_{23}^c} \quad (5.2)$$

$$\nu_{23}^c = \frac{K_{23}^c - \psi G_{23}^c}{K_{23}^c + \psi G_{23}^c} \quad (5.3)$$

where,

$$\psi = 1 + \frac{4K_{23}^c \nu_{12}^{c^2}}{E_1^c}$$

In this chapter, the fiber is assumed to be linear elastic, transversely isotropic, with “1” designating its longitudinal direction. Its stiffness tensor, \mathbf{C}^f , can be written in terms of fiber properties as Eq. (5.1) by replacing the superscript “c” with “f”. The matrix material is an isotropic elastic-damaging solid, and its nonlinear response is modeled using a modified J_2 deformation theory of plasticity through a secant moduli approach, as discussed in Section 4.2. As a result, the composite effective stress versus strain response is extended to the nonlinear regime by substituting secant moduli into Eq. (5.1).

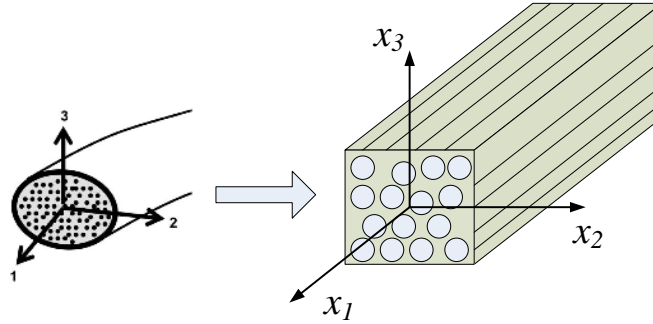


Figure 5.2: Fiber tow is represented as a unidirectional fiber-reinforced composite.

5.3 Micromechanics Model

In order to predict the composite effective nonlinear response, the micromechanics model at the fiber and matrix scale should be able to capture the spatial variations in the local fields of the constituent materials. The key to the proposed micromechanics model is to relate the composite strains (the strain applied on the fiber-matrix microstructure) to the local matrix strains through a 6 by 6 transformation matrix, \mathbf{F} ,

as,

$$\begin{pmatrix} \epsilon_{11}^m \\ \epsilon_{22}^m \\ \epsilon_{33}^m \\ \gamma_{12}^m \\ \gamma_{13}^m \\ \gamma_{23}^m \end{pmatrix} = \begin{bmatrix} F_{11} & F_{12} & F_{13} & F_{14} & F_{15} & F_{16} \\ F_{21} & F_{22} & F_{23} & F_{24} & F_{25} & F_{26} \\ F_{31} & F_{32} & F_{33} & F_{34} & F_{35} & F_{36} \\ F_{41} & F_{42} & F_{43} & F_{44} & F_{45} & F_{46} \\ F_{51} & F_{52} & F_{53} & F_{54} & F_{55} & F_{56} \\ F_{61} & F_{62} & F_{63} & F_{64} & F_{65} & F_{66} \end{bmatrix} \begin{pmatrix} \epsilon_{11}^c \\ \epsilon_{22}^c \\ \epsilon_{33}^c \\ \gamma_{12}^c \\ \gamma_{13}^c \\ \gamma_{23}^c \end{pmatrix} \quad (5.4)$$

The F_{ij} components can be computed by imposing a single non-zero composite strain on the fiber-matrix microstructure and solving the resulting matrix strain fields. In the present model, the axial properties, including the axial tension (E_1^c and ν_{12}^c) and axial shear (G_{12}^c), are computed through a two-phase CCM, which is subsequently used for the computation of F_{i1} , F_{i4} , and F_{i5} . The rest of the components in the \mathbf{F} matrix are determined via an extended three-phase GSCM, which also gives the composite transverse properties, K_{23}^c and G_{23}^c . The procedure to compute each component in the \mathbf{F} matrix as well the composite effective constants are provided in the following section. It should be noted that the proposed micromechanics model is based upon the homogenization techniques that are originally used to compute the composite effective moduli, hence, both the fiber and matrix are assumed to be linear elastic. When the matrix stiffness is reduced due to microdamage, the nonlinear response of the matrix is modeled through a secant moduli approach, in which the matrix elastic properties are replaced with the corresponding secant moduli.

5.3.1 Computation of E_1^c , ν_{12}^c , and F_{i1} components by applying ϵ_{11}^c

When a unidirectional fiber-reinforced composite is subjected to a uniform axial strain, ϵ_{11}^c , the response of the fiber and matrix can be best studied using the concentric cylinder model (CCM), [75, 160], in which the composite material is represented by an inner fiber core and an outer matrix annulus. It assumes that the size of the concentric pair varies such that the entire volume of the composite can be filled with the cylinders, while the ratio of the fiber radius to the matrix radius keeps constant to maintain the fiber volume fraction. A representative single cylinder unit with fiber radius a and matrix outer radius b is shown in Figure 5.3, and the resulting fiber volume fraction is $V_f = \frac{a^2}{b^2}$.

Since the concentric cylinders are loaded along the fiber direction, the response is axisymmetric, and there are no shear stresses present. In addition, if end effects are ignored, the stresses and the strains are independent of the axial direction. The axisymmetric displacement fields for the fiber and matrix in cylindrical coordinates

are [160],

$$\begin{aligned} U_r^f(x, r) &= A^f r \quad (0 \leq r \leq a) & U_r^m(x, r) &= A^m r + \frac{B^m}{r} \quad (a \leq r \leq b) \\ U_x^f(x, r) &= \epsilon_{11}^f x \quad (0 \leq r \leq a) & U_x^m(x, r) &= \epsilon_{11}^m x \quad (a \leq r \leq b) \end{aligned} \quad (5.5)$$

where U_r and U_x are the radial and axial displacements, respectively. A^f , A^m , and B^m are the constants to be determined from the boundary conditions. ϵ_{11}^f and ϵ_{11}^m are the axial strains for the fiber and matrix, respectively, which are constants to satisfy the Saint-Venant's principle. The strains in the fiber and matrix can be obtained from strain-displacement relations and are related to the stress components through material constitutive law. The continuity conditions at the fiber-matrix interface are,

$$U_r^f(a) = U_r^m(a), \quad U_x^f(x, a) = U_x^m(x, a), \quad \text{and} \quad \sigma_r^f(a) = \sigma_r^m(a) \quad (5.6)$$

The continuity condition for the axial displacements immediately gives $\epsilon_{11}^f = \epsilon_{11}^m = \epsilon_{11}^c$. The composite effective properties are determined by equating the strain energy of the concentric pair to that of the equivalent homogenized composite material. Following the procedure given in [160], the closed-form expressions for E_{12} and ν_{12} are,

$$E_1^c = E_1^f V_f + E^m (1 - V_f) + \frac{4V_f(1 - V_f)(\nu_{12}^f - \nu^m)^2 G^m}{\frac{G^m(1 - V_f)}{K_{23}^f} + \frac{G^m V_f}{K_{23}^m} + 1} \quad (5.7)$$

$$\nu_{12}^c = \nu_{12}^f V_f + \nu^m (1 - V_f) + \frac{V_f(1 - V_f)(\nu_{12}^f - \nu^m) \left(\frac{G^m}{K_{23}^m} - \frac{G^m}{K_{23}^f} \right)}{\frac{G^m(1 - V_f)}{K_{23}^f} + \frac{G^m V_f}{K_{23}^m} + 1} \quad (5.8)$$

In order to compute the F_{i1} 's, the only nonzero strain components prescribed on the concentric pair is ϵ_{11}^c . Hence, the lateral surface of the cylinder is constrained, following,

$$U_r(b) = 0 \quad (5.9)$$

Solving Eq. (5.6) and (5.9) gives the three unknown constants, A^f , A^m , and B^m , in terms of ϵ_{11}^c . With these constants, the matrix strain field, readily determined from

the displacement field, are related to the applied composite strain as,

$$\begin{aligned}
\epsilon_{xx}^m &= \epsilon_{11}^c \\
\epsilon_{rr}^m &= \frac{V_f \left(\frac{\nu_{12}^f}{K_{23}^m} - \frac{\nu^m}{K_{23}^f} \right)}{\frac{V_f}{K_{23}^f} + \frac{1-2\nu^m}{K_{23}^f} + \frac{1-V_f}{K_{23}^m}} \left(1 + \frac{b^2}{r^2} \right) \epsilon_{11}^c \\
\epsilon_{\theta\theta}^m &= \frac{V_f \left(\frac{\nu_{12}^f}{K_{23}^m} - \frac{\nu^m}{K_{23}^f} \right)}{\frac{V_f}{K_{23}^f} + \frac{1-2\nu^m}{K_{23}^f} + \frac{1-V_f}{K_{23}^m}} \left(1 - \frac{b^2}{r^2} \right) \epsilon_{11}^c
\end{aligned} \tag{5.10}$$

These matrix strains can be further transformed to the Cartesian coordinates through the transformation relations provided in Appendix B. Hence, the F_{i1} components are found to be,

$$\begin{aligned}
F_{11} &= 1 \\
F_{21} &= \frac{V_f \left(\frac{\nu_{12}^f}{K_{23}^m} - \frac{\nu^m}{K_{23}^f} \right)}{\frac{V_f}{K_{23}^f} + \frac{1-2\nu^m}{K_{23}^f} + \frac{1-V_f}{K_{23}^m}} \left[1 + \left(\frac{b}{r} \right)^2 \cos 2\theta \right] \\
F_{31} &= \frac{V_f \left(\frac{\nu_{12}^f}{K_{23}^m} - \frac{\nu^m}{K_{23}^f} \right)}{\frac{V_f}{K_{23}^f} + \frac{1-2\nu^m}{K_{23}^f} + \frac{1-V_f}{K_{23}^m}} \left[1 - \left(\frac{b}{r} \right)^2 \cos 2\theta \right] \\
F_{61} &= 2 \frac{V_f \left(\frac{\nu_{12}^f}{K_{23}^m} - \frac{\nu^m}{K_{23}^f} \right)}{\frac{V_f}{K_{23}^f} + \frac{1-2\nu^m}{K_{23}^f} + \frac{1-V_f}{K_{23}^m}} \left(\frac{b}{r} \right)^2 \sin 2\theta \\
F_{41} &= F_{51} = 0
\end{aligned} \tag{5.11}$$

5.3.2 Computation of G_{12}^c and F_{i4} components by applying γ_{12}^c

In order to analyze the axial shear response of the concentric cylinders, it is convenient to view the representative concentric cylinder unit projected onto the $x_1 - x_2$ plane, as shown in Figure 5.4. The outer boundary of the concentric cylinders are subjected to displacement fields such that the an overall axial shear of γ_{12}^c is produced. The resulting displacements for the fiber in a cylindrical coordinate system

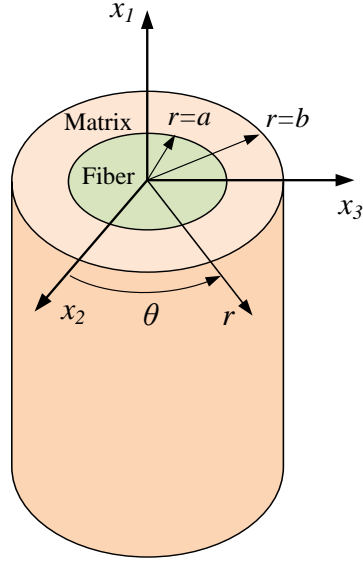


Figure 5.3: Two-phase concentric cylinder model.

are,

$$\begin{aligned}
 U_x^f &= \left(A^f r + \frac{B^f}{r} \right) \cos \theta \\
 U_\theta^f &= -C^f x \sin \theta \\
 U_r^f &= C^f x \cos \theta
 \end{aligned} \tag{5.12}$$

and the displacements in the matrix are,

$$\begin{aligned}
 U_x^m &= \left(A^m r + \frac{B^m}{r} \right) \cos \theta \\
 U_\theta^m &= -C^m x \sin \theta \\
 U_r^m &= C^m x \cos \theta
 \end{aligned} \tag{5.13}$$

where A^f , B^f , C^f , A^m , B^m and C^m are the unknown constants to be determined from the boundary conditions. The nonzero stresses in the fiber that results from the displacement fields are,

$$\begin{aligned}
 \tau_{xr}^f &= G_{12}^f \left(A^f + C^f - \frac{B^f}{r^2} \right) \cos \theta \\
 \tau_{x\theta}^f &= -G_{12}^f \left(A^f + C^f + \frac{B^f}{r^2} \right) \sin \theta
 \end{aligned} \tag{5.14}$$

and the stresses in the matrix are,

$$\begin{aligned}\tau_{xr}^m &= G^m \left(A^m + C^m - \frac{B^m}{r^2} \right) \cos \theta \\ \tau_{x\theta}^m &= -G^m \left(A^m + C^m + \frac{B^m}{r^2} \right) \sin \theta\end{aligned}\tag{5.15}$$

Since the displacement at the center of the fiber should be bounded, $B^f = 0$. The displacement and traction continuity conditions at the fiber-matrix interface are,

$$\begin{aligned}U_x^f(x, \theta, a) &= U_x^m(x, \theta, a) \\ U_\theta^f(x, \theta, a) &= U_\theta^m(x, \theta, a) \\ U_r^f(x, \theta, a) &= U_r^m(x, \theta, a) \\ \tau_{xr}^f(x, \theta, a) &= \tau_{xr}^m(x, \theta, a)\end{aligned}\tag{5.16}$$

Note that the second and third equations in Eq. (5.16) result in the same relation. Furthermore, the displacements at the outer boundary of the concentric cylinders must satisfy the imposed boundary conditions,

$$\begin{aligned}U_x^m(x, \theta, b) &= 0 \\ U_\theta^m(x, \theta, b) &= -\gamma_{12}^c x \sin \theta \\ U_r^m(x, \theta, b) &= \gamma_{12}^c x \cos \theta\end{aligned}\tag{5.17}$$

Similarly, the last two equations in Eq. (5.17) provide the same result. The unknown constants, A^f , C^f , A^m , B^m and C^m , are solved in terms of γ_{12}^c through Eq. (5.16)-(5.17). These results are further substituted into Eq. (5.15) to obtain the matrix stresses. Since the shear stress at $r = b$ and $\theta = 0$ in the cylindrical coordinate system coincides with that in the Cartesian coordinate system, the composite effective axial modulus, G_{12} , can be determined by dividing the shear stress by the shear strain, resulting in,

$$G_{12}^c = G^m \frac{G_{12}^f(1 + V_f) + G^m(1 - V_f)}{G_{12}^f(1 - V_f) + G^m(1 + V_f)}\tag{5.18}$$

The non-zero strains in the matrix become,

$$\begin{aligned}\gamma_{x\theta}^m &= \frac{\left[r^2(G_{12}^f + G^m) + b^2(G_{12}^f - G^m)V_f \right]}{r^2 \left[G_{12}^f + G^m - V_f(G_{12}^f - G^m) \right]} \sin \theta \gamma_{12}^c \\ \gamma_{xr}^m &= \frac{\left[r^2(G_{12}^f + G^m) - b^2(G_{12}^f - G^m)V_f \right]}{r^2 \left[G_{12}^f + G^m - V_f(G_{12}^f - G^m) \right]} \cos \theta \gamma_{12}^c\end{aligned}\quad (5.19)$$

Furthermore, the components of F_{i4} are computed by transforming these matrix strains through the transformation relations provided in Appendix B as,

$$\begin{aligned}F_{44} &= \frac{G_{12}^f + G^m}{G_{12}^f + G^m - V_f(G_{12}^f - G^m)} + \frac{V_f(G_{12} - G^m)}{G_{12}^f + G^m - V_f(G_{12}^f - G^m)} \left(\frac{b}{r} \right)^2 \cos 2\theta \\ F_{54} &= \frac{(G_{12}^f - G^m)V_f}{G_{12}^f + G^m - V_f(G_{12}^f - G^m)} \left(\frac{b}{r} \right)^2 \sin 2\theta \\ F_{14} &= F_{24} = F_{34} = F_{64} = 0\end{aligned}\quad (5.20)$$

A dual result for F_{i5} components can be obtained by applying a single strain γ_{13}^c .

$$\begin{aligned}F_{45} &= \frac{(G_{12}^f - G^m)V_f}{G_{12}^f + G^m - V_f(G_{12}^f - G^m)} \left(\frac{b}{r} \right)^2 \sin 2\theta \\ F_{55} &= \frac{G_{12}^f + G^m}{G_{12}^f + G^m - V_f(G_{12}^f - G^m)} - \frac{V_f(G_{12} - G^m)}{G_{12}^f + G^m - V_f(G_{12}^f - G^m)} \left(\frac{b}{r} \right)^2 \cos 2\theta \\ F_{15} &= F_{25} = F_{35} = F_{65} = 0\end{aligned}\quad (5.21)$$

It is worth noting that $F_{45} = F_{54}$, whereas F_{44} is different from F_{55} by a phase angle of $\frac{\pi}{2}$.

5.3.3 Computation of the transverse properties

Rather than the axial problem, in which a strain-type boundary condition is imposed on the outer surface of the concentric cylinder, the computation for the transverse response requires a traction-type boundary condition applied on the outer boundary. However, such type of boundary conditions are not always able to provide closed-form solutions, among which the most critical property is the transverse shear modulus. It was first proposed by Christensen and Lo [47] that the transverse shear problem can be best solved using the Generalized Self-Consistent Method (GSCM), in which both the fiber and matrix are concentrically embedded in an infinite homo-

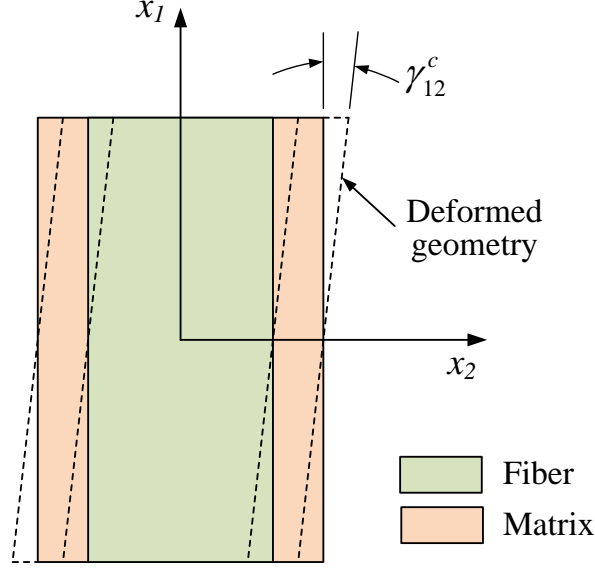


Figure 5.4: Projection of the concentric cylinders onto the $x_1 - x_2$ plane. The concentric pair is subjected to an axial shear strain, γ_{12}^c .

geneous medium of the equivalent composite properties. This three-phase cylinder model is illustrated in Figure 5.5, with fiber radius a and matrix outer radius b . Since only the transverse response is of interest, the three-phase cylinder model can be reduced into a 2D plane strain problem with the assumption that the fiber is infinitely long in the longitudinal direction. Hence, the composite stress-strain relation becomes,

$$\begin{Bmatrix} \sigma_{22}^c \\ \sigma_{33}^c \\ \tau_{23}^c \end{Bmatrix} = \begin{bmatrix} K_{23}^c + G_{23}^c & K_{23}^c - G_{23}^c & 0 \\ K_{23}^c - G_{23}^c & K_{23}^c + G_{23}^c & 0 \\ 0 & 0 & G_{23}^c \end{bmatrix} \begin{Bmatrix} \epsilon_{22}^c \\ \epsilon_{33}^c \\ \gamma_{23}^c \end{Bmatrix} \quad (5.22)$$

The Airy's stress function, ϕ , for such a problem in polar coordinates has the form,

$$\phi_i = \frac{M_i}{2} b^2 \ln r + \frac{N_i}{2} r^2 + \left[\frac{A_i}{2} r^2 + \frac{B_i}{2} \frac{r^4}{b^2} + \frac{C_i}{4} \frac{b^4}{r^2} + \frac{D_i}{2} b^2 \right] \cos 2\theta \quad (5.23)$$

where $i = 1, 2, 3$. The subscripts "1", "2" and "3" designate the fiber, matrix and equivalent composite properties respectively. The constants M_i , N_i , A_i , B_i , C_i and D_i are to be determined based upon the boundary conditions. The stresses, strains, and displacements for the fiber, matrix, and equivalent composite material can be computed from the stress function, material constitutive law, and strain-displacement

relations, as given in C.

The key to the three-phase cylinder model for the computation of transverse response is to impose a stress state such that a state of pure shear or transverse tension is achieved in the far field. In particular, the composite effective plane-strain bulk modulus, K_{23}^c , is determined from the biaxial stress state of $\sigma_{22}^c = \sigma_{33}^c = \bar{\sigma}$, while the transverse shear modulus, G_{23}^c , is computed under the far field stress state of $\sigma_{22}^c = -\sigma_{33}^c = \bar{\sigma}$. Though the determination of F'_{ij} s require a single strain to be imposed on the concentric cylinders, the results can be easily deduced from a single stress loading condition.

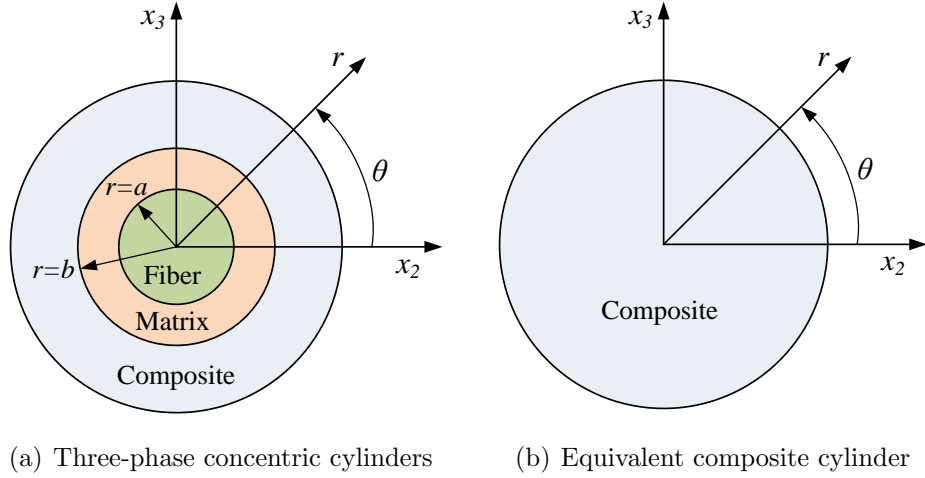


Figure 5.5: Illustration of the generalized self-consistent method.

5.3.3.1 Computation of K_{23}^c by applying biaxial stresses $\sigma_{22}^c = \sigma_{33}^c = \bar{\sigma}$

The computation of the effective plane-strain bulk modulus requires the elasticity problem to be axisymmetric, resulting in $A_i = B_i = C_i = D_i = 0$ ($i = 1, 2, 3$). By setting $N_3 = \bar{\sigma}$, a state of hydrostatic stress is reached as $r \rightarrow \infty$. The four unknown constants, N_1 , M_2 , N_2 , and M_3 , can be solved by imposing the traction and displacement continuity conditions as,

$$\begin{aligned}
 \sigma_{rr}^f(r = a) &= \sigma_{rr}^m(r = a) & U_r^f(r = a) &= U_r^m(r = a) \\
 \sigma_{rr}^m(r = b) &= \sigma_{rr}^c(r = b) & U_r^m(r = b) &= U_r^c(r = b)
 \end{aligned}
 \tag{5.24}$$

which yields,

$$\begin{bmatrix} 1 & -\frac{1}{2}\left(\frac{1}{V_f}\right) & -1 & 0 \\ 2\frac{G_{23}^f}{K_{23}^f} & \frac{G_{23}^f}{G^m}\frac{1}{V_f} & -2\frac{G_{23}^f}{K_{23}^m} & 0 \\ 0 & \frac{1}{2} & 1 & -\frac{1}{2} \\ 0 & -\frac{G_{23}}{G^m} & 2\frac{G_{23}}{K_{23}^m} & 1 \end{bmatrix} \begin{Bmatrix} N_1 \\ M_2 \\ N_2 \\ M_3 \end{Bmatrix} = \begin{Bmatrix} 0 \\ 0 \\ \bar{\sigma} \\ 2\frac{G_{23}}{K_{23}}\bar{\sigma} \end{Bmatrix} \quad (5.25)$$

Next, the internal strain energy of the three-phase cylinder model (Figure 5.5 (a)) is equated to that of the equivalent composite medium (Figure 5.5 (b)) based upon an important finding by Eshelby [48], which states that for a homogeneous medium containing an inclusion, the strain energy, U , under applied displacement conditions, is determined by,

$$U = U^o - \frac{1}{2} \int_s (T_i^o u_i - T_i u_i^o) dS \quad (5.26)$$

where S is the surface of the inclusion, U^o is the strain energy of the equivalent composite medium without inclusion, T_i^o and u_i^o are the tractions and displacements of the equivalent medium without inclusion, and T_i and u_i are the corresponding quantities for the composite medium with the inclusion. Obviously, the strain energy of the equivalent composite in Figure (5.5 (b)), U^{equiv} , is identical to that of the composite medium in Figure (5.5 (a)) if there is no inclusion, which yields $U^{equiv} = U^o$. Based on the strain energy equivalence stated previously, $U^{equiv} = U$. Using the notation for the tractions and corresponding displacements, Eq. (5.26) becomes,

$$\int_0^{2\pi} [\sigma_{rr}^o U_r - \sigma_{rr} U_r^o]_{r=b} b d\theta = 0 \quad (5.27)$$

where the stresses and displacements for the equivalent medium without inclusions are,

$$\sigma_{rr}^o = \bar{\sigma} \quad U_r^o = \frac{r}{2K_{23}}\bar{\sigma} \quad (5.28)$$

Substituting the results for the stresses and displacements of the equivalent composites (Eq. (C.6) and (C.12) in Appendix C respectively) as well as Eq. (5.28) into Eq. (5.27) gives,

$$M_3 = 0 \quad (5.29)$$

Thus, by solving the boundary conditions in Eq. (5.25) and setting M_3 to zero, the

effective plane-strain bulk modulus, K_{23} , can be obtained as,

$$K_{23}^c = K_{23}^m + \frac{V_f}{\frac{1}{K_{23}^f - K_{23}^m} + \frac{1 - V_f}{K_{23}^m + G^m}} \quad (5.30)$$

This result is the same as the one obtained from the two-phase CCM [75, 160]. In addition, the stresses, strains, and displacement fields for each constituent in the instance that the outer boundary of the equivalent composite material is subjected to biaxial tension are obtained through Eq. (C.4)-(C.12) in Appendix C.

5.3.3.2 Computation of G_{23}^c by applying normal stresses $\sigma_{22}^c = -\sigma_{33}^c = \bar{\sigma}$

The state of stress, $\sigma_{22} = -\sigma_{33} = \bar{\sigma}$ is achieved in the far field ($r \rightarrow \infty$) by setting $M_i = N_i = 0$ ($i = 1, 2, 3$) and $A_3 = -\bar{\sigma}$. Hence, there are eight unknowns, $A_1, B_1, A_2, B_2, C_2, D_2, C_3$, and D_3 to be determined from the continuity conditions of the traction and displacement at the two material interfaces as,

$$\begin{aligned} \sigma_{rr}^f(r = a) &= \sigma_{rr}^m(r = a) & \sigma_{r\theta}^f(r = a) &= \sigma_{r\theta}^m(r = a) \\ U_r^f(r = a) &= U_r^m(r = a) & U_\theta^f(r = a) &= U_\theta^m(r = a) \\ \sigma_{rr}^m(r = b) &= \sigma_{rr}^c(r = b) & \sigma_{r\theta}^m(r = b) &= \sigma_{r\theta}^c(r = b) \\ U_r^m(r = b) &= U_r^c(r = b) & U_\theta^m(r = b) &= U_\theta^c(r = b) \end{aligned} \quad (5.31)$$

The boundary value problem can be written in a matrix form as,

$$[B] \{d\} = \{f\} \quad (5.32)$$

where,

$$\begin{aligned}
B = & \begin{bmatrix}
-1 & 0 & 1 & 0 & 0 & 0 & 0 & 0 & 0 & 0 \\
1 & 3V_f & -1 & -3V_f & 0 & \frac{3}{2}(\frac{1}{V_f})^2 & \frac{3}{2}(\frac{1}{V_f})^2 & 2\frac{1}{V_f} & 0 & 0 \\
-2 & 2(\frac{G_f^{23}}{K_{23}^f} - 1)V_f & 2\frac{G_{23}^f}{G^m} & -2\frac{G_{23}^f}{G^m} & -2\frac{G_{23}^f}{G^m} & -\frac{G_{23}^f}{G^m}(\frac{1}{V_f})^2 & -\frac{G_{23}^f}{G^m}(\frac{1}{V_f})^2 & -2\frac{G_{23}^f}{G^m} & 0 & 0 \\
2 & 2(\frac{G_f^{23}}{K_{23}^f} + 2)V_f & -2\frac{G_{23}^f}{G^m} & -2\frac{G_{23}^f}{G^m} & -2\frac{G_{23}^f}{G^m} & -\frac{G_{23}^f}{G^m}(\frac{1}{V_f})^2 & -\frac{G_{23}^f}{G^m}(\frac{1}{V_f})^2 & 2\frac{G_{23}^f}{K_{23}^m} & 0 & 0 \\
0 & 0 & -1 & 0 & 0 & -\frac{3}{2} & -\frac{3}{2} & -2 & \frac{3}{2} & 2 \\
0 & 0 & 1 & 3 & 0 & -\frac{3}{2} & -\frac{3}{2} & -1 & \frac{3}{2} & 1 \\
0 & 0 & -2\frac{G_{23}^f}{G^m} & 2\frac{G_{23}^f}{G^m} & 2\frac{G_{23}^f}{G^m} & \frac{G_{23}^f}{G^m} & \frac{G_{23}^f}{G^m} & 2\frac{G_{23}^f}{G^m} & -1 & -2(\frac{G_{23}^f}{K_{23}^m} + 1) \\
0 & 0 & 2\frac{G_{23}^f}{G^m} & 2\frac{G_{23}^f}{G^m} & 2\frac{G_{23}^f}{G^m} & \frac{G_{23}^f}{G^m} & \frac{G_{23}^f}{G^m} & -2\frac{G_{23}^f}{K_{23}^m} & -1 & 2\frac{G_{23}^f}{K_{23}^m}
\end{bmatrix} \\
& \text{(5.33)}
\end{aligned}$$

$$\begin{aligned}
d &= \left[A_1 \quad B_1 \quad A_2 \quad B_2 \quad C_2 \quad D_2 \quad C_3 \quad D_3 \right]^T \\
f &= \left[0 \quad 0 \quad 0 \quad 0 \quad \bar{\sigma} \quad -\bar{\sigma} \quad 2\bar{\sigma} \quad -2\bar{\sigma} \right]^T
\end{aligned}$$

Eshelby's results on the strain energy equivalence gives,

$$\int_0^{2\pi} [\sigma_{rr}^o U_r + \sigma_{r\theta}^o U_\theta - \sigma_{rr} U_r^o - \sigma_{r\theta} U_\theta^o]_{r=b} b \, d\theta = 0 \quad (5.34)$$

where the stresses and displacements for the equivalent medium without the inclusions are,

$$\begin{aligned}
\sigma_{rr}^o &= \tau_{23} \cos 2\theta & \sigma_{r\theta}^o &= -\tau_{23} \sin 2\theta \\
U_r^o &= \frac{r}{2G_{23}} \tau_{23} \cos 2\theta & U_\theta^o &= -\frac{r}{2G_{23}} \tau_{23} \sin 2\theta
\end{aligned} \quad (5.35)$$

Similarly, the substitution of the stresses and displacements of the composite material (Eq. (C.6) and (C.12) in Appendix C respectively) as well as Eq. (5.35) into Eq. (5.34) results in,

$$D_3 = 0 \quad (5.36)$$

Thus, if the boundary conditions in Eq. (5.32) are solved, and we set D_3 to be zero, it gives the results for the composite effective transverse shear modulus through a quadratic equation as,

$$A \left(\frac{G_{23}^c}{G^m} \right)^2 + B \left(\frac{G_{23}^c}{G^m} \right) + C = 0 \quad (5.37)$$

where,

$$\begin{aligned}
A &= a_0 + a_1 V_f + a_2 V_f^2 + a_3 V_f^3 + a_4 V_f^4 \\
B &= b_0 + b_1 V_f + b_2 V_f^2 + b_3 V_f^3 + b_4 V_f^4 \\
C &= c_0 + c_1 V_f + c_2 V_f^2 + c_3 V_f^3 + c_4 V_f^4
\end{aligned}$$

with,

$$\begin{aligned}
a_0 &= -2G^{m^2} (2G^m + K_{23}^m) \left[2G_{23}^f G^m + K_{23}^f (G_{23}^f + G^m) \right] \left[2G_{23}^f G^m + K_{23}^m (G_{23}^f + G^m) \right] \\
a_1 &= 8G^{m^2} (G_{23}^f - G^m) \left[2G_{23}^f G^m + K_{23}^f (G_{23}^f + G^m) \right] (G^{m^2} + G^m K_{23}^m + K_{23}^{m^2}) \\
a_2 &= -12G^{m^2} K_{23}^{m^2} (G_{23}^f - G^m) \left[2G_{23}^f G^m + K_{23}^f (G_{23}^f + G^m) \right] \\
a_3 &= 8G^{m^2} \left\{ G_{23}^{f^2} G^{m^2} K_{23}^f + G_{23}^{f^2} G^m K_{23}^m (K_{23}^f - G^m) + K_{23}^{m^2} \left[G_{23}^f G^m (G_{23}^f - 2G^m) + \right. \right. \\
&\quad \left. \left. K_{23}^f (G_{23}^f - G^m) (G_{23}^f + G^m) \right] \right\} \\
a_4 &= 2G^{m^2} (G_{23}^f - G^m) (2G^m + K_{23}^m) \left[K_{23}^f G^m K_{23}^m - G_{23}^f (2G^m (K_{23}^f - K_{23}^m) + K_{23}^f K_{23}^m) \right]
\end{aligned}$$

$$\begin{aligned}
b_0 &= 4G^{m^3} \left[2G_{23}^f G^m + K_{23}^f (G_{23}^f + G^m) \right] \left[2G_{23}^f G^m + K_{23}^m (G_{23}^f + G^m) \right] \\
b_1 &= 8G^{m^2} K_{23}^m (G_{23}^f - G^m) \left[2G_{23}^f G^m + (G_{23}^f + G^m) K_{23}^f \right] (G^m - K_{23}^m) \\
b_2 &= -2a_2 \\
b_3 &= -2a_3 \\
b_4 &= -4G^{m^3} (G_{23}^f - G^m) \left[K_{23}^f G^m K_{23}^m - G_{23}^f (2G^m (K_{23}^f - K_{23}^m) + K_{23}^f K_{23}^m) \right]
\end{aligned}$$

$$\begin{aligned}
c_0 &= 2G^{m^2} K_{23}^m \left[2G_{23}^f G^m + K_{23}^f (G_{23}^f + G^m) \right] \left[2G_{23}^f G^m + K_{23}^m (G_{23}^f + G^m) \right] \\
c_1 &= 8G^{m^2} K_{23}^{m^2} (G_{23}^f - G^m) \left[2G_{23}^f G^m + K_{23}^f (G_{23}^f + G^m) \right] \\
c_2 &= a_2 \\
c_3 &= a_3 \\
c_4 &= -2G^{m^2} K_{23}^m (G_{23}^f - G^m) \left[K_{23}^f G^m K_{23}^m - G_{23}^f (2G^m (K_{23}^f - K_{23}^m) + K_{23}^f K_{23}^m) \right]
\end{aligned}$$

Finally, a complete set of stresses, strains, and displacements for each constituent under a stress deformation of transverse shear is obtained through Eq.(C.4)-(C.12) in Appendix C.

5.3.3.3 Computation of F_{i2} , F_{i3} , and F_{i6} components

So far, the stress and strain fields of each constituent in the three-phase cylinder model have been determined for the cases that a stress deformation of $\sigma_{22}^c = \sigma_{33}^c = \bar{\sigma}$

or $\sigma_{22}^c = -\sigma_{33}^c = \bar{\sigma}$ is imposed. The matrix strain fields due to a single normal stress, either $\sigma_{22}^c = \bar{\sigma}$ or $\sigma_{33}^c = \bar{\sigma}$, can be obtained through the superposition of the aforementioned two stress states; while the state of pure shear, $\tau_{23}^c = \bar{\sigma}$, can be easily deduced from the stress state of $\sigma_{22}^c = -\sigma_{33}^c = \bar{\sigma}$ by changing θ to $\theta + \pi/4$.

It should be noted that the determination of the \mathbf{F} matrix requires a single strain to be applied on the composite medium. For example, in order to determine the F_{i2} components, a single normal strain, ϵ_{22}^c , should be imposed, and all the other strain components are enforced to be zero, resulting in stress states of $\sigma_{22}^c = (K_{23}^c + G_{23}^c) \epsilon_{22}^c$, $\sigma_{33}^c = (K_{23}^c - G_{23}^c) \epsilon_{22}^c$, and $\tau_{23}^c = 0$ based upon the the composite constitutive relation in Eq. (5.22). Since the elasticity problem due to a single applied stress has been solved, the matrix strain fields due to ϵ_{22}^c can be easily obtained by superposing the results from the two stresses, σ_{22}^c and σ_{33}^c . Thus, the matrix strains are related to ϵ_{22}^c in polar coordinates as,

$$\begin{aligned} \epsilon_{rr}^m = \frac{1}{4G^m \bar{\sigma}} \left\{ K_{23}^c \left(M_2 \frac{b^2}{r^2} + 2 \frac{G^m}{K_{23}^m} N_2 \right) + G_{23}^c \left[-2A_2 + 6 \left(\frac{G^m}{K_{23}^m} \right. \right. \right. \\ \left. \left. \left. - 1 \right) B_2 \frac{r^2}{b^2} - 3C_2 \frac{b^4}{r^4} - 2 \left(\frac{G^m}{K_{23}^m} + 1 \right) D_2 \frac{b^2}{r^2} \right] \cos 2\theta \right\} \epsilon_{22}^c \end{aligned} \quad (5.38a)$$

$$\begin{aligned} \epsilon_{\theta\theta}^m = \frac{1}{4G^m \bar{\sigma}} \left\{ K_{23}^c \left(-M_2 \frac{b^2}{r^2} + 2 \frac{G^m}{K_{23}^m} N_2 \right) + G_{23}^c \left[2A_2 + 6 \left(\frac{G^m}{K_{23}^m} \right. \right. \right. \\ \left. \left. \left. + 1 \right) B_2 \frac{r^2}{b^2} + 3C_2 \frac{b^4}{r^4} - 2 \left(\frac{G^m}{K_{23}^m} - 1 \right) D_2 \frac{b^2}{r^2} \right] \cos 2\theta \right\} \epsilon_{22}^c \end{aligned} \quad (5.38b)$$

$$\gamma_{r\theta}^m = \frac{G_{23}^c}{2G^m \bar{\sigma}} \left[2A_2 + 6B_2 \frac{r^2}{b^2} - 3C_2 \frac{b^4}{r^4} - 2D_2 \frac{b^2}{r^2} \right] \sin 2\theta \epsilon_{22}^c \quad (5.38c)$$

Transforming these matrix strains to the Cartesian coordinates using Eq. (B.1) gives the non-vanishing components in F_{i2} as,

$$\begin{aligned} F_{22} = \frac{1}{4G^m \bar{\sigma}} \left\{ \left[2K_{23}^c \frac{G^m}{K_{23}^m} N_2 - G_{23}^c \left(2A_2 + 6B_2 \frac{r^2}{b^2} \right) \right] + \left[K_{23}^c M_2 \frac{b^2}{r^2} \right. \right. \\ \left. \left. + 2G_{23}^c \frac{G^m}{K_{23}^m} \left(3B_2 \frac{r^2}{b^2} - D_2 \frac{b^2}{r^2} \right) \right] \cos 2\theta - \left[G_{23}^c \left(3C_2 \frac{b^4}{r^4} + 2D_2 \frac{b^2}{r^2} \right) \right] \cos 4\theta \right\} \end{aligned} \quad (5.39a)$$

$$\begin{aligned} F_{32} = \frac{1}{4G^m \bar{\sigma}} \left\{ \left[2K_{23}^c \frac{G^m}{K_{23}^m} N_2 + G_{23}^c \left(2A_2 + 6B_2 \frac{r^2}{b^2} \right) \right] - \left[K_{23}^c M_2 \frac{b^2}{r^2} \right. \right. \\ \left. \left. - 2G_{23}^c \frac{G^m}{K_{23}^m} \left(3B_2 \frac{r^2}{b^2} - D_2 \frac{b^2}{r^2} \right) \right] \cos 2\theta + \left[G_{23}^c \left(3C_2 \frac{b^4}{r^4} + 2D_2 \frac{b^2}{r^2} \right) \right] \cos 4\theta \right\} \end{aligned} \quad (5.39b)$$

$$F_{62} = \frac{1}{2G^m\bar{\sigma}} \left[K_{23}^c M_2 \frac{b^2}{r^2} \sin 2\theta - G_{23}^c \left(3C_2 \frac{b^4}{r^4} + 2D_2 \frac{b^2}{r^2} \right) \sin 4\theta \right] \quad (5.39c)$$

Similarly, the F_{i3} components can be computed by imposing a single strain ϵ_{33}^c , and the resulting non-vanishing components are,

$$F_{23} = \frac{1}{4G^m\bar{\sigma}} \left\{ \left[2K_{23}^c \frac{G^m}{K_{23}^m} N_2 + G_{23}^c \left(2A_2 + 6B_2 \frac{r^2}{b^2} \right) \right] + \left[K_{23}^c M_2 \frac{b^2}{r^2} - 2G_{23}^c \frac{G^m}{K_{23}^m} \left(3B_2 \frac{r^2}{b^2} - D_2 \frac{b^2}{r^2} \right) \right] \cos 2\theta + \left[G_{23}^c \left(3C_2 \frac{b^4}{r^4} + 2D_2 \frac{b^2}{r^2} \right) \right] \cos 4\theta \right\} \quad (5.40a)$$

$$F_{33} = \frac{1}{4G^m\bar{\sigma}} \left\{ \left[2K_{23}^c \frac{G^m}{K_{23}^m} N_2 - G_{23}^c \left(2A_2 + 6B_2 \frac{r^2}{b^2} \right) \right] - \left[K_{23}^c M_2 \frac{b^2}{r^2} + 2G_{23}^c \frac{G^m}{K_{23}^m} \left(3B_2 \frac{r^2}{b^2} - D_2 \frac{b^2}{r^2} \right) \right] \cos 2\theta - \left[G_{23}^c \left(3C_2 \frac{b^4}{r^4} + 2D_2 \frac{b^2}{r^2} \right) \right] \cos 4\theta \right\} \quad (5.40b)$$

$$F_{63} = \frac{1}{2G^m\bar{\sigma}} \left[K_{23}^c M_2 \frac{b^2}{r^2} \sin 2\theta + G_{23}^c \left(3C_2 \frac{b^4}{r^4} + 2D_2 \frac{b^2}{r^2} \right) \sin 4\theta \right] \quad (5.40c)$$

The matrix strains due to a single composite strain γ_{23}^c can be obtained from the case where a transverse shear stress deformation is imposed in the far field of the three-phase cylinder. The composite transverse stress and strain are simply related by $\tau_{23}^c = G_{23}^c \gamma_{23}^c$, where $\tau_{23}^c = \bar{\sigma}$ is deduced from the stress state $\sigma_{22}^c = -\sigma_{33}^c = \bar{\sigma}$ in Section 5.3.3.2 by changing θ to $\theta + \pi/4$. Thus the F_{i6} components are computed from the matrix strains due to γ_{23}^c as,

$$F_{26} = \frac{G_{23}^c}{4G^m\bar{\sigma}} \left[\left(3C_2 \frac{b^4}{r^4} + 2D_2 \frac{b^2}{r^2} \right) \sin 4\theta + 2 \frac{G^m}{K_{23}^m} \left(3B_2 \frac{r^2}{b^2} - D_2 \frac{b^2}{r^2} \right) \sin 2\theta \right] \quad (5.41a)$$

$$F_{36} = \frac{G_{23}^c}{4G^m\bar{\sigma}} \left[- \left(3C_2 \frac{b^4}{r^4} + 2D_2 \frac{b^2}{r^2} \right) \sin 4\theta + 2 \frac{G^m}{K_{23}^m} \left(3B_2 \frac{r^2}{b^2} - D_2 \frac{b^2}{r^2} \right) \sin 2\theta \right] \quad (5.41b)$$

$$F_{66} = \frac{G_{23}^c}{2G^m\bar{\sigma}} \left[- \left(2A_2 + 6B_2 \frac{r^2}{b^2} \right) + \left(3C_2 \frac{b^4}{r^4} + 2D_2 \frac{b^2}{r^2} \right) \cos 4\theta \right] \quad (5.41c)$$

5.3.4 Matrix strain contours under a single applied composite strain

With the computation of the \mathbf{F} matrix in the aforementioned sections, all the matrix strain components can be obtained by knowing the applied composite strains. In order to validate the proposed micromechanics model, the computed matrix strain fields under a globally prescribed single composite strain using the current analytical solutions are compared against the results from a FE model. The FE model utilized to analyze the axial tension and axial shear problem is a 3D two-phase cylinder model,

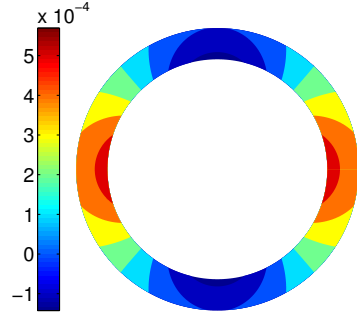
while the one used to solve for the transverse tension and transverse shear problem is a 3D three-phase model, in which both the fiber and matrix are concentrically embedded in the equivalent composite medium. The details of the FE model as well as the boundary conditions for each case are provided in Appendix D.

Since the composite is assumed to be transversely isotropic, only four loading conditions are considered, including axial tension, axial shear, transverse tension, and transverse shear. In each case, a strain value of 0.1% is prescribed to the relevant component, and the rest of the strain components are enforced to be zero. Since the composite undergoes small deformation, both the fiber and matrix are linear elastic in this regime. The elastic properties of the constituent materials are summarized in Table 5.1, which are taken from various sources [75, 19]. Both S-2 glass fiber and SC-15 epoxy resin are isotropic, while IM-7 carbon fiber is transversely isotropic. The fiber volume fraction is set to 60% in each case.

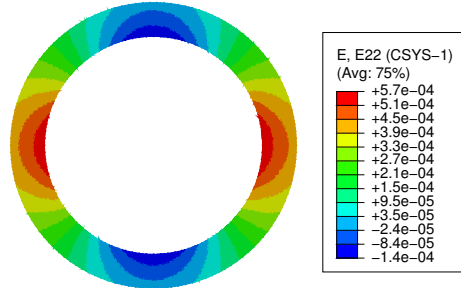
Table 5.1: Elastic properties for IM-7 carbon fiber, S-2 glass fiber, and SC-15 matrix.

	E_1 GPa	E_2 GPa	ν_{12} -	G_{12} GPa	G_{23} GPa
IM7 Carbon Fiber	276.0	15.0	0.279	12.0	5.02
S-2 Glass Fiber	114.2	114.2	0.22	46.8	46.8
SC-15 Matrix	2.487	2.487	0.35	0.921	0.921

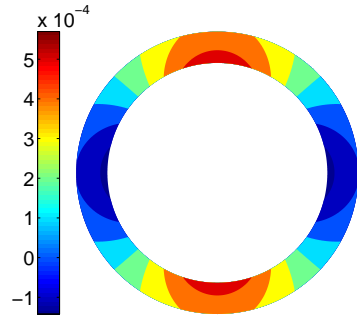
Figures 5.6–5.9 show the comparison of the matrix strain contour of each component under various applied composite strains for a IM-7 carbon fiber composite. The results for the glass fiber is not shown here. It can be concluded that the proposed micromechanics model provides accurate prediction of the spatial variation of the matrix fields when the composite is subjected to loading. Capturing the strain and stress concentrations in the matrix material is important to determine the damage and failure characteristics of composites such as nonlinear stress versus strain response, strain to failure, strength, and fatigue life. In Section 5.4, a multi-scale computational framework is established to compute the composite nonlinear behavior, in which the proposed analytical method is employed for the subscale micromechanical analysis.



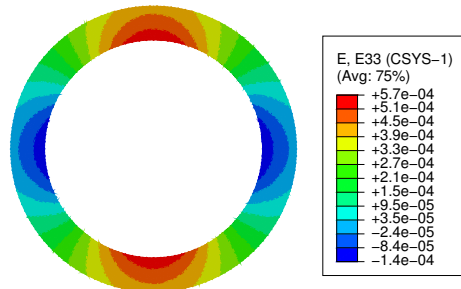
(a) ϵ_{22}^m from the proposed method



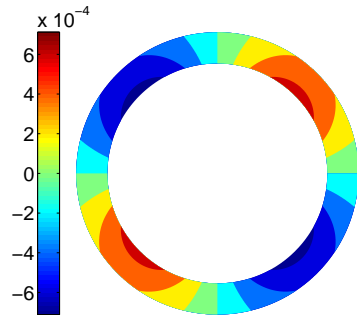
(b) ϵ_{22}^m from corresponding FEA



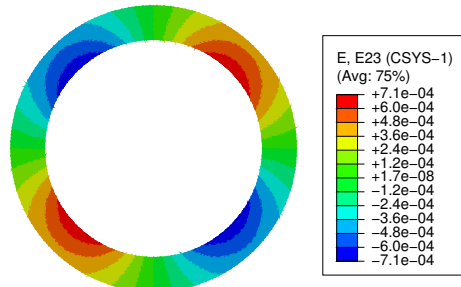
(c) ϵ_{33}^m from the proposed method



(d) ϵ_{33}^m from corresponding FEA



(e) γ_{23}^m from the proposed method



(f) γ_{23}^m from corresponding FEA

Figure 5.6: Matrix strain contours under $\epsilon_{11}^c = 0.1\%$. The constituent fiber is IM-7 carbon fiber.

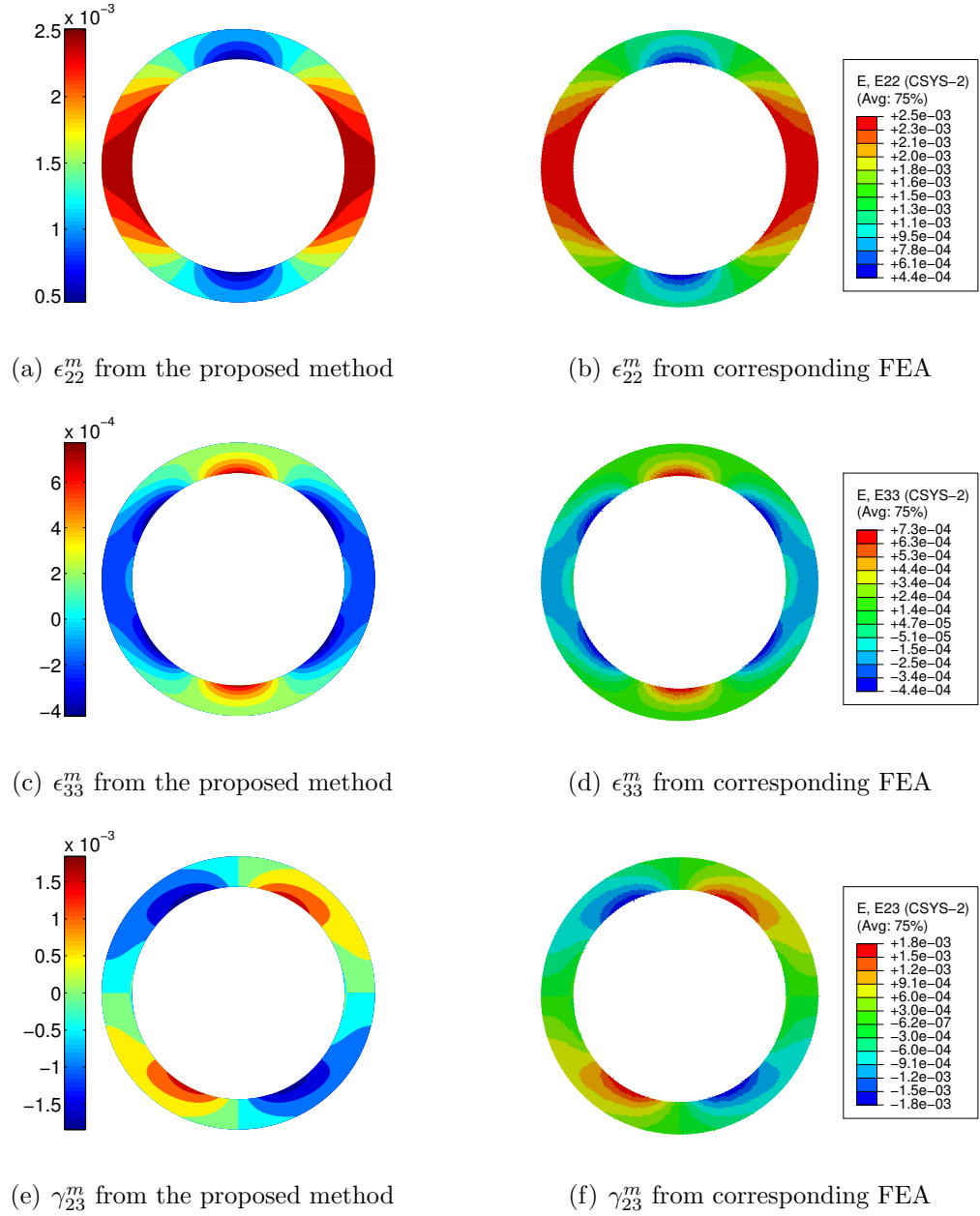
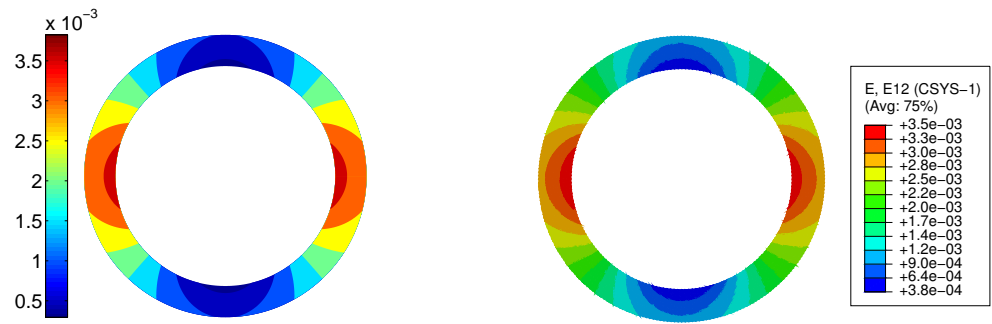
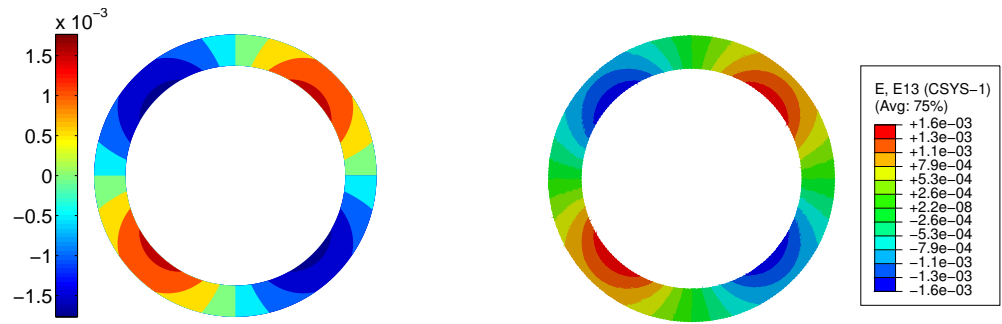


Figure 5.7: Matrix strain contours under $\epsilon_{22}^c = 0.1\%$. The constituent fiber is IM-7 carbon fiber.



(a) γ_{12}^m from the proposed method

(b) γ_{12}^m from corresponding FEA



(c) γ_{13}^m from the proposed method

(d) γ_{13}^m from corresponding FEA

Figure 5.8: Matrix strain contours under $\gamma_{12}^c = 0.1\%$. The constituent fiber is IM-7 carbon fiber.

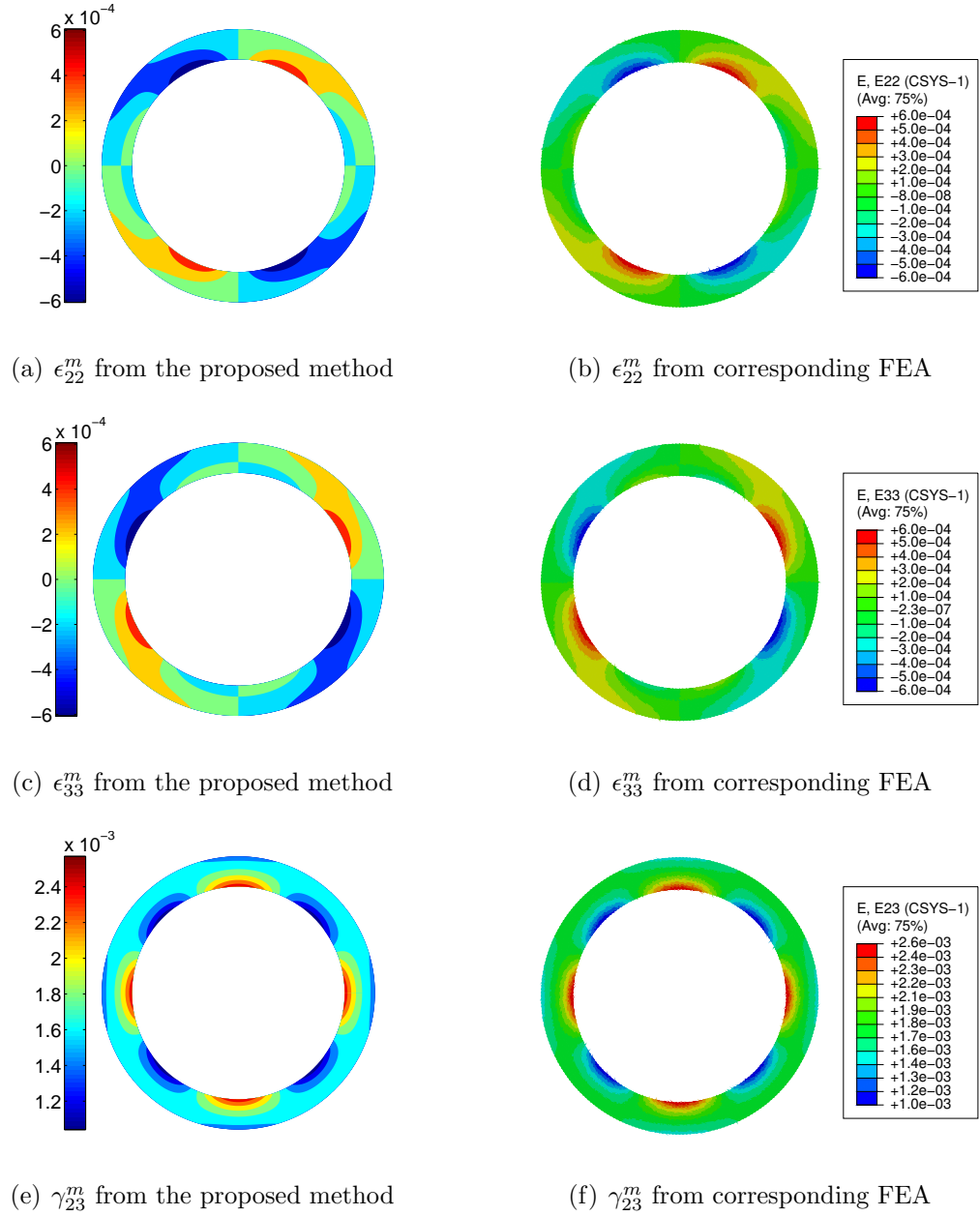


Figure 5.9: Matrix strain contours under $\gamma_{23}^c = 0.1\%$. The constituent fiber is IM-7 carbon fiber.

5.4 Multiscale Modeling Methodology for Nonlinear Composites

The macroscopic nonlinear response of composite materials are influenced by matrix microdamage at the subscale. The motivation of the current study is to relate the subscale micromechanical analysis to the composite effective response at the macroscale through a multiscale modeling framework. The key to the proposed model is the selection of two scalar variables that characterize the evolution of the matrix microdamage based upon the strain contours computed in Section 5.3.4. The proposed model is different from previous mean-field methods, [60, 62], in that the extreme value of the matrix strains are utilized rather than the average value to determine the composite nonlinear damage progression.

The multiscale methodology established in this research is based upon two scales. For the macro-scale, lamina-level analysis of a fiber-reinforced laminated structure, or fiber tow-level analysis for a textile composite is conducted by utilizing effective homogenized properties to compute stress and strains in the lamina or fiber tow. Simultaneously, it is intended to carry out the subscale analysis, at the fiber and matrix level, using the micromechanics model presented in Section 5.3, in which the constituent stress and strain fields are provided in closed form. The commercially available finite element software, ABAQUS (version 6.10), is used for the macroscale FE model, and the micromechanics model at the subscale is implemented at each integration point of the macroscale, using a user defined material subroutine, UMAT. This subroutine is called at each integration point at each increment, and the material constitutive law is updated through user-defined options.

At the start of each increment, the material state (stress, strain, and solution-dependent state variables) from the previous equilibrium step and the strain increments in the current step are passed into the UMAT through the ABAQUS solver. In the n th increment, the total strain, ϵ_{ij}^n , is calculated by adding the current strain increment, $d\epsilon_{ij}^n$, to the strain in the previous step, ϵ_{ij}^{n-1} , as $\epsilon_{ij}^n = \epsilon_{ij}^{n-1} + d\epsilon_{ij}^n$. In the multiscale computational scheme, the strains at each integration point in the FE model, are applied to the subscale micromechanics model. These integration point strains can be treated as the effective composite strains (or macro strains) that are applied on a discrete fiber-matrix microstructure. The constituent strain fields therefore can be computed in closed form by knowing the globally applied strains through the micromechanical analysis discussed in Section 5.3.

However, it should be noted that the resulting matrix strain fields vary in space

as shown in Figure 5.6–5.9, hence the matrix equivalent strain, computed using Eq. (4.16), has spatial variation as well. In the current fully analytical computational scheme, it is hypothesized that the composite nonlinear behavior can be characterized using two scalar variables that are related to the matrix equivalent strain. This idea is similar to the mean-field theories in which the average value of the strain fields are utilized to determine the matrix nonlinear progression. In the present study, the two scalar variables that govern the evolution of matrix microdamage are defined based upon the maximum and average value of the square of the matrix equivalent strain at the fiber-matrix interface, respectively, as,

$$V_{max} = \max \left\{ \frac{1}{2} [(\bar{\epsilon}_{11}^m - \bar{\epsilon}_{22}^m)^2 + (\bar{\epsilon}_{22}^m - \bar{\epsilon}_{33}^m)^2 + (\bar{\epsilon}_{33}^m - \bar{\epsilon}_{11}^m)^2] + \frac{3}{4} (\bar{\gamma}_{12}^{m^2} + \bar{\gamma}_{13}^{m^2} + \bar{\gamma}_{23}^{m^2}) \right\} \quad (5.42)$$

$$V_{avg} = \text{avg} \left\{ \frac{1}{2} [(\bar{\epsilon}_{11}^m - \bar{\epsilon}_{22}^m)^2 + (\bar{\epsilon}_{22}^m - \bar{\epsilon}_{33}^m)^2 + (\bar{\epsilon}_{33}^m - \bar{\epsilon}_{11}^m)^2] + \frac{3}{4} (\bar{\gamma}_{12}^{m^2} + \bar{\gamma}_{13}^{m^2} + \bar{\gamma}_{23}^{m^2}) \right\} \quad (5.43)$$

where $\bar{\epsilon}_{ij}^m$ is the matrix strain at the fiber-matrix interface ($r = a$). Physically, the average term is dominant in the matrix strain field when the fiber volume fraction is low, while the maximum value dominates the result for high fiber volume fraction. Therefore, a weight function of V_{max} and V_{avg} can be written as,

$$V_{weight} = V_f^n V_{max} + (1 - V_f^n) V_{avg} \quad (5.44)$$

where n is dependent on the fiber-to-matrix stiffness ratio such that the effect of constituent properties can be accounted for. In this research, it assumes,

$$n = 2 \sqrt{\left(\frac{E^m}{E_2^f} + \frac{G^m}{G_{23}^f} \right)} \quad (5.45)$$

Consequently, two matrix equivalent strains can be computed; one is based upon the weight function in Eq. (5.44), while the other is based upon the average value in Eq. (5.43), as,

$$\epsilon_{m,1}^{eq} = \frac{1}{1 + \nu_s} \sqrt{V_{weight}} \quad \text{and} \quad \epsilon_{m,2}^{eq} = \frac{1}{1 + \nu_s} \sqrt{V_{avg}} \quad (5.46)$$

Once the matrix equivalent strain is resolved, the matrix stiffness tensor is degraded as a secant solid according to the nonlinear damage model presented in Section

4.2. It is further hypothesized that the matrix secant moduli calculated using $\epsilon_{m,1}^{eq}$ are subsequently used to compute the composite effective secant moduli, E_1^c , ν_{12}^c , K_{23}^c , and G_{23}^c using Eq. (5.7), (5.8), (5.30), and (5.37), respectively; while the matrix secant moduli determined from $\epsilon_{m,2}^{eq}$ is used to compute G_{12}^c using Eq. (5.18). Consequently, if matrix microdamage occurs, the stiffness of the subscale microstructure is reduced based upon the proposed secant moduli approach. The subscale stiffness tensors are subsequently used to update the global stiffness and stresses in the macroscale FE model. Therefore, the influence of matrix microdamage at the subscale manifests as the degradation of the global stiffness of the composite, and the composite nonlinear response at the macroscale is captured.

5.5 Model Validation

In order to verify the proposed method to compute the composite nonlinear response, a discrete FE model is utilized to evaluate the accuracy of the prediction. The effective elastic moduli of the composite are computed as a function of fiber volume fraction varying from 20% to 80%. The five elastic constants obtained from the proposed method are compared against the results from the FEA as well as other analytical models such as the CCM and Mori-Tanaka (M-T) method [49], as shown in Section 5.5.2. The composite nonlinear response is presented in Section 5.5.3. Fiber volume fractions of 50%, 60%, and 70% are selected to examine the effect of fiber volume fraction on the accuracy of the prediction. Two types of constituent fibers, IM-7 carbon and S-2 glass, are studied in this research. The elastic properties of the fibers and matrix are provided in Table 5.1. The nonlinear properties of SC-15 matrix are given in Table 5.2.

Table 5.2: The nonlinear properties of SC-15 matrix.

	σ_y^m (MPa)	K_1 (MPa)	K_2
SC-15 Matrix	30	4500	60

5.5.1 Finite Element Model

A unidirectional fiber-reinforced composite can be modeled at the fiber-matrix level through a RUC with detailed fiber geometries and constituent properties. Though this method is computationally expensive, it offers accurate prediction of the compos-

its constitutive behavior, including inelastic response and fracture. In this study, the results from the FE model serves as a standard to verify the proposed micromechanics based multi-scale model for computing the composite nonlinear response.

The microstructure of a unidirectional composite is represented by the RUC composed of a hexagonally packed array of fibers, as shown in Figure 5.10, resulting in a transversely isotropic solid. In fiber-reinforced composites, individual fibers are randomly distributed in the matrix medium, exhibiting a certain degree of randomness depending on the manufacturing process. Therefore, in this study, the center fiber is slightly offset to break the symmetry of the geometry. The effect of fiber randomness and the size of RUC have been addressed in [119]. In addition, the RUC deforms like a jigsaw puzzle such that periodic boundary conditions are required to ensure the continuity between the adjacent RUCs. The periodic boundary conditions are imposed on pairs of opposite boundary surfaces as, [151],

$$\begin{aligned}
u_1(L_1, x_2, x_3) - u_1(0, x_2, x_3) &= E_{11}L_1 \\
u_2(L_1, x_2, x_3) - u_2(0, x_2, x_3) &= 2E_{12}L_1 \\
u_3(L_1, x_2, x_3) - u_3(0, x_2, x_3) &= 2E_{13}L_1 \\
u_1(x_1, L_2, x_3) - u_1(x_1, 0, x_3) &= 2E_{12}L_2 \\
u_2(x_1, L_2, x_3) - u_2(x_1, 0, x_3) &= E_{22}L_2 \\
u_3(x_1, L_2, x_3) - u_3(x_1, 0, x_3) &= 2E_{23}L_2 \\
u_1(x_1, x_2, L_3) - u_1(x_1, x_2, 0) &= 2E_{13}L_3 \\
u_2(x_1, x_2, L_3) - u_2(x_1, x_2, 0) &= 2E_{23}L_3 \\
u_3(x_1, x_2, L_3) - u_3(x_1, x_2, 0) &= E_{33}L_3
\end{aligned} \tag{5.47}$$

where u_1 , u_2 , and u_3 denote the displacements in the 1, 2, and 3 directions, respectively, L_1 , L_2 , and L_3 , are the corresponding edge lengths, and E_{ij} , are the macroscopic tensorial strains of the RUC determined by the displacements imposed on the boundaries. The corresponding macroscopic stresses of the RUC are computed from the force resultants acting on the surface boundaries divided by the cross sectional area. The composite effective stress versus effective strain response is represented by the macroscopic stresses and strains of the RUC, which are related to the non-homogeneous stress and strain fields within the RUC based upon energy equivalence, [151]. To obtain a full characterization of the composite nonlinear response, four loading scenarios are considered, including axial tension, transverse tension, axial shear, and transverse shear. Both carbon and glass fibers are linear elastic, while the matrix

is modeled as an elastic-damaging solid using a secant modulus approach as presented in Section 4.2. The analysis was carried out using the commercially available code ABAQUS, in which the matrix constitutive law is implemented through a UMAT.

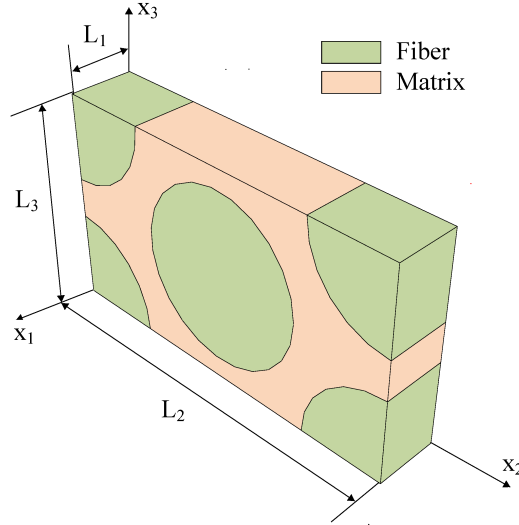
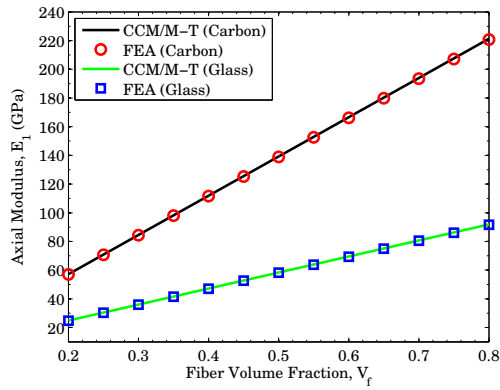


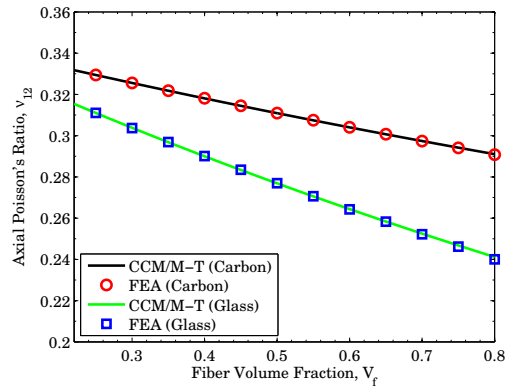
Figure 5.10: 3D finite element model.

5.5.2 Elastic Properties

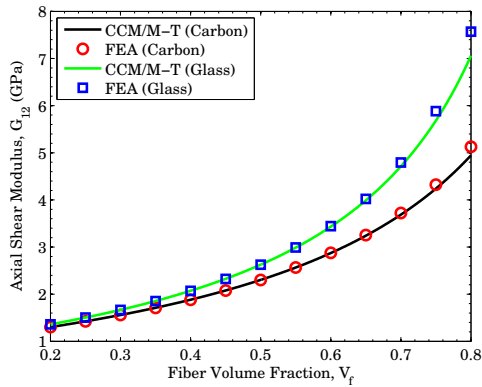
In this section, the effective elastic moduli of a unidirectional composite are computed using various micromechanics models, including the CCM, M-T method, GSCM, and direct FEA. The formulations for the CCM and M-T method are provided in Appendix E. It is worth noting that the CCM cannot provide a closed-form solution for G_{23} , and thus Hashin’s lower bound is used instead (discussed in Appendix E). Hence, not surprisingly, the CCM and M-T method yield the same results. In the present study, the GSCM is extended to compute G_{23} and K_{23} , however, the rest of the moduli, E_1 , ν_{12} , and G_{12} , are still determined from the CCM. It should be noted that E_2 is computed according to Eq. (5.2), which depends on G_{23} , K_{23} , E_1 , and ν_{12} . In the instance that the extended GSCM is used, the determination of E_2 involves the axial properties (E_1 and ν_{12}) computed from the CCM, hence such a method for computing E_2 is actually based upon both the GSCM and the CCM, and denoted as “Proposed Method”. In the FE model, the fiber volume fraction varies from 20% to 80% in increments of 5%. The results of the effective moduli computed from various micromechanics models are shown in Figure 5.5.2.



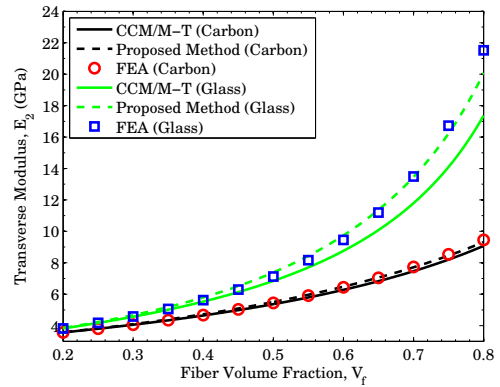
(a) Axial Modulus



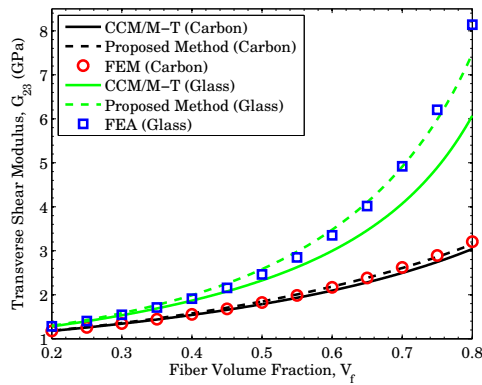
(b) Axial Poisson's Ratio



(c) Axial Shear Modulus



(d) Transverse Modulus



(e) Transverse Shear Modulus

Figure 5.11: The composite effective elastic moduli computed from various micromechanics models.

5.5.2.1 Axial Moduli: E_1 , ν_{12} , and G_{12}

The effective axial modulus, E_1 , and the effective axial Poisson's ratio, ν_{12} , computed from the analytical models (CCM and M-T method) are in good agreement with the FE results. As shown in Figure 5.5.2 (a) and (b), these two properties vary almost linearly with fiber volume fraction, indicating that the effective moduli can be approximated by a simple rule of mixture. In contrast to the linear variation, the effective axial shear modulus, G_{12} , exhibits significant nonlinearity with respect to the fiber volume fraction, as shown in Figure 5.5.2 (c). Overall, the predictions from the theoretical models agree with the FE results; however, when the fiber volume fraction is high ($V_f > 75\%$), differences exist, and the elasticity solutions yield the lower values. It is also worth noting that the scatter is larger for glass/SC-15 than carbon/SC-15. One possible reason is that as the fiber volume fraction increases, the fibers are close to each other and the effects of fiber interactions are significant, which are neglected in these theoretical models but accounted for in the FE model. This effect is critical with the increased fiber volume fraction, particularly in the case that the mismatch of the constituent properties is large. These results also suggest that there should be a restriction on the fiber volume fraction to ensure the accuracy of these theoretical methods.

5.5.2.2 Transverse Moduli: E_2 and G_{23}

The predictions for the effective transverse modulus, E_2 , and the effective transverse shear modulus, G_{23} , are shown in Figure 5.5.2 (d) and (e), respectively. Both properties are highly nonlinear with fiber volume fraction, and present similar trends as observed in the case with G_{12} . When the fiber volume fraction is low ($V_f < 30\%$), the proposed method almost coincides with the CCM and M-T method, and is in good agreement with the FE result. As the fiber volume fraction increases, the proposed method predicts higher moduli than the other two analytical methods, which confirms that the lower values of G_{23} correspond to Hashin's lower bound. For $30\% < V_f < 55\%$, the results from the FE model lie in between the proposed method and the CCM/M-T method; however, the predictions from various models are reasonably close to each other. As the fiber volume fraction gets higher, the moduli computed from the FE model are closer to the predictions based upon the proposed method. For $V_f > 75\%$, the FE model provides higher values than all the theoretical models, which is in accord with the findings for G_{12} . One possible reason leading to this discrepancy has been discussed in the previous section.

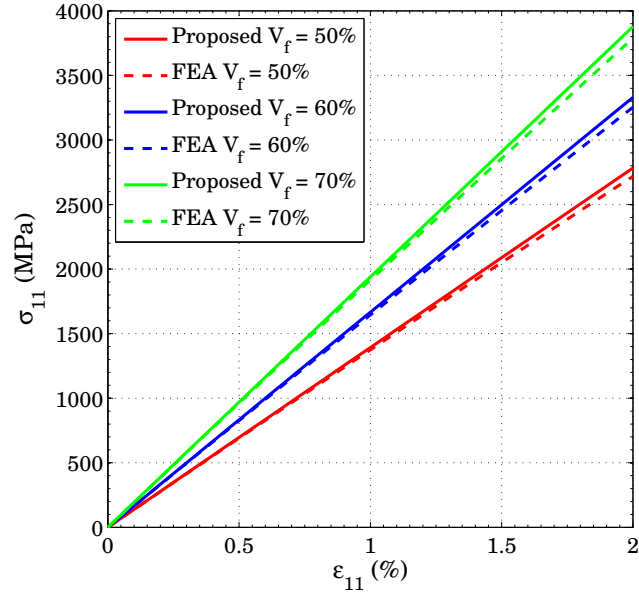
The difference between the proposed method and the CCM (or M-T method) is obvious for glass/SC-15 with fiber volume fraction greater than 30%. The difficulty in the prediction for the transverse properties is primarily due to the non-uniform stresses and strains within the fiber and matrix [47, 161], resulting in complicated boundary conditions for the elasticity problems. This non-uniform effect is more significant in a composite system with a high fiber volume fraction ($V_f > 55\%$) and large mismatch in the constituent properties (the fiber-to-matrix modulus ratio greater than 10). The proposed method, which is an extension to the original GSCM and based upon a three-phase cylinder model, is able to provide appropriate boundary conditions for the fiber and matrix because of the outer equivalent composite medium. Hence, the proposed method is desirable for the unidirectional fiber-reinforced composite with relatively high fiber volume fraction ($V_f > 55\%$) and large fiber-to-matrix modulus ratio.

5.5.3 Nonlinear Response

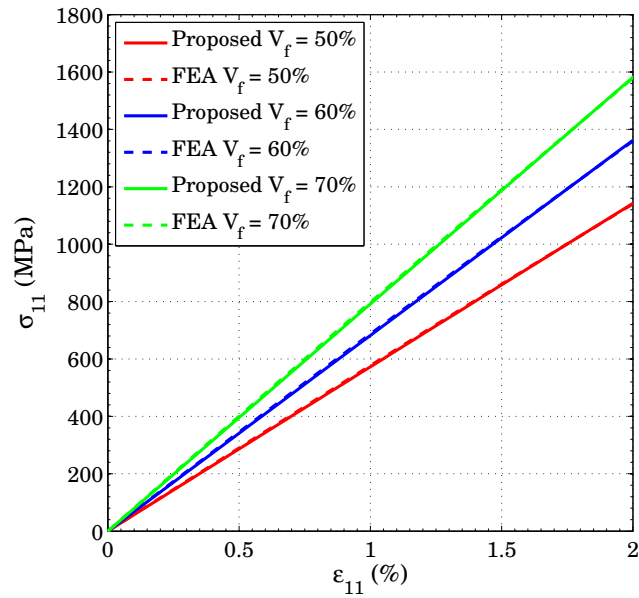
The comparison between the proposed method and the FE model for the prediction of the composite nonlinear stress versus strain response is shown in Figure 5.12–5.15. The axial normal stress-strain response, as shown in Figure 5.12, exhibits almost linear response during the deformation since the composite axial behavior is dominated by the fiber properties. As a result, the carbon-epoxy composite presents higher stiffness than the glass-epoxy composite for axial tension. Significant nonlinearity in the stress versus strain response is shown in the transverse normal, axial shear, and transverse shear loading cases, since these properties are dominated by the matrix material. The effective composite stiffness is degraded with respect to the evolution of microdamage in the matrix. It should be noted that the present model only considers matrix pre-peak nonlinear response, therefore, the resulting composite stress-strain responses are plotted in the range before the SC-15 polymer matrix reaches the failure strain of 4.2%.

The transverse normal and transverse shear responses are shown in Figure 5.13 and 5.15, respectively. These two properties are determined from the weight function defined in Eq. (5.44), suggesting that the fiber volume fraction and the fiber-to-matrix stiffness ratio affect the choice of the scalar variables that characterize the composite nonlinear responses. In particular, when the fiber volume fraction is low or the fiber-to-matrix stiffness ratio approaches one, the resulting composite nonlinear behavior tends to be dominated by the average value of the matrix strain at the fiber-matrix interface, while on the other hand, the maximum value is dominant for either high

fiber volume fraction or large fiber-to-matrix stiffness ratio. It should be noted that IM-7 carbon fiber is transversely isotropic, and its transverse stiffness is significantly lower than that of S-2 glass, as shown in Table 5.1. Even though the proposed method is an approximation based upon the choice of the scalar variables, it offers good predictions for both composite systems with fiber volume fraction varying from 50% to 70%. The results for the axial shear response, as shown in Figure 5.14, present increased accuracy of prediction with decreased fiber volume fraction from 70% to 50%. Since this property is determined from the average matrix strain at the fiber-matrix interface, it tends to overpredict the nonlinear response when the fiber volume fraction is high. However, in comparison with the full FEA, the proposed method still offers a good prediction for fiber volume fraction up to 70%.

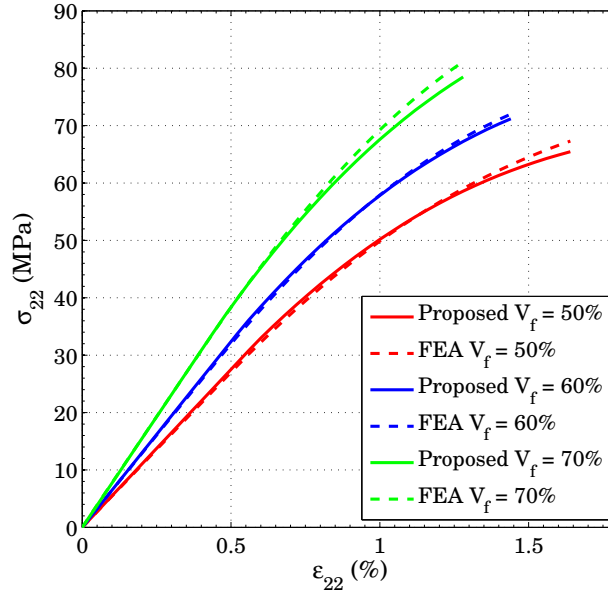


(a) IM-7 carbon – SC-15 epoxy.

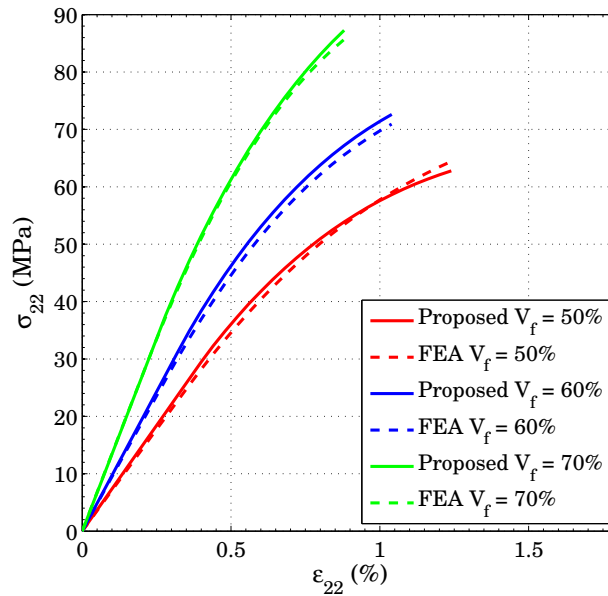


(b) S-2 glass – SC-15 epoxy.

Figure 5.12: The composite effective axial normal stress versus strain response.

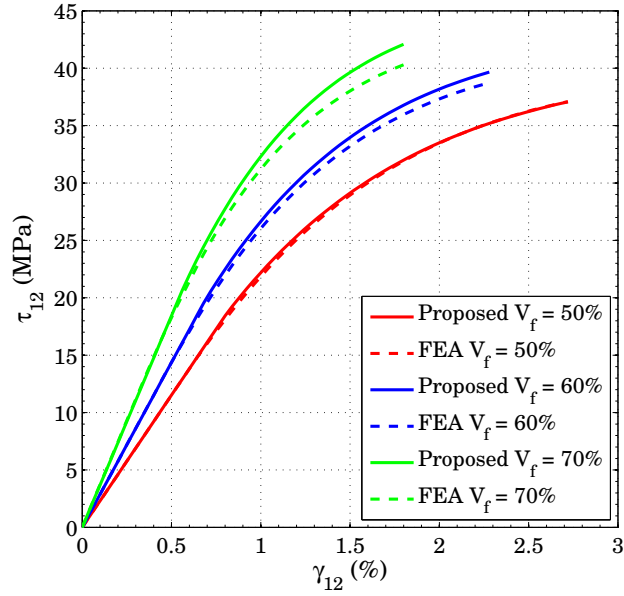


(a) IM-7 carbon – SC-15 epoxy.

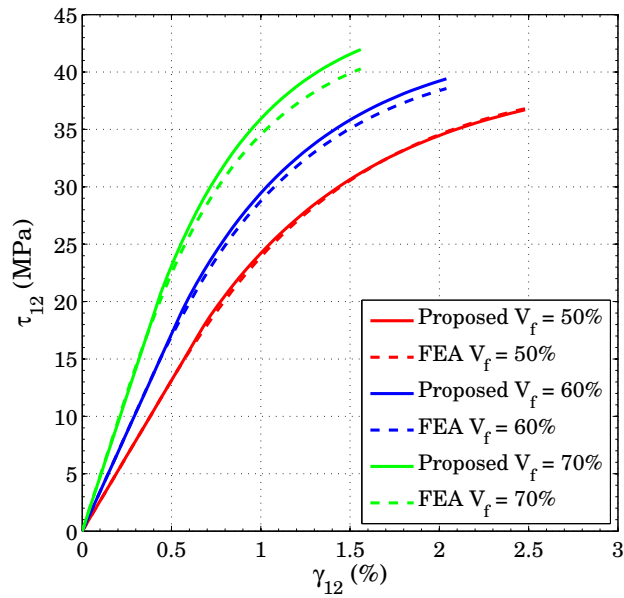


(b) S-2 glass – SC-15 epoxy.

Figure 5.13: The composite effective transverse normal stress versus strain response.

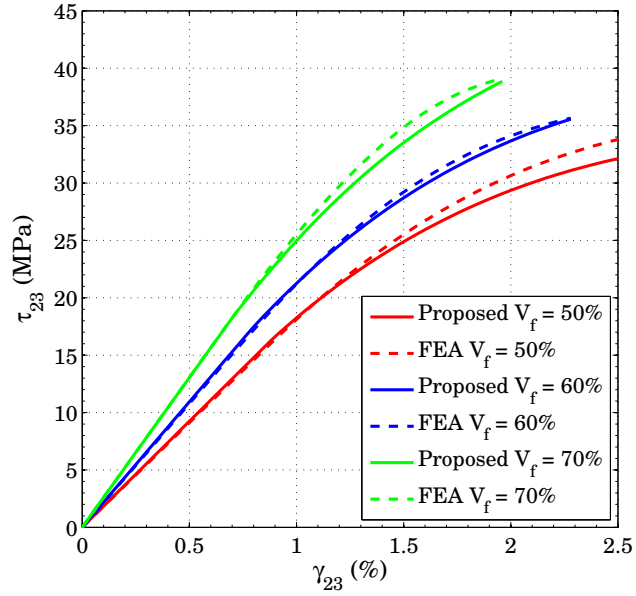


(a) IM-7 carbon – SC-15 epoxy.

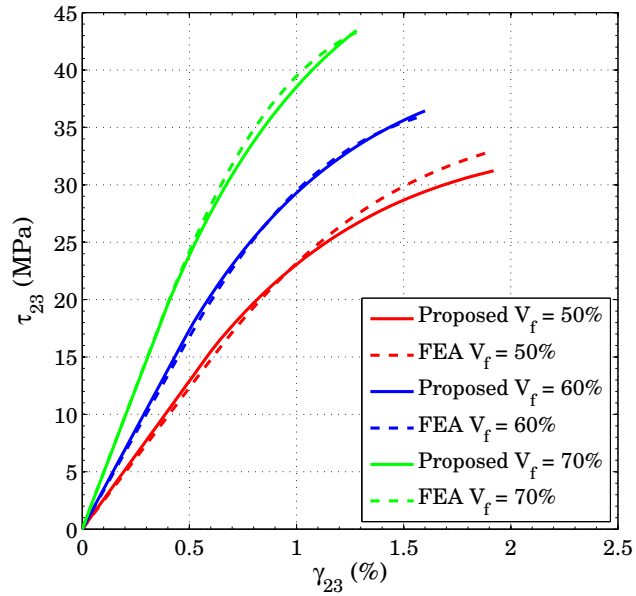


(b) S-2 glass – SC-15 epoxy.

Figure 5.14: The composite effective axial shear stress versus strain response.



(a) IM-7 carbon – SC-15 epoxy.



(b) S-2 glass – SC-15 epoxy.

Figure 5.15: The composite effective transverse shear stress versus strain response.

5.6 Conclusions

In this chapter, a novel, two-scale micromechanics model is established for computing the nonlinear response of a unidirectional composite (or a single fiber tow). Since the results are presented in closed form, the model is suitable to be used in a multiscale computational framework for large scale structural analysis. In the proposed method, the axial tension and axial shear problem are solved through a two-phase CCM, while the transverse tension and transverse shear are studied using an extended three-phase GSCM. The matrix strains are related to the applied composite strains through a 6 by 6 transformation matrix, and the resolved spatial variations of the matrix fields are correlated well with the FEA results.

In the elastic regime, the transverse properties (E_2^c and G_{23}^c) are better predicted using the proposed method than the CCM or M-T method. It has been shown that the proposed method predicts higher transverse properties (E_2^c and G_{23}^c) than the CCM and M-T method, and the difference is more significant for an isotropic constituent fiber than for an orthotropic fiber. It is worth noting that all the theoretical models underestimate the effective moduli E_2^c , G_{12}^c , and G_{23}^c when the fiber volume fraction is greater than 75%. However, this high volume fraction is hard to achieve for a unidirectional fiber-reinforced composite using the current manufacturing technique.

In order to capture the composite nonlinear response, it is further hypothesized that the evolution of the composite nonlinear response is governed by two scalar variables that are defined as the maximum and mean value of the matrix equivalent strain at the fiber-matrix interface, according to Eq. (5.43) and (5.44), respectively. Once the matrix stiffness tensor is degraded through a modified J_2 deformation theory, the matrix secant moduli are subsequently used to compute the composite secant moduli. In particular, E_1^c , ν_{12}^c , K_{23}^c , and G_{23}^c are computed based upon the matrix secant moduli determined from Eq. (5.44), while G_{12}^c is calculated using the matrix secant moduli determined from Eq. (5.43). Therefore, the influence of matrix microdamage at the microscale manifests as the degradation of the effective composite stiffness at the macroscale through a secant moduli approach. Compared with a full 3D FE model, the proposed method provides a good prediction of the composite nonlinear stress versus strain response. The predictive capability of the model has been illustrated through two distinct composite material systems, carbon and glass, for fiber volume fraction varying from 50% to 70%. Since fully analytical solutions are utilized for the subscale micromechanical analysis, the proposed method offers a distinct computational advantage and is suitable for large scale progressive damage

and failure analysis of composite material structures. The implementation of the proposed micromechanics model within the fiber tow in a mesoscale textile composite model is presented in Chapter [VII](#).

CHAPTER VI

Fiber Tow Failure Mechanisms

6.1 Introduction

In Chapter V, it is assumed that the fiber tow pre-peak nonlinear response is attributed to the evolution of matrix microdamage developed at the subscale. Such behavior is captured through a two-scale model, in which the subscale micromechanical analysis at the fiber and matrix level is carried out in closed form. The deterioration of the matrix moduli due to microdamage is manifested as the progressive degradation of the fiber tow stiffness. Therefore, in the pre-peak nonlinear regime, no macroscopic damage criterion is required to drive the damage progression in the fiber tow. However, more catastrophic failure mechanisms have been observed in the experiment, such as fiber tow breakage, tow kinking, and transverse cracking, resulting in a loss of load carrying capability at the macroscale, followed by a post-peak strain softening response in the stress versus strain response. Since the positive definiteness of the tangent stiffness matrix is lost, the aforementioned two-scale model will provide mesh dependent results in a FE framework if no characteristic length is introduced. Moreover, when catastrophic failure modes are observed, the fiber tow no longer can be assumed to be a continuum. As a result, the micromechanics model established in Chapter V is not suitable for modeling the post-peak softening response.

In order to restore mesh objectivity in the post-peak strain softening regime, a traction separation law should be utilized to associate the total energy dissipation during failure progression with the fracture toughness of the material through a characteristic length scale. Discussion on various mesh objective methods is provided in Chapter IV, Section 4.1. It should be noted that multiple failure modes have been observed in fiber tows, depending on the constituent (fiber and matrix) properties and loading conditions. Therefore, performing failure analysis on the fiber and matrix level is motivated. The transverse compression and shear of a unidirectional

fiber-reinforced composite have been studied by Totry et al. [156, 158, 159] through a micromechanics based FE model. Recently, Pineda et al. [116] studied the progressive failure behavior of a unidirectional lamina subjected to transverse tension and compression by implementing the crack band theory within the high-fidelity generalized method of cells model. These micromechanics models provide deep understanding on failure progression of a unidirectional composite, however, they are computationally expensive, and thus are not suitable to be implemented in a multiscale computational model for 3DTCs. Alternatively, phenomenological failure criteria are utilized to predict the macroscopic failure response of a unidirectional composite or a single fiber tow by assuming the existence of a certain type of failure mode. This work was pioneered by Hashin [162], and was later improved and implemented within a FE framework by a number of researchers [112, 113, 114, 115] to demonstrate the predictive capability of this methodology. The use of phenomenological failure criteria offers distinct computational efficiency compared with the micromechanics model, while the physics of various failure mechanisms is preserved.

The purpose of this chapter is to examine the failure modes of a single fiber tow and to perform failure analysis using a mesh objective method. Various failure modes are discussed in Section 6.2, among which the two most critical modes are tow kinking in compression and tow breakage in tension. A micromechanical analysis based upon the two-scale model proposed in Chapter V is carried out to numerically determine the compressive strength of a fiber tow, which is difficult to measure through experiment. Aspects including matrix in-situ property, fiber misalignment, and mesh objectivity are discussed in Section 6.3. The obtained compressive strength is used as the failure initiation criterion for a fiber tow subjected to compression. The progressive failure evolution is modeled within a FE framework as demonstrated in Section 6.4.

6.2 Failure Mechanisms of a Single Fiber Tow

In textile composites, fiber tows are surrounded by a polymer matrix, resulting in a complicated state of stress. Due to the heterogeneity of the microstructure and the complexity of the stress fields, fiber tows exhibit multiple failure modes, including tow kinking in compression, tow breakage in tension, shear banding, and transverse and shear cracking. In some instances, the fiber tow can delaminate from the surrounding matrix at high strain rates, as shown by Pankow et al. [79] through a split Hopkinson pressure bar test. Shear bands are observed when the textile composite is subjected to through-the-thickness compression [2, 79]. Generally, the failure modes of a fiber

tow can be grouped into two types, *fiber failure modes* that include tow breakage in tension and tow kinking in compression, and *matrix failure modes* in which the failure plane is parallel to the fiber direction, as shown in Figure 6.1 and 6.2, respectively. This assumption is the same as the one made by Hashin [162]. In the matrix failure modes, there exist three stress components on the crack plane, σ_{nn} , σ_{nt} , and σ_{nl} , which are the couplings between σ_{22} , σ_{33}, σ_{23} , σ_{12} , and σ_{13} . Thus the matrix failure modes account for cracks growing along the transverse normal, axial shear, and transverse shear directions, predicated on the strength and toughness of the polymer matrix material.

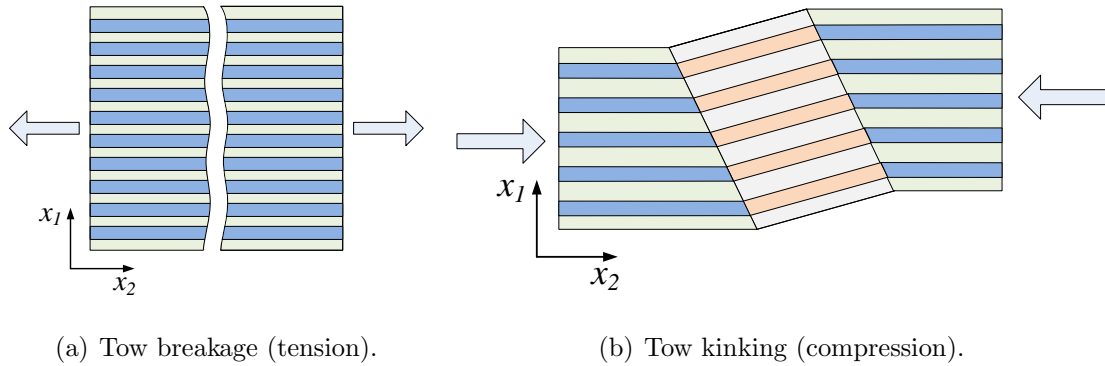


Figure 6.1: Fiber failure modes.

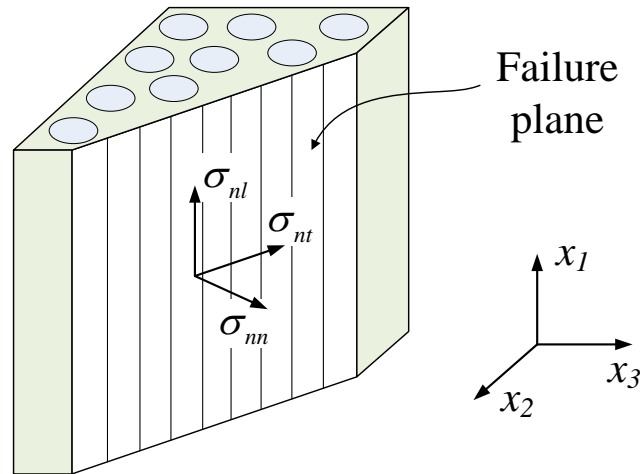


Figure 6.2: Matrix failure mode.

It is evident from experiment that when a 3DTC is subjected to flexural loading, the major failure modes for a fiber tow are the fiber failure modes that include tow

kinking and tensile breakage. Even though the matrix failure mode, such as transverse cracking, has been observed inside the tow during deformation, this matrix dominant failure mode does not lead to a noticeable loss in load carrying capability, and therefore the resulting post-peak strain softening response is ignored. However, it should be noted that the pre-peak nonlinear response due to the evolution of matrix microdamage is correctly modeled using the two-scale model discussed in Chapter V.

6.3 Compressive Failure: A Micromechanical Study on Kink Banding

The response of a single fiber tow, which consists of thousands of fibers embedded in a matrix medium, is equivalent to that of a unidirectional lamina of the same fiber volume fraction. Since it is difficult to experimentally measure the compressive strength of a fiber tow, the purpose of this section is to numerically compute the tow compressive strength through a micromechanics based model. The computed compressive strength is subsequently used as the failure initiation criterion for a single fiber tow subjected to compression. The failure evolution, modeled using the SCA, is presented in Section 6.4.

The compressive strength of a unidirectional fiber-reinforced composite is significantly lower than the tensile strength due to the unique failure characteristic known as kink banding. Since the load carrying capability of the composite has been limited by the compressive strength, kinking has been determined as a strength controlling mechanism of failure. This critical failure mode has been extensively studied by a number of researchers, such as Budiansky and Fleck [84], Kyriakides et al. [85], Schultheisz and Waas [86], Waas and Schultheisz [87], Lee and Waas [88], Basu and Waas [89], Feld et al. [90, 91], and Prabhakar and Waas [59, 92]. The main physical event associated with the kink band formation is the rotation of the fibers in a band within a degrading matrix. The rotation of fibers gives rise to localized shear strains that drive the shear degradation of the matrix material between the fibers. The shear degradation in turn increases the rotation of the fibers, creating a positive feedback loop that culminates in a limit-load type instability. It is important to note that the formation of kink banding is an *evolutionary event* that is driven by the external loading with the evolutionary parameters being the band rotation and the fiber rotation within the bands.

Since kink banding occurs at the fiber-matrix level, it is critical to model the evolution of kinking through a full micromechanics FE model, as presented by Kyri-

akides et al. [85], Vogler et al. [163], Hsu et al. [164], and Yerramalli and Waas [165]. These FE models containing individual fibers and surrounding matrix provide deep understanding on the kink band formation and the subsequent evolution process. On the other hand, a more computationally efficient model on the lamina level has been developed to predict the kinking strength. These models consider the effect of matrix nonlinearity at the microscale as the nonlinear stress versus strain relation at the lamina level, or mesoscale. The lamina nonlinear response can be obtained either from simple tension and shear tests [117], or from a micromechanics based computational model. The nonlinear progression can be dictated through a nonlinear constitutive law, such as Schapery theory [111] or Hill’s anisotropic plasticity theory [166]. The direct implementation of the lamina level nonlinear constitutive relations within a FE framework to predict the kind band formation has been presented by Basu et al. [89], Song et al. [26], and Zhang et al. [31]. The key in these models is to allow the principal orthotropic material axis to rotate as a function of deformation. The rotations of the fibers induce large and localized shear strains, which in turn degrade the matrix shear modulus and allow the fiber to rotate more easily, resulting in a localized band. It is noted that kink banding is not an isolated event, and may also occur in concert with splitting. Lee and Waas [88] were the first to consider the possibility of splitting in conjunction with kink banding, while recent work by Prabhakar and Waas [59, 92] provided a comprehensive account of failure mode interaction between kinking and splitting in the compressive failure of composites.

6.3.1 Micromechanics-Based Two-Scale Model for a Single Fiber Tow

In this research, the two-scale model established in Chapter V is used to predict the kinking strength of a fiber tow. For the macro-scale, lamina-level analysis of a fiber-reinforced laminated structure, or fiber tow-level analysis of a textile composite is conducted by utilizing effective homogenized properties to compute stress and strains in the lamina or fiber tow. Simultaneously, it is intended to carry out the subscale analysis, at the fiber and matrix level, using the micromechanics model presented in Section 5.3, in which the constituent stress and strain fields are provided in closed form. The commercially available finite element software, ABAQUS (version 6.10), is used for the macroscale FEA, and the micromechanics model at the subscale is implemented at each integration point of the macroscale, using a user defined material subroutine, UMAT. This subroutine is called at each integration point at each increment, and the material constitutive law is updated through user-defined options.

6.3.1.1 Fiber Misalignment

In textile composites, the kink bands of interest are formed within a single finite tow composed of individual fibers and matrix. Fibers are assumed to be misaligned with respect to the locus of an undulating tow. Cox et al. [167] used photographic digitization technique to statistically determine the fiber misalignment angles in a tow that ideally was assumed to be straight. However, they also concluded that it was impossible to obtain accurate fiber misalignment angles for severely crimped tows. In this research, two different material systems are presented, which are the layer-to-layer interlock (Albany 2) and the Z-fiber interlock (hybrid architectures). It is obvious that the fiber tows in Albany 2 exhibit more crimpness than that in the hybrid panels. The fiber misalignment angles assumed for Albany 2 and the hybrid textile composites are 1.5° and 1° , respectively, whereas a misalignment angle of $1^\circ - 2^\circ$ has been observed in pre-preg based laminates. It is of interest to experimentally determine the fiber initial misalignment angle in a wavy tow, and this work is left for future study.

6.3.2 In-Situ Matrix Properties

The in-situ response of the polymer matrix material inside a fiber-reinforced composite is different from the virgin resin properties due to curing process. Obtaining the matrix in-situ behavior, especially the shear response, is important to predict the composite compressive strength, as pointed out by Kyriakides [85]. Yerramalli and Waas [168] characterized the matrix in-situ shear response through a torsion test on a unidirectional fiber-reinforced composite cylinder. Later, Ng et al. [169] proposed to determine the lamina in-situ shear response through a tension test on a $\pm 45^\circ$ symmetric laminate in conjunction with a computational micromechanics model.

In this study, the matrix in-situ properties are characterized using the method demonstrated in [169]. Tension tests were carried out on both $\pm 45^\circ$ symmetric IM-7 carbon/SC-15 epoxy laminate and $\pm 45^\circ$ symmetric S-2 glass/SC-15 epoxy laminate. The laminated composites were manufactured using the same curing cycles as the ones used for making the hybrid panels. Tests were performed by Mr. Brian Justusson at the Army Research Laboratory.

The obtained in-situ uniaxial stress versus strain responses of the matrix materials in both carbon and glass laminates are shown in Figure 6.3, and the results are compared against the uniaxial responses of the virgin resin in both tension and compression. It can be immediately concluded that the matrix material behaves differently in

the two types of fiber-reinforced composite, especially in the nonlinear regime. Since the coefficient of thermal expansion of the glass fiber is different from that of the carbon, different residual stresses are generated within the matrix materials in the two types of laminates during the same curing cycles, resulting in a difference in the effective in-situ response. Moreover, the matrix in-situ stress versus strain responses obtained from both laminates show a hardening response in the regime where the virgin resin has already reached the strain to failure. It should be noted that the in-situ matrix is computed from the shear stress versus shear strain of the laminate, in which the presence of the fibers can bridge the evolution of matrix cracking, resulting in a hardening effect. However, it is not evident that the matrix can present the same hardening response when the composite is in compression. The focus of the current study is to compute the compressive strength of a single fiber tow, therefore, this hardening effect is not considered. The matrix nonlinear properties used in the current two-scale model are extracted from the in-situ stress-strain response before the failure strain of the virgin resin is reached. Figure 6.4 shows matrix nonlinear stress-strain responses that are used to compute the compressive strength of the carbon and glass tows through the two-scale model proposed in Chapter V, in which the matrix stiffness tensor is degraded through a modified J_2 deformation theory of plasticity. It should be noted that the two-scale micromechanics based model only considers matrix pre-peak nonlinear response, while the post-peak strain softening behavior is not accounted for. The in-situ nonlinear properties for the matrix inside both carbon and glass tows are summarized in Table 6.1.

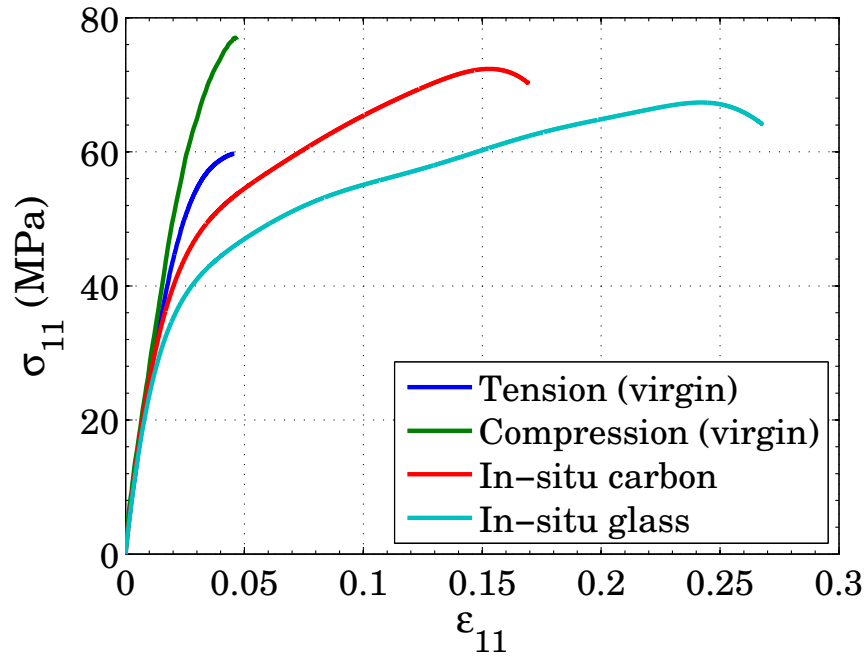


Figure 6.3: Uniaxial responses of SC-15 epoxy resin obtained from the four different tests.

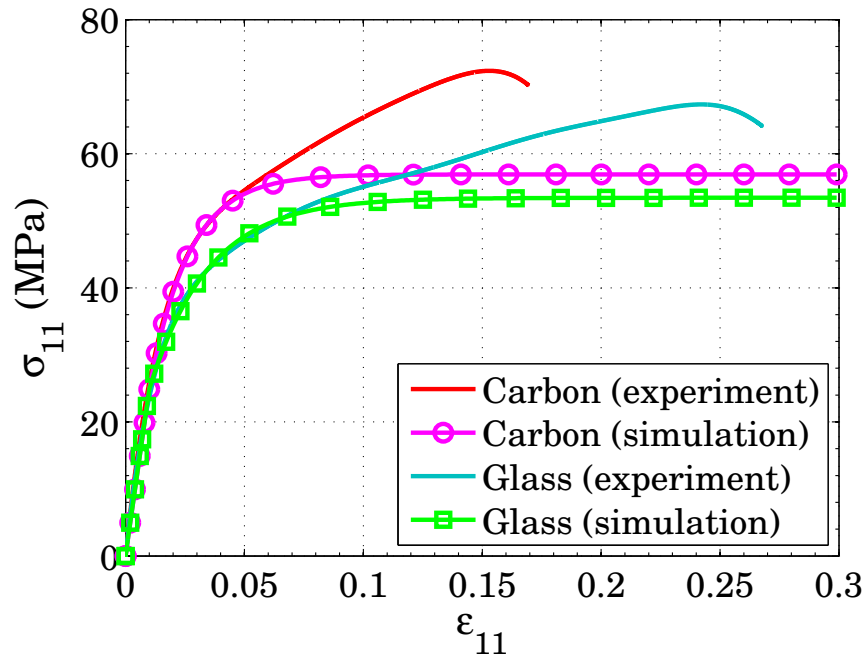


Figure 6.4: The stress versus strain responses of SC-15 epoxy resin used in the two-scale micromechanics model to compute the fiber tow compressive strength.

Table 6.1: Nonlinear matrix properties used in the two-scale micromechanics model to compute the fiber tow compressive strength.

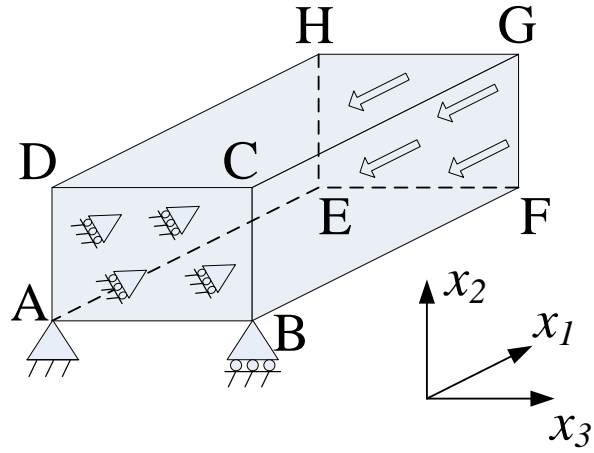
	σ_y^m (MPa)	K_1 (MPa)	K_2
In-Situ Carbon	25	3500	60
In-Situ Glass	25	1700	40

6.3.3 FE Model

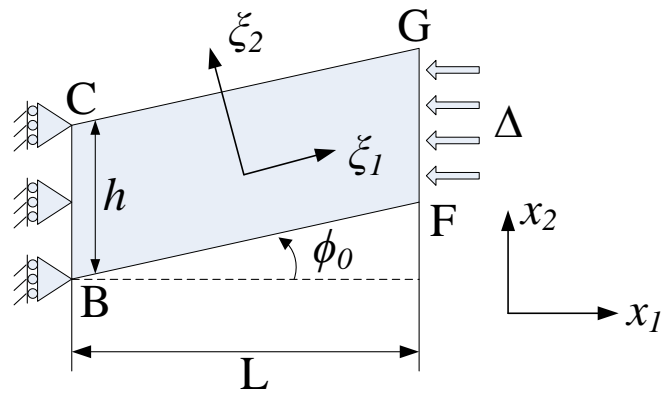
The fiber tow is modeled as a rectangular solid with an initial imperfection angle of ϕ_0 , as schematically shown in Figure 6.5. The axial length (L) is 2.5 mm, and both the thickness (h) and width (b) are 1 mm. The aspect ratio (AR) of the tow, defined by the ratio L/h , is kept to be 2.5 throughout the analysis. To achieve a uniaxial compression loading condition, the left surface ABCD is constrained from moving along the x_1 -direction ($U_1 = 0$), while the right surface EFGH is subjected to a compressive axial displacement Δ ($U_1 = -\Delta$). Point A is additionally fixed in both the x_2 - and x_3 -directions ($U_2 = U_3 = 0$), and point B is constrained in the x_2 -direction ($U_2 = 0$) to prevent rigid body motion. Dynamic implicit analysis in the ABAQUS standard solver is used to capture the post-peak load drop after the kink band formation. 3D linear solid elements C3D8 available in the ABAQUS element library are used throughout the analysis. A mesh sensitivity study is carried out using the three different discretization sizes summarized in Table 6.2.

Table 6.2: Three different mesh sizes used in the mesh sensitivity study to compute the fiber tow compressive strength.

	Mesh Size (mm)	Number of Elements
Mesh A	0.15	833
Mesh B	0.10	2500
Mesh C	0.075	5577



(a) 3D view.



(b) Side view.

Figure 6.5: Boundary conditions for the fiber tow subjected to uniaxial compression with initial fiber misalignment angle ϕ_0 . $\xi_1 - \xi_2$ coordinate system designates the instantaneous material frame where “1” defines the fiber direction.

6.3.4 Results: Compressive Strength

The load-end shortening ($P - \Delta$) data are normalized by using,

$$\sigma_{11} = \frac{P}{A}, \quad \epsilon_{11} = \frac{\Delta}{L} \quad (6.1)$$

where A and L denote the initial cross-sectional area and the axial length, respectively. Figure 6.6 shows the compressive response of the glass fiber tow with a fiber volume fraction of 58% and an imperfection angle of 1° . The mesh objectivity is demonstrated through the normalized stress versus strain responses using the three different mesh sizes. The predicted peak stress is independent of the mesh size, while there is little variation in the post-peak residual stress.

The deformed shapes at the load levels annotated in Figure 6.6 are shown in Figure 6.7, in which the contour plots show the axial shear strains in the instantaneous material frame $\zeta_1 - \zeta_2$, as illustrated in Figure 6.5(b). The initial fiber misalignment initiates localized shear strains that drive the rotation of fibers, which is evident from the rotation of the material instantaneous coordinates. With continued loading, deformation starts to localize within a finite band, in which the rotation of the fibers in turn facilitate the shear degradation, creating a positive feedback loop that culminates in a limit-load type instability. Beyond the peak load, the load drops continuously with additional rotation of the fibers within the band, manifested as a kinked band of fibers.

The post-peak deformed shapes with the three different mesh sizes are shown in Figure 6.8, in which the kink band width is defined as the length of the band that contains highly rotated fibers. The kink band widths for the three different mesh sizes are 0.51 mm, 0.53 mm, and 0.42 mm, respectively. This small difference in the kink band width explains the little variation in the post-peak residual stress shown in Figure 6.6. However, it should be pointed out that the final kink band width is determined by fiber breakage due to bending, which is evident from the experiment as shown in Figure 3.13. Since the fiber breakage is not accounted for in the present two-scale model, the resulting post-peak response may be only used as a reference, and cannot be used for the subsequent failure analysis. Therefore, only the predicted compressive strength from the two-scale model is used as an input in the subsequent failure analysis, and the post-peak response is modeled using the SCA discussed in Section 6.4. Further investigation of the post-kink behavior within a micromechanics viewpoint, including the analysis of matrix failure and fiber breakage, is motivated.

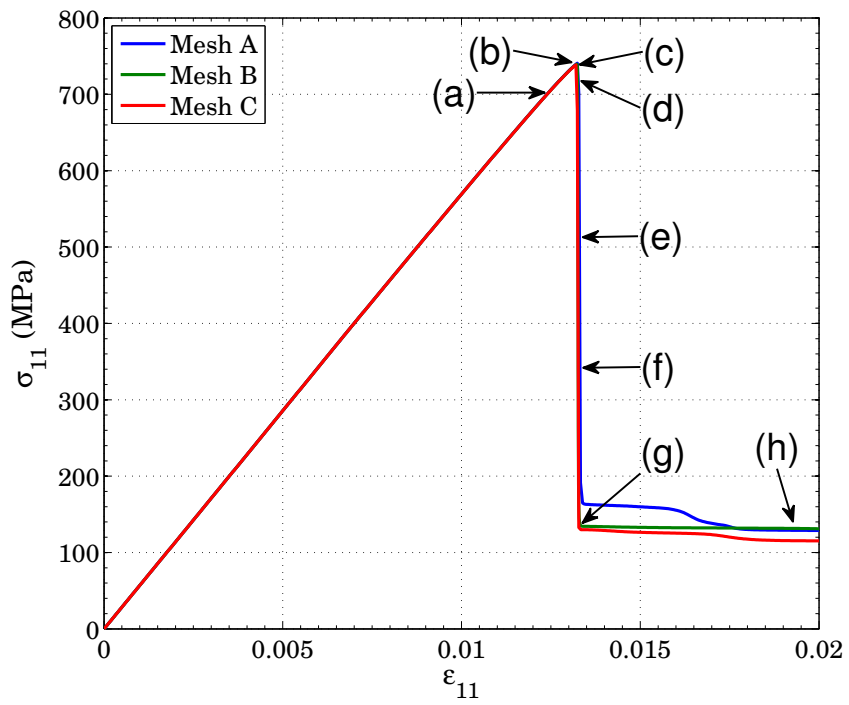


Figure 6.6: Normalized axial stress versus strain response for glass fiber tow using the three different mesh sizes. The initial fiber misalignment angle is 1° , and the fiber volume fraction is 60%.

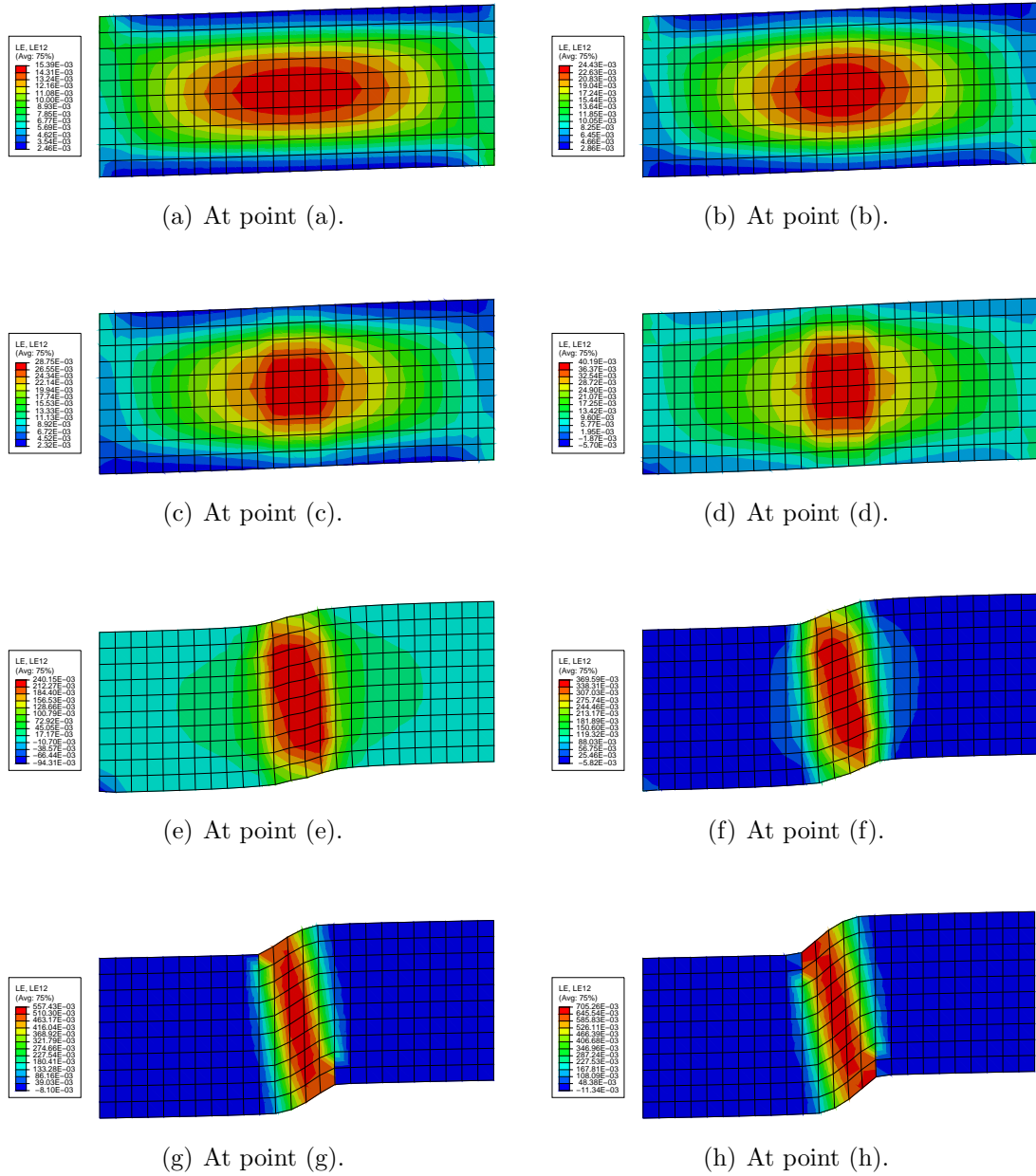
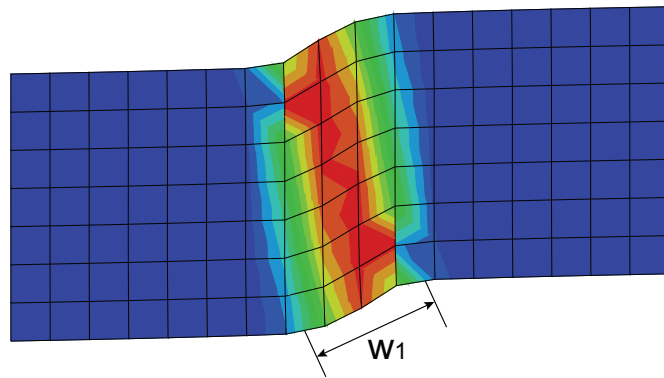
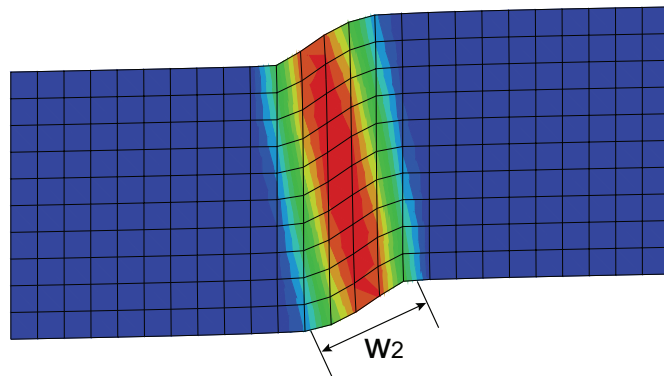


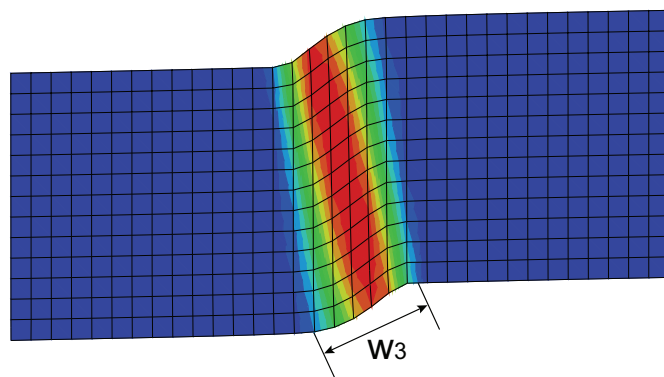
Figure 6.7: Deformed shapes at various loading levels. The contours show the axial shear strain in the instantaneous material frame $\zeta_1 - \zeta_2$ illustrated in Figure 6.5(b).



(a) Mesh A. The bandwidth is 0.51 mm



(b) Mesh B. The bandwidth is 0.43 mm



(c) Mesh C. The bandwidth is 0.42 mm

Figure 6.8: Kink band formation computed using the three different mesh sizes.

Table 6.3: Computed compressive strength for carbon and glass fiber tows using various initial fiber misalignment angles.

Imperfection Angle	Carbon Tow ($V_f = 60\%$)	Glass Tow ($V_f = 58\%$)	Glass Tow ($(V_f = 60\%)$)
1 deg	977 MPa	720 MPa	740 MPa
1.5 deg	762 MPa	579 MPa	592 MPa
2 deg	628 MPa	484 MPa	496 MPa

6.4 Implementation of the SCA to Model the Failure Response of a Single Fiber Tow

The failure response of fiber tows (post-peak softening response) is modeled using the SCA formulated in Section 4.3. The fiber tow is assumed to fail either in compression due to kink banding or in tension due to tow breakage. It is further assumed that when the critical stress (either tension or compression) is reached, the crack plane aligns perpendicular to the fiber direction. Therefore, the crack orientation transformation matrix, \mathbf{N} , defined in Eq. (4.19), is determined by the material orientation rather than the state of stress. The computation of \mathbf{N} using the direction cosines in the material coordinate frame is provided in Appendix A. If the total stress and strain components are ordered as,

$$\boldsymbol{\sigma} = \begin{bmatrix} \sigma_{11} & \sigma_{22} & \sigma_{33} & \sigma_{12} & \sigma_{13} & \sigma_{23} \end{bmatrix}^T \quad (6.2)$$

$$\boldsymbol{\epsilon} = \begin{bmatrix} \epsilon_{11} & \epsilon_{22} & \epsilon_{33} & \gamma_{12} & \gamma_{13} & \gamma_{23} \end{bmatrix}^T \quad (6.3)$$

where “1” designates the fiber direction, \mathbf{N} is simply reduced to,

$$\mathbf{N} = \begin{bmatrix} 1 & 0 & 0 \\ 0 & 0 & 0 \\ 0 & 0 & 0 \\ 0 & 1 & 0 \\ 0 & 0 & 1 \\ 0 & 0 & 0 \end{bmatrix} \quad (6.4)$$

The constitutive relation at the crack interface thus can be written as,

$$\begin{Bmatrix} \sigma_{11}^{cr} \\ \tau_{12}^{cr} \\ \tau_{13}^{cr} \end{Bmatrix} = \begin{bmatrix} D_c & 0 & 0 \\ 0 & G_{c1} & 0 \\ 0 & 0 & G_{c2} \end{bmatrix} \begin{Bmatrix} \epsilon_{12}^{cr} \\ \gamma_{12}^{cr} \\ \gamma_{13}^{cr} \end{Bmatrix} \quad (6.5)$$

where D_c dictates the crack evolution across the crack interface, and G_{c1} and G_{c2} are the crack shear moduli. Since the crack normal is aligned with the fiber direction, D_c is governed by the fiber failure modes that include both tow breakage in tension and tow kinking in compression.

It is worth noting that the tow compressive failure evolution is different from the tensile failure behavior. In the experiment, when the fiber tow fails under compression, the formation of kink band limits the peak load, while additional kink bands are developed with continued deformation, resulting in a “load plateau”. It indicates that even though the fibers are broken within the kink band, load is still transferred through the band, allowing for stress redistribution. On the other hand, when the tensile failure occurs, the material loses the load-carrying capability completely, resulting in a significant load drop as shown in Chapter III. Therefore, a specific traction-separation law is designed to account for the different failure characteristics for tension and compression, as illustrated in Figure 6.9. It is assumed that when failure progresses under compression, the crack interface can carry 50% of the compressive strength in the post-peak regime, while fracture energy is completely dissipated for tensile failure.

Study on the post-kinking response is critical to determine the amount of the load that can be transferred after kink band formation [170]. In the present study, a parametric study is utilized to understand how the failure characteristics of the fiber tow affect the composite macroscopic response, as shown in Chapter VII.

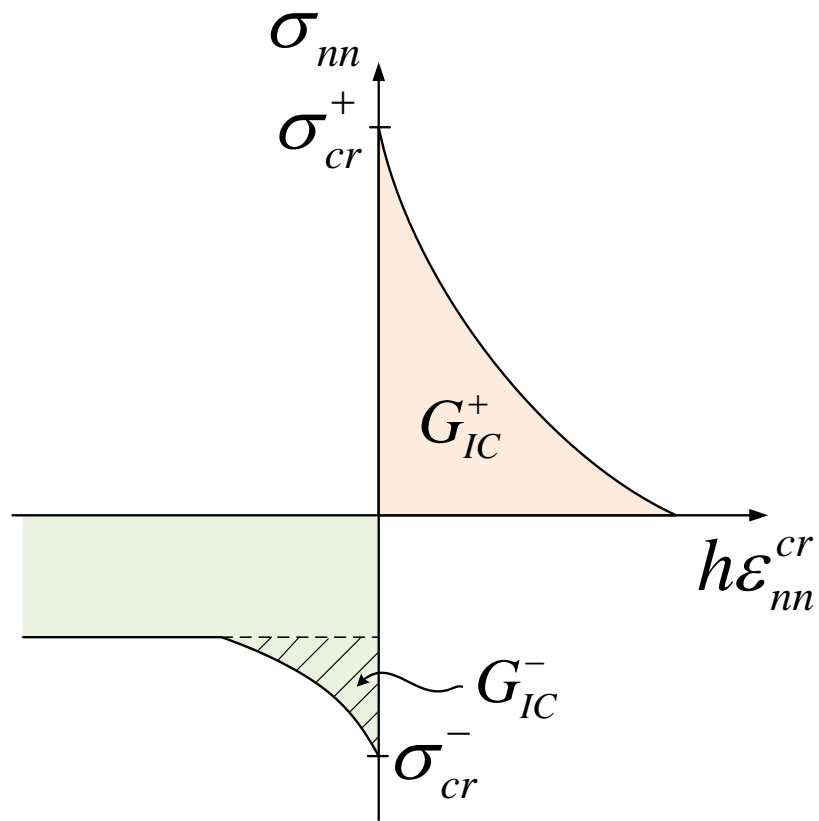


Figure 6.9: Traction-separation law for fiber tows that accounts for the difference between tension and compression.

6.5 Conclusion

Various failure modes that exist in a fiber tow have been studied, among which the fiber failure modes that include tow kinking in compression and tow breakage in tension are considered as the dominant failure modes. Tow kinking is studied through a two-scale micromechanics model, in which the fiber tow is homogenized at the mesoscale, while the subscale micromechanical analysis at the fiber-matrix level is carried out through an analytical approach using the model developed in Chapter V. The computed kinking strength is affected by the matrix in-situ properties and initial fiber misalignment angle, while the result is independent of the mesoscale mesh size. The obtained kinking strength is used as the failure initiation criterion for the fiber tow subjected to compression. The failure evolution is modeled using the SCA with a specific traction-separation law that is designed for the fiber tow. The failure plane is assumed to be perpendicular to the fiber direction for both tension and compression. It is further assumed that when the tow fails in compression due to kinking, the crack interface can carry 50% of the compressive strength after the kink band formation. On the other hand, if the fiber tow fails in tension, the fracture energy due to tow tensile breakage is released completely. The implementation of the fiber tow failure response in the multiscale model of 3DTCs is provided in Chapter VII.

CHAPTER VII

Mechanics Based Multiscale Modeling of Progressive Damage and Failure of 3D Woven Composites

7.1 Introduction

Textile composites have demonstrated enhanced mechanical performance and tailored properties achieved by optimizing textile architecture and types of constituent fibers [5, 4, 67, 69, 171]. Early studies on this class of materials are primarily focused on the prediction of composite homogenized properties based upon textile architecture using simplified analytical methods [8, 9, 10, 11]. Even though the effect of geometry imperfections arising from the manufacturing process can be accounted for in the analytical model developed by Pankow et al. [12], this model is only focused on the elastic response and does not consider any failure mechanisms. Textile composites exhibit progressive damage and failure behavior, accompanied by various modes of failure, including fiber tow kinking in compression, tow breakage in tension, and matrix cracking, as shown in Chapter III. The damage and failure developed in the constituents (tows and matrix) manifests as progressive degradation of composite stiffness, resulting in a macroscopically nonlinear stress versus strain response. Therefore, in order to predict the strength of textile composites, it is motivated to develop a textile architecture based model that incorporates damage and failure mechanics for the constituent materials.

One of the difficulties in the modeling of textile composites lies in their complicated internal microstructure. A dry textile preform is composed of fiber tows that are either woven or braided to each other according to the predefined specification. The preform is subsequently infused with epoxy resin using the VARTM process, as discussed in Chapter II. In this fabrication process, atmospheric pressure is applied on the textile

perform through the plastic covering, while the mold pressure is exerted on the other side, forcing the fiber tows to settle and find new positions that are different from the predesigned one. In 2D textile composites with multiple layers of textile preforms stacked on top of each other, these layers can penetrate into each other under the pressure, resulting in a phenomenon known as *nesting* [1]. It has been pointed out by Lomov et al. [172] and Zhang et al. [31] that this unintended geometrical deviation of textile architecture can play a key role on the mechanical properties of this type of material. Therefore, it is important to obtain the geometry characteristics of the as-fabricated composite to establish a predictive textile architecture based model.

Characterization of the actual geometry of textile reinforcements is usually carried out using an optical microscope by inspecting the cross sections of a composite panel [11, 173, 31]. The internal structural variation of textile architecture has been studied by Desplentere et al. [174] through an X-ray microCT. The measured fabric geometric parameters are directly used as inputs to a “virtual” textile model created using a textile software such as WiseTex [33]. Although modeling the exact fabric geometry is possible using a computed-aided drawing software, the model usually encounters difficulty in the subsequent FEA if the fiber tows are interacting with each other [2]. In some instance, the model tends to contain a large number of elements caused by the irregular geometry of the matrix material sitting between the tows, and therefore it is not suitable for large scale structural analysis.

Textile composites exhibit periodicity in their microstructure, allowing them to be modeled using a collection of RUCs. An efficient computational model for textile composites requires a “minimum” region to be modeled with appropriately applied boundary conditions. Whitcomb et al. [175] exploited the periodicity and symmetries existing in a textile composite, and derived the boundary conditions for the RUC of a eight-harness stain weave composite. The technique was later generalized for materials with periodic microstructure, including both 2D and 3D textile composites [176]. The concept of “equivalent subcell” is used for the smallest region that need to be modeled in a textile architecture based model. However, it should be pointed out that in the analysis of textile composites, the minimum size of the RUC needs to be determined through a convergence study such that the predicted composite macroscopic response remains unchanged beyond a certain RUC size. The RUC should not only represent the geometric characteristics of textile architecture, but also have to capture all the macroscopic behavior, including linear, nonlinear, and failure responses.

Mesoscale FE models, in which the textile composite is modeled using a collection

of RUCs that is composed of fiber tows and surrounding matrix, have been widely adopted to determine the composite macroscopic properties, stress and strain fields in the constituents, location of damage initiation, and damage progression. When damage occurs, the constituent properties are degraded based upon the observed damage modes via a CDM approach [34, 177, 35, 36]. Ivanov et al. [37] investigated the damage and failure behavior of a triaxially braided textile composite (TBTC) subject to tension. In their mesoscale FE model, Puck’s failure criterion [113] is utilized to predict the damage initiation and crack orientation for matrix intra-yarn cracks. The progressive deterioration of the yarn stiffness is modeled using the degradation scheme of Murakami-Ohno [178] in conjunction with the damage evolution law of Ladeveze [179] based upon the average stress state of the yarns. The effect of matrix cracking on the compressive strength of a 2D triaxially braided composite has been studied by Song et al. ([27]).

Although CDM is able to capture damage and failure in a composite through a set of scalar variables, this method is pathologically mesh dependent since no characteristic length scale is associated with damage evolution. Discussion on various mesh objective methods is provided in Chapter IV. Moreover, each damage variable used in CDM is associated with a unique damage mode that needs to be determined from a specifically designed experiment. Characterization of these variables is required for each material system with different textile architecture and loading conditions. In addition, it is difficult to measure these damage variables for the constituents within the textile composite, for example, the damage progression inside a fiber tow. Thus, it is motivated to develop a computation model at the microscale (at the fiber-matrix level) to predict the damage and failure initiation at the fiber tow level. A parametric study on damage variables is also expected to understand how the damage developed at the constituent level affects the composite macroscopic response.

The focus of this chapter is to establish a mechanics based multiscale computational model for 3DTCs subjected to three-point bending, including both quasi-static and dynamic responses. The model is developed based upon a global-local modeling strategy, in which the influence of textile architecture is incorporated in a mesoscale model that contains detailed geometric information for the fiber tows and matrix, while the composite is homogenized at the macroscale. Details including the construction of the multiscale model and implementation of constitutive relations that encompass damage and failure are provided in Section 7.2. The predictive capability of the proposed model is illustrated by comparing the computational results with the experiments, including the load-deflection response and progressive failure

characteristics, such as matrix cracking, tow kinking, and tow tensile fracture. The computational results for the layer-to-layer architecture (Albany 2) are presented in Section 7.3. The progressive failure responses of hybrid 3DTCs are presented in Section 7.4, including both quasi-static and dynamic analysis.

7.2 Multiscale Modeling Framework

The hierarchical nature of textile composites enables them to be differentiated into three different levels, each of which is associated with a characteristic length scale. Generally, the *microscale* is referred to the fibers and matrix within the fiber tows, while structural level analysis of textile composites is considered as the *macroscale*. The scale in-between is the *mesoscale*, which defines the internal structures of textile reinforcements on the tow level using a set of RUCs. The analysis at the microscale provides the constitutive relations of fiber tows (including both linear and nonlinear analysis) that are subsequently used in the mesoscale analysis. The mesoscale model, which accounts for textile architecture and incorporates damage constitutive laws and failure criteria, is able to determine the damage and failure characteristics that finally manifest as the deterioration of composite homogenized mechanical properties at the macroscale.

7.2.1 Global-Local Hybrid Finite Element Model

The computational model developed in this work is focused on the flexural response of 3DTCs, predominately under three-point bending, including both quasi-static and dynamic responses. It has been shown in the experiments (discussed in Chapter III) that the primary damage modes, including fiber tow kinking, tow breakage, and matrix cracking, are observed nearly in the region under the loading point. Thus, it is suitable to model such a response through a global-local modeling framework, in which a textile architecture based model is utilized for the area in the vicinity of the loading point, while a homogenized model is employed for the regions that are far away from the “hot spots” where no damage event is observed.

Figure 7.1 illustrates the three hierarchical levels involved in the proposed global-local multiscale model for 3DTCs. In the macroscale model, the composite beam is homogenized as a linear elastic orthotropic solid since no damage occurs. The computation of the composite effective properties is provided in Section 7.2.2. The textile architecture based model is considered as a mesoscale model that contains a collection of RUCs composed of fiber tows embedded in a matrix medium. The construction of

the mesoscale model is discussed in Section 7.2.3. The fiber tow constitutive relations (used in the mesoscale model) are determined from a subsequent micromechanical analysis that is carried out at the fiber level, referred to as the microscale. The constituent properties including the damage and failure characteristics for the matrix and constituent tows are summarized in Section 7.2.4 and Section 7.2.5, respectively. The connection between the models of different scales and the boundary conditions for both quasi-static and dynamic analysis are presented in Section 7.2.6.

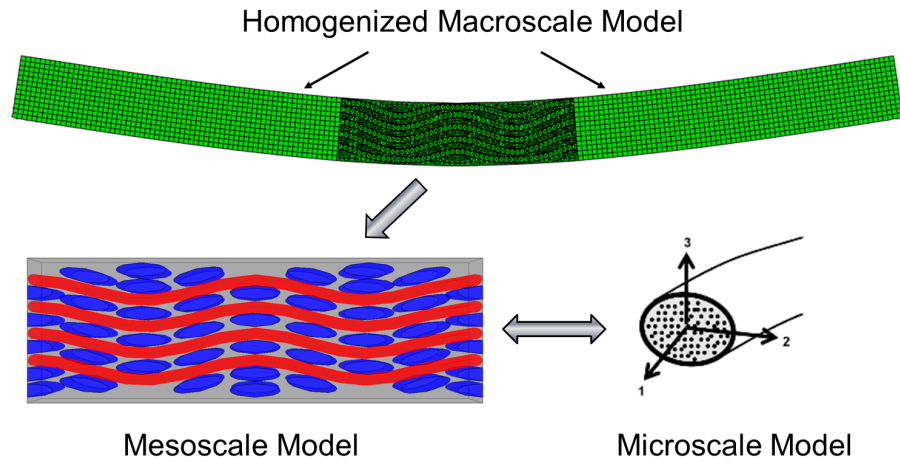


Figure 7.1: Illustration of the three different scales used in the proposed global-local modeling framework.

It should be mentioned that the progressive failure analysis is coupled with the constituent post-peak softening behavior, resulting in unstable numerical solutions in a FE framework. Even though the specimen is deformed under a quasi-static loading condition, the development of failure modes, for example, fiber tow kinking, can cause a local instability or “snap-through” phenomenon that leads to convergence issues in a static implicit analysis. Sometimes an implicit dynamic analysis scheme can be utilized for computing the softening response in a quasi-static system by introducing inertia effects to regularize the unstable behavior [180]. In Chapter IV, the post-strain softening response for a monolithic matrix material is computed using the dynamic implicit solver available in the commercial finite element codes ABAQUS. However, when multiple damage and failure modes are developed in the FE model, the implicit solvers usually encounter convergence difficulty, resulting in small time increment at each iteration step. In this instance, an explicit analysis offers a computational advan-

tage since each increment is computed using an explicit central-difference integration rule without solving a set of simultaneous equations that are required for the implicit solvers. Although the explicit analysis is time intensive, the computational time can be reduced significantly owing to the recent advances in the parallel computing technique. However, it should be noted that the implicit solver usually provides accurate and reliable results since the convergence is checked at each time increment. In the present study, the quasi-static analysis was performed using both the implicit and the explicit solvers available in ABAQUS, while the drop tower simulation is carried out using the explicit scheme.

7.2.2 Determination of the Homogenized Composite Properties

In the macroscale model, the composite beam is homogenized as an orthotropic solid, the properties of which can be characterized through nine material constants. In this research, an analytical model proposed by Quek et al. [11] is employed to compute the composite effective properties based upon the constituent (fiber and matrix) properties, fiber volume fractions within the fiber tows, tow orientations, and volume fraction of each constituent (warp tows, weft tows, Z-fibers, and matrix). The RUC of Albany2 can be broken into three constituents, including the warp tows, weft tows, and matrix; while the hybrid composite contains an additional constituent of Z-fibers, as shown in Figure 7.3. The key assumption of the proposed model is that all the constituents, including the fiber tows and surrounding matrix, carry the same amount of strains during deformation. Thus, the homogenized composite properties are computed based upon the volume average of the constituent properties. The accuracy of this model on the prediction of the in-plane properties of a 2D triaxially braided textile composite has been evaluated in Ref. [11].

Details of the computation of the composite orthotropic properties are documented in Appendix F. The material constants for Albany 2 and the thin unsymmetric hybrid composite are summarized in Table 7.1. The subscripts “x”, “y”, and “z” designate the axes illustrated in Figure 7.2 and 7.3 for Albany 2 and the thin unsymmetric hybrid panel respectively. The warp and weft Young’s moduli (E_x and E_z respectively) of Albany2 obtained from the tension tests are $13.28 \pm 4.23\%$ GPa and $19.76 \pm 1.93\%$ GPa, respectively [181]. The experimental values of the warp and weft Young’s moduli for the thin unsymmetric specimen are $31.78 \pm 11.34\%$ GPa and $34.47 \pm 3.58\%$ GPa, respectively [22]. Overall, the elastic moduli computed using the proposed method are correlated well with the experiment.

Table 7.1: Homogeneous properties of the macroscale model. x , y , and z designate the axes shown in Figure 7.2 for Albany 2 and Figure 7.3 for the thin unsymmetric hybrid panel.

	Albany 2	Thin Unsymmetric
E_x (GPa)	16.7	31.2
E_y (GPa)	6.87	6.80
E_z (GPa)	19.1	36.9
ν_{xz}	0.07	0.04
ν_{xy}	0.45	0.43
ν_{zy}	0.49	0.42
G_{xz}	2.32	1.98
G_{xy}	2.80	2.15
G_{zy}	3.27	2.15

7.2.3 Construction of the Mesoscale Model

The mesoscale model is a collection of RUCs that are composed of fiber tows embedded in a polymer matrix medium. The model is created using the measured fiber tow geometries obtained from the microscopic characterization discussed in Section 2.5. The geometric information for Albany 2 and the thin unsymmetric hybrid composite are summarized in Table 2.2 and Table 2.3, respectively.

As discussed in Chapter II, the textile geometric imperfections arising from the curing and consolidation process cause the rotations of fiber tows and interactions between each other. Modeling the full repeated textile pattern requires advanced topology techniques and may result in meshing difficulties. At this point two different mesoscale models are proposed with a focus on each axial geometry. In each model only a unit width of the fiber tows were modeled along its axial direction, as illustrated in Figure 7.2. The tows running along the width (or along the out-of-plane direction) are assumed to be straight. 3D linear tetrahedron solid elements are used in the mesoscale model, whereas the homogenous model is meshed using 3D linear brick elements.

The hybrid Z-fiber architecture has a series of rigid warp and weft tows, therefore, it experiences less geometric distortion than those in the layer-to-layer architecture. Figure 7.3 shows the RUC for the thin unsymmetric hybrid composite, which is created based upon the measured tow geometries presented in Table 2.3. The corners

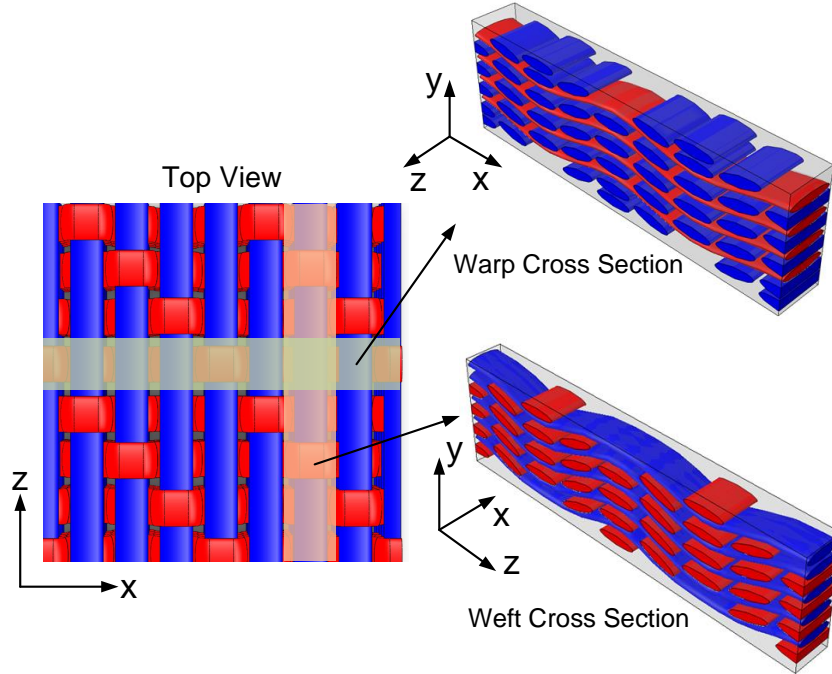
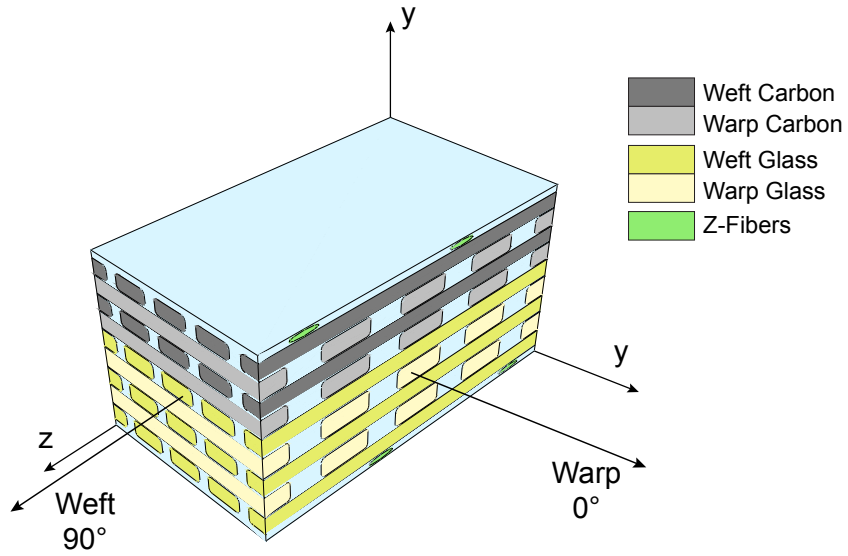


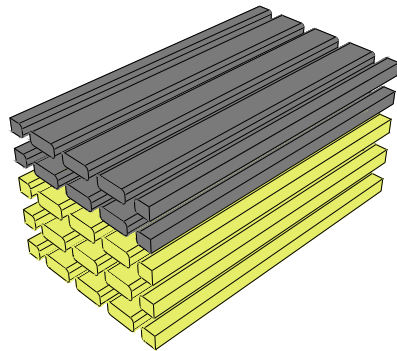
Figure 7.2: Mesoscale model for Albany 2. In each model, only a unit width of fiber tows are modeled along its axial direction. The tows running along the width are assumed to be straight.

of each fiber tow is rounded to eliminate stress concentrations resulting from the geometric singularity. Moreover, the warp and weft layers are separated by a thin layer of matrix of 0.05 mm in thickness to allow for correct load transfer between the fiber tows [2]. The Z-fibers are inserted in-between the warp tows and drawn from top to bottom following a zig-zag weaving path. The mesoscale model for the thin unsymmetric hybrid 3DTC was first created in a similar way of Albany 2 that only a unit width of the axial fiber tow is modeled, named as Model A, as shown in Figure 7.4(a). A size-effect study was carried out by doubling the width of Model A and increasing the length by 4.3 mm, named as Model B, as shown in Figure 7.4(b).

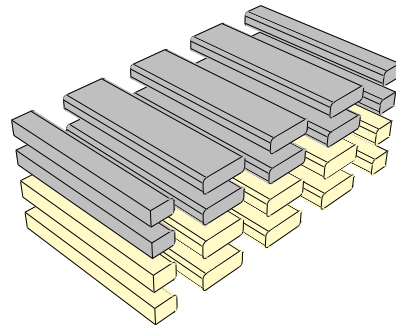
In the global-local modeling framework, it is critical to determine the size of the RUCs used in the mesoscale model through a convergence study, in which the size of the mesoscale model is kept as a parameter. A critical size is determined based upon the fact that the computed flexural response remains unchanged beyond a certain size of the RUCs. The determination of the critical size of the mesoscale textile architecture model is important to ensure accurate strength prediction with minimal computational effort. In the present study, the length of the mesoscale for Albany 2 is 40 mm, and that for the thin unsymmetric hybrid composite is 25.8 mm. The size has been chosen so that the damage and failure modes can be fully developed within in the



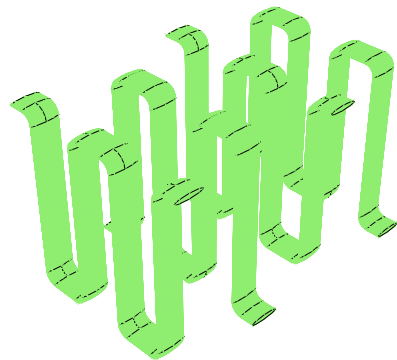
(a) Thin unsymmetric hybrid 3DTC architecture.



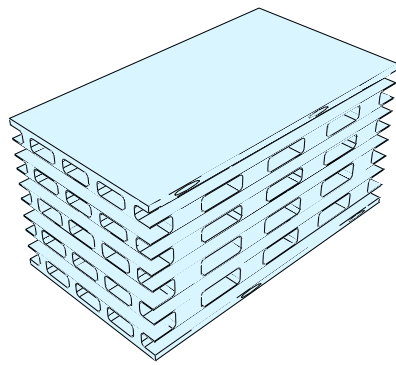
(b) Weft tows.



(c) Warp tows.

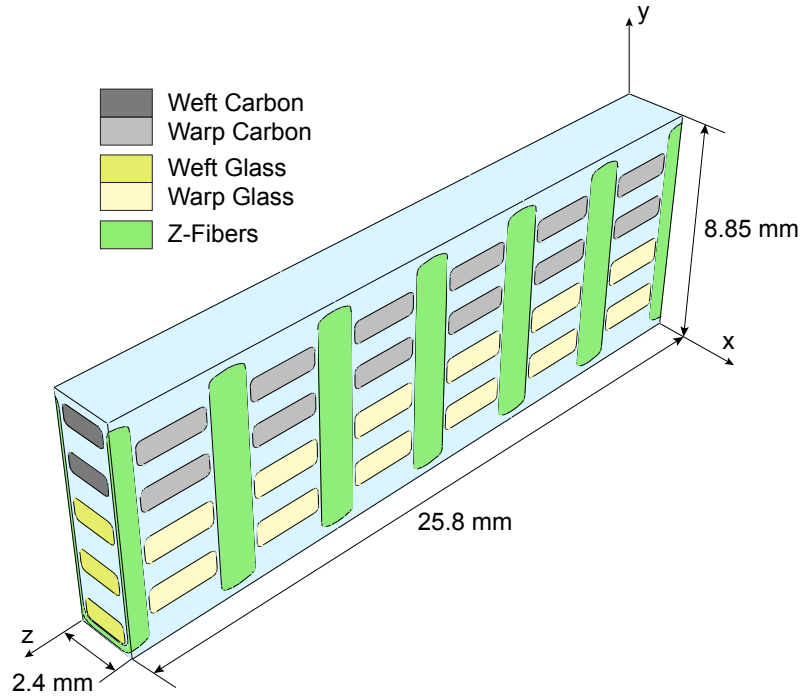


(d) Z-fibers.

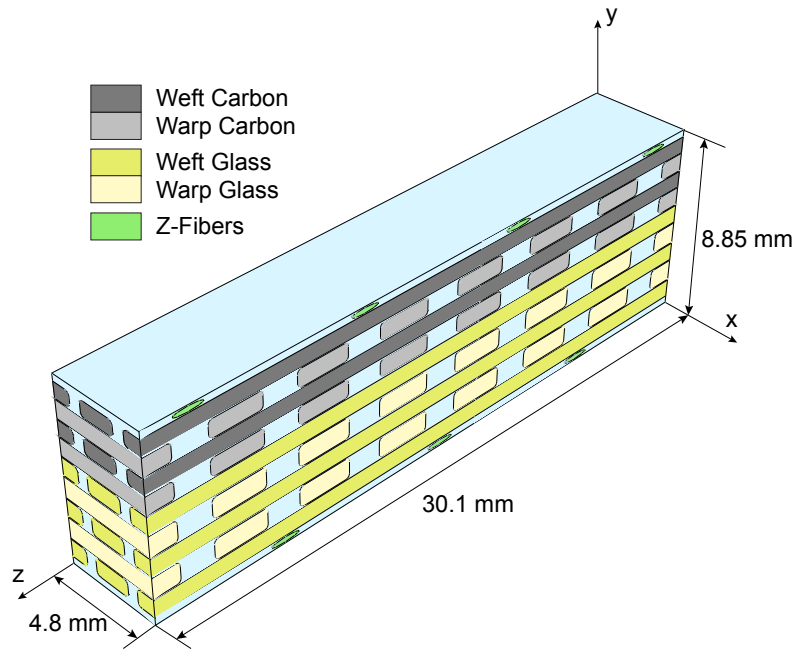


(e) Matrix.

Figure 7.3: RUC for thin unsymmetric hybrid 3DTC. The RUC is broken down into various constituents.



(a) Model A. One fiber tow is modeled in the widthwise direction (x -direction).



(b) Model B. Two fiber tows are modeled in the widthwise direction (x -direction).

Figure 7.4: Mesoscale models for thin unsymmetric hybrid 3DTC. The two models are different in width and length.

RUCs and the resulting load-displacement response in the elastic regime is unaffected beyond the selected size. A systematic study on the size effect of the mesoscale model on the predicted failure response is recommended for further investigation.

7.2.4 Matrix Constitutive Relations Used in the Mesoscale Model

The key in the proposed mesoscale model is to implement damage and failure constitutive relations for the fiber tows and surrounding polymer matrix. In the mesoscale model, the matrix in-between the fiber tows is considered as a damaging-fracture solid. The modeling strategy for such a nonlinear material is presented in Chapter IV. The pre-peak nonlinear stress versus strain response, which is attributed to matrix microdamage, is modeled using a modified J_2 deformation theory of plasticity through a secant moduli approach. The pre-peak nonlinear response is governed by the yield stress, σ_y , and two material constants, K_1 , and K_2 , as presented in Section 4.2.

The evolution of matrix microdamage results in macroscopic cracking, followed by a post-peak strain softening behavior, which is characterized as a failure mechanism due to the loss of the positive definiteness of the material tangent stiffness tensor. The progression of matrix macroscopic cracking is modeled using the SCA (formulated in Section 4.3), in which the cracks are assumed to be smeared out over a certain width within a finite element. In Chapter IV, both tension and compression failure modes have been formulated, however, only tensile cracking is considered in this chapter. Therefore, the cracks are initiated based on the maximum principal stress, and grow under pure mode-I condition with the orientations aligned in the plane of the maximum principal stress. In the SCA, the mesh objectivity is restored by relating the post-peak strain softening response to a traction-separation law through a characteristic element length. Thus, the total amount of energy dissipated during failure in a continuum element can be equated to the fracture toughness defined for a cohesive element of the same size. The initiation of matrix tensile cracking is determined by the critical stress, σ_{cr} , while the failure evolution is governed by the mode-I fracture toughness, G_{IC} . The matrix nonlinear properties and failure characteristics used in the mesoscale FE model are summarized in Table 7.2

7.2.5 Fiber Tow Constitutive Relations Used in the Mesoscale Model

In the mesoscale model, the fiber tows are homogenized as a transversely isotropic nonlinear solid, while at the microscale each fiber tow is considered as a heterogeneous

Table 7.2: Matrix nonlinear properties and failure characteristics used in the mesoscale FE model.

σ_y (MPa)	K_1 (MPa)	K_2 –	σ_{cr} (MPa)	G_{IC} (N/mm)
25	1700	40	50	1.5

material that is composed of thousands of individual fibers. The evolution of matrix microdamage developed at the microscale manifests as progressive degradation of the fiber tow stiffness, resulting in a pre-prek nonlinear stress versus strain response at the mesoscale. In the proposed multiscale modeling scheme, such a progressive damage behavior of fiber tows is captured using a novel, two-scale, micromechanics based model that is established in Chapter V. In the proposed scheme, the mesoscale tow-level analysis is conducted by utilizing the effective homogenized properties to compute the local fields in each fiber tow. Simultaneously, it is intended to carry out a micromechanical analysis, at the fiber and matrix level, using the micromechanics model presented in Section 5.3, in which the constituent stress and strain fields are provided in closed form. The commercially available finite element software, ABAQUS (version 6.12), is used for the mesoscale FE model, and the micromechanics model at the subscale is implemented at each integration point of the mesoscale model, using a user defined material subroutine (UMAT for implicit analysis or VUMAT for explicit analysis). This subroutine is called at each integration point at each increment, and the material constitutive law is updated through user-defined options.

At the start of each increment, the fiber tow states (stress, strain, and solution-dependent state variables) from the previous equilibrium step and the strain increments in the current step are passed into the UMAT or VUMAT through the ABAQUS solver. In the n th increment, the total strain, ϵ_{ij}^n , is calculated by adding the current strain increment, $d\epsilon_{ij}^n$, to the strain in the previous step, ϵ_{ij}^{n-1} , as $\epsilon_{ij}^n = \epsilon_{ij}^{n-1} + d\epsilon_{ij}^n$. In the two-scale modeling scheme, the strains at each integration point in the FE model, are applied to the subscale micromechanics model. These integration point strains can be treated as the effective tow strains that are applied on a discrete fiber-matrix microstructure. The constituent strain fields therefore can be computed in closed form by knowing the globally applied strains using the micromechanics model presented in Section 5.3.

It should be noted that the resulting matrix strain fields through the micromechanical analysis vary in space, as shown in Figure 5.6–5.9. In Chapter V, it is

hypothesized that the fiber tow nonlinear behavior is governed by two scalar variables, V_{max} and V_{avg} , which are defined based upon the maximum and average value of the matrix equivalent strain at the fiber-matrix interface, respectively, as shown in Eq. (5.42) and (5.43). In addition, a weight function, V_{weight} , is constructed to account for the effects of fiber-to-matrix stiffness ratio and fiber volume fractions. In the present fiber tow system, since the fiber is significantly stiffer than the matrix material with a fiber volume fraction around 60% , it is reasonable to assume that $V_{weight} \approx V_{max}$.

Once the matrix equivalent strain is resolved, the matrix stiffness tensor is degraded as a secant solid according to the nonlinear damage model presented in Section 4.2. It is further hypothesized that the matrix secant moduli calculated using V_{max} are subsequently used to compute the tow effective secant moduli, E_1^t , ν_{12}^t , K_{23}^t , and G_{23}^t ; whereas the matrix secant moduli determined from V_{avg} is used to compute G_{12}^t . Consequently, if matrix microdamage occurs, the stiffness of the subscale microstructure is reduced based upon the proposed secant moduli approach. The subscale stiffness tensors are subsequently used to update the fiber tow stiffness and stresses in the mesoscale FE model.

The elastic properties of the constituent fibers and matrix are provided in Table 7.3, and the resulting elastic properties of the fiber tows computed using the proposed micromechanics model are presented in Table 7.4. It has been mentioned in Section 6.3.2 that the matrix behaves differently inside the different constituent fibers, especially in the nonlinear regime. Thus, different matrix nonlinear properties are used for the carbon and glass tows in the micromechanics model, as summarized in Table 7.5.

Table 7.3: Elastic properties of the fibers and matrix used in the FE model.

	E_1 (GPa)	E_2 (GPa)	ν_{12} –	G_{12} (GPa)	G_{23} (GPa)
IM7 Carbon	276.0	15.0	0.279	12.0	5.02
S-2 Glass	93.8		0.23	38.1	
Kevlar	112		0.36	41.2	
SC-15 Matrix	2.487		0.35	0.921	

The fracture model of a single fiber tow is established in Chapter VI. In the present study, the fiber tow is assumed to fail either in compression due to kink banding or

Table 7.4: Elastic properties of fiber tows computed using the proposed micromechanics model.

	V_f (%)	E_1 (GPa)	E_2 (GPa)	ν_{12} –	G_{12} (GPa)	G_{23} (GPa)
Glass Tow (Albany 2)	60	57.29	9.558	0.27	3.380	3.416
Glass Tow (Hybrid)	58	55.46	9.025	0.27	3.197	3.213
Carbon Tow (Hybrid)	60	166.6	6.478	0.30	2.873	2.186
Kevlar Tow (Hybrid)	68	68.20	9.678	0.36	3.401	3.442

Table 7.5: Matrix nonlinear properties used in the two-scale micromechanics model for modeling the pre-peak nonlinear response of the fiber tows.

	σ_y (MPa)	K_1 (MPa)	K_2 –
Carbon Tow	25	3500	60
Glass Tow	25	1700	40

in tension due to tow breakage. The failure evolution is modeled using the SCA with a specifically designed traction-separation law to account for the different failure responses shown in tension and compression. In particular, when the tow fails in compression due to kinking, it is assumed that the crack interface can carry 50% of the compressive strength after the kink band formation, whereas, if the fiber tow fails in tension, the fracture energy due to tow tensile breakage is released completely.

The procedure for computing the fiber tow compressive strength is presented in Section 6.3. It is further assumed that the fiber misalignment angles for Albany 2 and hybrid 3DTCs are 1.5° and 1° , respectively. The tensile strengths of the carbon and glass tows are taken from Refs. [76] and [77] respectively. The tow fracture toughness, including both tension and compression failure, is difficult to be measure. In this instance, a parametric study is used to understand the tow failure response. Table 7.6 summarizes the failure characteristics of the constituent tows used in this study.

Table 7.6: Failure characteristics of the constituent tows.

			σ_{cr} (MPa)	G_{IC} (N/mm)
Albany 2	Glass	Tension	1700 – 1900	40 – 45
		Compression	592	2 – 4
Hybrid	Glass	Tension	1700 – 1900	40 – 45
		Compression	720	2 – 4
	Carbon	Tension	1700 – 1900	20 – 60
		Compression	977	2 – 4

7.2.6 Boundary Conditions and Analysis Procedures

Figure 7.5 illustrates the boundary conditions of the global-local FEA model that is utilized to compute the flexural response of 3DTCs subject to three-point bending. The region under the loading point is modeled using a textile architecture based mesoscale model, while the rest of the beam is homogenized at the macroscale. The connection between the mesoscale and macroscale model is enforced by requiring displacement continuities between the two regions across the common boundaries. In order to account for the geometric distortion of the layer-by-layer woven fabric and shorten the computational time, only a narrow width of the specimen is modeled in the mesoscale model. Therefore, it is assumed that the flexural response is uniform through the width of the specimen, and the surface ABCD and EFGH are constrained in the z -direction ($U_3 = 0$) to prevent the out-of-plane movement. Theoretically one of the outer surface (either surface ABCD or surface EFGH) should remain free, however, when multiple failure modes developed during deformation, the free surface of the mesoscale model tends to bend out of the plane, resulting in an instability of the global structure. It should be noted that the applied out-of-plane boundary conditions are much like a plane-strain assumption for a beam. Since the 3DTC investigated in this research is highly orthotropic with Poisson's ratio ν_{xz} close to zero (see Table 7.1), such an assumption should have little impact on the global bending stiffness.

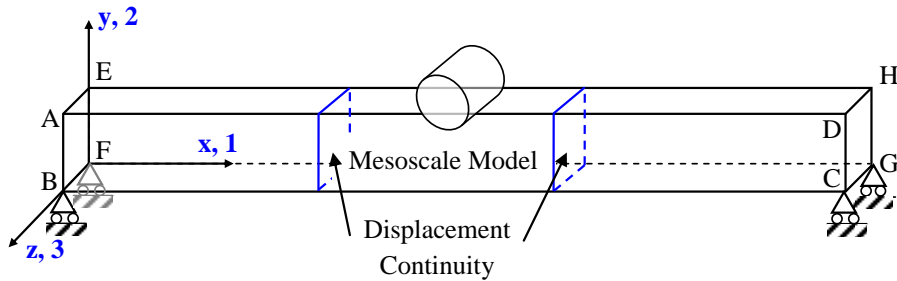


Figure 7.5: Boundary conditions for the 3DTC subjected to three-point bending. The flexural response is modeled using a global-local FE model.

In the quasi-static analysis, the top roller is modeled as a rigid body with enforced displacement along the y -direction. Both the left bottom edge BF and the right bottom edge CG are fixed in the y - and z -directions ($U_2 = U_3 = 0$) to achieve a three-point bend loading condition. The interaction between the roller and the top

surface of the specimen is modeled using a general contact algorithm available in the ABAQUS/Explicit analysis. A “hard” contact is assigned for the interface to prevent the penetration of the roller into the specimen. The interfacial frictional behavior (tangential behavior) is modeled through a penalty method with a friction coefficient of 0.3. Since an explicit scheme is employed for the quasi-static analysis, mass scaling is applied to the whole model such that the material density used in the simulation is increased by 100 times. The numerically increased density of the constituent material results in an artificial increase in the kinetic energy in the system that subsequently causes the vibration of the beam, especially at the beginning of the simulation. When the beam deforms further, the increased strain energy can suppress the effect of the artificial kinetic energy and the solutions become stable.

In order to simulate the drop tower tests, a point mass is attached to the roller to represent the weight of the impactor. In addition, a concentric load, which simulates the gravity force of the dropped weight that exerts on the specimen, is applied on the roller through this mass point along the negative y - direction. Instead of modeling the whole falling process of the weight, the roller is placed 0.02 mm above the specimen with an initial impact velocity of 3866 mm/sec ($V_2 = -3866$ mm/sec). In the dynamic simulation, the constituent materials should be modeled using their true densities since the model should capture the correct kinetic energy in the system. However, since the duration of the dynamic simulation is significantly shorter than the quasi-static one, the dynamic analysis can achieve a reasonable computational time without using mass scaling. The contact between the impactor and the specimen is the same as the one used in the quasi-static analysis. Similarly, the edge BF and CG are fixed in the y - and z -directions to achieve a three-point bend loading condition.

7.3 Results: Albany 2 Subjected to Quasi-Static Three-Point Bending

This section presents the computational results of Albany 2, including both linear elastic and failure analysis. Both analysis is carried out using the implicit solver available in ABAQUS (version 6.12).

7.3.1 Elastic Response (Strain Contours)

The computed surface strain fields are compared against the experimental DIC contours in the predamage regime. Figure 7.6 shows the comparison on the axial surface strains at a midpoint displacement of 2 mm. The proposed architecture

based FE model can successfully capture the strain localization that is developed during the flexural deformation. The site of the strain concentration in the regions of predominant tension indicates the onset of matrix cracking that is observed on the tensile side of the flexed beam, as shown in Section 7.3.2.

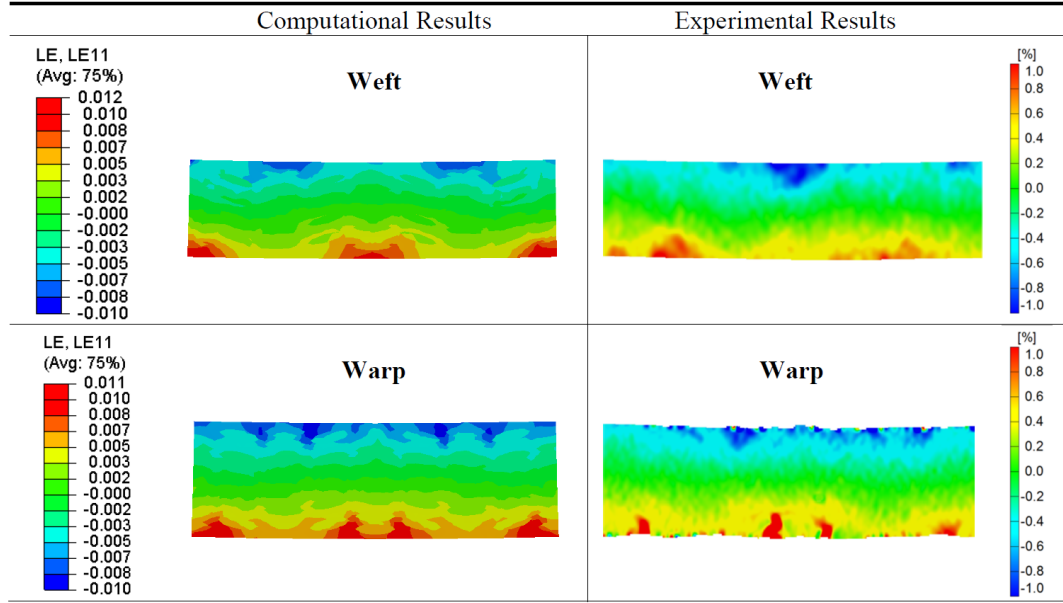


Figure 7.6: Comparison of the axial strain fields at a load point displacement of 2 mm (Albany 2).

7.3.2 Progressive Damage and Failure Response

Since it is difficult to experimentally determine the failure characteristics of a single fiber tow within a 3DTC, a parametric study is utilized to understand the how the constituent failure behavior affects the composite macroscopic response. For Albany 2, three different cases are considered, with a focus on the tensile failure properties, as summarized in Table 7.7.

Table 7.7: Failure characteristics used in the three different cases for Albany 2.

	σ_{cr}^- (MPa)	G_{IC}^- (N/mm)	σ_{cr}^+ (MPa)	G_{IC}^+ (N/mm)
Case A	592	4	1700	40
Case B	592	4	1700	45
Case C	592	4	1900	40

The computational load-displacement responses of the three different cases are compared against the experimental results, as shown in Figure 7.7. The Abany2 specimen is loaded along the warp direction under quasi-static three point bending. It can be concluded that the proposed model offers a good prediction on the elastic flexural stiffness, kink band initiation and progression. However, the final catastrophic failure is not fully captured in the current computational framework. Both Case A and B predict a lower strain to failure than the experimental result. Case C shows an increase in load for the deformation between 10.5 mm and 12 mm, while in the experiment the load is still in the “plateau” regime. The fiber tow progressive failure response are shown in Figure 7.9 for Case B, where the color contours illustrate the absolute values of the tow crack strains. Since the fiber tow is modeled using the SCA, the crack strains indicate kink band formation on the compression side and tow breakage on the tension side. As shown in Figure 7.9, the predicted “load plateau” between point (2) and (5) dictates the progression of kink banding on the compression side. A significant load drop occurs at point (6), where the bottom fiber tow breakage is observed, as shown in Figure 7.9(f). The ABAQUS implicit solver encounters convergence difficulty after point (6). The evolution of matrix cracking is shown in Figure 7.8

The parametric study suggests that both the tow tensile strength and fracture toughness affect the final composite catastrophic failure response. It is also worth noting that tow transverse failure is observed in the weft tows (the tows running along the z-direction) at the end of the experiment, however, this failure mode is not accounted for in the current model. Even though the transverse tows have little contribution to the composite flexural stiffness, this type of failure mechanism can affect the energy dissipation during the failure progress, much like the effect of matrix cracking. This work is left for future study.

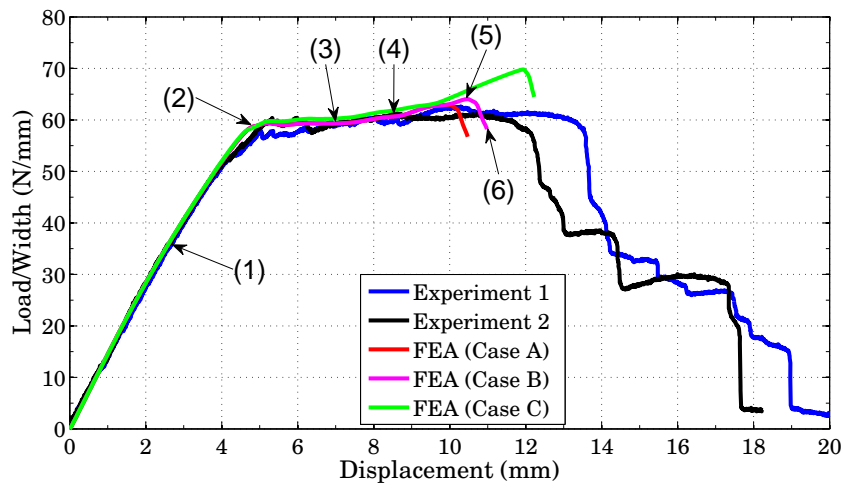


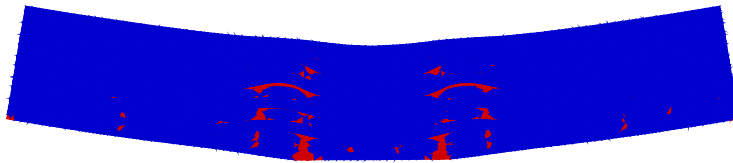
Figure 7.7: Comparison of the load-displacement responses obtained from the experiment and the computational model. The Albany 2 specimen is loaded along the warp direction. The evolution of matrix cracking and the deformed shapes of the fiber tows at the labeled points are shown in Figure 7.8 and Figure 7.9, respectively.



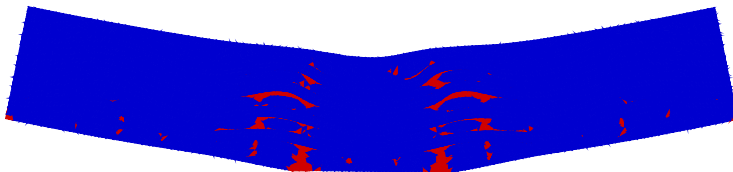
(a) At point (1).



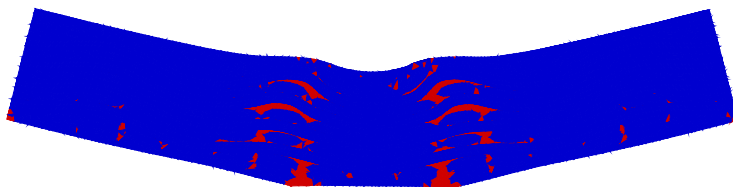
(b) At point (2).



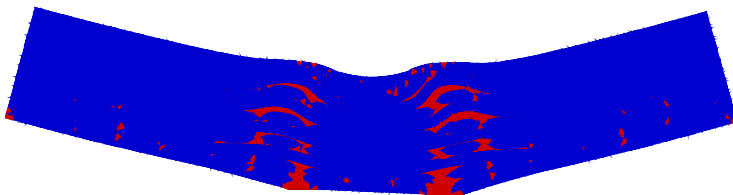
(c) At point (3).



(d) At point (4).

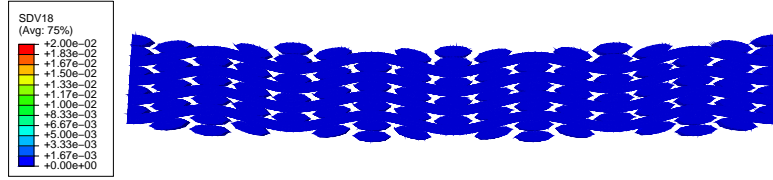


(e) At point (5).

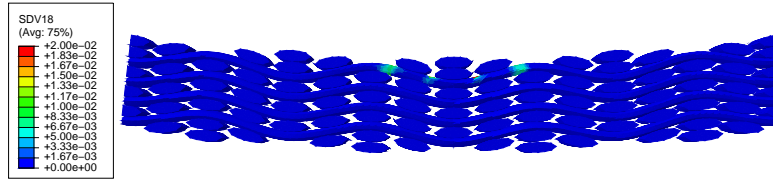


(f) At point (6).

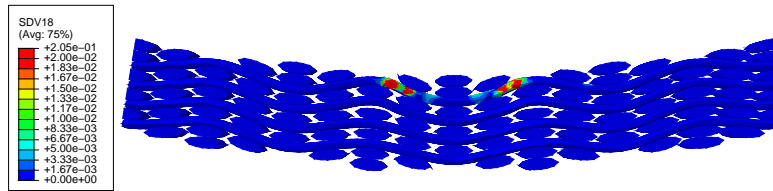
Figure 7.8: Evolution of matrix cracking during the deformation (Albany 2, Case B). The cracked elements are shown in red.



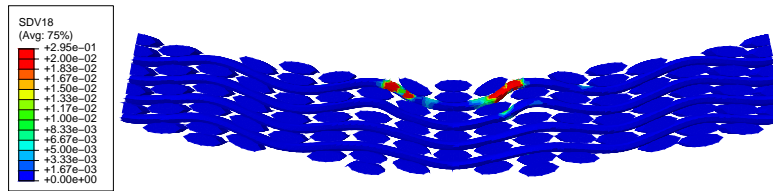
(a) At point (1).



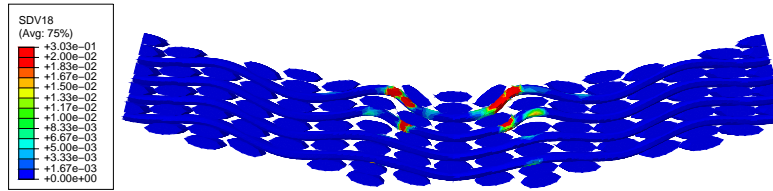
(b) At point (2).



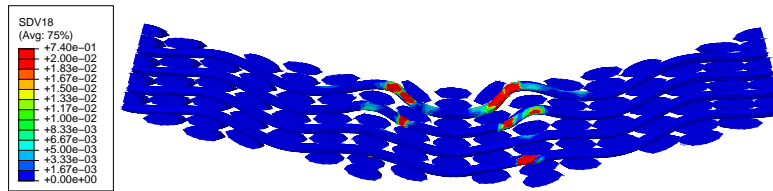
(c) At point (3).



(d) At point (4).



(e) At point (5).



(f) At point (6).

Figure 7.9: Evolution of fiber tow crack strains during the deformation (Albany 2, Case B). The crack strains are shown in absolute values.

7.4 Results: Hybrid 3DTC

The computational results for hybrid 3DTCs are presented in this section, including both quasi-static and dynamic analysis discussed in Section 7.4.1 and Section 7.4.2, respectively. The model is focused on the thin unsymmetric hybrid panel loaded along the weft direction.

7.4.1 Quasi-Static analysis

The quasi-static analysis of the thin unsymmetric hybrid panel is carried out on the “glass layer in compression” configuration. Both the implicit and explicit solvers are used to compute the composite flexural response. The failure characteristics of the constituent tows used in the FE model are summarized in Table 7.8.

Table 7.8: Failure characteristics used in the quasi-static analysis for the thin unsymmetric hybrid composite with the “glass layer in compression” configuration.

σ_{cr}^- (MPa) (Glass)	G_{IC}^- (N/mm) (Glass)	σ_{cr}^+ (MPa) (Carbon)	G_{IC}^+ (N/mm) (Carbon)
720	4	3000	40

First, the mesoscale model that contains one single fiber tow in the widthwise direction (Model A in Figure 7.4(a)) is used in the global-local model. The load-displacement responses computed using the two different FE solvers are compared against the experimental results, as shown in Figure 7.10. The computational model offers a good prediction on the initial stiffness, kink band formation and progression. The final load drop due to tow breakage is captured using the explicit solver, whereas, the implicit solver encounters convergence issues. The deformed shape corresponds to the last step of the implicit simulation is shown in Figure 7.11, indicating that the bottom tow failure has not occurred yet. Both tensile and compressive tow failure modes are captured through the explicit analysis, as shown in Figure 7.12, in which the color contours illustrate the absolute values of the tow crack strains.

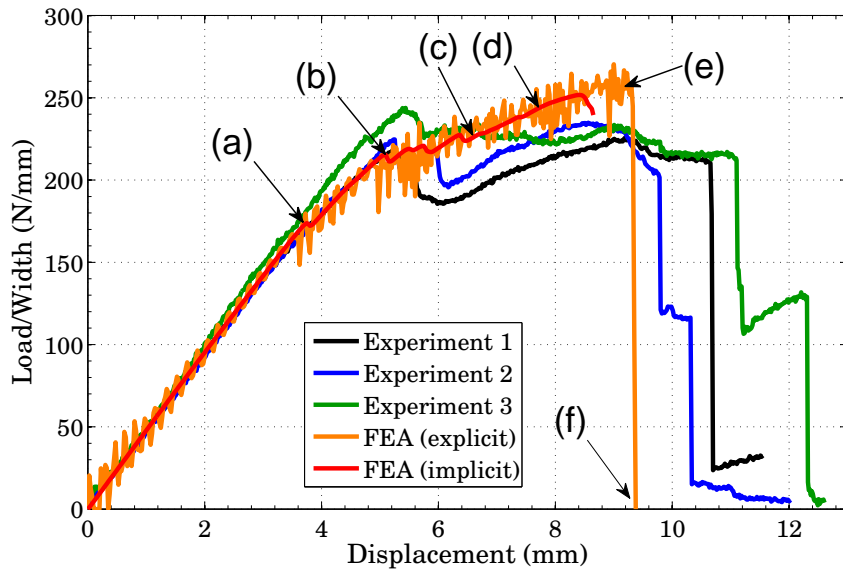
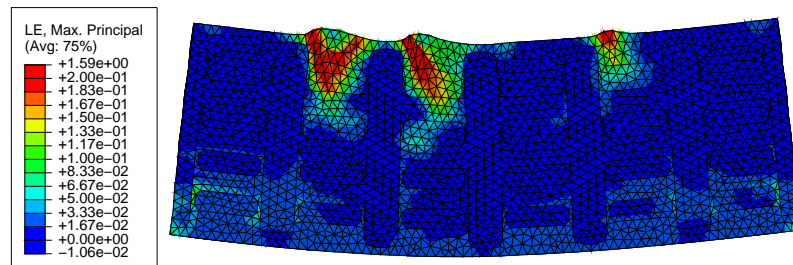
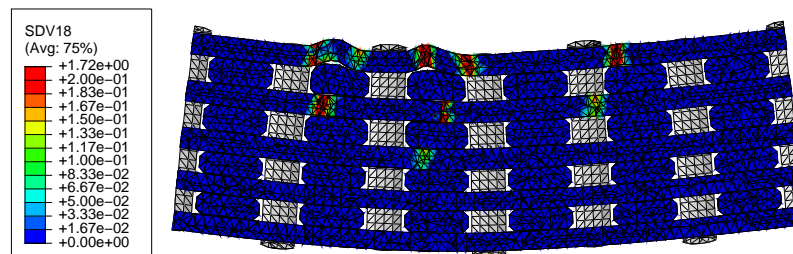


Figure 7.10: Comparison of the load-displacement responses obtained from the experiment and the computational model using Model A. The thin unsymmetric hybrid panel is loaded along the weft direction under quasi-static three point bending with the glass layers in compression. The deformed shapes at the labeled points are shown in Figure 7.12.

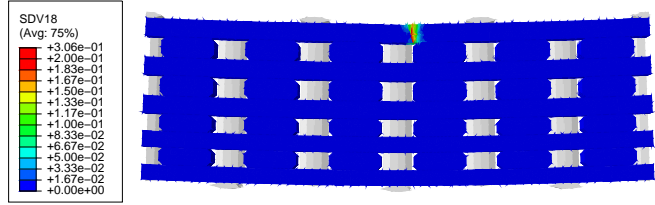


(a) Maximum strains.

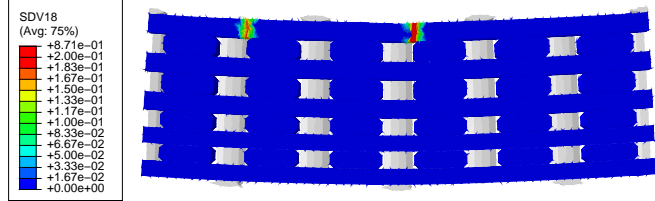


(b) Tow crack strains. The matrix material is removed.

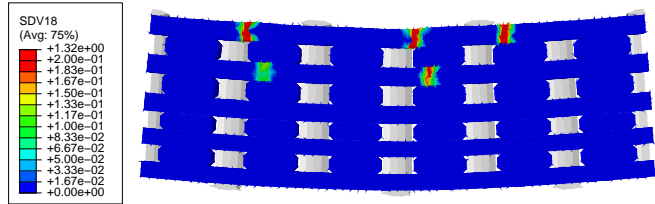
Figure 7.11: Deformed shapes at the last step of the implicit simulation.



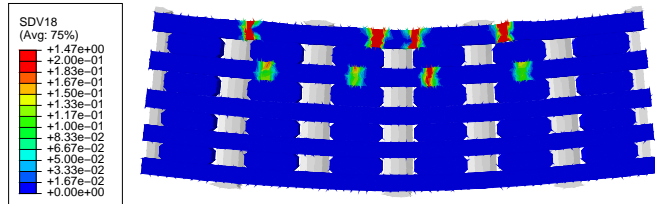
(a) At point (a).



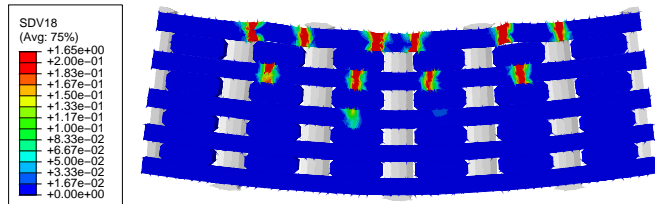
(b) At point (b).



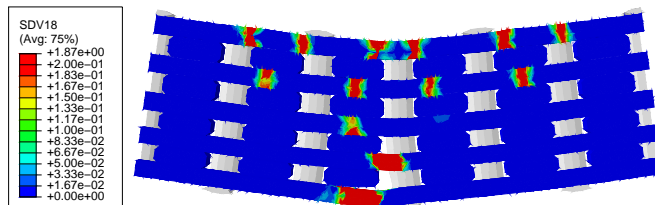
(c) At point (c).



(d) At point (d).



(e) At point (e).



(f) At point (f).

Figure 7.12: Evolution of fiber tow crack strains during the deformation computed using the explicit solver (hybrid). The crack strains are shown in absolute values.

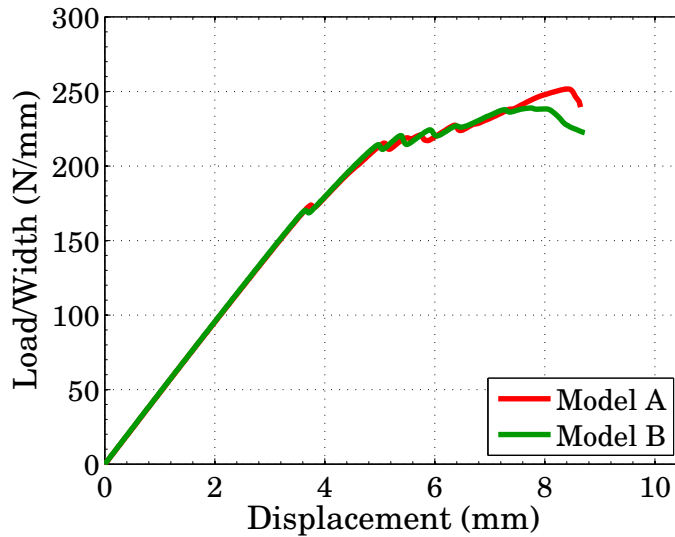


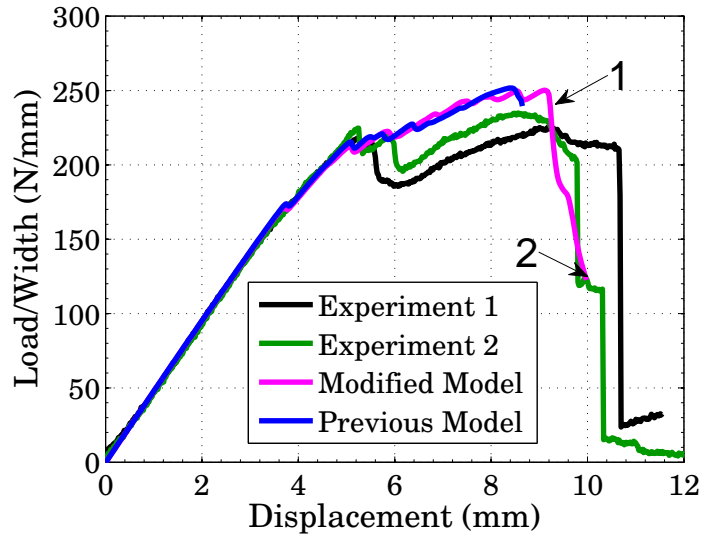
Figure 7.13: Load-displacement responses obtained from the two different mesoscale models.

The load-displacement responses obtained from the two mesoscale models of different sizes (shown in Figure 7.4) are compared against each other, as shown in Figure 7.13. Since the implicit analysis is utilized, neither of the models captures the final load drop due to convergence difficulty. Very little difference has been observed in the predicted deformation responses between the two models, while Model A offers a distinct computational advantage, and therefore this model will be used in the subsequent studies.

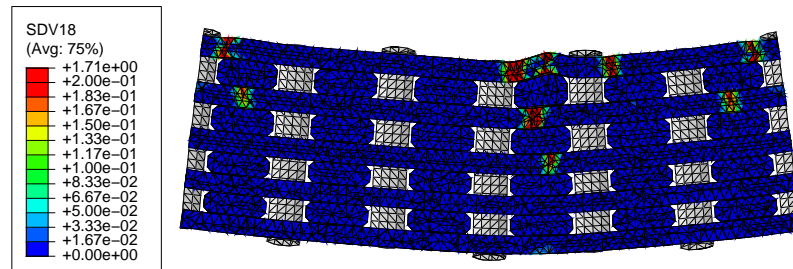
As mentioned previously, the implicit solver encounter convergence issues before the bottom fiber tow reaches the ultimate tensile strength. It has been shown in Figure 7.11 that the surrounding matrix near the kink bands (in regions of predominant tension) experiences large rotation, which can result in excessive distortion of these elements that makes the solver difficult to converge, while these matrix elements actually has little contribution to the overall stiffness. In order to examine the effect of matrix cracking on the compression side, a modified model is proposed in which the post-peak softening response of the matrix is suppressed in the region above the mid-plane that is under predominantly compression loading, while matrix cracking is accounted for in the lower half of the specimen using the SCA.

The load-displacement response obtained from the modified model is shown in Figure 7.14(a), in which the load drop due to tow tensile breakage is successfully captured, as shown in Figure 7.14(b) and (c). It should be noted that the uniaxial tests on the pure polymer matrix show different deformation responses for tension and

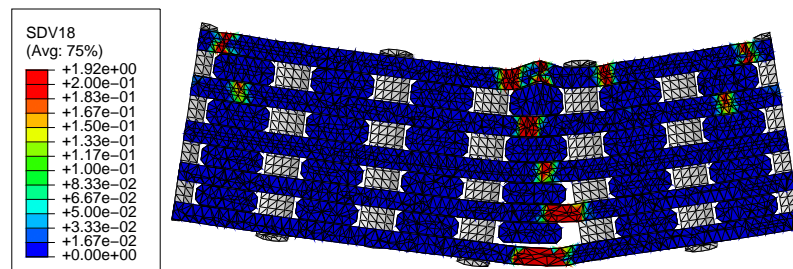
compression, as discussed in Section 2.7. Thus, a material model that can account for both tension and compression failure is recommended for future investigation.



(a) Load-displacement responses.



(b) At point (1).



(c) At point (2).

Figure 7.14: Deformation response obtained from the modified model compared against the previous result. The modified model is able to capture the tow tensile breakage.

7.4.2 Dynamic Analysis (Drop Tower Test)

The dynamic response is investigated through the drop tower tests with an impact velocity of 3866 mm/sec (152 in/sec). Both the “glass layer in compression” and “carbon layer in compression” configurations have been examined in order to determine the architecture-dependent effect. The mesoscale model that contains a single fiber in the widthwise direction (Model A in Figure 7.4(a)) is used throughout the dynamic analysis. A thorough parametric study is performed for the “glass layer in compression” configuration, with a focus on the tow fracture toughness. The failure characteristics used in these two testing configurations are summarized in Table 7.9 and 7.10.

Table 7.9: Failure characteristics used in the drop tower simulation for the thin unsymmetric hybrid composite with the “glass layer in compression” configuration.

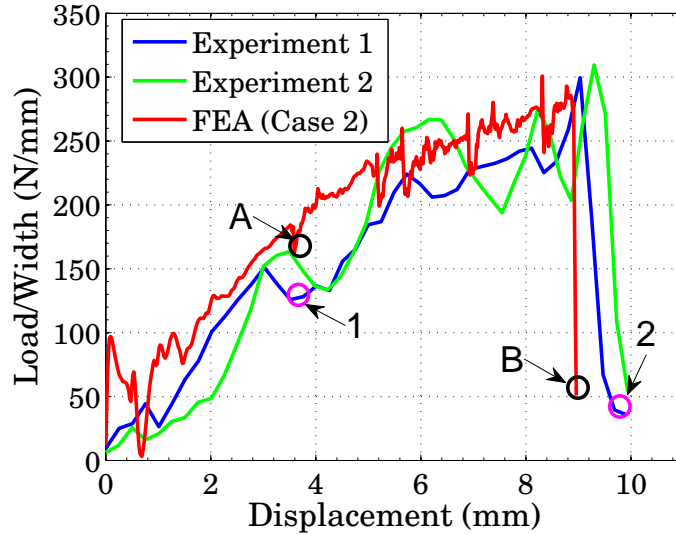
	σ_{cr}^- (MPa) (Glass)	G_{IC}^- (N/mm) (Glass)	σ_{cr}^+ (MPa) (Carbon)	G_{IC}^+ (N/mm) (Carbon)
Case 1	720	2	3000	40
Case 2	720	4	3000	40
Case 3	720	8	3000	40
Case 4	720	4	3000	20
Case 5	720	4	3000	60

Table 7.10: Failure characteristics used in the drop tower simulation for the thin unsymmetric hybrid composite with the “carbon layer in compression” configuration.

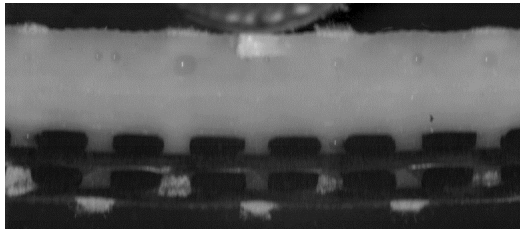
σ_{cr}^- (MPa) (Carbon)	G_{IC}^- (N/mm) (Carbon)	σ_{cr}^+ (MPa) (Glass)	G_{IC}^+ (N/mm) (Glass)
977	4	1700	40

Figure 7.15 shows the comparison between the computational and experimental results for the “glass layer in compression” configuration, in which the failure characteristics summarized in Case 2 is used in the FE model. Although both results show “chattering” responses in the recorded loads during the deformation, the proposed model is able to capture the overall flexural response, including the nonlinear deformation history and final catastrophic failure.

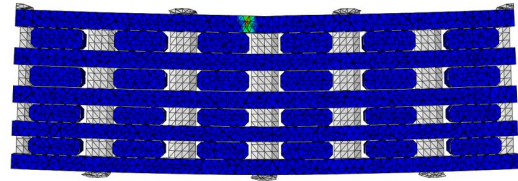
The effect of the tow failure characteristics on the composite flexural response is presented in figure 7.16. It is evident from Case 1, 2, and 5 that the composite flexural strain to failure can be increased by increasing the tow tensile fracture toughness. This finding agrees with the result of Albany 2 (presented in Section 7.3.2) that the tow tensile fracture toughness can affect the composite catastrophic failure response. The results from Case 1, 2, and 3 show that the even though the compressive fracture toughness has little effect on the composite progressive damage response, it can affect the final failure behavior, such as the flexural strain to failure. It is worth noting that during the progressive failure process, multiple damage and failure modes are developed and interacting with each other. Therefore, it is critical to understand the influence of each mode on the composite macroscopic response.



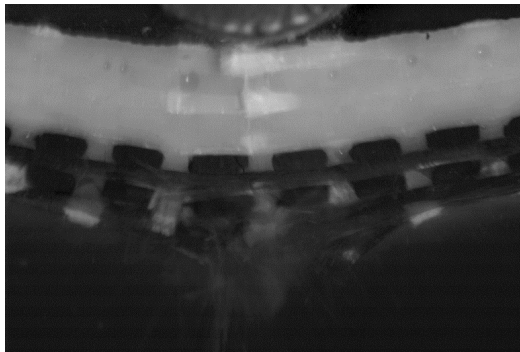
(a) Load-displacement responses.



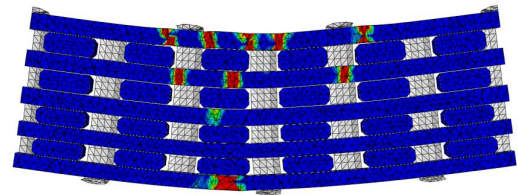
(b) At point (1). Kink banding is observed in the experiment.



(c) At point (A). Kinking is captured in the FE model illustrated by tow crack strains.



(d) At point (2). Tow tensile breakage is observed in the experiment.



(e) At point (B). Tow tensile breakage is captured in the FE model illustrated by tow crack strains.

Figure 7.15: Comparison of the deformation responses obtained from the experiment and the computational model with the failure characteristics of Case 2. The thin unsymmetric hybrid composite panel is loaded along the left direction with the glass layers in compression. The initial impact velocity is 3866 mm/sec (152 in/sec).

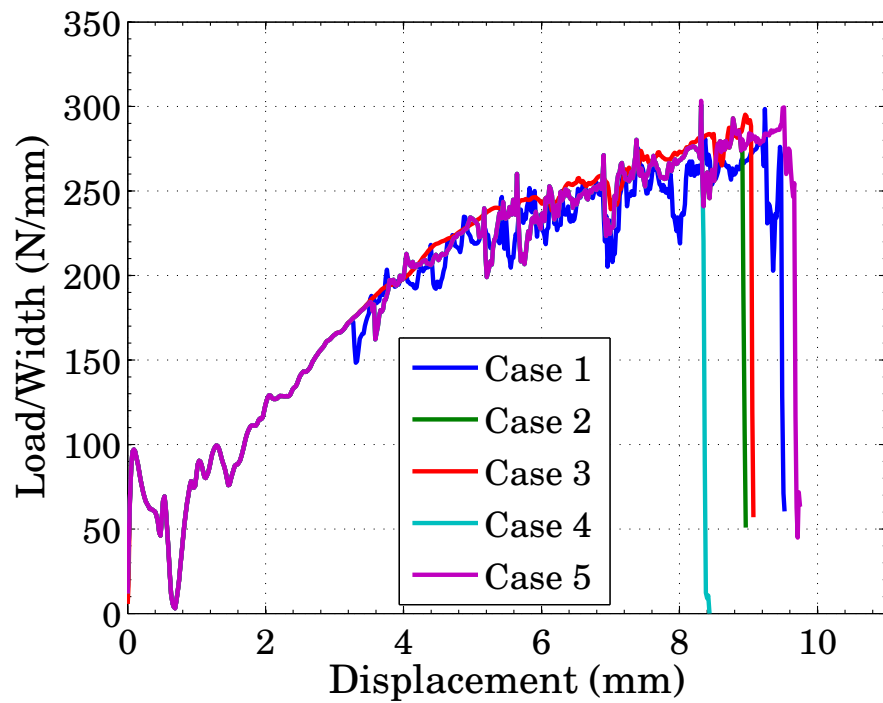
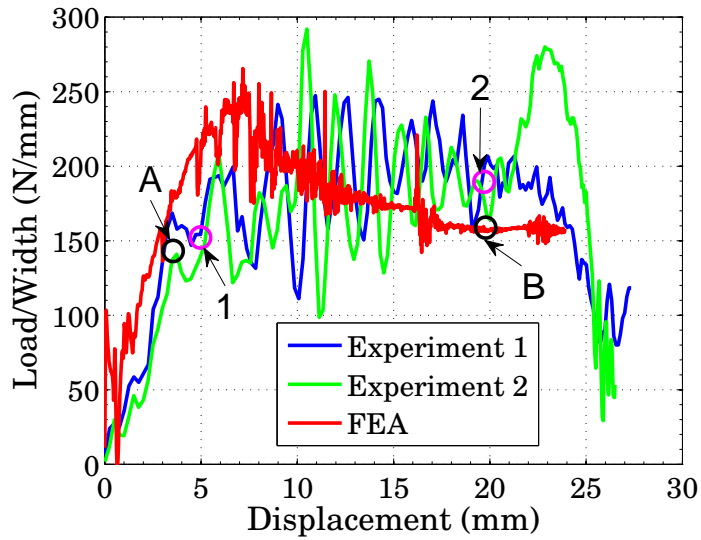
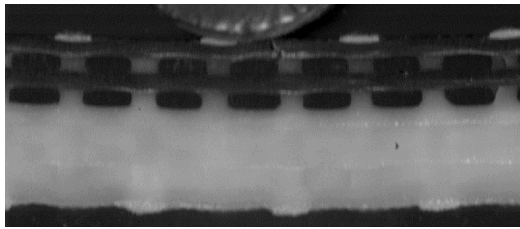


Figure 7.16: Load-displacement responses for various cases used in the parametric study. The failure characteristics for each case are summarized in Table 7.9. The thin unsymmetric hybrid composite panel is loaded along the left direction with the glass layers in compression. The initial impact velocity is 3866 mm/sec (152 in/sec).

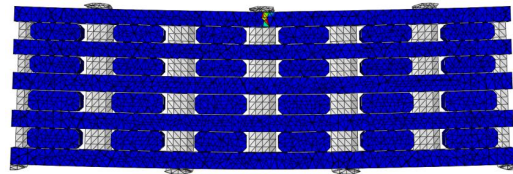
The computational result for the “carbon layer in compression” is presented in Figure 7.17. It is worth noting that in the experiment, this configuration shows considerable damage tolerance, and the specimen still demonstrates load-carrying capability in the post-peak regime. This aspect has been successfully captured in the current modeling framework.



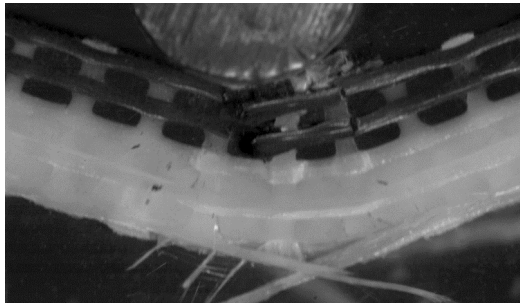
(a) Load-displacement responses.



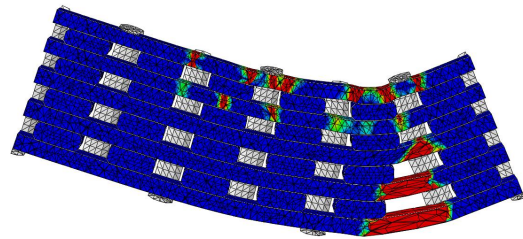
(b) At point (1). Kink banding is observed in the experiment.



(c) At point (A). Kinking is captured in the FE model illustrated by tow crack strains.



(d) At point (2). Tow tensile breakage is observed in the experiment.



(e) At point (B). Tow tensile breakage is captured in the FE model illustrated by tow crack strains.

Figure 7.17: Comparison of the deformation responses obtained from the experiment and the computational model. The thin unsymmetric hybrid composite panel is loaded along the weft direction with the carbon layers in compression. The initial impact velocity is 3866 mm/sec (152 in/sec).

7.5 Conclusions

A mechanics based multiscale FE model is proposed to predict the flexural response of 3DTCs subjected to three-point bending, including both quasi-static and dynamic responses. The model is developed based upon a global-local modeling strategy, in which a textile architecture based mesoscale model is utilized for the area in the vicinity of the loading point, while a homogenized macroscale model is employed for the regions that are far away from the “hot spots” where no damage event is observed. The mesoscale model is a collection of RUCs that are composed of fiber tows embedded in a surrounding matrix medium. The pre-peak nonlinear response of the fiber tows is modeled using the two-scale model developed in Chapter V, in which the subscale micromechanical analysis is carried out in closed form. The post-peak strain softening responses of both the fiber tow and the surrounding polymer matrix are modeled through the SCA.

The load-deflection response, along with the observed damage events, including matrix cracking, tow kinking, and tow tensile breakage, are successfully predicted through the proposed model for the two distinct material systems, Albany 2 and hybrid 3DTCs. A parametric study on the tow failure characteristics is carried out to understand the effect of the constituent properties on the composite macroscopic response. The proposed model is also able to capture the architecture-dependent effect exhibited in the unsymmetric hybrid panels by simulating the drop tower tests. Since all the inputs are from the constituent level, the model is useful in understanding how the 3DTC response is influenced by the geometry and textile architecture, the constitutive response of the constituents, and details of any unintended geometrical deviations of textile architecture.

CHAPTER VIII

Concluding Remarks

In this research, the flexural response of various 3DTCs has been examined experimentally and modeled using a mechanics based multiscale FE model. Two distinct types of 3DTCs, a layer-to-layer interlock glass fiber 3DTC and Z-fiber orthogonal interlock hybrid 3DTC, have been studied in order to understand the architecture-dependent effect. The microscopy studies on the cured composite sample show that the fabrication process has a great impact on the final textile architecture, making it deviate from the ideal designed one. The measured tow dimensions along with the constituent properties are subsequently used as inputs to a textile architecture based mesoscale FE model.

The experimental results of numerous flexural tests show a similar progressive failure response. It is observed that the load deviates from the initial proportional loading due to fiber tow kinking on the compressive side of the specimen. With continued deformation, additional kink bands are formed on the compressive side, while the progression of matrix cracking is captured using a DIC technique. The observed “load plateau” indicates that this class of materials exhibit considerable damage tolerance. The final significant load drop was observed due to fiber tow rupture on the tensile side. The flexural response of hybrid textile composites show a strong dependence on the fiber lay-ups, and the addition of carbon fiber layers do not always improve the performance, including the bending modulus, flexural strength, and strain to failure.

The dynamic response shows a similar load-deflection trend and progressive damage behavior compared with the quasi-static response. The highest peak load is obtained at the loading of 2 in/sec, while the elevated loading rates achieved using the drop tower result in a decrease in the peak load that is controlled by the tow kinking strength. However, it should be pointed out that the drop tower facility is different from the MTS machine in that additional kinetic energy is introduced to the

testing framework by the dropped weight. Thus, the progressive damage and failure response of 3DTCs is also affected by the energy transfer between the kinetic energy of the dropped impactor to the strain energy stored in the deformed beam.

Although the experimental results show an architecture-dependent effect, fiber tow kinking on the compressive side of the specimen is determined to be a strength limiting mechanism for this class of materials. The tow kinking phenomenon along with matrix cracking (due to strain localization) indicate the importance of the textile architecture on the failure response of 3DTCs. The experimental results are subsequently used as a basis for developing a multiscale mechanics model for 3DTC deformation, damage and failure response, predominantly under three-point bending. The model is developed based upon a global-local modeling strategy, in which a textile architecture based mesoscale model is utilized for the area in the vicinity of the loading point, while a homogenized macroscale model is employed for the regions that are far away from the “hot spots” where no damage event is observed. The mesoscale model is a collection of RUCs that are composed of fiber tows embedded in a surrounding matrix medium.

In the mesoscale model, the matrix microdamage, manifested as the pre-peak nonlinear stress versus strain response, is modeled using a modified J_2 deformation theory of plasticity. The secant moduli are degraded with the progression of microdamage, however, the positive definiteness of the tangent stiffness tensor is still preserved. The accumulation of matrix microdamage finally results in matrix macroscopic cracking, followed by a post-peak strain softening behavior that is modeled through the SCA. This method has demonstrated the capability to provide a mesh objective result since a characteristic length is introduced to relate the post-peak softening response to a traction-separation law. Therefore, the total energy release rate during failure in a continuum element is equal to the material fracture toughness.

A novel, micromechanics based, two-scale model is proposed to model the pre-peak nonlinear response of a single fiber tow in the mesoscale model. The microstructure of the fiber tow is represented as a unidirectionally aligned fiber-reinforced composite, resulting in a transversely isotropic solid at the mesoscale. The effective fiber tow response is computed through micromechanical analysis using the fiber-matrix concentric cylinder model as the basic repeat unit. In addition, micromechanics is used to relate the fiber tow strains to the fiber and matrix strains through a 6 by 6 transformation matrix. The resolved spatial variation of the matrix fields are compared with the corresponding FE model to demonstrate the accuracy of the proposed micromechanics model. The evolution of the fiber tow nonlinear response is assumed to be governed by two scalar, strain based variables that are related to the extreme

value of an appropriately defined matrix equivalent strain, and the matrix secant moduli are used to compute the tow secant moduli for nonlinear analysis.

Various fiber tow failure modes have been studied, among which the fiber failure modes that include tow kinking in compression and tow breakage in tension are considered as the dominant failure modes. The compressive strength of a fiber tow is numerically determined through the aforementioned two-scale model, in which the subscale micromechanical analysis at the fiber-matrix level is carried out in closed form. It has been found that the computed kinking strength is affected by the matrix in-situ properties and initial fiber misalignment angle, while the result is independent of the mesoscale mesh size. The obtained kinking strength is used as the failure initiation criterion for the fiber tow subjected to compression. The failure evolution is modeled using the SCA with a traction-separation law that is specifically designed for the fiber tow. The failure plane is assumed to be perpendicular to the fiber direction for both tension and compression. It is further assumed that when the tow fails in compression due to kinking, the crack interface can carry 50% of the compressive strength after the kink band formation. On the other hand, if the fiber tow fails in tension, the fracture energy due to tow tensile breakage is released completely.

The load-deflection response, along with the observed damage events, including matrix cracking, tow kinking, and tow tensile breakage, are successfully predicted through the proposed model for the two distinct 3DTCs, Albany 2 and hybrid 3DTCs. A parametric study on the tow failure characteristics is carried out to understand the effect of the constituent properties on the composite macroscopic response. The proposed model is also able to capture the architecture-dependent effect exhibited in the unsymmetric hybrid panels by simulating the drop tower tests. Since all the inputs are from the constituent level, the model is useful in understanding how the 3DTC response is influenced by the geometry and textile architecture, the constitutive response of the constituents, and details of any unintended geometrical deviations of textile architecture.

APPENDICES

APPENDIX A

Determination of the Crack Orientation Transformation Matrix

This appendix provides the derivation of the crack orientation transformation matrix, \mathbf{N} , in Section 4.3.1.

The transformation of stress components in the Cartesian coordinate system follows the second-order tensor transformation rule as,

$$\sigma'_{ij} = a_{ip}a_{jq}\sigma_{pq} \quad (\text{A.1})$$

where a_{ij} 's are the direction cosines governing the space vector transformation as,

$$x'_i = a_{ip}x_p \quad (\text{A.2})$$

As given in [182], the stress tensor transformation can be written in matrix form as,

$$\begin{Bmatrix} \sigma'_{11} \\ \sigma'_{22} \\ \sigma'_{33} \\ \sigma'_{12} \\ \sigma'_{13} \\ \sigma'_{23} \end{Bmatrix} = \begin{bmatrix} \mathbf{K}_1 & 2\mathbf{K}_2 \\ \mathbf{K}_3 & \mathbf{K}_4 \end{bmatrix} \begin{Bmatrix} \sigma_{11} \\ \sigma_{22} \\ \sigma_{33} \\ \sigma_{12} \\ \sigma_{13} \\ \sigma_{23} \end{Bmatrix} \quad (\text{A.3})$$

where,

$$\mathbf{K}_1 = \begin{bmatrix} a_{11}^2 & a_{12}^2 & a_{13}^2 \\ a_{21}^2 & a_{22}^2 & a_{23}^2 \\ a_{31}^2 & a_{32}^2 & a_{33}^2 \end{bmatrix} \quad (\text{A.4a})$$

$$\mathbf{K}_2 = \begin{bmatrix} a_{11}a_{12} & a_{11}a_{13} & a_{12}a_{13} \\ a_{21}a_{22} & a_{21}a_{23} & a_{22}a_{23} \\ a_{31}a_{32} & a_{31}a_{33} & a_{32}a_{33} \end{bmatrix} \quad (\text{A.4b})$$

$$\mathbf{K}_3 = \begin{bmatrix} a_{11}a_{21} & a_{12}a_{22} & a_{13}a_{23} \\ a_{11}a_{31} & a_{12}a_{32} & a_{13}a_{33} \\ a_{21}a_{31} & a_{22}a_{32} & a_{23}a_{33} \end{bmatrix} \quad (\text{A.4c})$$

$$\mathbf{K}_4 = \begin{bmatrix} a_{11}a_{22} + a_{12}a_{21} & a_{11}a_{23} + a_{13}a_{21} & a_{12}a_{23} + a_{13}a_{22} \\ a_{11}a_{32} + a_{12}a_{31} & a_{11}a_{33} + a_{13}a_{31} & a_{12}a_{33} + a_{13}a_{32} \\ a_{21}a_{32} + a_{22}a_{31} & a_{21}a_{33} + a_{23}a_{31} & a_{22}a_{33} + a_{23}a_{32} \end{bmatrix} \quad (\text{A.4d})$$

Noting that Eq. A.3 can be alternatively written as,

$$\boldsymbol{\sigma}' = \mathbf{K}\boldsymbol{\sigma} \quad (\text{A.5})$$

where,

$$\mathbf{K} = \begin{bmatrix} \mathbf{K}_1 & 2\mathbf{K}_2 \\ \mathbf{K}_3 & \mathbf{K}_4 \end{bmatrix} \quad (\text{A.6})$$

and,

$$\mathbf{K}^{-1} = \begin{bmatrix} \mathbf{K}_1 & 2\mathbf{K}_3 \\ \mathbf{K}_2 & \mathbf{K}_4 \end{bmatrix} \quad (\text{A.7})$$

According to Ref. [182], the strain tensor transformation is given as,

$$\boldsymbol{\epsilon}' = [\mathbf{K}^{-1}]^T \boldsymbol{\epsilon} = \begin{bmatrix} \mathbf{K}_1 & 2\mathbf{K}_2 \\ 2\mathbf{K}_3 & \mathbf{K}_4 \end{bmatrix} \quad (\text{A.8})$$

where engineering shear strains are used, i.e.,

$$\boldsymbol{\epsilon} = \begin{bmatrix} \epsilon_{11} & \epsilon_{22} & \epsilon_{33} & \gamma_{12} & \gamma_{13} & \gamma_{23} \end{bmatrix}^T \quad (\text{A.9})$$

Taking the inverse of Eq. (A.8),

$$\boldsymbol{\epsilon} = \left([\mathbf{K}^{-1}]^T \right)^{-1} \boldsymbol{\epsilon}' \quad (\text{A.10})$$

i.e.,

$$\boldsymbol{\epsilon} = [\mathbf{K}]^T \boldsymbol{\epsilon}' = \begin{bmatrix} \mathbf{K}_1^T & \mathbf{K}_3^T \\ 2\mathbf{K}_2^T & \mathbf{K}_4^T \end{bmatrix} \boldsymbol{\epsilon}' \quad (\text{A.11})$$

Assuming that the global coordinates are the 1 – 2 – 3 coordinates, while the local crack orients in the 1' – 2' – 3' coordinate system with the crack normal aligned in the 1'-direction (see Fig. A.1),

$$\begin{pmatrix} \epsilon_{11} \\ \epsilon_{22} \\ \epsilon_{33} \\ \gamma_{12} \\ \gamma_{13} \\ \gamma_{23} \end{pmatrix} = \begin{bmatrix} \mathbf{N} \end{bmatrix} \begin{pmatrix} \epsilon'_{11} \\ \gamma'_{12} \\ \gamma'_{13} \end{pmatrix} \quad (\text{A.12})$$

and,

$$\begin{pmatrix} \sigma'_{11} \\ \sigma'_{12} \\ \sigma'_{13} \end{pmatrix} = \begin{bmatrix} \mathbf{N}^T \end{bmatrix} \begin{pmatrix} \sigma_{11} \\ \sigma_{22} \\ \sigma_{33} \\ \sigma_{12} \\ \sigma_{13} \\ \sigma_{23} \end{pmatrix} \quad (\text{A.13})$$

where,

$$\mathbf{N} = \begin{bmatrix} a_{11}^2 & a_{11}a_{21} & a_{11}a_{31} \\ a_{12}^2 & a_{12}a_{22} & a_{12}a_{32} \\ a_{13}^2 & a_{13}a_{23} & a_{13}a_{33} \\ 2a_{11}a_{12} & a_{11}a_{22} + a_{12}a_{21} & a_{11}a_{32} + a_{12}a_{31} \\ 2a_{11}a_{13} & a_{11}a_{23} + a_{13}a_{21} & a_{11}a_{33} + a_{13}a_{31} \\ 2a_{12}a_{13} & a_{12}a_{23} + a_{13}a_{22} & a_{12}a_{33} + a_{13}a_{32} \end{bmatrix} \quad (\text{A.14})$$

When the SCA is implemented for a fiber tow, the crack plane is assumed to be perpendicular to the fiber direction. Thus, the 1'-axis that defines the crack normal coincides with the 1-axis that denotes the fiber direction, and \mathbf{N} is further reduced

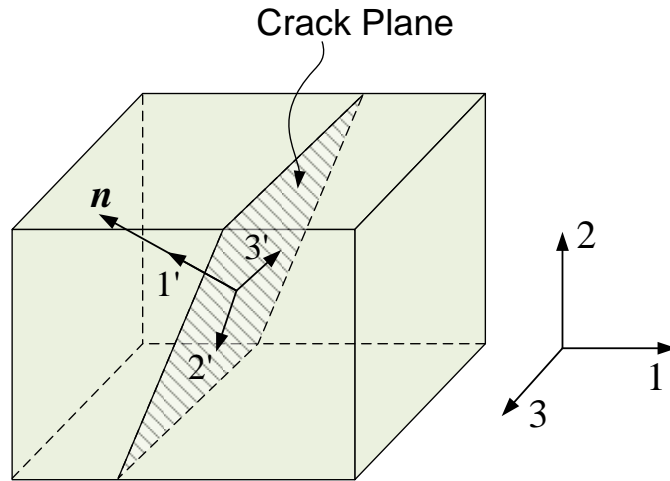


Figure A.1: Crack orientation. The local crack orients in the $1' - 2' - 3'$ coordinate with the crack normal aligned with the $1'$ -direction

to,

$$\mathbf{N} = \begin{bmatrix} 1 & 0 & 0 \\ 0 & 0 & 0 \\ 0 & 0 & 0 \\ 0 & 1 & 0 \\ 0 & 0 & 1 \\ 0 & 0 & 0 \end{bmatrix} \quad (\text{A.15})$$

APPENDIX B

Transformations between the Cartesian and Cylindrical Coordinates

It is convenient to formulate the concentric cylinder model and the extended generalized self-consistent method in the cylindrical coordinates $(x - r - \theta)$. The resulting strains are transformed to the Cartesian coordinates $(x_1 - x_2 - x_3)$ through,

$$\begin{aligned}\epsilon_{11} &= \epsilon_{xx} \\ \epsilon_{22} &= \epsilon_{rr} \cos^2 \theta + \epsilon_{\theta\theta} \sin^2 \theta - \gamma_{r\theta} \sin \theta \cos \theta \\ \epsilon_{33} &= \epsilon_{rr} \sin^2 \theta + \epsilon_{\theta\theta} \cos^2 \theta + \gamma_{r\theta} \sin \theta \cos \theta \\ \gamma_{12} &= \gamma_{xr} \cos \theta - \gamma_{x\theta} \sin \theta \\ \gamma_{13} &= \gamma_{x\theta} \cos \theta + \gamma_{xr} \sin \theta \\ \gamma_{23} &= 2(\epsilon_{rr} - \epsilon_{\theta\theta}) \sin \theta \cos \theta + \gamma_{r\theta}(\cos^2 \theta - \sin^2 \theta)\end{aligned}\tag{B.1}$$

APPENDIX C

Formulation for the Extended Generalized Self-Consistent Method

The stresses can be derived from the Airy's stress function as shown in Timoshenko and Goodier [183] as,

$$\begin{aligned}\sigma_{rr} &= \frac{1}{r} \frac{\partial \phi}{\partial r} + \frac{1}{r^2} \frac{\partial^2 \phi}{\partial \theta^2} \\ \sigma_{\theta\theta} &= \frac{\partial^2 \phi}{\partial r^2} \\ \sigma_{r\theta} &= -\frac{\partial}{\partial r} \left(\frac{1}{r} \frac{\partial \phi}{\partial \theta} \right)\end{aligned}\tag{C.1}$$

and the strains are related to the displacements as,

$$\begin{aligned}\epsilon_{rr} &= \frac{\partial U_r}{\partial r} \\ \epsilon_{\theta\theta} &= \frac{1}{r} \frac{\partial U_\theta}{\partial \theta} + \frac{U_r}{r} \\ \gamma_{r\theta} &= \frac{1}{r} \frac{\partial U_r}{\partial \theta} + \frac{\partial U_\theta}{\partial r} - \frac{U_\theta}{r}\end{aligned}\tag{C.2}$$

where U_r and U_θ are radial and hoop displacements in polar coordinates. Since the displacements should be finite at $r = 0$, and the stresses must be bounded as $r \rightarrow \infty$, it follows that,

$$M_1 = C_1 = D_1 = B_3 = 0\tag{C.3}$$

Hence, the stresses for the fiber are,

$$\begin{aligned}
\sigma_{rr}^f &= N_1 - A_1 \cos 2\theta \\
\sigma_{\theta\theta}^f &= N_1 + \left[A_1 + 6B_1 \frac{r^2}{b^2} \right] \cos 2\theta \\
\sigma_{r\theta}^f &= \left[A_1 + 3B_1 \frac{r^2}{b^2} \right] \sin 2\theta
\end{aligned} \tag{C.4}$$

the stresses for the matrix are,

$$\begin{aligned}
\sigma_{rr}^m &= \frac{1}{2} M_2 \frac{b^2}{r^2} + N_2 + \left[-A_2 - \frac{3}{2} C_2 \frac{b^4}{r^4} - 2D_2 \frac{b^2}{r^2} \right] \cos 2\theta \\
\sigma_{\theta\theta}^m &= -\frac{1}{2} M_2 \frac{b^2}{r^2} + N_2 + \left[A_2 + 6B_2 \frac{r^2}{b^2} + \frac{3}{2} C_2 \frac{b^4}{r^4} \right] \cos 2\theta \\
\sigma_{r\theta}^m &= \left[A_2 + 3B_2 \frac{r^2}{b^2} - \frac{3}{2} C_2 \frac{b^4}{r^4} - D_2 \frac{b^2}{r^2} \right] \sin 2\theta
\end{aligned} \tag{C.5}$$

and the stresses for the composite are,

$$\begin{aligned}
\sigma_{rr}^c &= \frac{1}{2} M_3 \frac{b^2}{r^2} + N_3 + \left[-A_3 - \frac{3}{2} C_3 \frac{b^4}{r^4} - 2D_3 \frac{b^2}{r^2} \right] \cos 2\theta \\
\sigma_{\theta\theta}^c &= -\frac{1}{2} M_3 \frac{b^2}{r^2} + N_3 + \left[A_3 + \frac{3}{2} C_3 \frac{b^4}{r^4} \right] \cos 2\theta \\
\sigma_{r\theta}^c &= \left[A_3 - \frac{3}{2} C_3 \frac{b^4}{r^4} - D_3 \frac{b^2}{r^2} \right] \sin 2\theta
\end{aligned} \tag{C.6}$$

According to the 2D plane-strain constitutive relations in Eq. (5.22), the strains for the fiber are calculated as,

$$\begin{aligned}
\epsilon_{rr}^f &= \frac{1}{4G_{23}^f} \left\{ 2N_1 \frac{G_{23}^f}{K_{23}^f} + \left[-2A_1 + 6B_1 \left(\frac{G_{23}^f}{K_{23}^f} - 1 \right) \frac{r^2}{b^2} \right] \cos 2\theta \right\} \\
\epsilon_{\theta\theta}^f &= \frac{1}{4G_{23}^f} \left\{ 2N_1 \frac{G_{23}^f}{K_{23}^f} + \left[2A_1 + 6B_1 \left(\frac{G_{23}^f}{K_{23}^f} + 1 \right) \frac{r^2}{b^2} \right] \cos 2\theta \right\} \\
\gamma_{r\theta}^f &= \frac{1}{2G_{23}^f} \left[2A_1 + 6B_1 \frac{r^2}{b^2} \right] \sin 2\theta
\end{aligned} \tag{C.7}$$

the strains for the matrix are,

$$\begin{aligned}
\epsilon_{rr}^m &= \frac{1}{4G^m} \left\{ \left[M_2 \frac{b^2}{r^2} + 2N_2 \frac{G^m}{K_{23}^m} \right] + \left[-2A_2 + 6B_2 \left(\frac{G^m}{K_{23}^m} - 1 \right) \frac{r^2}{b^2} - 3C_2 \frac{b^4}{r^4} \right. \right. \\
&\quad \left. \left. - 2D_2 \left(\frac{G^m}{K_{23}^m} + 1 \right) \frac{b^2}{r^2} \right] \cos 2\theta \right\} \\
\epsilon_{\theta\theta}^m &= \frac{1}{4G^m} \left\{ \left[-M_2 \frac{b^2}{r^2} + 2N_2 \frac{G^m}{K_{23}^m} \right] + \left[2A_2 + 6B_2 \left(\frac{G^m}{K_{23}^m} + 1 \right) \frac{r^2}{b^2} + 3C_2 \frac{b^4}{r^4} \right. \right. \\
&\quad \left. \left. - 2D_2 \left(\frac{G^m}{K_{23}^m} - 1 \right) \frac{b^2}{r^2} \right] \cos 2\theta \right\} \\
\gamma_{r\theta}^m &= \frac{1}{2G^m} \left[2A_2 + 6B_2 \frac{r^2}{b^2} - 3C_2 \frac{b^4}{r^4} - 2D_2 \frac{b^2}{r^2} \right] \sin 2\theta
\end{aligned} \tag{C.8}$$

and the strains for the equivalent composite are,

$$\begin{aligned}
\epsilon_{rr}^c &= \frac{1}{4G_{23}^c} \left\{ \left[M_3 \frac{b^2}{r^2} + 2N_3 \frac{G_{23}^c}{K_{23}^c} \right] + \left[-2A_3 - 3C_3 \frac{b^4}{r^4} - 2D_3 \left(\frac{G_{23}^c}{K_{23}^c} + 1 \right) \frac{b^2}{r^2} \right] \cos 2\theta \right\} \\
\epsilon_{\theta\theta}^c &= \frac{1}{4G_{23}^c} \left\{ \left[-M_3 \frac{b^2}{r^2} + 2N_3 \frac{G_{23}^c}{K_{23}^c} \right] + \left[2A_3 + 3C_3 \frac{b^4}{r^4} - 2D_3 \left(\frac{G_{23}^c}{K_{23}^c} - 1 \right) \frac{b^2}{r^2} \right] \cos 2\theta \right\} \\
\gamma_{r\theta}^c &= \frac{1}{2G_{23}^c} \left[2A_3 - 3C_3 \frac{b^4}{r^4} - 2D_3 \frac{b^2}{r^2} \right] \sin 2\theta
\end{aligned} \tag{C.9}$$

Finally, the displacements can be calculated based upon the strain-displacement relations in Eq.(C.2). The displacements for the fiber are,

$$\begin{aligned}
U_r^f &= \frac{b}{4G_{23}^f} \left\{ 2N_1 \frac{G_{23}^f}{K_{23}^f} \frac{r}{b} + \left[-2A_1 \frac{r}{b} + 2B_1 \left(\frac{G_{23}^f}{K_{23}^f} - 1 \right) \frac{r^3}{b^3} \right] \cos 2\theta \right\} \\
U_\theta^f &= \frac{b}{4G_{23}^f} \left[2A_1 \frac{r}{b} + 2B_1 \left(\frac{G_{23}^f}{K_{23}^f} + 2 \right) \frac{r^3}{b^3} \right] \sin 2\theta
\end{aligned} \tag{C.10}$$

the displacements for the matrix are,

$$\begin{aligned}
U_r^m &= \frac{b}{4G^m} \left\{ \left[-M_2 \frac{b}{r} + 2N_2 \frac{G^m}{K_{23}^m} \frac{r}{b} \right] + \left[-2A_2 \frac{r}{b} + 2B_2 \left(\frac{G^m}{K_{23}^m} - 1 \right) \frac{r^3}{b^3} + C_2 \frac{b^3}{r^3} \right. \right. \\
&\quad \left. \left. + 2D_2 \left(\frac{G^m}{K_{23}^m} + 1 \right) \frac{b}{r} \right] \cos 2\theta \right\} \\
U_\theta^m &= \frac{b}{4G^m} \left[2A_2 \frac{r}{b} + 2B_2 \left(\frac{G^m}{K_{23}^m} + 2 \right) \frac{r^3}{b^3} + C_2 \frac{b^3}{r^3} - 2D_2 \frac{G^m}{K_{23}^m} \frac{b}{r} \right] \sin 2\theta
\end{aligned} \tag{C.11}$$

and the displacements for the composite are,

$$\begin{aligned}
U_r^c &= \frac{b}{4G_{23}^c} \left\{ \left[-M_3 \frac{b}{r} + 2N_3 \frac{G_{23}^c}{K_{23}^c} \frac{r}{b} \right] + \left[-2A_3 \frac{r}{b} + C_3 \frac{b^3}{r^3} + 2D_3 \left(\frac{G_{23}^c}{K_{23}^c} + 1 \right) \frac{b}{r} \right] \cos 2\theta \right\} \\
U_\theta^c &= \frac{b}{4G_{23}^c} \left[2A_3 \frac{r}{b} + C_3 \frac{b^3}{r^3} - 2D_3 \frac{G_{23}^c}{K_{23}^c} \frac{b}{r} \right] \sin 2\theta
\end{aligned} \tag{C.12}$$

APPENDIX D

Computation of the Matrix Strain Fields Using Finite Element Analysis

Two different FEA models are utilized to compute the matrix strain fields in Section 5.3.4. The axial problems, including axial tension and axial shear, are analyzed using a 3D two-phase cylinder model as schematically shown in Fig. 5.3. When the cylinder is subjected to an axial tension, the problem is axisymmetric, hence, $U_\theta = 0$, is enforced everywhere on the boundary. To ensure a single axial strain is prescribed on the cylinder, one end of the cylinder is fixed ($U_x(x = 0) = 0$), while the other end is subjected to an axial displacement, δ . The outer lateral surface is constrained ($U_r(r = b) = 0$) such that only a single axial strain is present. The overall axial strain is calculated as δ/L , where L is the length of the cylinder. The boundary conditions for the axial shear problem are given by, Eq. (5.17), with one end fixed. Note that L should be large enough to ignore boundary effects at the ends.

To analyze the transverse problem, a three-phase cylinder model is utilized as illustrated in Fig. D.1, in which both the fiber and the matrix are concentrically embedded in an equivalent composite medium. The composite properties are calculated using Eq. (5.7), (5.8), (5.18), (5.30), and (5.37). Since the equivalent composite medium is assumed to be large enough to produce uniform stress and strain distributions at the boundary, the outer boundary of the composite is modeled as rectangular so that the boundary conditions can be enforced easily. The boundary conditions for transverse normal and transverse shear loading are summarized in Table D.1.

Table D.1: Boundary conditions for the transverse normal and transverse shear problem. The boundary conditions are prescribed on each outer surface of the rectangle. L_1 , L_2 , and L_3 are the length of the rectangle along x_1 , x_2 , and x_3 directions, respectively.

	Transverse normal	Transverse shear
	$\epsilon_{22}^c = \bar{\epsilon}$	$\gamma_{23}^c = \bar{\gamma}$
ABCD	$U_1 = 0$	$U_1 = 0$
EFGH	$U_1 = 0$	$U_1 = 0$
AEHD	$U_2 = 0$	$U_2 = 0, U_3 = 0$
BFGC	$U_2 = \bar{\epsilon} L_2$	$U_2 = 0, U_3 = \bar{\gamma} L_2$
ABFE	$U_3 = 0$	$U_3 = \bar{\gamma} x_2$
DCGH	$U_3 = 0$	$U_3 = \bar{\gamma} x_2$

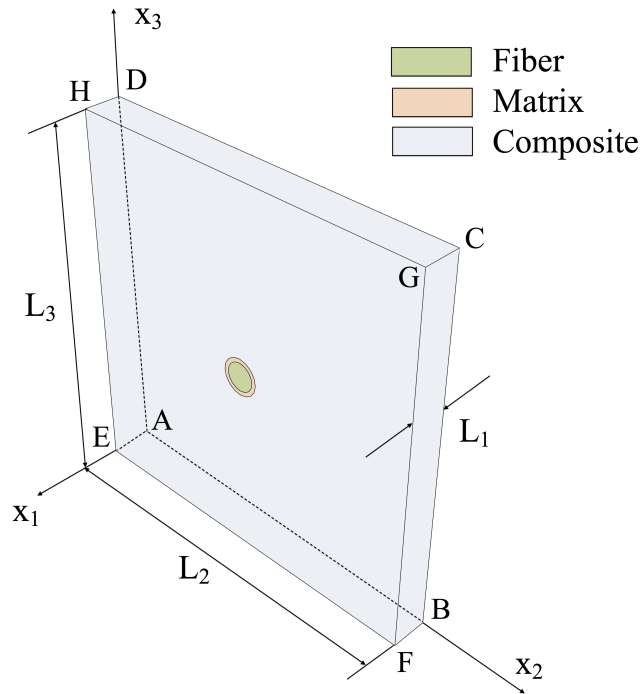


Figure D.1: Three-phase finite element model for the transverse problem.

APPENDIX E

Formulations for the Concentric Cylinder Model and Mori-Tanaka Method

E.1 Concentric Cylinder Model

The concentric cylinder model was first proposed by Hashin and Rosen [40], in which a unidirectional fiber-reinforced composite is represented by an assemblage of concentric cylinders. In each concentric pair, the inner cylinder representing the fiber is embedded in an annulus of the matrix, resulting in a transversely isotropic material. The size of the concentric pair varies such that the entire volume of the composite can be filled with the cylinders, while the ratio of the fiber radius to the matrix radius is kept constant to maintain the correct fiber volume fraction. The key is to impose traction or displacement boundary conditions on the cylinders and equate the strain energy of the concentric pair (fiber-matrix cylinder) to that of the equivalent homogeneous composite material. Hence, the effective properties of the composite can be computed in terms of the constituent (fiber and matrix) properties and the volume fraction of each constituent based upon the theory of elasticity.

The closed-form expressions for the effective moduli E_1 , ν_{12} , K_{23} , and G_{12} are presented in [75, 160]. In their work, both fiber and matrix are treated as isotropic solids. The effect of fiber orthotropy was extensively studied by Knott and Herakovich [184, 185]. In this paper, a simple and compact form of equations for the composite

effective elastic moduli are obtained by using the fiber constitutive relation as,

$$\begin{aligned}
E_1 &= E_1^f V_f + E^m (1 - V_f) + \frac{4V_f(1 - V_f)(\nu_{12}^f - \nu^m)^2 G^m}{\frac{G^m(1-V_f)}{K_{23}^f} + \frac{G^m V_f}{K_{23}^m} + 1} \\
\nu_{12} &= \nu_{12}^f V_f + \nu^m (1 - V_f) + \frac{V_f(1 - V_f)(\nu_{12}^f - \nu^m) \left(\frac{G^m}{K_{23}^m} - \frac{G^m}{K_{23}^f} \right)}{\frac{G^m(1-V_f)}{K_{23}^f} + \frac{G^m V_f}{K_{23}^m} + 1} \\
K_{23} &= K_{23}^m + \frac{V_f}{\frac{1}{K_{23}^f - K_{23}^m} + \frac{1 - V_f}{K_{23}^m + G^m}} \\
G_{12} &= G^m \frac{G_{12}^f (1 + V_f) + G^m (1 - V_f)}{G_{12}^f (1 - V_f) + G^m (1 + V_f)}
\end{aligned} \tag{E.1}$$

It is impossible to find a closed-form solution for G_{23} using the concentric cylinder model. Usually, Hashin's lower bound [45] for G_{23} is accepted and used in conjunction with Eq. (E.1) to form a complete set five independent elastic constants. Thus, it is assumed that,

$$G_{23} = G^m \left[1 + \frac{V_f}{\frac{G^m}{G_{23}^f - G^m} + \frac{(K_{23}^m + 2G^m)(1 - V_f)}{2(K_{23}^m + G^m)}} \right] \tag{E.2}$$

E.2 Mori-Tanaka Method

An alternative way to compute the composite effective moduli is based upon the work by Mori and Tanaka [49], who first investigated the average internal stress in the matrix of a material containing inclusions with eigenstrains. By Combining their work with Eshelby's solutions [48] for an ellipsoidal inclusion inside an infinite matrix medium, Tandon and Weng [57] obtained closed-form solutions to the five independent elastic constants of a unidirectional fiber-reinforced composite. A more compact form of the solution was presented by Benveniste [58] through a direct and simple approach based upon the concept of strain concentration tensors. The derivations are briefly summarized here.

For a fiber-reinforced composite material, the composite average stresses ($\bar{\sigma}$) and strains ($\bar{\epsilon}$) are the volume average of the corresponding quantities in the fiber and matrix as,

$$\begin{aligned}
\bar{\sigma} &= V_f \bar{\sigma}^f + (1 - V_f) \bar{\sigma}^m \\
\bar{\epsilon} &= V_f \bar{\epsilon}^f + (1 - V_f) \bar{\epsilon}^m
\end{aligned} \tag{E.3}$$

where V_f is the fiber volume fraction, $\bar{\boldsymbol{\sigma}}^f$ and $\bar{\boldsymbol{\epsilon}}^f$ are the average stresses and strains in the fiber, and $\bar{\boldsymbol{\sigma}}^m$ and $\bar{\boldsymbol{\epsilon}}^m$ are the average quantities in the matrix. The composite effective stiffness tensor, \mathbf{C} , is given by,

$$\bar{\boldsymbol{\sigma}} = \mathbf{C}\bar{\boldsymbol{\epsilon}} \quad (\text{E.4})$$

According to the previous formulations [57, 58], the average strains in the fiber and matrix can be further written as,

$$\bar{\boldsymbol{\epsilon}}^m = \bar{\boldsymbol{\epsilon}}^0 + \tilde{\boldsymbol{\epsilon}}^m \quad (\text{E.5})$$

$$\bar{\boldsymbol{\epsilon}}^f = \bar{\boldsymbol{\epsilon}}^0 + \tilde{\boldsymbol{\epsilon}}^m + \tilde{\boldsymbol{\epsilon}}^f \quad (\text{E.6})$$

where $\bar{\boldsymbol{\epsilon}}^0$ are the uniform strains in the far field, $\tilde{\boldsymbol{\epsilon}}^m$ are the perturbed strains in the matrix due to the presence of the fibers, and $\tilde{\boldsymbol{\epsilon}}^f$ are perturbed strains in a fiber with respect to the matrix. The average strains in the fiber and matrix are related to the corresponding average stresses through,

$$\bar{\boldsymbol{\sigma}}^f = \mathbf{C}^f \bar{\boldsymbol{\epsilon}}^f \quad (\text{E.7})$$

$$\bar{\boldsymbol{\sigma}}^m = \mathbf{C}^m \bar{\boldsymbol{\epsilon}}^m$$

where \mathbf{C}^f and \mathbf{C}^m are the stiffness tensors for the fiber and matrix, respectively. Furthermore, Eshelby's equivalent principle [48] results in,

$$\mathbf{C}^f (\bar{\boldsymbol{\epsilon}}^0 + \tilde{\boldsymbol{\epsilon}}^m + \tilde{\boldsymbol{\epsilon}}^f) = \mathbf{C}^m (\bar{\boldsymbol{\epsilon}}^0 + \tilde{\boldsymbol{\epsilon}}^m + \tilde{\boldsymbol{\epsilon}}^f - \boldsymbol{\epsilon}^*) \quad (\text{E.8})$$

where $\boldsymbol{\epsilon}^* = \mathbf{S}^{-1}\tilde{\boldsymbol{\epsilon}}^f$, and \mathbf{S} is the fourth-order Eshelby's transformation tensor, the components of which depend on the geometry of the inclusions and the elastic moduli of the matrix. For a unidirectional fiber-reinforced composite material, the inclusion can be represented as a circular cylinder with large (infinite) aspect ratio. The non-

zero components of the fourth-order Eshelby's transformation tensor are [55],

$$\begin{aligned}
S_{2222} = S_{3333} &= \frac{5 - 4\nu^m}{8(1 - \nu^m)} \\
S_{2233} = S_{3322} &= \frac{4\nu^m - 1}{8(1 - \nu^m)} \\
S_{2211} = S_{3311} &= \frac{\nu^m}{2(1 - \nu^m)} \\
S_{2323} &= \frac{3 - 4\nu^m}{8(1 - \nu^m)} \\
S_{1212} = S_{1313} &= \frac{1}{4}
\end{aligned}$$

where ν^m is the Poisson's ratio of the matrix.

The average strains in the fiber and matrix can be related through a transformation matrix, \mathbf{T} , by substituting Eq.(E.5) and (E.6) into (E.8) as,

$$\bar{\boldsymbol{\epsilon}}^f = \mathbf{T}\bar{\boldsymbol{\epsilon}}^m \quad (\text{E.9})$$

where,

$$\mathbf{T} = [\mathbf{I} + \mathbf{S}(\mathbf{C}^m)^{-1}(\mathbf{C}^f - \mathbf{C}^m)]^{-1} \quad (\text{E.10})$$

Finally, the composite stiffness tensor can be computed by the use of Eq. (E.3), (E.7) and (E.9) as [58],

$$\mathbf{C} = \mathbf{C}^m + [V_f(\mathbf{C}^f - \mathbf{C}^m)\mathbf{T}] [V_f\mathbf{T} + (1 - V_f)]^{-1} \quad (\text{E.11})$$

Hence, the effective elastic moduli of the composite material can be obtained by knowing the components of the stiffness tensor. It is worth noting that the elastic moduli, E_1 , ν_{12} , G_{12} and K_{23} computed using the M-T method are exactly the same as the results from the CCM (Eq. (E.1)), and G_{23} from the M-T method is identical to Hashin's lower bound (Eq. (E.2)).

APPENDIX F

Computation of the Macroscopic Effective Properties of 3D Textile Composites

The effective elastic properties of the 3DTCs are computed using an analytical model developed based upon the method proposed by Quek et al. [11]. The purpose of the proposed model is to determine the homogenized properties through the constituent (fiber and matrix) properties, fiber volume fractions of both warp and weft tows, tow orientations, volume fraction of each constituent (warp tow, weft tow, Z-fiber, and matrix), and stacking sequences in hybrid composites. The RUC of Albany 2 can be broken down into three constituents, including the warp tows (0°), weft tows (90°), and matrix; while the RUC of the hybrid composite contains an additional constituent, the Z-fibers. The key assumption of the proposed model is that all the constituents, including the fiber tows and surrounding matrix, carry the same amount of strains during deformation. Thus, the homogenized composite properties are computed based upon the volume average of the constituent properties. The accuracy of this model on the prediction of the in-plane properties of a 2D triaxially braided textile composite has been demonstrated in Ref. [11].

F.1 Fiber Tow Stiffness in the 1 – 2 – 3 Coordinate System (Local Coordinates)

A single fiber tow consists of thousands of individual fibers embedded in a surrounding matrix medium, the microstructure of which can be represented as a unidirectionally aligned fiber-reinforced composite. When the fiber tow undulates along its longitudinal direction, each infinitesimal section of a fiber tow can be considered

as a unidirectional composite, with its local coordinates aligned with the tow orientation, as schematically shown in Figure 5.2. The effective response of such a material is transversely isotropic, requiring five independent constants to form the local fiber tow stiffness tensor. The computation of fiber tow elastic properties in terms of the fiber and matrix properties is given in Section 5.3.

F.2 Stiffness in the $x' - y' - z'$ Coordinate System (Ply Coordinates)

Each infinitesimal section of an undulating tow makes an angle β with the x' -axis in the $x' - z'$ plane, as shown in Fig. F.1. The fiber tow undulation can be measured from the cross-sectional microscopic images of the specimen. Here, we assumed that the shape of the fiber can be dictated using a periodic function, $f(x')$, as,

$$z' = f(x') \quad (\text{F.1})$$

Therefore,

$$\tan(\beta) = \frac{df(x')}{dx'} \quad (\text{F.2})$$

$$\hat{m} = \cos(\beta) = \frac{1}{1 + \tan^2(\beta)} \quad (\text{F.3})$$

$$\hat{n} = \sin(\beta) = \frac{\tan(\beta)}{1 + \tan^2(\beta)} \quad (\text{F.4})$$

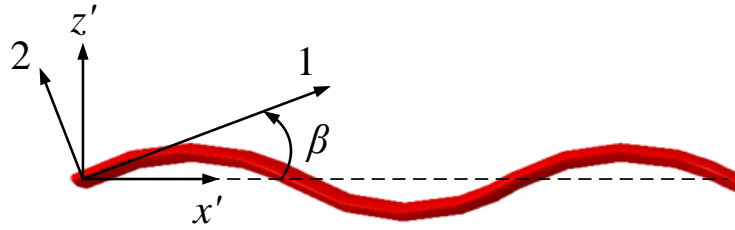


Figure F.1: $x' - z'$ plane profile of an undulating fiber tow.

The contribution of the undulating tows to the stiffness in the $x' - z'$ plane is determined by averaging the transformed local stiffness over the length of the period, L , as,

$$\{\sigma\}^{\text{ply}} = \frac{1}{L} \int_0^L [\hat{T}_1]^{-1} [Q^{\text{local}}] [R] [\hat{T}_1] [R]^{-1} dx' \{\epsilon\}^{\text{ply}} \quad (\text{F.5})$$

$$\{\sigma\}^{\text{ply}} = [\bar{Q}] \{\epsilon\}^{\text{ply}} \quad (\text{F.6})$$

where $[\hat{T}_1]$ is the transformation matrix, and $[R]$ relates engineering strains to tensorial strains.

$$[\hat{T}_1] = \begin{bmatrix} \hat{m}^2 & 0 & \hat{n}^2 & 0 & 2\hat{m}\hat{n} & 0 \\ 0 & 1 & 0 & 0 & 0 & 0 \\ \hat{n}^2 & 0 & \hat{m}^2 & 0 & -2\hat{m}\hat{n} & 0 \\ 0 & 0 & 0 & \hat{m} & 0 & -\hat{n} \\ -\hat{m}\hat{n} & 0 & \hat{m}\hat{n} & 0 & \hat{m}^2 - \hat{n}^2 & 0 \\ 0 & 0 & 0 & \hat{n} & 0 & \hat{m} \end{bmatrix} \quad (\text{F.7})$$

$$[R] = \begin{bmatrix} 1 & 0 & 0 & 0 & 0 & 0 \\ 0 & 1 & 0 & 0 & 0 & 0 \\ 0 & 0 & 1 & 0 & 0 & 0 \\ 0 & 0 & 0 & 2 & 0 & 0 \\ 0 & 0 & 0 & 0 & 2 & 0 \\ 0 & 0 & 0 & 0 & 0 & 2 \end{bmatrix} \quad (\text{F.8})$$

For Albany 2, it is reasonable to assume that the fiber tow undulates as a geometric sine wave with a wavelength of $2L$ and an amplitude of A . These values can be determined by measuring the microscopic images taken on the cross sections. The hybrid composite have almost straight warp and weft tows, therefore, their ply coordinates are aligned with the local tow coordinates.

F.3 Stiffness in the $x - y - z$ Coordinate System (Global Coordinates)

The total averaged stress-strain relation in the $x' - y' - z'$ coordinates is transformed to a representation in the $x - y - z$ coordinate system of the RUC, through a rotation about the (z/z') axis with an angle α . This angle is used to define the orientation of each ply. For the $[0/90]$ lay-up, α is 0° for the warp plies and 90° for

the weft plies. The global stresses are calculated as,

$$\{\sigma\}^{\text{ply}} = [T_1]^{-1}[\bar{Q}][R][T_1][R]^{-1} \{\epsilon\}^{\text{ply}} = [Q]^{\text{ply}} \{\epsilon\}^{\text{ply}} \quad (\text{F.9})$$

where $[R]$ corresponds to Eq. (F.8), and $[T_1]$ is given by,

$$[T_1] = \begin{bmatrix} m^2 & n^2 & 0 & 0 & 0 & 2mn \\ n^2 & m^2 & 0 & 0 & 0 & -2mn \\ 0 & 0 & 1 & 0 & 0 & 0 \\ 0 & 0 & 0 & m & -n & 0 \\ 0 & 0 & 0 & n & m & 0 \\ -mn & mn & 0 & 0 & 0 & m^2 - n^2 \end{bmatrix} \quad (\text{F.10})$$

F.4 RUC Stiffness

The stiffness contribution of each ply is then assembled while taking into account the respective volume fraction of each constituent within the RUC. The volume fraction of each constituent can be determined by analyzing the microscopic images of the specimen. The effective homogenized stiffness of RUC is computed based upon the assumption that all the constituents carry the same amount of strain, and the global stiffness matrix of the RUC is determined using the definition of volume averaged stresses.

In the following calculation, “ i ” denotes each constituent, V_i is the volume of each constituent, and \hat{V}_i is the volume fraction of each constituent.

$$V_{\text{RUC}} = \left\{ \sum_{i=1}^N V_i \right\} \quad (\text{F.11})$$

$$\hat{V}_i = \frac{V_i}{V_{\text{RUC}}} \quad (\text{F.12})$$

The stress-strain relationship for a RUC is defined by,

$$\{\sigma\} = [Q^{\text{RUC}}] \{\epsilon\} \quad (\text{F.13})$$

where,

$$Q_{\text{RUC}} = \sum_{i=1}^N Q^i \hat{V}_i \quad (\text{F.14})$$

Hence,

$$\begin{aligned}\langle \sigma_{ij} \rangle_{\text{RUC}} &= \frac{1}{V_{\text{RUC}}} \left\{ \int_{V_{\text{RUC}}} \sigma_{ij} dV \right\} = \frac{1}{V_{\text{RUC}}} \left\{ \int_{V_1} \sigma_{ij}^1 dV_1 + \int_{V_2} \sigma_{ij}^2 dV_2 + \dots \right\} \quad (\text{F.15}) \\ &= \frac{1}{V_{\text{RUC}}} \left\{ \sum_{i=1}^N \int_{V_i} \sigma_{ij}^i dV_i \right\}\end{aligned}$$

Substituting in the stress versus strain relation for the i^{th} constituent gives,

$$\langle \sigma_{ij} \rangle_{\text{RUC}} = \frac{1}{V_{\text{RUC}}} \left\{ \sum_{i=1}^N \int_{V_i} Q_{ijkl}^i \epsilon_{kl}^i dV_i \right\} \quad (\text{F.16})$$

According to the iso-strain assumption,

$$\epsilon_{kl}^i = \epsilon_{kl}^{\text{RUC}} \quad (\text{F.17})$$

The constitutive relations for the RUC becomes,

$$\langle \epsilon_{ij}^{\text{RUC}} \rangle = \frac{1}{V_{\text{RUC}}} = \left\{ \sum_{i=1}^N \int_{V_i} Q_{ijkl}^i dV_i \right\} \epsilon_{kl}^{\text{RUC}} \quad (\text{F.18})$$

or,

$$\langle \epsilon_{ij}^{\text{RUC}} \rangle = \left\{ \sum_{i=1}^N Q_{ijkl}^i \hat{V}_i \right\} \epsilon_{kl}^{\text{RUC}} \quad (\text{F.19})$$

Thus,

$$\langle \epsilon_{ij}^{\text{RUC}} \rangle = [Q_{ijkl}^{\text{RUC}}] \epsilon_{kl}^{\text{RUC}} \quad (\text{F.20})$$

where,

$$[Q^{\text{RUC}}] = \sum_{i=1}^N Q_{ijkl}^i \hat{V}_i \quad (\text{F.21})$$

The compliance of the stiffness matrix is computed by inverting the stiffness matrix as,

$$[S^{\text{RUC}}] = [Q^{\text{RUC}}]^{-1} \quad (\text{F.22})$$

Finally the effective engineering constants of the RUC can be determined based

upon the global compliance matrix through,

$$\begin{aligned}
 E_x &= \frac{1}{S_{11}^{\text{RUC}}} & E_y &= \frac{1}{S_{22}^{\text{RUC}}} & E_z &= \frac{1}{S_{33}^{\text{RUC}}} \\
 G_{yz} &= \frac{1}{S_{44}^{\text{RUC}}} & G_{zx} &= \frac{1}{S_{55}^{\text{RUC}}} & G_{xy} &= \frac{1}{S_{66}^{\text{RUC}}} \\
 \nu_{xy} &= -\frac{S_{12}^{\text{RUC}}}{S_{11}^{\text{RUC}}} & \nu_{xz} &= -\frac{S_{13}^{\text{RUC}}}{S_{11}^{\text{RUC}}} & \nu_{yz} &= -\frac{S_{23}^{\text{RUC}}}{S_{22}^{\text{RUC}}}
 \end{aligned} \tag{F.23}$$

BIBLIOGRAPHY

BIBLIOGRAPHY

- [1] Long, A. C., *Design and manufacture of textile composites*, Woodhead Publishing Limited in association with The Textile Institute, Cambridge, England, 1st ed., 2005.
- [2] Pankow, M. R., *The Deformation Response of 3D Woven Composites Subjected to High Rates of Loading*, Ph.D. thesis, University of Michigan, 2010.
- [3] Gong, J. C. and Sankar, B. V., “Impact properties of three-dimensional braided graphite/epoxy composites,” *Journal of Composite Materials*, Vol. 25, 1991, pp. 715–731. doi:[10.1177/002199839102500606](https://doi.org/10.1177/002199839102500606).
- [4] Baucom, J. N. and Zikry, M. A., “Evolution of failure mechanisms in 2D and 3D woven composite systems under quasi-static perforation,” *Journal of Composite Materials*, Vol. 37, 2003, pp. 1651–1674. doi:[10.1177/002199803035178](https://doi.org/10.1177/002199803035178).
- [5] Luo, Y., Lv, L., Sun, B., Qiu, Y., and Gu, B., “Transverse impact behavior and energy absorption of three-dimensional orthogonal hybrid woven composites,” *Composite Structures*, Vol. 81, No. 2, Nov. 2007, pp. 202–209. doi:[10.1016/j.compstruct.2006.08.011](https://doi.org/10.1016/j.compstruct.2006.08.011).
- [6] Pankow, M., Salvi, A., Waas, A., Yen, C., and Ghiorse, S., “Resistance to delamination of 3D woven textile composites evaluated using End Notch Flexure (ENF) tests: Experimental results,” *Composites Part A: Applied Science and Manufacturing*, Vol. 42, No. 10, Oct. 2011, pp. 1463–1476. doi:[10.1016/j.compositesa.2011.06.013](https://doi.org/10.1016/j.compositesa.2011.06.013).
- [7] McPherson, A., “A new dimension for aerospace: The growing interest for 3-D wovens in the aerospace market,” 2012, <http://www.compositesmanufacturingblog.com/2012/12/a-new-dimension-for-aerospace>.
- [8] Cox, B., Dadkhah, M., Inman, R., Morris, W., and Zupon, J., “Mechanisms of compressive failure in 3D composites,” *Acta Metallurgica et Materialia*, Vol. 40, No. 12, Dec. 1992, pp. 3285–3298. doi:[10.1016/0956-7151\(92\)90042-D](https://doi.org/10.1016/0956-7151(92)90042-D).
- [9] Sankar, B. V. and Marrey, R. V., “Analytical method for micromechanics of textile composites,” *Composites Science and Technology*, Vol. 57, No. 6, Jan. 1997, pp. 703–713. doi:[10.1016/S0266-3538\(97\)00030-4](https://doi.org/10.1016/S0266-3538(97)00030-4).

- [10] Huang, Z. M., “The mechanical properties of composites reinforced with woven and braided fabrics,” *Composites Science and Technology*, Vol. 60, No. 4, March 2000, pp. 479–498. doi:[10.1016/S0266-3538\(99\)00148-7](https://doi.org/10.1016/S0266-3538(99)00148-7).
- [11] Quek, S. C., Waas, A. M., Shahwan, K. W., and Agaram, V., “Analysis of 2D triaxial flat braided textile composites,” *International Journal of Mechanical Sciences*, Vol. 45, No. 6-7, June 2003, pp. 1077–1096. doi:[10.1016/j.ijmecsci.2003.09.003](https://doi.org/10.1016/j.ijmecsci.2003.09.003).
- [12] Pankow, M., Attard, C., and Waas, a. M., “Specimen size and shape effect in split Hopkinson pressure bar testing,” *The Journal of Strain Analysis for Engineering Design*, Vol. 44, No. 8, Nov. 2009, pp. 689–698. doi:[10.1243/03093247JSA538](https://doi.org/10.1243/03093247JSA538).
- [13] Cox, B. N., Dadkhah, M. S., and Morris, W., “On the tensile failure of 3D woven composites,” *Composites Part A: Applied Science and Manufacturing*, Vol. 27, No. 6, Jan. 1996, pp. 447–458. doi:[10.1016/1359-835X\(95\)00053-5](https://doi.org/10.1016/1359-835X(95)00053-5).
- [14] Huang, H. J. and Waas, A. M., “Modeling and predicting the compression strength limiting mechanisms in Z-pinned textile composites,” *Composites Part B: Engineering*, Vol. 40, No. 6, Sept. 2009, pp. 530–539. doi:[10.1016/j.compositesb.2009.02.004](https://doi.org/10.1016/j.compositesb.2009.02.004).
- [15] Rao, M., Sankar, B., and Subhash, G., “Effect of Z-yarns on the stiffness and strength of three-dimensional woven composites,” *Composites Part B: Engineering*, Vol. 40, No. 6, Sept. 2009, pp. 540–551. doi:[10.1016/j.compositesb.2009.01.011](https://doi.org/10.1016/j.compositesb.2009.01.011).
- [16] Quinn, J., McIlhagger, A., and McIlhagger, R., “Examination of the failure of 3D woven composites,” *Composites Part A: Applied Science and Manufacturing*, Vol. 39, No. 2, Feb. 2008, pp. 273–283. doi:[10.1016/j.compositesa.2007.10.012](https://doi.org/10.1016/j.compositesa.2007.10.012).
- [17] Callus, P., Mouritz, A., Bannister, M., and Leong, K., “Tensile properties and failure mechanisms of 3D woven GRP composites,” *Composites Part A: Applied Science and Manufacturing*, Vol. 30, No. 11, Nov. 1999, pp. 1277–1287. doi:[10.1016/S1359-835X\(99\)00033-0](https://doi.org/10.1016/S1359-835X(99)00033-0).
- [18] Leong, K., Lee, B., Herszberg, I., and Bannister, M., “The effect of binder path on the tensile properties and failure of multilayer woven CFRP composites,” *Composites Science and Technology*, Vol. 60, No. 1, Jan. 2000, pp. 149–156. doi:[10.1016/S0266-3538\(99\)00108-6](https://doi.org/10.1016/S0266-3538(99)00108-6).
- [19] Pankow, M., Yen, C. F., Rudolph, M., Justusson, B., Zhang, D., and Waas, A. M., “Experimental investigation on the deformation response of hybrid 3D woven composites,” *Proceedings of the 53rd AIAA/ASME/ASCE/AHS/ASC Structures, Structural Dynamics, and Materials Conference, Honolulu, Hawaii, USA.*, 2012, AIAA 2012-1572.

- [20] Lomov, S., Ivanov, D., Truong, T., Verpoest, I., Baudry, F., Vanden Bosche, K., and Xie, H., “Experimental methodology of study of damage initiation and development in textile composites in uniaxial tensile test,” *Composites Science and Technology*, Vol. 68, No. 12, Sept. 2008, pp. 2340–2349. doi:[10.1016/j.compscitech.2007.07.005](https://doi.org/10.1016/j.compscitech.2007.07.005).
- [21] Ivanov, D., Ivanov, S., Lomov, S., and Verpoest, I., “Strain mapping analysis of textile composites,” *Optics and Lasers in Engineering*, Vol. 47, No. 3-4, March 2009, pp. 360–370. doi:[10.1016/j.optlaseng.2008.05.013](https://doi.org/10.1016/j.optlaseng.2008.05.013).
- [22] Pankow, M., Rudolph, M., Justusson, B., Zhang, D., Waas, A. M., and Yen, C. F., “Experimental investigation on the deformation response of hybrid 3D woven composites,” *Composites: Part A*, in preparation.
- [23] Cox, B., Dadkhah, M., Morris, W., and Flintoff, J., “Failure mechanisms of 3D woven composites in tension, compression, and bending,” *Acta Metallurgica et Materialia*, Vol. 42, No. 12, Dec. 1994, pp. 3967–3984. doi:[10.1016/0956-7151\(94\)90174-0](https://doi.org/10.1016/0956-7151(94)90174-0).
- [24] Quek, S. C., Waas, A. M., Shahwan, K. W., and Agaram, V., “Compressive response and failure of braided textile composites: Part 1 experiments,” *International Journal of Non-Linear Mechanics*, Vol. 39, No. 4, June 2004, pp. 635–648. doi:[10.1016/S0020-7462\(03\)00018-0](https://doi.org/10.1016/S0020-7462(03)00018-0).
- [25] De Carvalho, N., Pinho, S., and Robinson, P., “An experimental study of failure initiation and propagation in 2D woven composites under compression,” *Composites Science and Technology*, Vol. 71, No. 10, July 2011, pp. 1316–1325. doi:[10.1016/j.compscitech.2011.04.019](https://doi.org/10.1016/j.compscitech.2011.04.019).
- [26] Song, S., Waas, A. M., Shahwan, K. W., Faruque, O., and Xiao, X. S., “Compression response, strength and post-peak response of an axial fiber reinforced tow,” *International Journal of Mechanical Sciences*, Vol. 51, No. 7, July 2009, pp. 491–499. doi:[10.1016/j.ijmecsci.2009.03.008](https://doi.org/10.1016/j.ijmecsci.2009.03.008).
- [27] Song, S., Waas, A. M., Shahwan, K. W., and Faruque, O., “Effects of Matrix Microcracking on the Response of 2D Braided Textile Composites Subjected to Compression Loads,” *Journal of Composite Materials*, Vol. 44, No. 2, Aug. 2010, pp. 221–240. doi:[10.1177/0021998309341345](https://doi.org/10.1177/0021998309341345).
- [28] Lomov, S., Huysmans, G., Luo, Y., Parnas, R., Prodromou, A., Verpoest, I., and Phelan, F., “Textile composites: modelling strategies,” *Composites Part A: Applied Science and Manufacturing*, Vol. 32, No. 10, Oct. 2001, pp. 1379–1394. doi:[10.1016/S1359-835X\(01\)00038-0](https://doi.org/10.1016/S1359-835X(01)00038-0).
- [29] Pineda, E. J., *A Novel Multiscale Physics-Based Progressive Damage and Failure Modeling Tool for Advanced Composite Structures*, Ph.D. thesis, University of Michigan, 2011.

- [30] Bogdanovich, a. E., “Multi-scale modeling, stress and failure analyses of 3-D woven composites,” *Journal of Materials Science*, Vol. 41, No. 20, Aug. 2006, pp. 6547–6590. doi:[10.1007/s10853-006-0197-2](https://doi.org/10.1007/s10853-006-0197-2).
- [31] Zhang, D., Waas, a. M., Pankow, M., Yen, C. F., and Ghiorse, S., “Flexural Behavior of a Layer-to-Layer Orthogonal Interlocked Three-Dimensional Textile Composite,” *Journal of Engineering Materials and Technology*, Vol. 134, No. 3, 2012, pp. 031009. doi:[10.1115/1.4006501](https://doi.org/10.1115/1.4006501).
- [32] Pankow, M., Waas, A., Yen, C., and Ghiorse, S., “Modeling the response, strength and degradation of 3D woven composites subjected to high rate loading,” *Composite Structures*, Vol. 94, No. 5, April 2012, pp. 1590–1604. doi:[10.1016/j.compstruct.2011.12.010](https://doi.org/10.1016/j.compstruct.2011.12.010).
- [33] Verpoest, I. and Lomov, S., “Virtual textile composites software : Integration with micro-mechanical, permeability and structural analysis,” *Composites Science and Technology*, Vol. 65, No. 15-16, Dec. 2005, pp. 2563–2574. doi:[10.1016/j.compscitech.2005.05.031](https://doi.org/10.1016/j.compscitech.2005.05.031).
- [34] Hufenbach, W., Böhm, R. and Kroll, L., and Langkamp, A., “Theoretical and experimental investigation of anisotropic damage in textile-reinforced composite structures,” *Mechanics of Composite Materials*, Vol. 40, No. 6, Jan. 2004, pp. 519–532.
- [35] Kurashiki, T., Nakai, H., Hirosawa, S., Imura, M., Zako, M., Verpoest, I., and Lomov, S., “Mechanical Behaviours for Textile Composites by FEM Based on Damage Mechanics,” *Key Engineering Materials*, Vol. 334-335, 2007, pp. 257–260. doi:[10.4028/www.scientific.net/KEM.334-335.257](https://doi.org/10.4028/www.scientific.net/KEM.334-335.257).
- [36] Gorbatikh, L., Ivanov, D., Lomov, S., and Verpoest, I., “On modelling of damage evolution in textile composites on meso-level via property degradation approach,” *Composites Part A: Applied Science and Manufacturing*, Vol. 38, No. 12, Dec. 2007, pp. 2433–2442. doi:[10.1016/j.compositesa.2007.08.017](https://doi.org/10.1016/j.compositesa.2007.08.017).
- [37] Ivanov, D. S., Baudry, F., Van Den Broucke, B., Lomov, S. V., Xie, H., and Verpoest, I., “Failure analysis of triaxial braided composite,” *Composites Science and Technology*, Vol. 69, No. 9, July 2009, pp. 1372–1380. doi:[10.1016/j.compscitech.2008.09.013](https://doi.org/10.1016/j.compscitech.2008.09.013).
- [38] Bogdanovich, A. E., “Three-dimensional analysis of anisotropic spatially reinforced structures,” *Composites Manufacturing*, Vol. 4, No. 4, Dec. 1993, pp. 173–186. doi:[10.1016/0956-7143\(93\)90002-P](https://doi.org/10.1016/0956-7143(93)90002-P).
- [39] Bogdanovich, A. E., “Progressive failure modeling and strength predictions of 3-D woven composites,” *Proceedings of 50th AIAA/ASME/ASCE/AHS/ASC Structures, Structural Dynamics, and Materials Conference*, No. May, Palm Springs, California, 2009, pp. AIAA 2009–2658.

- [40] Hashin, Z. and Rosen, B. W., “The elastic moduli of fiber-reinforced materials,” *Journal of Applied Mechanics*, Vol. 31, No. 2, 1964, pp. 223–232. doi:[10.1115/1.3629590](https://doi.org/10.1115/1.3629590).
- [41] Hashin, Z. and Shtrikman, S., “On some variational principles in anisotropic and nonhomogeneous elasticity,” *Journal of the Mechanics and Physics of Solids*, Vol. 10, No. 4, Oct. 1962, pp. 335–342. doi:[10.1016/0022-5096\(62\)90004-2](https://doi.org/10.1016/0022-5096(62)90004-2).
- [42] Hashin, Z. and Shtrikman, S., “A variational approach to the theory of the elastic behaviour of polycrystals,” *Journal of the Mechanics and Physics of Solids*, Vol. 10, No. 4, Oct. 1962, pp. 343–352. doi:[10.1016/0022-5096\(62\)90005-4](https://doi.org/10.1016/0022-5096(62)90005-4).
- [43] Hashin, Z. and Shtrikman, S., “A variational approach to the theory of the elastic behaviour of multiphase materials,” *Journal of the Mechanics and Physics of Solids*, Vol. 11, No. 2, March 1963, pp. 127–140. doi:[10.1016/0022-5096\(63\)90060-7](https://doi.org/10.1016/0022-5096(63)90060-7).
- [44] Hill, R., “Theory of mechanical properties of fibre-strengthened materials: I. Elastic behaviour,” *Journal of the Mechanics and Physics of Solids*, Vol. 12, No. 4, Sept. 1964, pp. 199–212. doi:[10.1016/0022-5096\(64\)90019-5](https://doi.org/10.1016/0022-5096(64)90019-5).
- [45] Hashin, Z., “On elastic behaviour of fibre reinforced materials of arbitrary transverse phase geometry,” *Journal of the Mechanics and Physics of Solids*, Vol. 13, No. 3, June 1965, pp. 119–134. doi:[10.1016/0022-5096\(65\)90015-3](https://doi.org/10.1016/0022-5096(65)90015-3).
- [46] Christensen, R. and Waals, F., “Effective stiffness of randomly oriented fibre composites,” *Journal of Composite Materials*, Vol. 6, No. 4, Oct. 1972, pp. 518–532. doi:[10.1177/002199837200600407](https://doi.org/10.1177/002199837200600407).
- [47] Christensen, R. and Lo, K., “Solutions for effective shear properties in three phase sphere and cylinder models,” *Journal of the Mechanics and Physics of Solids*, Vol. 27, No. 4, Aug. 1979, pp. 315–330. doi:[10.1016/0022-5096\(79\)90032-2](https://doi.org/10.1016/0022-5096(79)90032-2).
- [48] Eshelby, J. D., “The Determination of the Elastic Field of an Ellipsoidal Inclusion, and Related Problems,” *Proceedings of the Royal Society A: Mathematical, Physical and Engineering Sciences*, Vol. 241, No. 1226, Aug. 1957, pp. 376–396. doi:[10.1098/rspa.1957.0133](https://doi.org/10.1098/rspa.1957.0133).
- [49] Mori, T. and Tanaka, K., “Average stress in matrix and average elastic energy of materials with misfitting inclusions,” *Acta Metallurgica*, Vol. 21, No. 5, May 1973, pp. 571–574. doi:[10.1016/0001-6160\(73\)90064-3](https://doi.org/10.1016/0001-6160(73)90064-3).
- [50] Takao, Y., Taya, M., and Chou, T. W., “Stress Field Due to a Cylindrical Inclusion With Constant Axial Eigenstrain in an Infinite Elastic Body,” *Journal of Applied Mechanics*, Vol. 48, No. 4, 1981, pp. 853. doi:[10.1115/1.3157745](https://doi.org/10.1115/1.3157745).

- [51] Taya, M. and Chou, T.-W., “On two kinds of ellipsoidal inhomogeneities in an infinite elastic body: An application to a hybrid composite,” *International Journal of Solids and Structures*, Vol. 17, No. 6, Jan. 1981, pp. 553–563. doi:[10.1016/0020-7683\(81\)90018-4](https://doi.org/10.1016/0020-7683(81)90018-4).
- [52] Taya, M. and Mura, T., “On Stiffness and Strength of an Aligned Short-Fiber Reinforced Composite Containing Penny-Shaped Cracks in the Matrix,” *Journal of Composite Materials*, Vol. 15, No. 3, Jan. 1981, pp. 198–210. doi:[10.1177/002199838101500301](https://doi.org/10.1177/002199838101500301).
- [53] Weng, G., “Some elastic properties of reinforced solids, with special reference to isotropic ones containing spherical inclusions,” *International Journal of Engineering Science*, Vol. 22, No. 7, Jan. 1984, pp. 845–856. doi:[10.1016/0020-7225\(84\)90033-8](https://doi.org/10.1016/0020-7225(84)90033-8).
- [54] Tandon, G. and Weng, G., “Average stress in the matrix and effective moduli of randomly oriented composites,” *Composites Science and Technology*, Vol. 27, No. 2, Jan. 1986, pp. 111–132. doi:[10.1016/0266-3538\(86\)90067-9](https://doi.org/10.1016/0266-3538(86)90067-9).
- [55] Luo, H. and Weng, G., “On eshelby’s in a three-phase cylindrically concentric solid, and the elastic moduli of fiber-reinforced composites,” *Mechanics of Materials*, Vol. 8, No. 2-3, Dec. 1989, pp. 77–88. doi:[10.1016/0167-6636\(89\)90008-2](https://doi.org/10.1016/0167-6636(89)90008-2).
- [56] Mura, T., *Micromechanics of defects in solids*, Martinus Nijhoff Publishers, The Hague, 1982.
- [57] Tandon, G. P. and Weng, G. J., “The effect of aspect ratio of inclusions on the elastic properties of unidirectionally aligned composites,” *Polymer Composites*, Vol. 5, No. 4, Oct. 1984, pp. 327–333. doi:[10.1002/pc.750050413](https://doi.org/10.1002/pc.750050413).
- [58] Benveniste, Y., “A new approach to the application of Mori-Tanaka’s theory in composite materials,” *Mechanics of Materials*, Vol. 6, No. 2, June 1987, pp. 147–157. doi:[10.1016/0167-6636\(87\)90005-6](https://doi.org/10.1016/0167-6636(87)90005-6).
- [59] Prabhakar, P. and Waas, A. M., “Upscaling from a micro-mechanics model to capture laminate compressive strength due to kink banding instability,” *Computational Materials Science*, Vol. 67, Feb. 2013, pp. 40–47. doi:[10.1016/j.commatsci.2012.08.025](https://doi.org/10.1016/j.commatsci.2012.08.025).
- [60] Zhao, Y. H. and Weng, G. J., “Theory of plasticity for a class of inclusion and fiber-reinforced composites,” *Micromechanics and Inhomogeneity*, edited by G. Weng, M. Taya, and H. Abé, Springer, New York, 1990, pp. 599–622. doi:[10.1007/978-1-4613-8919-4_37](https://doi.org/10.1007/978-1-4613-8919-4_37).
- [61] Qiu, Y. P. and Weng, G. J., “A theory of plasticity for porous materials and particle-reinforced composites,” *Journal of Applied Mechanics*, Vol. 59, No. 2, 1992, pp. 261–268. doi:[10.1115/1.2899515](https://doi.org/10.1115/1.2899515).

- [62] Segurado, J., Llorca, J., and González, C., “On the accuracy of mean-field approaches to simulate the plastic deformation of composites,” *Scripta Materialia*, Vol. 46, No. 7, April 2002, pp. 525–529. doi:[10.1016/S1359-6462\(02\)00027-1](https://doi.org/10.1016/S1359-6462(02)00027-1).
- [63] Bažant, Z. P. and Oh, B. H., “Crack band theory for fracture of concrete,” *Matériaux et Constructions*, Vol. 16, No. 3, May 1983, pp. 155–177. doi:[10.1007/BF02486267](https://doi.org/10.1007/BF02486267).
- [64] Rots, G., Nauta, P., Kusters, G. M. A., and Blaauwendraad, J., “Smearred crack approach and fracture localization in concrete,” *HERON*, Vol. 30, No. 1, 1985, pp. 1–48.
- [65] Bažant, Z. P., “Can Multiscale-Multiphysics Methods Predict Softening Damage and Structural Failure?” *International Journal for Multiscale Computational Engineering*, Vol. 8, No. 1, 2010, pp. 61–67. doi:[10.1615/IntJMultCompEng.v8.i1.50](https://doi.org/10.1615/IntJMultCompEng.v8.i1.50).
- [66] Pineda, E., Bednarczyk, B., Waas, A., and Arnold, S., “On multiscale modeling using the generalized method of cells: Preserving energy dissipation across disparate length scales,” *CMC: Computers, Materials & Continua*, Vol. 35, No. 2, 2013, pp. 119–154. doi:[10.3970/cmc.2013.035.119](https://doi.org/10.3970/cmc.2013.035.119).
- [67] Mouritz, A., Bannister, M., Falzon, P., and Leong, K., “Review of applications for advanced three-dimensional fibre textile composites,” *Composites Part A: Applied Science and Manufacturing*, Vol. 30, No. 12, Dec. 1999, pp. 1445–1461. doi:[10.1016/S1359-835X\(99\)00034-2](https://doi.org/10.1016/S1359-835X(99)00034-2).
- [68] Grogan, J., Tekalur, S. A., Shukla, A., Bogdanovich, A., and Coffelt, R. A., “Ballistic resistance of 2D and 3D woven sandwich composites,” *Journal of Sandwich Structures and Materials*, Vol. 9, No. 3, May 2007, pp. 283–302. doi:[10.1177/1099636207067133](https://doi.org/10.1177/1099636207067133).
- [69] Hufenbach, W., Gude, M., and Ebert, C., “Hybrid 3D-textile reinforced composites with tailored property profiles for crash and impact applications,” *Composites Science and Technology*, Vol. 69, No. 9, 2009, pp. 1422 – 1426. doi:[10.1016/j.compscitech.2008.09.033](https://doi.org/10.1016/j.compscitech.2008.09.033).
- [70] Song, X., *Vacuum Assisted Resin Transfer Molding (VARTM): Model Development and Verification*, Ph.D. thesis, Virginia Polytechnic Institute and State University, 2003.
- [71] Chen, R., Dong, C., Liang, Z., Zhang, C., and Wang, B., “Flow modeling and simulation for vacuum assisted resin transfer molding process with the equivalent permeability method,” *Polymer Composites*, Vol. 25, No. 2, April 2004, pp. 146–164. doi:[10.1002/pc.20012](https://doi.org/10.1002/pc.20012).
- [72] Song, S., Waas, A. M., Shahwan, K. W., Xiao, X., and Faruque, O., “Braided textile composites under compressive loads: Modeling the response, strength

- and degradation,” *Composites Science and Technology*, Vol. 67, No. 15-16, Dec. 2007, pp. 3059–3070. doi:[10.1016/j.compscitech.2007.06.008](https://doi.org/10.1016/j.compscitech.2007.06.008).
- [73] AGY, “Advanced Materials: Solutions for Demanding Applications,” 2004, http://www.agy.com/technical_info/graphics_PDFs/Advanced_Materials.pdf.
- [74] DuPont, “Kevlar Technical Guide,” http://www2.dupont.com/Kevlar/en_US/assets/downloads/KEVLAR_Technical_Guide.pdf.
- [75] Herakovich, C. T., *Mechanics of Fibrous Composites*, John Wiley & Sons, Inc., 1998.
- [76] AGY, “High Strength Glass Fibers,” 2006, http://www.agy.com/technical_info/graphics_PDFs/HighStrengthTechPaperEng.pdf.
- [77] Hexcel, “HexTow IM7 Carbon Fiber,” 2010, <http://www.hexcel.com/resources/datasheets/carbon-fiber-data-sheets/im7.pdf>.
- [78] Zhou, Y., Pervin, F., Biswas, M. a., Rangari, V. K., and Jeelani, S., “Fabrication and characterization of montmorillonite clay-filled SC-15 epoxy,” *Materials Letters*, Vol. 60, No. 7, April 2006, pp. 869–873. doi:[10.1016/j.matlet.2005.10.042](https://doi.org/10.1016/j.matlet.2005.10.042).
- [79] Pankow, M., Salvi, A., Waas, A., Yen, C., and Ghiorse, S., “Split Hopkinson pressure bar testing of 3D woven composites,” *Composites Science and Technology*, Vol. 71, No. 9, June 2011, pp. 1196–1208. doi:[10.1016/j.compscitech.2011.03.017](https://doi.org/10.1016/j.compscitech.2011.03.017).
- [80] Quek, S. C., Waas, A. M., Shahwan, K. W., and Agaram, V., “Failure mechanics of triaxially braided carbon composites under combined bending-compression loading,” *Composites Science and Technology*, Vol. 66, No. 14, Nov. 2006, pp. 2548–2556. doi:[10.1016/j.compscitech.2006.01.022](https://doi.org/10.1016/j.compscitech.2006.01.022).
- [81] ASTM Standard D790-10, “Standard test methods for flexural properties of unreinforced and reinforced plastics and electrical insulating materials,” ASTM International, West Conshohocken, PA, 2010. doi:[10.1520/D0790-10](https://doi.org/10.1520/D0790-10).
- [82] Reddy, J. N., *Mechanics of Laminated Composite Plates: Theory and Analysis*, CRC Press, Inc, 1997.
- [83] Lekhnitskii, S. G., Tsai, S. W., and Cheron, T., *Anisotropic Plates*, Gordon and Breach Science Publishers, New York, New York, 1968.
- [84] Budiansky, B. and Fleck, N., “Compressive failure of fibre composites,” *Journal of the Mechanics and Physics of Solids*, Vol. 41, No. 1, Jan. 1993, pp. 183–211. doi:[10.1016/0022-5096\(93\)90068-Q](https://doi.org/10.1016/0022-5096(93)90068-Q).
- [85] Kyriakides, S., Arseculeratne, R., Perry, E. J., and Liechti, K. M., “On the compressive failure of fiber reinforced composites,” *International Journal of Solids and Structures*, Vol. 32, No. 6/7, 1995, pp. 689–738. doi:[10.1016/0020-7683\(94\)00157-R](https://doi.org/10.1016/0020-7683(94)00157-R).

- [86] Schultheisz, C. R. and Waas, A. M., “Compressive failure of composites, part I: Testing and micromechanical theories,” *Progress in Aerospace Sciences*, Vol. 32, No. 1, Jan. 1996, pp. 1–42. doi:[10.1016/0376-0421\(94\)00002-3](https://doi.org/10.1016/0376-0421(94)00002-3).
- [87] Waas, A. M. and Schultheisz, C. R., “Compressive failure of composites, part II: Experimental studies,” *Progress in Aerospace Sciences*, Vol. 32, No. 1, Jan. 1996, pp. 43–78. doi:[10.1016/0376-0421\(94\)00003-4](https://doi.org/10.1016/0376-0421(94)00003-4).
- [88] Lee, S. H. and Waas, A. M., “Compressive response and failure of fiber reinforced unidirectional composites,” *International Journal of Fracture*, Vol. 100, No. 3, 1999, pp. 275–306. doi:[10.1023/A:1018779307931](https://doi.org/10.1023/A:1018779307931).
- [89] Basu, S., Waas, A. M., and Ambur, D. R., “A macroscopic model for kink banding instabilities in fiber composites,” *Journal of Mechanics of Materials and Structures*, Vol. 1, No. 6, 2006.
- [90] Feld, N., Allix, O., Baranger, E., and Guimard, J.-M., “Micro-mechanical prediction of UD laminates behavior under combined compression up to failure: influence of matrix degradation,” *Journal of Composite Materials*, Vol. 45, No. 22, July 2011, pp. 2317–2333. doi:[10.1177/0021998311401084](https://doi.org/10.1177/0021998311401084).
- [91] Feld, N., Allix, O., Baranger, E., and Guimard, J.-M., “A micromechanics-based mesomodel for unidirectional laminates in compression up to failure,” *Journal of Composite Materials*, Vol. 46, No. 23, Jan. 2012, pp. 2893–2909. doi:[10.1177/0021998311434170](https://doi.org/10.1177/0021998311434170).
- [92] Prabhakar, P. and Waas, A. M., “Interaction between kinking and splitting in the compressive failure of unidirectional fiber reinforced laminated composites,” *Composite Structures*, Vol. 98, April 2013, pp. 85–92. doi:[10.1016/j.compstruct.2012.11.005](https://doi.org/10.1016/j.compstruct.2012.11.005).
- [93] Kachanov, L. M., “On the Time to Rupture under Creep Conditions,” *Izvestiya Akademii Nauk SSSR, Otdeleniya Tekhnika Nauk*, Vol. 8, No. 1, 1958, pp. 26 – 31.
- [94] Kachanov, L. M., *Introduction to Continuum Damage Mechanics*, Martinus Nijhoff Publishers, Dordrecht, The Netherlands, 1986.
- [95] Lemaitre, J., *A Course on Damage Mechanics*, Springer-Verlag, Berlin, Heidelberg, New York, 2nd ed., 1996.
- [96] Lemaitre, J. and Chaboche, J.-L., *Mechanics of Solid Materials*, Cambridge University Press.
- [97] Lemaitre, J. and Desmorat, R., *Engineering Damage Mechanics*, Springer-Verlag, Berlin, Heidelberg, New York, 2005.
- [98] Skrzypek, J. J., *Anisotropic Behavior of Damaged Materials*, Springer-Verlag, Berlin, Heidelberg, New York, 2003.

- [99] Krajcinovic, D., *Damage Mechanics*, Elsevier, Amsterdam, The Netherlands, 1996.
- [100] Dvorak, G. J., Laws, N., and Hejazi, M., “Analysis of progressive matrix cracking in composite laminates I. Thermoelastic properties of a ply with cracks,” *Journal of Composite Materials*, Vol. 19, No. 3, Jan. 1985, pp. 216–234. doi:[10.1177/002199838501900302](https://doi.org/10.1177/002199838501900302).
- [101] Talreja, R., “A Continuum Mechanics Characterization of Damage in Composite Materials,” *Proceedings of the Royal Society of London. A. Mathematical and Physical Sciences*, Vol. 399, No. 1817, 1985, pp. 195–216. doi:[10.1098/rspa.1985.0055](https://doi.org/10.1098/rspa.1985.0055).
- [102] Talreja, R., “Transverse Cracking and Stiffness Reduction in Composite Laminates,” *Journal of Composite Materials*, Vol. 19, No. 4, Jan. 1985, pp. 355–375. doi:[10.1177/002199838501900404](https://doi.org/10.1177/002199838501900404).
- [103] Matzenmiller, A., Lubliner, J., and Taylor, R., “A constitutive model for anisotropic damage in fiber-composites,” *Mechanics of Materials*, Vol. 20, No. 2, April 1995, pp. 125–152. doi:[10.1016/0167-6636\(94\)00053-0](https://doi.org/10.1016/0167-6636(94)00053-0).
- [104] Maimí, P., Camanho, P., Mayugo, J., and Dávila, C., “A continuum damage model for composite laminates: Part I Constitutive model,” *Mechanics of Materials*, Vol. 39, No. 10, Oct. 2007, pp. 897–908. doi:[10.1016/j.mechmat.2007.03.005](https://doi.org/10.1016/j.mechmat.2007.03.005).
- [105] Maimí, P., Camanho, P., Mayugo, J., and Dávila, C., “A continuum damage model for composite laminates: Part II Computational implementation and validation,” *Mechanics of Materials*, Vol. 39, No. 10, Oct. 2007, pp. 909–919. doi:[10.1016/j.mechmat.2007.03.006](https://doi.org/10.1016/j.mechmat.2007.03.006).
- [106] Pijaudier-Cabot, G. and Bažant, Z. P., “Nonlocal damage theory,” *Journal of Engineering Mechanics*, Vol. 113, No. 10, Oct. 1987, pp. 1512–1533. doi:[10.1061/\(ASCE\)0733-9399\(1987\)113:10\(1512\)](https://doi.org/10.1061/(ASCE)0733-9399(1987)113:10(1512)).
- [107] Jirásek, M., “Comparative study on finite elements with embedded discontinuities,” *Computer Methods in Applied Mechanics and Engineering*, Vol. 188, No. 1-3, July 2000, pp. 307–330. doi:[10.1016/S0045-7825\(99\)00154-1](https://doi.org/10.1016/S0045-7825(99)00154-1).
- [108] Askes, H., Pamin, J., and de Borst, R., “Dispersion analysis and element-free Galerkin solutions of second- and fourth-order gradient-enhanced damage models,” *International Journal for Numerical Methods in Engineering*, Vol. 49, No. 6, Oct. 2000, pp. 811–832. doi:[10.1002/1097-0207\(20001030\)49:6<811::AID-NME985>3.0.CO;2-9](https://doi.org/10.1002/1097-0207(20001030)49:6<811::AID-NME985>3.0.CO;2-9).
- [109] Pamin, J., Askes, H., and de Borst, R., “Two gradient plasticity theories discretized with the element-free Galerkin method,” *Computer Methods in Applied Mechanics and Engineering*, Vol. 192, No. 20-21, May 2003, pp. 2377–2403. doi:[10.1016/S0045-7825\(03\)00263-9](https://doi.org/10.1016/S0045-7825(03)00263-9).

- [110] Park, S. and Schapery, R., “A viscoelastic constitutive model for particulate composites with growing damage,” *International Journal of Solids and Structures*, Vol. 34, No. 8, March 1997, pp. 931–947. doi:[10.1016/S0020-7683\(96\)00066-2](https://doi.org/10.1016/S0020-7683(96)00066-2).
- [111] Schapery, R., “A theory of mechanical behavior of elastic media with growing damage and other changes in structure,” *Journal of the Mechanics and Physics of Solids*, Vol. 38, No. 2, Jan. 1990, pp. 215–253. doi:[10.1016/0022-5096\(90\)90035-3](https://doi.org/10.1016/0022-5096(90)90035-3).
- [112] Puck, A., “Failure analysis of FRP laminates by means of physically based phenomenological models,” *Composites Science and Technology*, Vol. 58, No. 7, July 1998, pp. 1045–1067. doi:[10.1016/S0266-3538\(96\)00140-6](https://doi.org/10.1016/S0266-3538(96)00140-6).
- [113] Puck, A. and Schürmann, H., “Failure analysis of FRP laminates by means of physically based phenomenological models,” *Composites Science and Technology*, Vol. 62, No. 12-13, Sept. 2002, pp. 1633–1662. doi:[10.1016/S0266-3538\(01\)00208-1](https://doi.org/10.1016/S0266-3538(01)00208-1).
- [114] Camanho, P. P., Dávila, C. G., Pinho, S. T., Iannucci, L., and Robinson, P., “Prediction of in situ strengths and matrix cracking in composites under transverse tension and in-plane shear,” *Composites Part A: Applied Science and Manufacturing*, Vol. 37, No. 2, Feb. 2006, pp. 165–176. doi:[10.1016/j.compositesa.2005.04.023](https://doi.org/10.1016/j.compositesa.2005.04.023).
- [115] Camanho, P., Maimí, P., and Dávila, C., “Prediction of size effects in notched laminates using continuum damage mechanics,” *Composites Science and Technology*, Vol. 67, No. 13, Oct. 2007, pp. 2715–2727. doi:[10.1016/j.compscitech.2007.02.005](https://doi.org/10.1016/j.compscitech.2007.02.005).
- [116] Pineda, E. J., Bednarczyk, B. A., Waas, A. M., and Arnold, S. M., “Progressive failure of a unidirectional fiber-reinforced composite using the method of cells: Discretization objective computational results,” *International Journal of Solids and Structures*, Vol. 50, No. 9, May 2013, pp. 1203–1216. doi:[10.1016/j.ijsolstr.2012.12.003](https://doi.org/10.1016/j.ijsolstr.2012.12.003).
- [117] Sicking, D. L., *Mechanical Characterization of Nonlinear Laminated Composites with Transverse Crack Growth*, Ph.D. thesis, Texas A&M University, 1992.
- [118] Rots, J. G., “Smearred and discrete representations of localized fracture,” *International Journal of Fracture*, Vol. 51, No. 1, Sept. 1991, pp. 45–59. doi:[10.1007/BF00020852](https://doi.org/10.1007/BF00020852).
- [119] Heinrich, C. and Waas, A. M., “Investigation of progressive damage and fracture in laminated composites using the smeared crack approach,” *Proceedings of the 53rd AIAA/ASME/ASCE/AHS/ASC Structures, Structural Dynamics, and Materials Conference, Honolulu, Hawaii, USA., 2012*, AIAA 2012-1537.

- [120] de Borst, R. and Nauta, P., “Non-orthogonal cracks in a smeared finite element model,” *Engineering Computations*, Vol. 2, No. 1, 1985, pp. 35–46. doi:[10.1108/eb023599](https://doi.org/10.1108/eb023599).
- [121] Bažant, Z. P. and Gambarova, P. G., “Rough cracks in reinforced concrete,” *Journal of the Structural Division*, Vol. 106, 1980, pp. 819–842.
- [122] Walraven, J. C., *Aggregate Interlock: A Theoretical and Experimental Analysis.*, Ph.D. thesis, Delft University of Technology, 1980.
- [123] Walraven, J. C. and Reinhardt, H. W., “Theory and experiments on the mechanical behaviour of cracks in plain and reinforced concrete subjected to shear loading,” *HERON*, Vol. 26, No. 1A.
- [124] Gambarova, P. G. and Karakoç, C., “A new approach to the analysis of the confinement role in regularly cracked concrete elements,” *Transactions 7th SMIRT Conference H (Paper H5/7)(Chicago, 1983)*, 1983, pp. 251–261.
- [125] de Borst, R., “Fracture in quasi-brittle materials: a review of continuum damage-based approaches,” *Engineering Fracture Mechanics*, Vol. 69, No. 2, Jan. 2002, pp. 95–112. doi:[10.1016/S0013-7944\(01\)00082-0](https://doi.org/10.1016/S0013-7944(01)00082-0).
- [126] Ortiz, M. and Pandolfi, A., “Finite-deformation irreversible cohesive elements for three-dimensional crack-propagation analysis,” *International Journal for Numerical Methods in Engineering*, Vol. 44, No. 9, 1999, pp. 1267–1282. doi:[10.1002/\(SICI\)1097-0207\(19990330\)44:9<1267::AID-NME486>3.0.CO;2-7](https://doi.org/10.1002/(SICI)1097-0207(19990330)44:9<1267::AID-NME486>3.0.CO;2-7).
- [127] Hoek, E. and Bieniawski, Z., “Brittle fracture propagation in rock under compression,” *International Journal of Fracture Mechanics*, Vol. 1, No. 3, Sept. 1965, pp. 137–155. doi:[10.1007/BF00186851](https://doi.org/10.1007/BF00186851).
- [128] Horii, H. . and Nemat-Nasser, S., “Brittle failure in compression: splitting, faulting and brittle-ductile transition,” *Philosophical Transactions of the Royal Society of London . Series A , Mathematical and Physical Science*, Vol. 319, No. 1549, 1986, pp. 337–374.
- [129] Ashby, M. F. and Sammis, C. G., “The damage mechanics of brittle solids in compression,” *Pure and Applied Geophysics PAGEOPH*, Vol. 133, No. 3, May 1990, pp. 489–521. doi:[10.1007/BF00878002](https://doi.org/10.1007/BF00878002).
- [130] Chen, W. and Ravichandran, G., “Failure mode transition in ceramics under dynamic multiaxial compression,” *International Journal of Fracture*, Vol. 101, No. 1-2, 2000, pp. 141–159. doi:[10.1023/A:1007672422700](https://doi.org/10.1023/A:1007672422700).
- [131] Fung, Y. C. and Tong, P., *Classical and Computational Solid Mechanics*, World Scientific, 2001.
- [132] Chen, W.-F. and Han, D.-J., *Plasticity for Structural Engineers*, J. Ross Publishing, 2007.

- [133] Wang, M. L., McAninch, I. M., and La Scale, J. J., “Materials characterization of high-temperature epoxy resin: SC-79 and SC-15/SC-79 blend,” Tech. rep., Army Research Laboratory, March 2011, ARL-TR-5484.
- [134] Aboudi, J., Arnold, S. M., and Bednarczyk, B. A., *Micromechanics of Composite Materials: A Generalized Multiscale Analysis Approach*, Elsevier, 1st ed., 2013.
- [135] Nemat-Nasser, S., Iwakuma, T., and Hejazi, M., “On composites with periodic structure,” *Mechanics of Materials*, Vol. 1, No. 3, Sept. 1982, pp. 239–267. doi:[10.1016/0167-6636\(82\)90017-5](https://doi.org/10.1016/0167-6636(82)90017-5).
- [136] Accorsi, M. and Nemat-Nasser, S., “Bounds on the overall elastic and instantaneous elastoplastic moduli of periodic composites,” *Mechanics of Materials*, Vol. 5, No. 3, Sept. 1986, pp. 209–220. doi:[10.1016/0167-6636\(86\)90018-9](https://doi.org/10.1016/0167-6636(86)90018-9).
- [137] Dvorak, G. J. and Benveniste, Y., “On transformation strains and uniform fields in multiphase elastic media,” *Proceedings: Mathematical and Physical Sciences*, Vol. 437, No. 1900, 1992, pp. 291–310.
- [138] Dvorak, G. J., “Transformation field analysis of inelastic composite materials,” *Proceedings: Mathematical and Physical Sciences*, Vol. 437, No. 1900, 1992, pp. 311–327.
- [139] Michel, J. and Suquet, P., “Nonuniform transformation field analysis,” *International Journal of Solids and Structures*, Vol. 40, No. 25, Dec. 2003, pp. 6937–6955. doi:[10.1016/S0020-7683\(03\)00346-9](https://doi.org/10.1016/S0020-7683(03)00346-9).
- [140] Ponte Castañeda, P., “Exact second-order estimates for the effective mechanical properties of nonlinear composite materials,” *Journal of the Mechanics and Physics of Solids*, Vol. 44, No. 6, June 1996, pp. 827–862. doi:[10.1016/0022-5096\(96\)00015-4](https://doi.org/10.1016/0022-5096(96)00015-4).
- [141] Ponte Castañeda, P., “Second-order homogenization estimates for nonlinear composites incorporating field fluctuations: I–theory,” *Journal of the Mechanics and Physics of Solids*, Vol. 50, No. 4, April 2002, pp. 737–757. doi:[10.1016/S0022-5096\(01\)00099-0](https://doi.org/10.1016/S0022-5096(01)00099-0).
- [142] Ponte Castañeda, P., “Second-order homogenization estimates for nonlinear composites incorporating field fluctuations: II–applications,” *Journal of the Mechanics and Physics of Solids*, Vol. 50, No. 4, April 2002, pp. 759–782. doi:[10.1016/S0022-5096\(01\)00098-9](https://doi.org/10.1016/S0022-5096(01)00098-9).
- [143] Aboudi, J., *Mechanics of Composite Materials: A Unified Micromechanical Approach*, Elsevier, Amsterdam, 1991.
- [144] Paley, M. and Aboudi, J., “Micromechanical analysis of composites by the generalized cells model,” *Mechanics of Materials*, Vol. 14, No. 2, Dec. 1992, pp. 127–139. doi:[10.1016/0167-6636\(92\)90010-B](https://doi.org/10.1016/0167-6636(92)90010-B).

- [145] Aboudi, J., Pindera, M.-J., and Arnold, S. M., “Linear thermoelastic higher-order theory for periodic multiphase materials,” *Journal of Applied Mechanics*, Vol. 68, No. 5, 2001, pp. 697–707. doi:[10.1115/1.1381005](https://doi.org/10.1115/1.1381005).
- [146] Aboudi, J., Pindera, M.-J., and Arnold, S. M., “Higher-order theory for periodic multiphase materials with inelastic phases,” *International Journal of Plasticity*, Vol. 19, No. 6, June 2003, pp. 805–847. doi:[10.1016/S0749-6419\(02\)00007-4](https://doi.org/10.1016/S0749-6419(02)00007-4).
- [147] Haj-Ali, R. and Aboudi, J., “Nonlinear micromechanical formulation of the high fidelity generalized method of cells,” *International Journal of Solids and Structures*, Vol. 46, No. 13, June 2009, pp. 2577–2592. doi:[10.1016/j.ijsolstr.2009.02.004](https://doi.org/10.1016/j.ijsolstr.2009.02.004).
- [148] Bednarczyk, B. A., Arnold, S. M., Aboudi, J., and Pindera, M.-J., “Local field effects in titanium matrix composites subject to fiber-matrix debonding,” *International Journal of Plasticity*, Vol. 20, No. 8-9, Aug. 2004, pp. 1707–1737. doi:[10.1016/j.ijplas.2003.11.019](https://doi.org/10.1016/j.ijplas.2003.11.019).
- [149] Bednarczyk, B. A., Aboudi, J., and Arnold, S. M., “Micromechanics modeling of composites subjected to multiaxial progressive damage in the constituents,” *AIAA Journal*, Vol. 48, No. 7, July 2010, pp. 1367–1378. doi:[10.2514/1.45671](https://doi.org/10.2514/1.45671).
- [150] Haj-Ali, R. and Aboudi, J., “Formulation of the high-fidelity generalized method of cells with arbitrary cell geometry for refined micromechanics and damage in composites,” *International Journal of Solids and Structures*, Vol. 47, No. 25-26, Dec. 2010, pp. 3447–3461. doi:[10.1016/j.ijsolstr.2010.08.022](https://doi.org/10.1016/j.ijsolstr.2010.08.022).
- [151] Sun, C. and Vaidya, R., “Prediction of composite properties from a representative volume element,” *Composites Science and Technology*, Vol. 56, No. 2, Jan. 1996, pp. 171–179. doi:[10.1016/0266-3538\(95\)00141-7](https://doi.org/10.1016/0266-3538(95)00141-7).
- [152] Xia, Z., Zhang, Y., and Ellyin, F., “A unified periodical boundary conditions for representative volume elements of composites and applications,” *International Journal of Solids and Structures*, Vol. 40, No. 8, April 2003, pp. 1907–1921. doi:[10.1016/S0020-7683\(03\)00024-6](https://doi.org/10.1016/S0020-7683(03)00024-6).
- [153] González, C. and LLorca, J., “Mechanical behavior of unidirectional fiber-reinforced polymers under transverse compression: Microscopic mechanisms and modeling,” *Composites Science and Technology*, Vol. 67, No. 13, Oct. 2007, pp. 2795–2806. doi:[10.1016/j.compscitech.2007.02.001](https://doi.org/10.1016/j.compscitech.2007.02.001).
- [154] Drugan, W. and Willis, J., “A micromechanics-based nonlocal constitutive equation and estimates of representative volume element size for elastic composites,” *Journal of the Mechanics and Physics of Solids*, Vol. 44, No. 4, April 1996, pp. 497–524. doi:[10.1016/0022-5096\(96\)00007-5](https://doi.org/10.1016/0022-5096(96)00007-5).
- [155] Segurado, J. and Llorca, J., “A numerical approximation to the elastic properties of sphere-reinforced composites,” *Journal of the Mechanics and Physics*

- of Solids*, Vol. 50, No. 10, Oct. 2002, pp. 2107–2121. doi:[10.1016/S0022-5096\(02\)00021-2](https://doi.org/10.1016/S0022-5096(02)00021-2).
- [156] Totry, E., González, C., and LLorca, J., “Influence of the loading path on the strength of fiber-reinforced composites subjected to transverse compression and shear,” *International Journal of Solids and Structures*, Vol. 45, No. 6, March 2008, pp. 1663–1675. doi:[10.1016/j.ijsolstr.2007.10.014](https://doi.org/10.1016/j.ijsolstr.2007.10.014).
- [157] Heinrich, C., Aldridge, M., Wineman, a. S., Kieffer, J., Waas, a. M., and Shahwan, K., “The influence of the representative volume element (RVE) size on the homogenized response of cured fiber composites,” *Modelling and Simulation in Materials Science and Engineering*, Vol. 20, No. 7, Oct. 2012, pp. 075007. doi:[10.1088/0965-0393/20/7/075007](https://doi.org/10.1088/0965-0393/20/7/075007).
- [158] Totry, E., González, C., and LLorca, J., “Prediction of the failure locus of C/PEEK composites under transverse compression and longitudinal shear through computational micromechanics,” *Composites Science and Technology*, Vol. 68, No. 15-16, Dec. 2008, pp. 3128–3136. doi:[10.1016/j.compscitech.2008.07.011](https://doi.org/10.1016/j.compscitech.2008.07.011).
- [159] Totry, E., Molina-Aldareguía, J. M., González, C., and LLorca, J., “Effect of fiber, matrix and interface properties on the in-plane shear deformation of carbon-fiber reinforced composites,” *Composites Science and Technology*, Vol. 70, No. 6, June 2010, pp. 970–980. doi:[10.1016/j.compscitech.2010.02.014](https://doi.org/10.1016/j.compscitech.2010.02.014).
- [160] Hyer, M. W. and Wass, A. M., “1.12 - Micromechanics of Linear Elastic Continuous Fiber Composites,” *Comprehensive Composite Materials*, edited by E. in Chief: Anthony Kelly and C. Zweben, Pergamon, Oxford, 2000, pp. 345 – 375. doi:[10.1016/B0-08-042993-9/00049-8](https://doi.org/10.1016/B0-08-042993-9/00049-8).
- [161] Christensen, R. M., “A critical evaluation for a class of micro-mechanics models,” *Journal of the Mechanics and Physics of Solids*, Vol. 38, No. 3, Jan. 1990, pp. 379–404. doi:[10.1016/0022-5096\(90\)90005-O](https://doi.org/10.1016/0022-5096(90)90005-O).
- [162] Hashin, Z., “Failure Criteria for Unidirectional Fiber Composites,” *Journal of Applied Mechanics*, Vol. 47, No. 2, 1980, pp. 329. doi:[10.1115/1.3153664](https://doi.org/10.1115/1.3153664).
- [163] Vogler, T., Hsu, S.-Y., and Kyriakides, S., “On the initiation and growth of kink bands in fiber composites. Part II: analysis,” *International Journal of Solids and Structures*, Vol. 38, No. 15, April 2001, pp. 2653–2682. doi:[10.1016/S0020-7683\(00\)00175-X](https://doi.org/10.1016/S0020-7683(00)00175-X).
- [164] Hsu, S.-Y., Vogler, T., and Kyriakides, S., “On the axial propagation of kink bands in fiber composites : Part II analysis,” *International Journal of Solids and Structures*, Vol. 36, No. 4, Feb. 1999, pp. 575–595. doi:[10.1016/S0020-7683\(98\)00030-4](https://doi.org/10.1016/S0020-7683(98)00030-4).

- [165] Yerramalli, C. S. and Waas, A. M., “The effect of fiber diameter on the compressive strength of composites - A 3D finite element based study,” *Computer Modeling in Engineering & Sciences*, Vol. 6, No. 1, 2004, pp. 1–16. doi:[10.3970/cmcs.2004.006.001](https://doi.org/10.3970/cmcs.2004.006.001).
- [166] Hill, R., “A theory of the yielding and plastic flow of anisotropic metals,” *Proceedings of the Royal Society A: Mathematical, Physical and Engineering Sciences*, Vol. 193, No. 1033, May 1948, pp. 281–297. doi:[10.1098/rspa.1948.0045](https://doi.org/10.1098/rspa.1948.0045).
- [167] Cox, B. N. and Dadkhah, M. S., “The macroscopic elasticity of 3D woven composites,” *Journal of Composite Materials*, Vol. 29, No. 6, April 1995, pp. 785–819. doi:[10.1177/002199839502900606](https://doi.org/10.1177/002199839502900606).
- [168] Yerramalli, C. S. and Waas, A. M., “In situ matrix shear response using torsional test data of fiber reinforced unidirectional polymer composites,” *Journal of Engineering Materials and Technology*, Vol. 124, No. 2, 2002, pp. 152. doi:[10.1115/1.1446471](https://doi.org/10.1115/1.1446471).
- [169] Ng, W. H., Salvi, A. G., and Waas, A. M., “Characterization of the in-situ non-linear shear response of laminated fiber-reinforced composites,” *Composites Science and Technology*, Vol. 70, No. 7, July 2010, pp. 1126–1134. doi:[10.1016/j.compscitech.2010.02.024](https://doi.org/10.1016/j.compscitech.2010.02.024).
- [170] Laffan, M., Pinho, S., Robinson, P., Iannucci, L., and McMillan, A., “Measurement of the fracture toughness associated with the longitudinal fibre compressive failure mode of laminated composites,” *Composites Part A: Applied Science and Manufacturing*, Vol. 43, No. 11, Nov. 2012, pp. 1930–1938. doi:[10.1016/j.compositesa.2012.04.009](https://doi.org/10.1016/j.compositesa.2012.04.009).
- [171] Pandya, K. S., Pothnis, J. R., Ravikumar, G., and Naik, N., “Ballistic impact behavior of hybrid composites,” *Materials & Design*, Vol. 44, Feb. 2013, pp. 128–135. doi:[10.1016/j.matdes.2012.07.044](https://doi.org/10.1016/j.matdes.2012.07.044).
- [172] Lomov, S., Verpoest, I., Peeters, T., Roose, D., and Zako, M., “Nesting in textile laminates: geometrical modelling of the laminate,” *Composites Science and Technology*, Vol. 63, No. 7, May 2003, pp. 993–1007. doi:[10.1016/S0266-3538\(02\)00318-4](https://doi.org/10.1016/S0266-3538(02)00318-4).
- [173] Karahan, M., Lomov, S. V., Bogdanovich, A. E., Mungalov, D., and Verpoest, I., “Internal geometry evaluation of non-crimp 3D orthogonal woven carbon fabric composite,” *Composites Part A: Applied Science and Manufacturing*, Vol. 41, No. 9, Sept. 2010, pp. 1301–1311. doi:[10.1016/j.compositesa.2010.05.014](https://doi.org/10.1016/j.compositesa.2010.05.014).
- [174] Desplentere, F., Lomov, S., Woerdeman, D., Verpoest, I., Wevers, M., and Bogdanovich, A., “Micro-CT characterization of variability in 3D textile architecture,” *Composites Science and Technology*, Vol. 65, No. 13, Oct. 2005, pp. 1920–1930. doi:[10.1016/j.compscitech.2005.04.008](https://doi.org/10.1016/j.compscitech.2005.04.008).

- [175] Whitcomb, J. D., Chapman, C. D., and Tang, X., “Derivation of Boundary Conditions for Micromechanics Analyses of Plain and Satin Weave Composites,” *Journal of Composite Materials*, Vol. 34, No. 9, May 2000, pp. 724–747. doi:[10.1177/002199830003400901](https://doi.org/10.1177/002199830003400901).
- [176] Tang, X. and Whitcomb, J. D., “General Techniques for Exploiting Periodicity and Symmetries in Micromechanics Analysis of Textile Composites,” *Journal of Composite Materials*, Vol. 37, No. 13, July 2003, pp. 1167–1189. doi:[10.1177/0021998303037013003](https://doi.org/10.1177/0021998303037013003).
- [177] Lomov, S., Ivanov, D., Verpoest, I., Zako, M., Kurashiki, T., Nakai, H., and Hirose, S., “Meso-FE modelling of textile composites: Road map, data flow and algorithms,” *Composites Science and Technology*, Vol. 67, No. 9, July 2007, pp. 1870–1891. doi:[10.1016/j.compscitech.2006.10.017](https://doi.org/10.1016/j.compscitech.2006.10.017).
- [178] Murakami, S., “Mechanical modeling of material damage,” *Journal of Applied Mechanics*, Vol. 55, No. 2, 1988, pp. 280. doi:[10.1115/1.3173673](https://doi.org/10.1115/1.3173673).
- [179] Ladèveze, P. and Lubineau, G., “An enhanced mesomodel for laminates based on micromechanics,” *Composites Science and Technology*, Vol. 62, No. 4, March 2002, pp. 533–541. doi:[10.1016/S0266-3538\(01\)00145-2](https://doi.org/10.1016/S0266-3538(01)00145-2).
- [180] SIMULIA, *Abqus Analysis User’s Manual, 6.12 edition*, Dassault Systems, 2012.
- [181] Pankow, M., Justusson, B., Rudolph, M., Waas, A. M., and Yen, C. F., “Effect of Z-fiber architecture on tensile fracture of 3D textile composites,” *International Journal of Solids and Structures*, in preparation.
- [182] Ting, T. C. T., *Anisotropic Elasticity: Theory and Applications*, Oxford University Press, New York, Oxford, 1996.
- [183] Timoshenko, S. P. and Goodier, J. N., *Theory of Elasticity*, McGraw-Hill, New York, 3rd ed., 1970.
- [184] Knott, T. W. and Herakovich, C. T., *Effect of Fiber Morphology on Composite Properties*, Virginia Polytechnic Institute and State University, Blacksburg, 1988.
- [185] Knott, T. W. and Herakovich, C. T., “Effect of fiber orthotropy on effective composite properties,” *Journal of Composite Materials*, Vol. 25, No. 6, 1991, pp. 732–759. doi:[10.1177/002199839102500607](https://doi.org/10.1177/002199839102500607).